

Investigating Neurovascular Coupling with Simultaneous High-Resolution fMRI and Calcium Recordings in Rats

Dissertation

der Mathematisch-Naturwissenschaftlichen Fakultät
der Eberhard Karls Universität Tübingen
zur Erlangung des Grades eines
Doktors der Naturwissenschaften
(Dr. rer. nat.)

vorgelegt von
Xuming Chen
aus Chongqing, China

Tübingen
2021

Gedruckt mit Genehmigung der Mathematisch-Naturwissenschaftlichen Fakultät der Eberhard Karls Universität Tübingen.

Tag der mündlichen Qualifikation:	08.11.2021
Dekan:	Prof. Dr. Thilo Stehle
1. Berichterstatter:	Prof. Dr. Hanspeter A. Mallot
2. Berichterstatter:	Assistant Prof. Dr. Xin Yu

Erklärung/Declaration

„Ich erkläre hiermit, dass ich die zur Promotion eingereichte Arbeit mit dem Titel: “ Investigating Neurovascular Coupling with Simultaneous High-resolution fMRI and Calcium Recordings in Rats” selbständig verfasst, nur die angegebenen Quellen und Hilfsmittel benutzt und wörtlich oder inhaltlich übernommene Stellen (alternativ: Zitate) als solche gekennzeichnet habe. Ich erkläre, dass die Richtlinien zur Sicherung guter wissenschaftlicher Praxis der Universität Tübingen (Beschluss des Senats vom 25.5.2000) beachtet wurden. Ich Amtliche Bekanntmachungen der Universität Tübingen 2015, Nr.5, S. 154 versichere an Eides statt, dass diese Angaben wahr sind und dass ich nichts verschwiegen habe. Mir ist bekannt, dass die falsche Abgabe einer Versicherung an Eides statt mit Freiheitsstrafe bis zu drei Jahren oder mit Geldstrafe bestraft wird.“

“I hereby declare that the thesis I submit for my doctorate with the title: “Investigating Neurovascular Coupling with Simultaneous High-resolution fMRI and Calcium Recordings in Rats” is my own independent work, that I used only the sources and resources cited and have clearly indicated all content adopted either word-for-word or in substance. I declare that the University of Tübingen’s guidelines to ensure good academic practice (Senate decision of 25.5.2000) have been observed. I solemnly swear that this information is true and that I have not concealed any relevant information. I am aware that making a false declaration is punishable by a fine or by a prison term of up to three years.”

Tübingen, den-----
Datum / Date

Unterschrift / Signature

Contents

ABBREVIATIONS -----	6
SUMMARY -----	7
ZUSAMMENFASSUNG -----	9
1. INTRODUCTION -----	11
1.1. FUNCTIONAL MAGNETIC RESONANCE IMAGING (fMRI) -----	11
1.1.1. BOLD Contrast-----	11
1.1.2. CBV fMRI-----	13
1.1.3. MRI-based Measurement of CBF-----	14
1.2. CELLULAR BASIS OF NEUROVASCULAR COUPLING (NVC) -----	15
1.2.1. Neurons-----	16
1.2.2. Astrocytes-----	17
2. LIST OF APPENDED MANUSCRIPTS AND STATEMENT OF CONTRIBUTIONS -----	19
3. OWN WORK -----	21
3.1. ULTRA-SLOW SINGLE-VESSEL BOLD AND CBV-BASED fMRI SPATIOTEMPORAL DYNAMICS AND THEIR CORRELATION WITH NEURONAL INTRACELLULAR CALCIUM SIGNALS -----	21
3.1.1. Background and Hypotheses-----	21
3.1.2. Results and Discussion-----	21
3.1.3. Conclusion-----	22
3.2. MAPPING OPTOGENETICALLY-DRIVEN SINGLE-VESSEL fMRI WITH CONCURRENT NEURONAL CALCIUM RECORDINGS IN THE RAT HIPPOCAMPUS -----	23
3.2.1. Background and Hypotheses-----	23
3.2.2. Results and Discussion-----	23
3.2.3. Conclusion-----	24
3.3. SINGLE-VESSEL CEREBRAL BLOOD VELOCITY fMRI TO MAP BLOOD VELOCITY BY PHASE-CONTRAST IMAGING -----	25
3.3.1. Background and Hypotheses-----	25
3.3.2. Results and Discussion-----	25
3.3.3. Conclusion-----	26
3.4. MRI-GUIDED ROBOTIC ARM DRIVES OPTOGENETIC fMRI WITH CONCURRENT Ca²⁺ RECORDING -----	27
3.4.1. Background and Hypotheses-----	27
3.4.2. Results and Discussion-----	27
3.4.3. Conclusion-----	28
4. SUMMARY AND OUTLOOK -----	29
5. REFERENCES -----	31
6. ACKNOWLEDGMENTS -----	39

Abbreviations

ASL: arterial spin labeling

A-V map: arteriole-venule map

B_0 : static magnetic field

BOLD: blood oxygen level dependent

bSSFP: balanced steady-state free precession

CBV: cerebral blood volume

CBF: cerebral blood flow

CMRO₂: cerebral metabolic rate of oxygen

Ca: calcium

ChR2: channelrhodopsin-2

COX-2: cyclooxygenase 2

Deoxy-Hb: deoxygenated hemoglobin

DSC: dynamic susceptibility contrast

fMRI: functional magnetic resonance imaging

GCaMP: green fluorescent protein (GFP)-Calmodulin fusion protein

GECIs: genetically encoded calcium indicators

IONs: iron oxide nanoparticles

LFP: local field potential

LH: lateral hypothalamus

MGE: multiple gradient echo

MgRA: MRI-guided robotic arm

MRI: magnetic resonance imaging

NO: nitric oxide

NVC: neurovascular coupling

NVCe: neurovascular coupling efficiency

Oxy-Hb: oxygenated hemoglobin

PC: phase-contrast

SDL: spreading depression-like

T: Tesla

T_2 : transverse relaxation time

UHF: ultra-high field

VPM: ventral posteromedial nucleus

Summary

Functional magnetic resonance imaging (fMRI) could indirectly infer brain activity from the tightly coupled vascular hemodynamic response (neurovascular coupling, NVC). Although the widespread applications of fMRI in animals and humans have revolutionized our capacity to visualize functional brain activity, the underlying regulatory mechanisms of NVC are not yet fully elucidated. The recent advent of ultra-high field MRI ($B_0 \geq 7$ T) affords increased sensitivity and specificity to achieve high-resolution fMRI mapping, which addresses us to establish and apply a high-resolution single-vessel fMRI mapping scheme with blood-oxygen-level-dependent (BOLD), cerebral-blood-volume (CBV), and phase-contrast (PC) MRI methods. Moreover, the technological advances in multimodal fMRI provide complementary readouts of neural activity with high spatiotemporal resolution and cellular specificity, bridging the gap between vascular hemodynamic signal and its underlying neural basis. Therefore, we are motivated to build our multimodal fMRI platform with simultaneous single-vessel fMRI mapping and fiber-based calcium recording in rats to explore distinct NVC events and deepen our present understanding of the NVC.

First, the single-vessel fMRI mapping method was established in the cortex of rats, obtaining the sensory-evoked/resting-state BOLD or CBV-weighted fMRI signals from individual penetrating venules or arterioles, respectively. With concurrent single-vessel fMRI mapping and neuronal calcium recording, we found a robust correlation between vessel-specific resting-state fMRI fluctuations (< 0.1 Hz) and ultra-slow neuronal calcium oscillations under light anesthesia. In addition, the single-vessel fMRI mapping was extended to awake humans, demonstrating that the ultra-slow BOLD fluctuations have a strong spatial correlation with sulcus veins (3 T) and intracortical veins of the visual cortex (9.4 T).

Second, the single-vessel fMRI mapping was further extended to the subcortical area to achieve large-scale hippocampal hemodynamic mapping in rats with optogenetic activation. To investigating the hippocampal neurovascular functions with our multimodal fMRI, we revealed the unique spatiotemporal patterns of the vessel-specific hippocampal hemodynamic responses associated with two hippocampal calcium events, i.e., optogenetically evoked vs. spreading depression-like calcium events. Based on the calcium events-related single-vessel hippocampal hemodynamic modeling, we demonstrated the significantly reduced neurovascular coupling efficiency

during spreading depression-like calcium events.

Third, the single-vessel BOLD/CBV fMRI mapping scheme was complemented with PC-MRI, permitting us to measure the blood flow velocity changes from both individual penetrating venules and arterioles in the somatosensory cortex of rats. This high-resolution PC-based blood flow velocity mapping method offers us a qualitative assessment of blood flow velocity changes at the level of the individual vessels, pointing out a new path to study the underlying NVC mechanisms.

Lastly, an MRI-guided robotic arm (MgRA) was built and applied to real-time position the optical fiber into the rat brain with high target precision, presenting great advantages over the common stereotaxic-assisted fiber implantation. Combining the whole-brain fMRI mapping with MgRA-guided rat brain interventions, e.g., circuit-specific optogenetic activation, GCamp-mediated calcium recording, or microinjection, this multimodal fMRI approach could offer us a powerful tool to assess the circuit-specific brain functions in rats.

Zusammenfassung

Die funktionelle Magnetresonanztomographie (fMRT) ist in der Lage, indirekt aus den eng gekoppelten vaskulären hämodynamischen Antworten auf die Gehirnaktivität zu schließen. Obwohl die weit verbreiteten Anwendungen von fMRT bei Tieren und Menschen unsere Fähigkeit zur Visualisierung der funktionellen Gehirnaktivität revolutioniert haben, sind die zugrunde liegenden regulatorischen Mechanismen von NVC noch nicht vollständig aufgeklärt. Das jüngste Aufkommen der ultrahochfeldigen MRT ($B_0 \geq 7 \text{ T}$) bietet eine erhöhte Empfindlichkeit und Spezifität, um eine hochauflösende fMRT-Mapping zu erreichen, die uns anspricht, um ein hochauflösendes eingefäßiges fMRT-Mapping-Schema mit blutsauerstoffpegelabhängigen (BOLD), zerebralen Blutvolumen (CBV) und Phasenkontrast-MRT-Methoden (PC) zu etablieren und anzuwenden. Darüber hinaus bieten die technologischen Fortschritte im multimodalen fMRT ergänzende Auslesungen neuronaler Aktivität mit hoher raumzeitlicher Auflösung und zellulärer Spezifität, die die Lücke zwischen dem vaskulären hämodynamischen Signal und der zugrunde liegenden neuronalen Basis überbrücken. Daher sind wir motiviert, unsere multimodale fMRI-Plattform mit gleichzeitiger Eingefäß-fMRT-Mapping und faserbasierter Kalziumaufzeichnung bei Ratten aufzubauen, um verschiedene NVC-Ereignisse zu erforschen und unser gegenwärtiges Verständnis des NVC zu vertiefen. Zunächst wurde die Einzelgefäß-fMRT-Mapping Methode im Rattenkortex etabliert, die den sensorisch evozierten/ruhenden BOLD- bzw. CBV-gewichteten fMRI-Signalen von einzelnen durchdringenden Venules bzw. Arteriolen erhielt. Bei gleichzeitiger Einzelgefäß-fMRT-Mapping und neuronaler Kalziumaufzeichnung fanden wir eine robuste Korrelation zwischen gefäßspezifischen fMRT-Schwankungen ($< 0,1 \text{ Hz}$) und ultralangsamem neuronalen Calciumoszillationen unter leichter Anästhesie. Darüber hinaus wurde die Einzelgefäß-fMRT-Mapping beim wachen Menschen verwendet, und es konnte gezeigt werden, dass die ultralangsamem BOLD-Schwankungen eine starke räumliche Korrelation mit den Sulcusvenen (3 T) und den intracortischen Venen des visuellen Kortex (9,4 T) aufweisen.

Zweitens wurde die die Einzelgefäß-fMRT-Mapping weiter auf den subkortikalen Bereich ausgedehnt, um eine großflächige hippocampale hämodynamische Kartierung bei Ratten mit optogenetischer Aktivierung zu erreichen. Zur Untersuchung der hippocampalen neurovaskulären Funktionen mit unserem multimodalen fMRT

enthüllten wir die einzigartigen raum-zeitlichen Muster der gefäßspezifischen hippocampalen hämodynamischen Reaktionen, die mit zwei hippocampalen Calciumereignissen assoziiert sind, d.h. optogenetisch evozierten vs. Spreading-Depression-ähnlichen Kalziumereignisse. Basierend auf der Kalziumereignissen bezogenen einschiffigen hippocampalen hämodynamischen Modellierung demonstrierten wir die signifikant reduzierte neurovaskuläre Kopplungseffizienz bei der Verbreitung von depressiven Kalziumereignissen.

Drittens wurde das BOLD/CBV-fMRT-Einzelgefäß-Mapping-Schema durch PC-MRT ergänzt, das es uns ermöglichte, die Veränderungen der Durchblutungsgeschwindigkeit sowohl von einzelnen durchdringenden Venulen als auch von Arteriolen im somatosensorischen Kortex von Ratten zu messen. Diese hochauflösende PC-basierte Blutflussgeschwindigkeits-Mapping-Methode bietet uns eine qualitative Bewertung von Veränderungen der Durchblutungsgeschwindigkeit auf der Ebene der einzelnen Gefäße und weist auf einen neuen Weg zur Untersuchung der zugrunde liegenden NVC-Mechanismen hin.

Schließlich wurde ein MRT-geführter Roboterarm (MgRA) gebaut und angewendet, um die optische Faser in Echtzeit in das Rattenhirn mit hoher Zielpräzision zu positionieren, was große Vorteile gegenüber der gemeinsamen stereotaxic-unterstützten Faserimplantation bietet. Durch die Kombination der FMRT-Mapping des ganzen Gehirns mit MgRA-geführten Interventionen des Rattengehirns, z. B. schaltungsspezifischer optogenetischer Aktivierung, GCamp-vermittelter Kalziumaufzeichnung oder Mikroinjektion, könnte uns dieser multimodale fMRT-Ansatz ein leistungsfähiges Werkzeug zur Beurteilung der schaltungsspezifischen Gehirnfunktionen bei Ratten bieten.

1. Introduction

1.1. Functional Magnetic Resonance Imaging (fMRI)

Since the early 1990s, the emergence of fMRI has greatly expanded our understanding of brain functions in both animals (Ogawa, et al., 1990a;Ogawa, et al., 1990b) and humans (Belliveau, et al., 1991;Kwong, et al., 1992;Bandettini, et al., 1992). Typically, fMRI reflects brain activity based on the indirect measurement of the changes in brain blood oxygenation, i.e., blood-oxygen-level-dependent (BOLD) contrast (Ogawa, et al., 1990a;Ogawa, et al., 1990b) or vasodilation, i.e., cerebral blood volume (CBV) fMRI (Mandeville, et al., 1998). Also, the cerebral blood flow (CBF) changes could be assessed by several fMRI approaches (Kwong, et al., 1992;Moran, 1982;Bryant, et al., 1984;Detre, et al., 1992). The recent advancements of the ultra-high field (UHF) MRI ($B_0 \geq 7$ T) motivate the MRI researchers in the pursuit of higher fMRI spatial resolution in animal (50~a few hundred μm) and human studies (submillimeter) (Zhao, et al., 2006;Goense, et al., 2016;Huber, et al., 2017;Dumoulin, et al., 2018). As the smaller voxel size could improve the ability to spatially distinguish different vascular compartments e.g., arteries and veins (Yu, et al., 2012;Moon, et al., 2013;Yu, et al., 2016), the high-resolution fMRI mapping gains increasing attention in investigating the vascular origin of the fMRI signal. In this thesis, the overarching purpose is to establish a high-resolution fMRI mapping scheme using the UHF MRI scanners (14 T for rats, 9.4 T for humans) with BOLD (rats/humans), CBV (based on the iron particles injection), and phase-contrast (PC) MRI, which would enable us to capture more detailed vascular dynamic information in anesthetized rats or awake humans. In the first part of the introduction, we will briefly describe the abovementioned three types of fMRI contrast mechanisms.

1.1.1. BOLD Contrast

In the late 1800s, several early observations in humans (Mosso, 1881) and animals (Roy and Sherrington, 1890) have first proposed the unique relationship between brain activity and the changes in CBF. A subsequent study in cats has reported the quantitative assessment of CBF changes during visual stimulation (Kety, 1950). In addition, the neural activity-induced CBF increase has been observed in human brains by using ^{133}Xe as the radioactive tracer (Lassen, et al., 1978). All these pioneering discoveries have supported the tight link between local brain activity and regional CBF

changes, which lays a solid foundation for most existing neuroimaging techniques. In 1990, the BOLD contrast (Ogawa, et al., 1990a;Ogawa, et al., 1990b) has been first described by Ogawa and colleagues, which stems from two important physiological phenomena (Pauling and Coryell, 1936;Fox and Raichle, 1986). On the one hand, the biophysical basis of BOLD contrast is derived from the differential magnetic properties between oxygenated (oxy-Hb) and deoxygenated hemoglobin (deoxy-Hb) in the red blood cells (Pauling and Coryell, 1936). The paramagnetic deoxy-Hb could distort the surrounding magnetic field and lead to MRI signal loss (Thulborn, et al., 1982). On the other hand, the physiological origin of BOLD contrast is based on the uncoupled relationship between regional CBF changes and oxygen consumption (cerebral metabolic rate of oxygen, CMRO₂), i.e., the stimulus-induced CBF increase supplies excessive oxygen than it demands, resulting in a net increase in the blood oxygen levels (Fox and Raichle, 1986;Fox, et al., 1988). Therefore, the relative decrease in the deoxy-Hb concentration following brain activation would present an increased T₂*-weighted BOLD fMRI signal in the activation brain area. In 1992, three independent groups almost simultaneously initiated the BOLD fMRI studies in humans, opening up a new era in exploring human brain functions (Kwong, et al., 1992;Bandettini, et al., 1992;Ogawa, et al., 1992). Given its non-invasive feature and widespread availability, BOLD contrast has rapidly blossomed into the dominant neuroimaging technique in cognitive neuroscience. Nevertheless, subsequent studies have further uncovered the complexity of the BOLD contrast mechanism, showing that the BOLD signals reflect the combined changes in regional CBF, CBV, CMRO₂, and cerebral glucose metabolism (Boxerman, et al., 1995;Buxton and Frank, 1997;Magistretti and Pellerin, 1999;Nugent, et al., 2015).

To better interpret the BOLD signal, the high-resolution fMRI technology with improved spatial specificity is highly motivated to provide a more accurate characterization of the vascular origin of the hemodynamic signal (Shih, et al., 2013;Bollmann and Barth, 2020;Fukuda, et al., 2021). Furthermore, an increasing amount of experimental studies have incorporated BOLD fMRI mapping with advanced electroencephalography (Sumiyoshi, et al., 2012) or electrophysiological (Logothetis, et al., 2001;Pan, et al., 2010) recordings to explore the underlying neural basis of BOLD fMRI signal. Remarkably, the pioneering studies in monkeys (Logothetis, et al., 2001;Goense and Logothetis, 2008) has made a significant breakthrough, pointing out that BOLD signal has a robust positive correlation with synaptic input (i.e., local field potentials, LFPs),

whereas less correlation with neuronal output (i.e., postsynaptic multiunit activity). However, the simultaneous BOLD and electrophysiology recordings remain technically challenging due to the large interference between these two modalities. More recent multimodal fMRI studies (Lee, et al., 2010;Schulz, et al., 2012;Albers, et al., 2018) have put attention in the emerging advanced techniques that enable to manipulate or monitor neuronal activity via the MRI compatible optical fiber, e.g., optogenetics (Lee, et al., 2010;Deisseroth, 2011) or genetically encoded calcium indicators (GECIs) (Kerr, et al., 2000;Nakai, et al., 2001).

In the first two studies of this thesis, we established the single-vessel BOLD fMRI mapping method in anesthetized rats (100 μm spatial resolution at 14 T) and awake humans (850 μm spatial resolution at 3 T; 500 μm spatial resolution at 9.4 T), depicting the venule-dominated functional activity and/or connectivity in the cortex (rats/humans) or hippocampus (Shatillo, et al.). To examine the neural basis of the venule-specific BOLD fMRI signal, we applied the simultaneous single-vessel BOLD fMRI and fiber-based neuronal calcium recordings in different brain areas of the anesthetized rats, which will be further introduced in section 1.2.1.

1.1.2. CBV fMRI

CBV is commonly defined as the blood volume (ml) in a specific amount of brain tissue (100 g) (Petrella and Provenzale, 2000). It is a key parameter in evaluating vascular reactivity and brain functions during physiological (Leenders, et al., 1990) and pathophysiological states (Sorensen, et al., 1999;Derdeyn, et al., 2002). Also, it has been identified as a sensitive readout to better interpret BOLD signals (Buxton and Frank, 1997;Van Zijl, et al., 1998). Hence, numerous neuroimaging techniques have been developed to offer the ability of CBV assessment, e.g., computed tomography (Koenig, et al., 1998), positron emission tomography (Grubb Jr, et al., 1978;Rich, 1997), and several MRI-based techniques (Villringer, et al., 1988;Østergaard, et al., 1998;Mandeville and Marota, 1999). To improve the spatial specificity and sensitivity in CBV MRI mapping, various exogenous or endogenous MRI contrast agents have been applied in animal and human studies (Mandeville, et al., 1998;Edelman, et al., 1990;Williams, et al., 1992;Lu, et al., 2003). For instance, superparamagnetic iron oxide nanoparticles (IONS) are widely utilized as negative contrast agents in CBV MRI studies (Weissleder, et al., 1990;Mandeville, et al., 2001;Mandeville, 2012). The stimulus-induced cerebral vasodilation causes an increase in blood volume, resulting in more superparamagnetic IONS within a specific imaging voxel. As the

superparamagnetic IONs could markedly shorten the T2* relaxation time and diminish the MRI signals, the CBV MRI signals present dark on T2*-weighted MRI images (Kim, et al., 2013;Marashdeh, et al., 2019). In this thesis, we performed the single-vessel CBV-weighted fMRI mapping in rats following the administration of intravascular IONs, demonstrating that the negative CBV-weighted fMRI signals are largely located at the individual arteriole voxels in the somatosensory cortex (section 3.1) and hippocampus (section 3.2).

1.1.3. MRI-based Measurement of CBF

CBF is defined as the blood volume (ml) flowing through a defined amount of brain tissue (100 g) per unit of time (min) (Petrella and Provenzale, 2000). The appropriate CBF increase is vital to ensure a sufficient supply of oxygen and nutrients, a well-timed removal of metabolic by-products (Fantini, et al., 2016), as well as to maintain the proper regulation of the brain temperature (Tarasoff-Conway, et al., 2015). Meanwhile, abnormal CBF changes have been detected in several neurological disorders (Bandera, et al., 2006;Kisler, et al., 2017), thereby, the quantitative CBF measurement is crucial in clinical practice to guide early diagnosis, timely therapy, or monitor the treatment outcome (Chalela, et al., 2000;Galbán, et al., 2009;Alsop, et al., 2010). So far, there are several commonly used MRI-based techniques to assess CBF, including dynamic susceptibility contrast MRI (DSC-MRI) (Villringer, et al., 1988), arterial spin labeling (ASL) (Williams, et al., 1992), and phase-contrast (PC) MRI (Bryant, et al., 1984). DSC-MRI relies on the fast acquisition of the T2/T2* MRI images during the first passage of gadolinium-based contrast bolus through the cerebral vasculature (Rosen, et al., 1990). The time-intensity curve is obtained with multiple-point acquisitions, which would be converted into the tissue concentration-time curve to estimate brain perfusion parameters (Essig, et al., 2013). DSC-MRI is extensively applied in routine clinical use, but it is limited in the use of exogenous tracer and its qualitative property. In contrast to DSC-MRI, ASL labels the blood water protons in the coming large brain-feeding arterials with radiofrequency pulses, which could act as the endogenous diffusible tracer to quantify CBF (Williams, et al., 1992;Koretsky, 2012). Given the short half-life of the labeled arterial blood water, ASL is suitable for longitudinal studies to track disease progression or therapeutic effect (Wierenga, et al., 2014;Zhang, et al., 2017). However, the accuracy of CBF estimation with ASL could be severely affected by the limited signal-to-noise ratio and several confounding factors, e.g., the labeling efficiency (Alsop and Detre, 1998) and the limited permeability of capillary water

(Parkes and Tofts, 2002). PC-MRI is an alternative non-invasive MRI method for quantitative CBF estimation, which gains increasing popularity in recent preclinical and clinical studies (Markl, et al., 2016;Wei, et al., 2019;Zong and Lin, 2019). Typically, a pair of bipolar magnetic gradient pulses are applied in the PC pulse sequence to provide flow sensitivity, resulting in no net phase shift for stationary spins, but a measurable flow-induced phase shift for flowing spins, which is linearly proportional to the speed of moving spins (Moran, 1982). Importantly, the velocity encoding parameter should be adjusted and properly set in PC-MRI studies, as it could determine the maximum detectable blood flow velocity in the vessel of interest (Lotz, et al., 2002). To address the limited resolution of conventional PC-MRI, we have employed the PC-MRI with 100 μm spatial resolution in anesthetized rats, which could offer us a novel tool to detect the blood flow velocity changes from individual penetrating arterioles and venules (section 3.3).

1.2. Cellular Basis of Neurovascular Coupling (NVC)

As previously discussed, the fMRI technique relies on the unique spatiotemporal coupling between neuronal activity and vascular response, which is known as neurovascular coupling (NVC) (Iadecola, 2004;Iadecola, 2017). Despite several potential cellular candidates (e.g., neurons, astrocytes, and pericytes) are proposed in mediating vascular responses, the cellular mechanisms underlying NVC are complex and still not fully understood (Attwell and Iadecola, 2002;Attwell, et al., 2010;Petzold and Murthy, 2011;Hillman, 2014). Over the past decades, optical brain imaging techniques (e.g., optical fiber-based calcium recording) combined with GECIs gain increasing interest in multimodal fMRI studies (Schulz, et al., 2012;Albers, et al., 2018), as it could provide the neural activity readout at the cell-specific level without interfering with the hemodynamic signal. Here, another goal of this thesis is to build a multimodal fMRI platform in rats with concurrent single-vessel fMRI mapping and GCamp-mediated calcium recording to investigate the specific NVC events at different brain states (e.g., task-related vs. resting-state; physiological vs. pathological state). In addition, the neuronal, glial, and vascular interactions would be a potential future direction in the application of our multimodal fMRI platform, which could provide more complementary information to deepen our understanding of the NVC mechanisms. In the following sections, we will mainly introduce the major contributions of neurons and astrocytes in mediating vascular responses in nearby vasculature.

1.2.1. Neurons

Active neurons enable to drive local vascular responses through various vasoactive substances (Cauli and Hamel, 2010). For example, synaptically-released glutamate could act on the postsynaptic ionotropic glutamate receptors and elevate intracellular calcium. The calcium-dependent enzymes (e.g., neuronal nitric oxide synthase and cyclooxygenase 2, COX-2) are further activated to produce potent vasodilators, such as nitric oxide (NO) and prostaglandins (Lecrux and Hamel, 2016). Meanwhile, the neuronally-derived glutamate could trigger the activation of metabotropic glutamate receptors in astrocytes, leading to the increased astrocytic calcium to further mediate vasodilation or vasoconstriction (Attwell, et al., 2010). Moreover, the neuronal activity-induced ionic changes, in particular, the elevated extracellular potassium ion concentration, have been suggested to drive the concentration-dependent vasodilation (Filosa, et al., 2006).

In recent years, the contribution of distinct neuronal cell types in the NVC process has gained growing attention (Cauli and Hamel, 2010). The cortical interneurons have been suggested as the key mediator in CBF regulation through the neuropeptide Y-derived vasoconstriction (Cauli, et al., 2004) or NO-induced vasodilation (Perrenoud, et al., 2012). In addition, the activation of pyramidal neurons has been reported to elicit increases in CBF by producing the COX-2 derived vasodilators (Lecrux, et al., 2011). Moreover, the cortical projection neurons have been posited to modulate regional blood flow via releasing norepinephrine (Bekar, et al., 2012), serotonin (Hamel, 2006), and acetylcholine (Hotta, et al., 2011).

Numerous studies have provided evidence that neurons play vital roles in initiating vascular responses through various signaling pathways, but the simultaneous high-resolution fMRI mapping with direct measurement of neural activity is still actively motivated by the need to deepen our understanding of the NVC process (Logothetis, et al., 2001;Schulz, et al., 2012). In this thesis, we applied a genetically encoded calcium sensor (GCaMP6f) to specifically target neurons in the rat cortex (section 3.1) or hippocampus (section 3.2) to mediate intracellular calcium recording. By merging the previously developed single-vessel fMRI mapping with fiber-based neuronal calcium recording, we find a robust positive correlation between vessel-specific fMRI signals and sensory/optogenetically-evoked neuronal calcium signals. Besides the evoked signals, we also observe the vessel-specific resting-state fMRI fluctuations (< 0.1 Hz) in the rat cortex, which presents a strong correlation with the concurrently

acquired neuronal calcium oscillations (section 3.1).

1.2.2. Astrocytes

Over the past few decades, astrocytes have been increasingly recognized as the structural and functional linkage between synapses and cerebral vasculature (Attwell, et al., 2010;Mishra, et al., 2016). On the one hand, a single astrocyte has numerous contacts with neighboring synapses through the perisynaptic astrocytic processes (Ventura and Harris, 1999;Nedergaard, et al., 2003). On the other hand, almost all of the vascular external surface (around 99%) is ensheathed by the specialized astrocytic processes named “endfeet” (Peters, et al., 1991;Mathiisen, et al., 2010). Given the unique anatomical feature of astrocytes, extensive attention has been given to identifying the specific role of astrocytes in the process of NVC (Gordon, et al., 2007;Iadecola and Nedergaard, 2007). In 2003, it has been first described in an in vitro brain slices study that glutamate-mediated astrocytic calcium increase could trigger vasodilation in the somatosensory cortex (Zonta, et al., 2003). In contrast, astrocytic calcium-induced vasoconstriction has been further observed in brain slices using two-photon microscopy (Mulligan and MacVicar, 2004). In the following whole-retina study, glial cells have been proved to drive both vasodilation and vasoconstriction (Metea and Newman, 2006). Meanwhile, Takano et al. have first provided the in vivo experimental evidence, showing the astrocytic calcium-mediated vasodilation of cortical arterioles (Takano, et al., 2006). Since then, the in vivo astrocytic calcium signaling has been extensively studied by using various calcium-sensitive dyes, e.g., Rhod-2 and Fluo-4 AM (Wang, et al., 2006;Winship, et al., 2007;Dombeck, et al., 2007;Petzold, et al., 2008;Schummers, et al., 2008;Thrane, et al., 2012;Nizar, et al., 2013;Bonder and McCarthy, 2014). Importantly, the presence of slow astrocytic calcium signals (Wang, et al., 2006;Nizar, et al., 2013), which appear after the onset of vascular responses has raised the question of how these delayed astrocytic calcium signals could initiate the following vascular responses. In the view of the potential limitations of commonly used calcium indicator dyes, which may affect the temporal dynamics of astrocytic calcium signal (Nimmerjahn, et al., 2004), subsequent in vivo studies have begun to express the GECIs to specifically target astrocytes, showing the fast astrocytic calcium signals that preceded the vascular responses (Otsu, et al., 2015;Wang, et al., 2018). Although the important role of astrocytes in NVC has been re-established, the cellular mechanisms of the astrocyte-modulated vascular responses are still a highly active research field for further enhancing our understanding of NVC. Notably, several key

experimental parameters should be carefully considered in future studies, such as the anesthetic effects (Thrane, et al., 2012) and the age of experimental animals (Sun, et al., 2013).

2. List of appended manuscripts and statement of contributions

Section 3.1.

1. He Y, Wang M, **Chen X**, Pohmann R, Polimeni JR, Scheffler K, Rosen BR, Kleinfeld D, Yu X. Ultra-slow single-vessel BOLD and CBV-based fMRI spatiotemporal dynamics and their correlation with neuronal intracellular calcium signals. *Neuron*. **2018**;97(4):925-39. e5.

Contributions: X.Y., D.K., and B.R. designed the research, Y.H., X.Y., M.W., and **X.C.** performed animal experiments, Y.H., X.Y. and R.P. acquired data, Y.H. analyzed data, K.S., R.P., J.R. and M.W. provided key technical support, and X.Y., D.K., and Y.H. wrote the manuscript.

Section 3.2.

2. **Chen X**, Sobczak F, Chen Y, Jiang Y, Qian C, Lu Z, Ayata C, Logothetis NK, Yu X. Mapping optogenetically-driven single-vessel fMRI with concurrent neuronal calcium recordings in the rat hippocampus. *Nature communications*. **2019**;10(1):1-12.

Contributions: X.Y., N.K., and **X.C.** designed the research; **X.C.** and X.Y. performed animal experiments; **X.C.**, Y.J., and F.S. performed data analysis; Y. C., C.Q., C.A. and Z.L. provided technical support; X.Y., N.K., C.A. and **X.C.** wrote the paper.

Section 3.3.

3. **Chen X**, Jiang Y, Choi S, Pohmann R, Scheffler K, Kleinfeld D, Yu X. Single-vessel cerebral blood flow velocity fMRI to map blood velocity by phase-contrast imaging. *PLOS Biology*, **2021**, under revision.

Contributions: X.Y., D.K. designed the research; **X.C.** and X.Y. performed animal experiments; **X.C.**, Y.J. performed data analysis; P.R., K.S., S.C. provided technical support; X.Y., D.K., and **X.C.** wrote the paper.

Section 3.4.

4. Chen Y, Pais-Roldan P, **Chen X**, Frosz MH, Yu X. MRI-guided robotic arm drives optogenetic fMRI with concurrent Ca^{2+} recording. Nature communications. **2019**;10(1):1-11.

Contributions: X.Y. designed and supervised the research. Y.C., X.Y., P.P.-R., and **X.C.** performed animal experiments. Y.C., X.Y., and P.P.-R. acquired data. Y.C. analyzed data. **X.C.** and M.H.F. provided key technical support. X.Y. and Y.C. wrote the manuscript.

3. Own work

3.1. Ultra-Slow Single-Vessel BOLD and CBV-Based fMRI Spatiotemporal Dynamics and Their Correlation with Neuronal Intracellular Calcium Signals

3.1.1. Background and Hypotheses

In recent years, the UHF-MRI (≥ 7 T) has provided us the enhanced sensitivity and specificity to achieve high-resolution fMRI mapping in animals (Yu, et al., 2016; Silva and Koretsky, 2002; Goense, et al., 2012) and humans (Goense, et al., 2016; Dumoulin, et al., 2018; Carr, et al., 2010). For example, the line-scanning fMRI method has been previously developed in rats, enabling us to detect the evoked vascular hemodynamic responses with 100 μm spatial resolution and 100 ms temporal resolution (Yu, et al., 2016). However, this method is not suitable to acquire the resting-state fMRI data in a real-time manner due to the reshuffled k-space acquisition scheme for image reconstruction. To address this limitation, we propose to apply the balanced steady-state free precession (bSSFP) method in rats to develop a high-resolution single-vessel fMRI method, aiming to capture the vessel-specific fMRI signals during task-related conditions or at resting-state. Also, we attempt to perform the concurrent single-vessel fMRI mapping and neuronal calcium recording to decipher the potential neuronal basis of the vessel-specific fMRI signals. Furthermore, we aim to extend the single-vessel BOLD fMRI mapping to awake humans to achieve mesoscopic human brain mapping.

3.1.2. Results and Discussion

First, we established the bSSFP-based single-vessel fMRI mapping (spatial resolution: 100 μm at 14 T) in the anesthetized rats with forepaw electrical stimulation, detecting the evoked BOLD or CBV-weighted fMRI signals from individual cortical venules or arterioles, respectively. In addition, the resting-state functional connectivity was mapped in the rat cortex with the bSSFP single-vessel fMRI method. By applying the seed-based correlation analysis, we found a robust venule-specific functional connectivity for ultra-slow BOLD fluctuations (< 0.1 Hz) in a large-scale extent (5 x 5 mm), while the arteriole-dominated functional connectivity for ultra-slow CBV oscillations (< 0.1 Hz) had a 2 mm spatial correlation length, which is coincident with the correlation scale for mouse cortical arterioles during vasomotion (Mateo, et al., 2017). Importantly, we observed that these unique spatiotemporal correlation patterns

of single-vessel fMRI fluctuations could be dampened during deep anesthesia (α -chloralose), which may be due to the anesthesia-induced suppression of neuronal activity (Chan, et al., 2015). By employing the cross-correlation analysis between BOLD/CBV fMRI fluctuations and the concurrently acquired neuronal calcium oscillations, we demonstrated the varied lag times (0.5~6 s) of fMRI signals relative to the calcium signals. The cross-correlation of calcium signals with CBV signals presented the mean lag time at 1.8 ± 0.2 s, while the BOLD signals from individual venules showed a significantly longer lag time relative to calcium oscillations (2.3 ± 0.2 s), indicating the passive dilation of venules in the deep cortical layers of the rat brain (Drew, et al., 2011). Apart from the single-vessel fMRI mapping in rats, we further implemented the single-vessel BOLD fMRI mapping in awake humans (spatial resolution: $850 \mu\text{m}/3$ T, $500 \mu\text{m}/9.4$ T), showing the sulcus vein-dominated functional connectivity at 3 T and intracortical vein-dominated functional connectivity at 9.4 T for BOLD signals fluctuated up to 0.1 Hz.

3.1.3. Conclusion

In this study, the single-vessel fMRI mapping scheme has been established in anesthetized rats and awake humans to map brain activity and functional connectivity at the level of individual vessels. Importantly, we detected the single-vessel BOLD/CBV fMRI fluctuations (< 0.1 Hz), which presented a strong correlation with simultaneous ultra-slow neuronal calcium oscillations under light anesthesia (α -chloralose). This work provides a multimodal fMRI platform with concurrent single-vessel fMRI mapping and GCamp-based calcium recording in rats, pointing out a broad way to explore the vascular and neuronal origins of fMRI signals during different brain states.

3.2. Mapping optogenetically-driven single-vessel fMRI with concurrent neuronal calcium recordings in the rat hippocampus

3.2.1. Background and Hypotheses

The hippocampus plays vital roles in memory (Squire, 1992;Eichenbaum, et al., 1999), learning (Jarrard, 1993), as well as the pathogenesis of several neurological disorders, e.g., epilepsy (De Lanerolle, et al., 1989) and Alzheimer's disease (Hyman, et al., 1984). Although numerous in vitro (Traub, et al., 2004;Butler and Paulsen, 2015) and in vivo (Attardo, et al., 2015;Kondo, et al., 2017) studies have focused on investigating the hippocampal neural network function, it is still challenging for the conventional fMRI to detect the vascular hemodynamic responses from individual hippocampal vessels. Building on our previously developed single-vessel fMRI method (section 3.1), the primary goal of this project is to accomplish the single-vessel hippocampal mapping with optogenetic activation. In addition, we aim to estimate the hippocampal NVC function during distinct hippocampal activities based on the simultaneous single-vessel hippocampal mapping with fiber-mediated calcium recording in rats.

3.2.2. Results and Discussion

With the coexpression of Channelrhodopsin-2 (ChR2, for optogenetic activation) and GCaMP6 (for fiber-based calcium recording) in the rat hippocampus, we first simultaneously acquired the optogenetically-evoked neuronal calcium transients in the hippocampus, as well as the evoked whole-brain BOLD signals using 3D echo-planar imaging (spatial resolution: 300 μm , temporal resolution: 1.5 s). For the hippocampal calcium signals, the stimulation light pulses were detected as sharp spikes due to the spectral wavelength cross-talk between optogenetic stimulation (473 nm) and GCaMP-based fluorescent signal excitation (488 nm). To address this issue, we expressed the red-shifted ChR2 variant (C1V1) in the hippocampus to mediate the optical activation at 590 nm. The C1V1-evoked calcium signals present a similar temporal dynamic pattern as the ChR2-evoked calcium signals, but with significantly reduced light pulse artifacts.

Furthermore, we employed the bSSFP method with 100 μm spatial resolution to achieve single-vessel hippocampal mapping, showing that the evoked BOLD signals are mainly located at hippocampal venules, while CBV-weighted signals are largely overlapped with hippocampal arterioles. It has been reported in previous histological studies that the penetrating hippocampal vessels are mainly aligned in parallel (Coyle,

1976;Coyle, 1978). Based on the single-vessel hippocampal mapping, we described that the hippocampal arterioles and venules are located interleave to each other through the ~6-8 mm saddle-like structure. Importantly, we kept a certain distance ($\geq 500 \mu\text{m}$) between the 2D single-vessel MRI slice and the optogenetic stimulation fiber to avoid the potential light-induced local blood flow changes (Rungta, et al., 2017). Consistent with previous optogenetic studies in the hippocampus (Osawa, et al., 2013;Weitz, et al., 2015), we observed robust epileptic events as a series of interictal LFP spikes paired with individual spontaneous calcium spikes following high-frequency optical activation. More interestingly, we detected the unique spreading depression-like (SDL) calcium transients between the interstimulus intervals (optical activation: 3/5 Hz, 8 s), which were also coupled with the widespread single-vessel fMRI signals. The SDL calcium events were detected with a high induction rate under 8 s stimulation ($\geq 50\%$ with 5/10 Hz, 8 s stimulation), which enabled us to statistically compare the NVC function associated with two forms of hippocampal calcium events, i.e., the optogenetically-evoked and SDL calcium events. By extracting the time courses of the BOLD signals from individual hippocampal venules, we found the optogenetically-evoked BOLD signals occurred concurrently within different hippocampal venules, while the BOLD signals from individual venules showed a propagation pattern as a function of distance to the stimulation fiber during SDL calcium events. By further applying an amplitude-modulated response modeling to evaluate the NVC efficiency (NVCe) of different hippocampal activities, we demonstrated the significantly reduced NVCe during SDL calcium events.

3.2.3. Conclusion

In this project, we have accomplished the single-vessel hippocampal mapping with simultaneous neuronal calcium recordings upon optogenetic activation, which extended the application of our multimodal fMRI platform to the subcortical regions. By modeling the single-vessel fMRI signals to the coupled calcium events, we offered a direct assessment to study the NVCe linked to distinct hippocampal activities, which could be potentially applied in future studies with different animal disease models, e.g., epilepsy and stroke.

3.3. Single-vessel cerebral blood velocity fMRI to map blood velocity by phase-contrast imaging

3.3.1. Background and Hypotheses

CBF is a crucial parameter for evaluating brain function in physiological (Fox and Raichle, 1986) and pathological states (Kisler, et al., 2017; Shen and Duong, 2016). Over the past decades, the PC-MRI has been extensively applied to encode the blood flow velocity in animal (Wei, et al., 2019) and human studies (Stoquart-ElSankari, et al., 2009; Chang, et al., 2011). However, given the limited resolution of conventional PC-MRI, there is still no direct PC-based blood flow velocity mapping at the single vessel level in rats. To address this issue, we propose to extend our single-vessel BOLD/CBV fMRI mapping scheme with PC-MRI to achieve the PC-based single-vessel cerebral blood velocity mapping in the deep layer cortex of anesthetized rats.

3.3.2. Results and Discussion

To optimize the PC-MRI sequence, we first performed an in vitro phantom experiment by using capillary tubings to mimic the penetrating cortical vessels (flow rate: 0.1~1 cm/s), showing a near-linear correlation between PC-detected blood flow velocities and the true velocities. The velocity offsets were observed at velocity zero during different conditions, which could be caused by the gradient imperfections (Bernstein, et al., 1998; Peeters, et al., 2005) or eddy current effects (Walker, et al., 1993). Furthermore, we implemented the PC-MRI with 100 μm spatial resolution to perform in vivo blood flow velocity mapping in rats. Importantly, to increase the focal B1 field sensitivity for achieving high-resolution flow velocity mapping, we closely attached a custom-made transceiver surface coil (6 mm diameter) just above the regions of interest. As previous single-vessel BOLD/CBV fMRI mapping (section 3.1, 3.2), an anatomical arteriole-venule (A-V) map was first created using the multi-gradient echo (MGE) sequence to specify the individual penetrating arterioles (shown as white dots) and venules (shown as dark dots) in the somatosensory cortex. Moreover, the 2D PC-MRI slice was aligned with the same geometry as the 2D MGE slice for directly overlapping the flow velocity map to the A-V map. As the penetrating cortical vessels have two main directions of blood flow, i.e., venule blood flows out of the cortex while the arteriole blood goes into the cortex (Pelc, et al., 1991), we used this property as two vectors to assign the positive and negative values in the flow velocity map, i.e., positive venule (shown as white dots) and negative arteriole (shown as dark dots) flow

velocities. In the end, we performed the single-vessel fMRI mapping scheme with BOLD, CBV, and PC-MRI in the same rats upon forepaw electrical stimulation, detecting the venule-specific BOLD signals, the arteriole-dominated CBV-weighted signals, and the sensory-evoked blood flow velocity increase from both penetrating venules and arterioles, i.e., more positive signal intensity values in venules and more negative signal intensity values in arterioles.

3.3.3. Conclusion

In this study, we have developed the single-vessel blood flow velocity mapping scheme with PC-MRI to detect the blood flow velocity changes from both arterioles and venules throughout the cortex of anesthetized rats. Combined with the single-vessel BOLD and CBV fMRI mapping, the PC-based single-vessel blood flow velocity mapping method would further enrich our single-vessel fMRI mapping scheme to enhance our understanding of functional brain activity.

3.4. MRI-guided robotic arm drives optogenetic fMRI with concurrent Ca²⁺ recording

3.4.1. Background and Hypotheses

Lately, the increased availability of multimodal neuroimaging techniques has offered us powerful tools to investigate the cellular mechanisms underlying NVC (Lee, et al., 2010;Schulz, et al., 2012;Albers, et al., 2018). The optical fiber is extensively applied in multimodal fMRI studies due to its non-magnetic properties (Wang, et al., 2018;Lee, 2012). To ensure the success of fiber implantation, a conventional stereotaxic device (Ferenczi, et al., 2016;Marshall, et al., 2016) is commonly used to guide the fiber insertion into the rodent brain with the coordinates calculated from the brain atlas (Paxinos and Watson, 2006). However, there are a few potential sources of failure during fiber insertion, such as incorrect head fixation, variability in animal/brain size or the location of bregma, as well as the potential brain shift after removing the dura mater (Miyagi, et al., 2007;Pallavaram, et al., 2010), which could induce the error of fiber implantation, in particular during targeting certain deep brain nuclei with only a few hundred-micrometer coverages (Liu, et al., 2015;Resendez, et al., 2016). To address this issue, we propose to build an MRI-guided robotic arm (MgRA) to assist the fiber-based rat brain intervention in real-time with high target accuracy and flexibility.

3.4.2. Results and Discussion

The feasibility and reliability of the MgRA-guided fiber implantation were first confirmed in an ex vivo experiment with perfused rat brains. In the later in vivo study, the MgRA-driven fiber insertion was applied to target the rat lateral hypothalamus (LH) for optogenetic activation, resulting in the widespread BOLD signals in LH regions as well as the projected basal forebrain regions. By registering the fMRI images of individual rats to the structural brain atlas, we observed the comparable activation patterns of optogenetically-evoked BOLD signals in LH regions across different animals.

With the assistance of MgRA, optical fiber was further implanted to the rat ventral posteromedial nucleus (VPM) for mediating the multiple-sites optical stimulation along the insertion path, while the neuronal calcium signals were concurrently recorded in the ipsilateral somatosensory cortex. The increased BOLD and calcium signals were reliably detected when the fiber tip moved towards the targeted VPM, whereas both signals decreased after the fiber tip passed through the targeted region. In addition, we employed the MgRA positioning device to perform the real-time injection of MnCl₂

solution through a hollow-core fiber (Russell, 2003), leading to the effective manganese delivery with limited diffusion, which is confirmed by the Mn-enhanced MRI signals (Pautler, et al., 1998).

3.4.3. Conclusion

In this project, an MRI-compatible robotic arm has been developed to achieve more accurate optic fiber implantation with real-time feedback from anatomical MRI images. With simultaneous whole-brain fMRI mapping, the MgRA-driven fiber insertion was applied to mediate optogenetic activation, calcium recording, or microinjection in rat brains, presenting a great advantage over the common stereotaxic-guided brain interventions in circuit-specific brain functional mapping.

4. Summary and Outlook

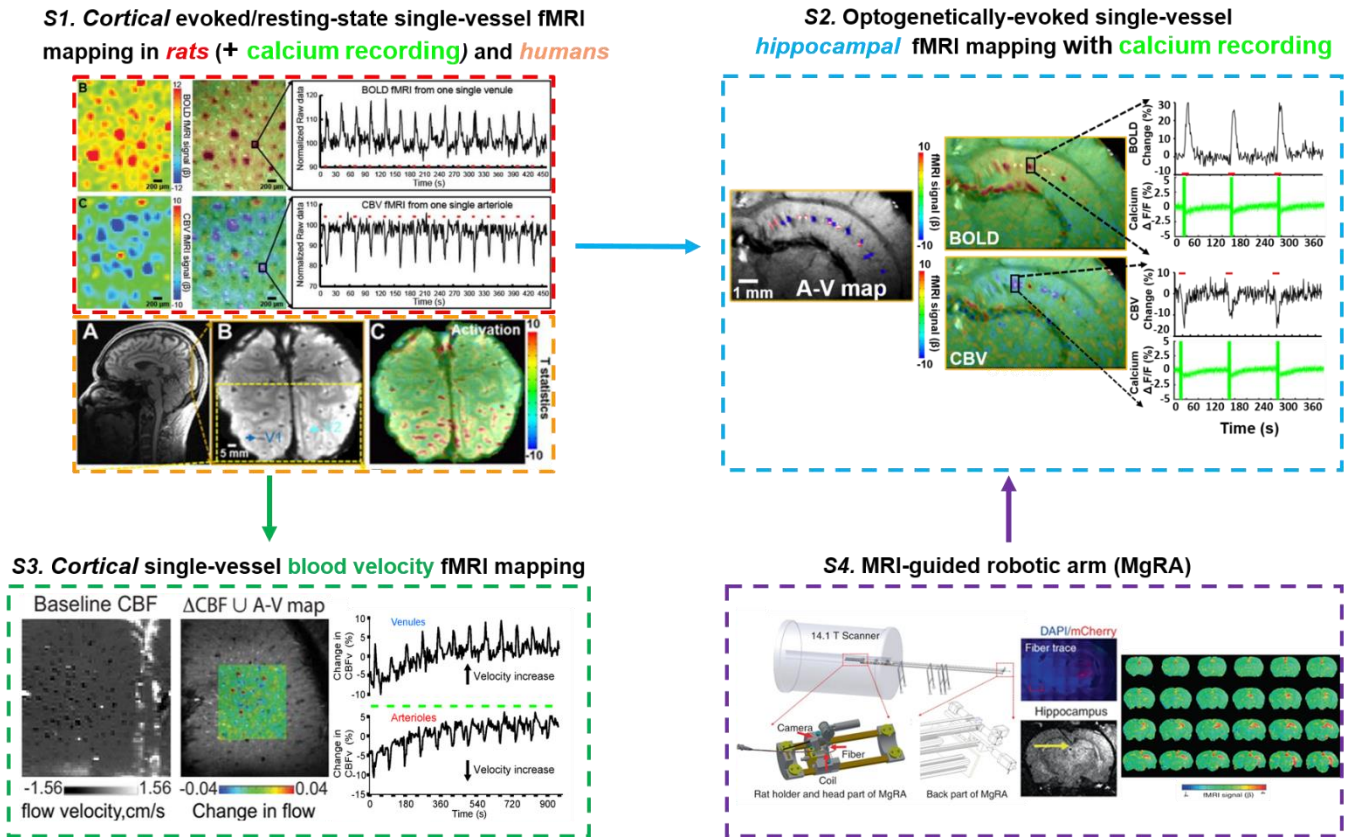


Figure 1. The graphic summary of the thesis

In this thesis, we have first developed a bSSFP-based single-vessel fMRI method in the cortex of anesthetized rats, obtaining the sensory-evoked BOLD or CBV-weighted fMRI signals from individual penetrating venules and arteries, respectively (section 3.1). In addition, the high-resolution resting-state fMRI mapping has been completed in rats and humans to map the dynamic functional connectivity at the single-vessel level, demonstrating the unique spatiotemporal dynamic patterns of ultra-slow vessel-specific fMRI fluctuations (< 0.1 Hz) (section 3.1). Moreover, we have extended the bSSFP-based single-vessel fMRI mapping to the subcortical brain regions (i.e., hippocampus) with fiber-based optogenetic activation to achieve high-resolution hippocampal hemodynamic mapping (section 3.2). Building on the abovementioned single-vessel fMRI mapping strategy, the PC-based single-vessel blood flow velocity mapping has been further accomplished in rats to detect the blood flow velocity

changes from both penetrating arteries and venules in the deep layer cortex (section 3.3). Therefore, we have established the single-vessel fMRI mapping scheme with BOLD, CBV, and PC-MRI using UHF MRI (14 T for rats, 9.4 T for humans), enabling us to detect the detailed vascular hemodynamics from individual blood vessels across multiple brain regions (somatosensory cortex vs. hippocampus) and at varied brain states (task-related vs. resting-state; physiological vs. pathological state).

Furthermore, we employed a multimodal imaging strategy in rats with concurrent single-vessel fMRI mapping and fiber-based calcium recording to assess the distinct NVC events in the somatosensory cortex or hippocampus. In the somatosensory cortex, we found a strong correlation between vessel-specific fMRI fluctuations and neuronal calcium oscillations (section 3.1). In the hippocampus, we demonstrated the significantly reduced NVCE during hippocampal SDL calcium events (section 3.2). In addition, we have built and applied a MgRA positioning device to real-time assist the fiber-based rat brain interventions in the 14 T MRI scanner (e.g., optogenetics, calcium recording, and microinjection) with high target accuracy and flexibility, offering us a powerful tool to further study the circuit-specific functional activity in rats. Taking together, we provide an important technical advance in achieving the single-vessel fMRI mapping with simultaneous neuronal calcium recording in the rat cortex or hippocampus, pioneering a new way to study the brain function and connectivity, as well as to explore the underlying NVC mechanism during different brain states.

As the high spatial resolution of the single-vessel fMRI method offers the ability to anatomically distinguish the individual blood vessels in both rat and human brains, one future direction of the single-vessel fMRI mapping could focus on identifying the potential vascular biomarkers, which may link to specific dynamic indicators of brain small vessel diseases or neurodegenerative diseases (Binnewijzend, et al., 2012; Pievani, et al., 2014). Moreover, the multi-slice acquisition strategy for single-vessel hippocampal mapping could be considered as the potential complement for further application, as it allows to cover the 3D hippocampal structure to perform multiple fiber implantation for concurrent hippocampal neuronal and astrocytic calcium recordings with optogenetic activation. Furthermore, the PC-based single-vessel blood flow velocity mapping would be applied in various animal models (e.g., Alzheimer's disease) and could be potentially translated into human studies to detect the blood flow velocity changes linked to vascular dementia (de Eulate, et al., 2017).

5. References

1. Ogawa S, Lee TM, Nayak AS, Glynn P. Oxygenation - sensitive contrast in magnetic resonance image of rodent brain at high magnetic fields. *Magnetic resonance in medicine*. 1990a;14(1):68-78.
2. Ogawa S, Lee T-M, Kay AR, Tank DW. Brain magnetic resonance imaging with contrast dependent on blood oxygenation. *proceedings of the National Academy of Sciences*. 1990b;87(24):9868-72.
3. Belliveau J, Kennedy D, McKinstry R, Buchbinder B, Weisskoff R, Cohen M, Vevea J, Brady T, Rosen B. Functional mapping of the human visual cortex by magnetic resonance imaging. *Science*. 1991;254(5032):716-9.
4. Kwong KK, Belliveau JW, Chesler DA, Goldberg IE, Weisskoff RM, Poncelet BP, Kennedy DN, Hoppel BE, Cohen MS, Turner R. Dynamic magnetic resonance imaging of human brain activity during primary sensory stimulation. *Proceedings of the National Academy of Sciences*. 1992;89(12):5675-9.
5. Bandettini PA, Wong EC, Hinks RS, Tikofsky RS, Hyde JS. Time course EPI of human brain function during task activation. *Magnetic resonance in medicine*. 1992;25(2):390-7.
6. Mandeville JB, Marota JJ, Kosofsky BE, Keltner JR, Weissleder R, Rosen BR, Weisskoff RM. Dynamic functional imaging of relative cerebral blood volume during rat forepaw stimulation. *Magnetic resonance in medicine*. 1998;39(4):615-24.
7. Moran PR. A flow velocity zeugmatographic interlace for NMR imaging in humans. *Magnetic resonance imaging*. 1982;1(4):197-203.
8. Bryant D, Payne J, Firmin DN, Longmore DB. Measurement of flow with NMR imaging using a gradient pulse and phase difference technique. *Journal of computer assisted tomography*. 1984;8(4):588-93.
9. Detre JA, Leigh JS, Williams DS, Koretsky AP. Perfusion imaging. *Magnetic resonance in medicine*. 1992;23(1):37-45.
10. Zhao F, Wang P, Hendrich K, Ugurbil K, Kim S-G. Cortical layer-dependent BOLD and CBV responses measured by spin-echo and gradient-echo fMRI: insights into hemodynamic regulation. *Neuroimage*. 2006;30(4):1149-60.
11. Goense J, Bohraus Y, Logothetis NK. fMRI at high spatial resolution: implications for BOLD-models. *Frontiers in computational neuroscience*. 2016;10:66.
12. Huber L, Handwerker DA, Jangraw DC, Chen G, Hall A, Stüber C, Gonzalez-Castillo J, Ivanov D, Marrett S, Guidi M. High-resolution CBV-fMRI allows mapping of laminar activity and connectivity of cortical input and output in human M1. *Neuron*. 2017;96(6):1253-63. e7.
13. Dumoulin SO, Fracasso A, van der Zwaag W, Siero JC, Petridou N. Ultra-high field MRI: Advancing systems neuroscience towards mesoscopic human brain function. *Neuroimage*. 2018;168:345-57.
14. Yu X, Glen D, Wang S, Dodd S, Hirano Y, Saad Z, Reynolds R, Silva AC, Koretsky AP. Direct imaging of macrovascular and microvascular contributions to BOLD fMRI in layers IV–V of the rat whisker–barrel cortex. *Neuroimage*. 2012;59(2):1451-60.
15. Moon CH, Fukuda M, Kim S-G. Spatiotemporal characteristics and vascular sources of neural-specific and-nonspecific fMRI signals at submillimeter columnar resolution. *Neuroimage*. 2013;64:91-103.
16. Yu X, He Y, Wang M, Merkle H, Dodd SJ, Silva AC, Koretsky AP. Sensory and optogenetically driven single-vessel fMRI. *Nature methods*. 2016;13(4):337-40.
17. Mosso A. Über den Kreislauf des Blutes im menschlichen Gehirn: von Veit & Company; 1881.
18. Roy CS, Sherrington CS. On the regulation of the blood-supply of the brain. *The Journal of physiology*. 1890;11(1-2):85-158.
19. Kety SS. Circulation and metabolism of the human brain in health and disease. *The American journal of medicine*. 1950;8(2):205-17.
20. Lassen NA, Ingvar DH, Skinhøj E. Brain function and blood flow. *Scientific American*. 1978;239(4):62-71.
21. Pauling L, Coryell CD. The magnetic properties and structure of hemoglobin, oxyhemoglobin

- and carbonmonoxyhemoglobin. *Proceedings of the National Academy of Sciences*. 1936;22(4):210-6.
22. Fox PT, Raichle ME. Focal physiological uncoupling of cerebral blood flow and oxidative metabolism during somatosensory stimulation in human subjects. *Proceedings of the National Academy of Sciences*. 1986;83(4):1140-4.
 23. Thulborn KR, Waterton JC, Matthews PM, Radda GK. Oxygenation dependence of the transverse relaxation time of water protons in whole blood at high field. *Biochimica et Biophysica Acta (BBA)-General Subjects*. 1982;714(2):265-70.
 24. Fox PT, Raichle ME, Mintun MA, Dence C. Nonoxidative glucose consumption during focal physiologic neural activity. *Science*. 1988;241(4864):462-4.
 25. Ogawa S, Tank DW, Menon R, Ellermann JM, Kim SG, Merkle H, Ugurbil K. Intrinsic signal changes accompanying sensory stimulation: functional brain mapping with magnetic resonance imaging. *Proceedings of the National Academy of Sciences*. 1992;89(13):5951-5.
 26. Boxerman JL, Hamberg LM, Rosen BR, Weisskoff RM. MR contrast due to intravascular magnetic susceptibility perturbations. *Magnetic resonance in medicine*. 1995;34(4):555-66.
 27. Buxton RB, Frank LR. A model for the coupling between cerebral blood flow and oxygen metabolism during neural stimulation. *Journal of cerebral blood flow & metabolism*. 1997;17(1):64-72.
 28. Magistretti PJ, Pellerin L. Cellular mechanisms of brain energy metabolism and their relevance to functional brain imaging. *Philosophical Transactions of the Royal Society of London Series B: Biological Sciences*. 1999;354(1387):1155-63.
 29. Nugent AC, Martinez A, D'alfonso A, Zarate CA, Theodore WH. The relationship between glucose metabolism, resting-state fMRI BOLD signal, and GABAA-binding potential: a preliminary study in healthy subjects and those with temporal lobe epilepsy. *Journal of Cerebral Blood Flow & Metabolism*. 2015;35(4):583-91.
 30. Shih Y-YI, Chen Y-Y, Lai H-Y, Kao Y-CJ, Shyu B-C, Duong TQ. Ultra high-resolution fMRI and electrophysiology of the rat primary somatosensory cortex. *Neuroimage*. 2013;73:113-20.
 31. Bollmann S, Barth M. New acquisition techniques and their prospects for the achievable resolution of fMRI. *Progress in Neurobiology*. 2020:101936.
 32. Fukuda M, Poplawsky AJ, Kim S-G. Time-dependent spatial specificity of high-resolution fMRI: insights into mesoscopic neurovascular coupling. *Philosophical Transactions of the Royal Society B*. 2021;376(1815):20190623.
 33. Sumiyoshi A, Suzuki H, Ogawa T, Riera JJ, Shimokawa H, Kawashima R. Coupling between gamma oscillation and fMRI signal in the rat somatosensory cortex: its dependence on systemic physiological parameters. *Neuroimage*. 2012;60(1):738-46.
 34. Logothetis NK, Pauls J, Augath M, Trinath T, Oeltermann A. Neurophysiological investigation of the basis of the fMRI signal. *nature*. 2001;412(6843):150-7.
 35. Pan W-j, Thompson G, Magnuson M, Majeed W, Jaeger D, Keilholz S. Simultaneous FMRI and electrophysiology in the rodent brain. *Journal of visualized experiments: JoVE*. 2010(42).
 36. Goense JB, Logothetis NK. Neurophysiology of the BOLD fMRI signal in awake monkeys. *Current Biology*. 2008;18(9):631-40.
 37. Lee JH, Durand R, Gradinaru V, Zhang F, Goshen I, Kim D-S, Fenno LE, Ramakrishnan C, Deisseroth K. Global and local fMRI signals driven by neurons defined optogenetically by type and wiring. *Nature*. 2010;465(7299):788-92.
 38. Schulz K, Sydekum E, Krueppel R, Engelbrecht CJ, Schlegel F, Schröter A, Rudin M, Helmchen F. Simultaneous BOLD fMRI and fiber-optic calcium recording in rat neocortex. *Nature methods*. 2012;9(6):597-602.
 39. Albers F, Wachsmuth L, van Alst TM, Faber C. Multimodal functional neuroimaging by simultaneous BOLD fMRI and fiber-optic calcium recordings and optogenetic control. *Molecular imaging and biology*. 2018;20(2):171-82.
 40. Deisseroth K. Optogenetics. *Nature methods*. 2011;8(1):26-9.
 41. Kerr R, Lev-Ram V, Baird G, Vincent P, Tsien RY, Schafer WR. Optical imaging of calcium transients in neurons and pharyngeal muscle of *C. elegans*. *Neuron*. 2000;26(3):583-94.
 42. Nakai J, Ohkura M, Imoto K. A high signal-to-noise Ca²⁺ probe composed of a single green

- fluorescent protein. *Nature biotechnology*. 2001;19(2):137-41.
43. Shatillo A, Lipponen A, Salo RA, Tanila H, Verkhatsky A, Giniatullin R, Gröhn OH. Spontaneous BOLD waves—A novel hemodynamic activity in Sprague-Dawley rat brain detected by functional magnetic resonance imaging. *Journal of Cerebral Blood Flow & Metabolism*. 2019;39(10):1949-60.
 44. Petrella JR, Provenzale JM. MR perfusion imaging of the brain: techniques and applications. *American Journal of roentgenology*. 2000;175(1):207-19.
 45. Leenders K, Perani D, Lammertsma A, Heather J, Buckingham P, Jones T, Healy M, Gibbs J, Wise R, Hatazawa J. Cerebral blood flow, blood volume and oxygen utilization: normal values and effect of age. *Brain*. 1990;113(1):27-47.
 46. Sorensen AG, Copen WA, Østergaard L, Buonanno FS, Gonzalez RG, Rordorf G, Rosen BR, Schwamm LH, Weisskoff RM, Koroshetz WJ. Hyperacute stroke: simultaneous measurement of relative cerebral blood volume, relative cerebral blood flow, and mean tissue transit time. *Radiology*. 1999;210(2):519-27.
 47. Derdeyn CP, Videen TO, Yundt KD, Fritsch SM, Carpenter DA, Grubb RL, Powers WJ. Variability of cerebral blood volume and oxygen extraction: stages of cerebral haemodynamic impairment revisited. *Brain*. 2002;125(3):595-607.
 48. Van Zijl PC, Eleff SM, Ulatowski JA, Oja JM, Uluğ AM, Traystman RJ, Kauppinen RA. Quantitative assessment of blood flow, blood volume and blood oxygenation effects in functional magnetic resonance imaging. *Nature medicine*. 1998;4(2):159-67.
 49. Koenig M, Klotz E, Luka B, Venderink DJ, Spittler JF, Heuser L. Perfusion CT of the brain: diagnostic approach for early detection of ischemic stroke. *Radiology*. 1998;209(1):85-93.
 50. Grubb Jr RL, Raichle ME, Higgins CS, Eichling JO. Measurement of regional cerebral blood volume by emission tomography. *Annals of Neurology: Official Journal of the American Neurological Association and the Child Neurology Society*. 1978;4(4):322-8.
 51. Rich DA. A brief history of positron emission tomography. *Journal of nuclear medicine technology*. 1997;25(1):4-11.
 52. Villringer A, Rosen BR, Belliveau JW, Ackerman JL, Lauffer RB, Buxton RB, Chao YS, Wedeenand VJ, Brady TJ. Dynamic imaging with lanthanide chelates in normal brain: contrast due to magnetic susceptibility effects. *Magnetic resonance in medicine*. 1988;6(2):164-74.
 53. Østergaard L, Smith DF, Vestergaard-Poulsen P, Hansen S, Gee AD, Gjedde A, Gyldensted C. Absolute cerebral blood flow and blood volume measured by magnetic resonance imaging bolus tracking: comparison with positron emission tomography values. *Journal of Cerebral Blood Flow & Metabolism*. 1998;18(4):425-32.
 54. Mandeville JB, Marota JJ. Vascular filters of functional MRI: spatial localization using BOLD and CBV contrast. *Magnetic Resonance in Medicine: An Official Journal of the International Society for Magnetic Resonance in Medicine*. 1999;42(3):591-8.
 55. Edelman RR, Mattle HP, Atkinson DJ, Hill T, Finn J, Mayman C, Ronthal M, Hoogewoud H, Kleefield J. Cerebral blood flow: assessment with dynamic contrast-enhanced T2*-weighted MR imaging at 1.5 T. *Radiology*. 1990;176(1):211-20.
 56. Williams DS, Detre JA, Leigh JS, Koretsky AP. Magnetic resonance imaging of perfusion using spin inversion of arterial water. *Proceedings of the National Academy of Sciences*. 1992;89(1):212-6.
 57. Lu H, Golay X, Pekar JJ, Van Zijl PC. Functional magnetic resonance imaging based on changes in vascular space occupancy. *Magnetic Resonance in Medicine: An Official Journal of the International Society for Magnetic Resonance in Medicine*. 2003;50(2):263-74.
 58. Weissleder R, Elizondo G, Wittenberg J, Rabito C, Bengele H, Josephson L. Ultrasmall superparamagnetic iron oxide: characterization of a new class of contrast agents for MR imaging. *Radiology*. 1990;175(2):489-93.
 59. Mandeville JB, Jenkins BG, Kosofsky BE, Moskowitz MA, Rosen BR, Marota JJ. Regional sensitivity and coupling of BOLD and CBV changes during stimulation of rat brain. *Magnetic Resonance in Medicine: An Official Journal of the International Society for Magnetic Resonance in Medicine*. 2001;45(3):443-7.
 60. Mandeville JB. IRON fMRI measurements of CBV and implications for BOLD signal. *Neuroimage*. 2012;62(2):1000-8.

61. Kim SG, Harel N, Jin T, Kim T, Lee P, Zhao F. Cerebral blood volume MRI with intravascular superparamagnetic iron oxide nanoparticles. *NMR in Biomedicine*. 2013;26(8):949-62.
62. Marashdeh M, Ababneh B, Lemine O, Alsadig A, Omri K, El Mir L, Sulieman A, Mattar E. The significant effect of size and concentrations of iron oxide nanoparticles on magnetic resonance imaging contrast enhancement. *Results in Physics*. 2019;15:102651.
63. Fantini S, Sassaroli A, Tgavalekos KT, Kornbluth J. Cerebral blood flow and autoregulation: current measurement techniques and prospects for noninvasive optical methods. *Neurophotonics*. 2016;3(3):031411.
64. Tarasoff-Conway JM, Carare RO, Osorio RS, Glodzik L, Butler T, Fieremans E, Axel L, Rusinek H, Nicholson C, Zlokovic BV. Clearance systems in the brain—implications for Alzheimer disease. *Nature reviews neurology*. 2015;11(8):457.
65. Bandera E, Botteri M, Minelli C, Sutton A, Abrams KR, Latronico N. Cerebral blood flow threshold of ischemic penumbra and infarct core in acute ischemic stroke: a systematic review. *Stroke*. 2006;37(5):1334-9.
66. Kisler K, Nelson AR, Montagne A, Zlokovic BV. Cerebral blood flow regulation and neurovascular dysfunction in Alzheimer disease. *Nature Reviews Neuroscience*. 2017;18(7):419.
67. Chalela JA, Alsop DC, Gonzalez-Atavales JB, Maldjian JA, Kasner SE, Detre JA. Magnetic resonance perfusion imaging in acute ischemic stroke using continuous arterial spin labeling. *Stroke*. 2000;31(3):680-7.
68. Galbán CJ, Chenevert TL, Meyer CR, Tsien C, Lawrence TS, Hamstra DA, Junck L, Sundgren PC, Johnson TD, Ross DJ. The parametric response map is an imaging biomarker for early cancer treatment outcome. *Nature medicine*. 2009;15(5):572-6.
69. Alsop DC, Dai W, Grossman M, Detre JA. Arterial spin labeling blood flow MRI: its role in the early characterization of Alzheimer's disease. *Journal of Alzheimer's Disease*. 2010;20(3):871-80.
70. Rosen BR, Belliveau JW, Vevea JM, Brady TJ. Perfusion imaging with NMR contrast agents. *Magnetic resonance in medicine*. 1990;14(2):249-65.
71. Essig M, Shiroishi MS, Nguyen TB, Saake M, Provenzale JM, Enterline D, Anzalone N, Dörfler A, Rovira À, Wintermark M. Perfusion MRI: the five most frequently asked technical questions. *American Journal of Roentgenology*. 2013;200(1):24-34.
72. Koretsky AP. Early development of arterial spin labeling to measure regional brain blood flow by MRI. *Neuroimage*. 2012;62(2):602-7.
73. Wierenga CE, Hays CC, Zlatar ZZ. Cerebral blood flow measured by arterial spin labeling MRI as a preclinical marker of Alzheimer's disease. *Journal of Alzheimer's Disease*. 2014;42(s4):S411-S9.
74. Zhang N, Gordon ML, Goldberg TE. Cerebral blood flow measured by arterial spin labeling MRI at resting state in normal aging and Alzheimer's disease. *Neuroscience & Biobehavioral Reviews*. 2017;72:168-75.
75. Alsop DC, Detre JA. Multisection cerebral blood flow MR imaging with continuous arterial spin labeling. *Radiology*. 1998;208(2):410-6.
76. Parkes LM, Tofts PS. Improved accuracy of human cerebral blood perfusion measurements using arterial spin labeling: accounting for capillary water permeability. *Magnetic Resonance in Medicine: An Official Journal of the International Society for Magnetic Resonance in Medicine*. 2002;48(1):27-41.
77. Markl M, Schnell S, Wu C, Bollache E, Jarvis K, Barker A, Robinson J, Rigsby C. Advanced flow MRI: emerging techniques and applications. *Clinical radiology*. 2016;71(8):779-95.
78. Wei Z, Chen L, Lin Z, Jiang D, Xu J, Liu P, van Zijl PC, Lu H. Optimization of phase - contrast MRI for the estimation of global cerebral blood flow of mice at 11.7 T. *Magnetic resonance in medicine*. 2019;81(4):2566-75.
79. Zong X, Lin W. Quantitative phase contrast MRI of penetrating arteries in centrum semiovale at 7T. *NeuroImage*. 2019;195:463-74.
80. Lotz J, Meier C, Leppert A, Galanski M. Cardiovascular flow measurement with phase-contrast MR imaging: basic facts and implementation. *Radiographics*. 2002;22(3):651-71.
81. Iadecola C. Neurovascular regulation in the normal brain and in Alzheimer's disease. *Nature Reviews Neuroscience*. 2004;5(5):347-60.

82. Iadecola C. The neurovascular unit coming of age: a journey through neurovascular coupling in health and disease. *Neuron*. 2017;96(1):17-42.
83. Attwell D, Iadecola C. The neural basis of functional brain imaging signals. *Trends in neurosciences*. 2002;25(12):621-5.
84. Attwell D, Buchan AM, Charpak S, Lauritzen M, MacVicar BA, Newman EA. Glial and neuronal control of brain blood flow. *Nature*. 2010;468(7321):232-43.
85. Petzold GC, Murthy VN. Role of astrocytes in neurovascular coupling. *Neuron*. 2011;71(5):782-97.
86. Hillman EM. Coupling mechanism and significance of the BOLD signal: a status report. *Annual review of neuroscience*. 2014;37:161-81.
87. Cauli B, Hamel E. Revisiting the role of neurons in neurovascular coupling. *Frontiers in neuroenergetics*. 2010;2:9.
88. Lecrux C, Hamel E. Neuronal networks and mediators of cortical neurovascular coupling responses in normal and altered brain states. *Philosophical Transactions of the Royal Society B: Biological Sciences*. 2016;371(1705):20150350.
89. Filosa JA, Bonev AD, Straub SV, Meredith AL, Wilkerson MK, Aldrich RW, Nelson MT. Local potassium signaling couples neuronal activity to vasodilation in the brain. *Nature neuroscience*. 2006;9(11):1397-403.
90. Cauli B, Tong X-K, Rancillac A, Serluca N, Lambolez B, Rossier J, Hamel E. Cortical GABA interneurons in neurovascular coupling: relays for subcortical vasoactive pathways. *Journal of Neuroscience*. 2004;24(41):8940-9.
91. Perrenoud Q, Geoffroy H, Gautier B, Rancillac A, Alfonsi F, Kessar N, Rossier J, Vitalis T, Gallopin T. Characterization of type I and type II nNOS-expressing interneurons in the barrel cortex of mouse. *Frontiers in neural circuits*. 2012;6:36.
92. Lecrux C, Toussay X, Kocharyan A, Fernandes P, Neupane S, Lévesque M, Plaisier F, Shmuel A, Cauli B, Hamel E. Pyramidal neurons are “neurogenic hubs” in the neurovascular coupling response to whisker stimulation. *Journal of Neuroscience*. 2011;31(27):9836-47.
93. Bekar LK, Wei HS, Nedergaard M. The locus coeruleus-norepinephrine network optimizes coupling of cerebral blood volume with oxygen demand. *Journal of Cerebral Blood Flow & Metabolism*. 2012;32(12):2135-45.
94. Hamel E. Perivascular nerves and the regulation of cerebrovascular tone. *Journal of applied physiology*. 2006;100(3):1059-64.
95. Hotta H, Uchida S, Kagitani F, Maruyama N. Control of cerebral cortical blood flow by stimulation of basal forebrain cholinergic areas in mice. *The Journal of Physiological Sciences*. 2011;61(3):201.
96. Mishra A, Reynolds JP, Chen Y, Gourine AV, Rusakov DA, Attwell D. Astrocytes mediate neurovascular signaling to capillary pericytes but not to arterioles. *Nature neuroscience*. 2016;19(12):1619-27.
97. Ventura R, Harris KM. Three-dimensional relationships between hippocampal synapses and astrocytes. *Journal of Neuroscience*. 1999;19(16):6897-906.
98. Nedergaard M, Ransom B, Goldman SA. New roles for astrocytes: redefining the functional architecture of the brain. *Trends in neurosciences*. 2003;26(10):523-30.
99. Peters A, Josephson K, Vincent SL. Effects of aging on the neuroglial cells and pericytes within area 17 of the rhesus monkey cerebral cortex. *The Anatomical Record*. 1991;229(3):384-98.
100. Mathiisen TM, Lehre KP, Danbolt NC, Ottersen OP. The perivascular astroglial sheath provides a complete covering of the brain microvessels: an electron microscopic 3D reconstruction. *Glia*. 2010;58(9):1094-103.
101. Gordon GR, Mulligan SJ, MacVicar BA. Astrocyte control of the cerebrovasculature. *Glia*. 2007;55(12):1214-21.
102. Iadecola C, Nedergaard M. Glial regulation of the cerebral microvasculature. *Nature neuroscience*. 2007;10(11):1369-76.
103. Zonta M, Angulo MC, Gobbo S, Rosengarten B, Hossmann K-A, Pozzan T, Carmignoto G. Neuron-to-astrocyte signaling is central to the dynamic control of brain microcirculation. *Nature*

- neuroscience. 2003;6(1):43-50.
104. Mulligan SJ, MacVicar BA. Calcium transients in astrocyte endfeet cause cerebrovascular constrictions. *Nature*. 2004;431(7005):195-9.
 105. Metea MR, Newman EA. Glial cells dilate and constrict blood vessels: a mechanism of neurovascular coupling. *Journal of Neuroscience*. 2006;26(11):2862-70.
 106. Takano T, Tian G-F, Peng W, Lou N, Libionka W, Han X, Nedergaard M. Astrocyte-mediated control of cerebral blood flow. *Nature neuroscience*. 2006;9(2):260-7.
 107. Wang X, Lou N, Xu Q, Tian G-F, Peng WG, Han X, Kang J, Takano T, Nedergaard M. Astrocytic Ca²⁺ signaling evoked by sensory stimulation in vivo. *Nature neuroscience*. 2006;9(6):816-23.
 108. Winship IR, Plaa N, Murphy TH. Rapid astrocyte calcium signals correlate with neuronal activity and onset of the hemodynamic response in vivo. *Journal of Neuroscience*. 2007;27(23):6268-72.
 109. Dombeck DA, Khabbaz AN, Collman F, Adelman TL, Tank DW. Imaging large-scale neural activity with cellular resolution in awake, mobile mice. *Neuron*. 2007;56(1):43-57.
 110. Petzold GC, Albeanu DF, Sato TF, Murthy VN. Coupling of neural activity to blood flow in olfactory glomeruli is mediated by astrocytic pathways. *Neuron*. 2008;58(6):897-910.
 111. Schummers J, Yu H, Sur M. Tuned responses of astrocytes and their influence on hemodynamic signals in the visual cortex. *Science*. 2008;320(5883):1638-43.
 112. Thrane AS, Thrane VR, Zeppenfeld D, Lou N, Xu Q, Nagelhus EA, Nedergaard M. General anesthesia selectively disrupts astrocyte calcium signaling in the awake mouse cortex. *Proceedings of the National Academy of Sciences*. 2012;109(46):18974-9.
 113. Nizar K, Uhlirova H, Tian P, Saisan PA, Cheng Q, Reznichenko L, Weldy KL, Steed TC, Sridhar VB, MacDonald CL. In vivo stimulus-induced vasodilation occurs without IP3 receptor activation and may precede astrocytic calcium increase. *Journal of Neuroscience*. 2013;33(19):8411-22.
 114. Bonder DE, McCarthy KD. Astrocytic Gq-GPCR-linked IP3R-dependent Ca²⁺ signaling does not mediate neurovascular coupling in mouse visual cortex in vivo. *Journal of Neuroscience*. 2014;34(39):13139-50.
 115. Nimmerjahn A, Kirchhoff F, Kerr JN, Helmchen F. Sulforhodamine 101 as a specific marker of astroglia in the neocortex in vivo. *Nature methods*. 2004;1(1):31-7.
 116. Otsu Y, Couchman K, Lyons DG, Collot M, Agarwal A, Mallet J-M, Pfrieger FW, Bergles DE, Charpak S. Calcium dynamics in astrocyte processes during neurovascular coupling. *Nature neuroscience*. 2015;18(2):210-8.
 117. Wang M, He Y, Sejnowski TJ, Yu X. Brain-state dependent astrocytic Ca²⁺ signals are coupled to both positive and negative BOLD-fMRI signals. *Proceedings of the National Academy of Sciences*. 2018;115(7):E1647-E56.
 118. Sun W, McConnell E, Pare J-F, Xu Q, Chen M, Peng W, Lovatt D, Han X, Smith Y, Nedergaard M. Glutamate-dependent neuroglial calcium signaling differs between young and adult brain. *Science*. 2013;339(6116):197-200.
 119. Silva AC, Koretsky AP. Laminar specificity of functional MRI onset times during somatosensory stimulation in rat. *Proceedings of the National Academy of Sciences*. 2002;99(23):15182-7.
 120. Goense J, Merkle H, Logothetis NK. High-resolution fMRI reveals laminar differences in neurovascular coupling between positive and negative BOLD responses. *Neuron*. 2012;76(3):629-39.
 121. Carr VA, Rissman J, Wagner AD. Imaging the human medial temporal lobe with high-resolution fMRI. *Neuron*. 2010;65(3):298-308.
 122. Mateo C, Knutsen PM, Tsai PS, Shih AY, Kleinfeld D. Entrainment of arteriole vasomotor fluctuations by neural activity is a basis of blood-oxygenation-level-dependent "resting-state" connectivity. *Neuron*. 2017;96(4):936-48. e3.
 123. Chan AW, Mohajerani MH, LeDue JM, Wang YT, Murphy TH. Mesoscale infraslow spontaneous membrane potential fluctuations recapitulate high-frequency activity cortical motifs. *Nature communications*. 2015;6(1):1-12.
 124. Drew PJ, Shih AY, Kleinfeld D. Fluctuating and sensory-induced vasodynamics in rodent cortex extend arteriole capacity. *Proceedings of the National Academy of Sciences*. 2011;108(20):8473-8.
 125. Squire LR. Memory and the hippocampus: a synthesis from findings with rats, monkeys, and

- humans. *Psychological review*. 1992;99(2):195.
126. Eichenbaum H, Dudchenko P, Wood E, Shapiro M, Tanila H. The hippocampus, memory, and place cells: is it spatial memory or a memory space? *Neuron*. 1999;23(2):209-26.
 127. Jarrard LE. On the role of the hippocampus in learning and memory in the rat. *Behavioral and neural biology*. 1993;60(1):9-26.
 128. De Lanerolle N, Kim J, Robbins RJ, Spencer D. Hippocampal interneuron loss and plasticity in human temporal lobe epilepsy. *Brain research*. 1989;495(2):387-95.
 129. Hyman BT, Van Hoesen GW, Damasio AR, Barnes CL. Alzheimer's disease: cell-specific pathology isolates the hippocampal formation. *Science*. 1984;225(4667):1168-70.
 130. Traub RD, Bibbig A, LeBeau FE, Buhl EH, Whittington MA. Cellular mechanisms of neuronal population oscillations in the hippocampus in vitro. *Annu Rev Neurosci*. 2004;27:247-78.
 131. Butler JL, Paulsen O. Hippocampal network oscillations—recent insights from in vitro experiments. *Current opinion in neurobiology*. 2015;31:40-4.
 132. Attardo A, Fitzgerald JE, Schnitzer MJ. Impermanence of dendritic spines in live adult CA1 hippocampus. *Nature*. 2015;523(7562):592-6.
 133. Kondo M, Kobayashi K, Ohkura M, Nakai J, Matsuzaki M. Two-photon calcium imaging of the medial prefrontal cortex and hippocampus without cortical invasion. *Elife*. 2017;6:e26839.
 134. Coyle P. Vascular patterns of the rat hippocampal formation. *Experimental neurology*. 1976;52(3):447-58.
 135. Coyle P. Spatial features of the rat hippocampal vascular system. *Experimental neurology*. 1978;58(3):549-61.
 136. Rungta RL, Osmanski B-F, Boido D, Tanter M, Charpak S. Light controls cerebral blood flow in naive animals. *Nature communications*. 2017;8(1):1-9.
 137. Osawa S-i, Iwasaki M, Hosaka R, Matsuzaka Y, Tomita H, Ishizuka T, Sugano E, Okumura E, Yawo H, Nakasato N. Optogenetically induced seizure and the longitudinal hippocampal network dynamics. *PloS one*. 2013;8(4):e60928.
 138. Weitz AJ, Fang Z, Lee HJ, Fisher RS, Smith WC, Choy M, Liu J, Lin P, Rosenberg M, Lee JH. Optogenetic fMRI reveals distinct, frequency-dependent networks recruited by dorsal and intermediate hippocampus stimulations. *Neuroimage*. 2015;107:229-41.
 139. Shen Q, Duong TQ. Magnetic resonance imaging of cerebral blood flow in animal stroke models. *Brain circulation*. 2016;2(1):20.
 140. Stoquart-ElSankari S, Lehmann P, Villette A, Czosnyka M, Meyer M-E, Deramond H, Balédent O. A phase-contrast MRI study of physiologic cerebral venous flow. *Journal of Cerebral Blood Flow & Metabolism*. 2009;29(6):1208-15.
 141. Chang W, Landgraf B, Johnson K, Kecskemeti S, Wu Y, Velikina J, Rowley H, Wieben O, Mistretta C, Turski P. Velocity measurements in the middle cerebral arteries of healthy volunteers using 3D radial phase-contrast HYPRFlow: comparison with transcranial Doppler sonography and 2D phase-contrast MR imaging. *American journal of neuroradiology*. 2011;32(1):54-9.
 142. Bernstein MA, Zhou XJ, Polzin JA, King KF, Ganin A, Pelc NJ, Glover GH. Concomitant gradient terms in phase contrast MR: analysis and correction. *Magnetic resonance in medicine*. 1998;39(2):300-8.
 143. Peeters JM, Bos C, Bakker CJ. Analysis and correction of gradient nonlinearity and B0 inhomogeneity related scaling errors in two - dimensional phase contrast flow measurements. *Magnetic Resonance in Medicine: An Official Journal of the International Society for Magnetic Resonance in Medicine*. 2005;53(1):126-33.
 144. Walker PG, Cranney GB, Scheidegger MB, Waseleski G, Pohost GM, Yoganathan AP. Semiautomated method for noise reduction and background phase error correction in MR phase velocity data. *Journal of Magnetic Resonance Imaging*. 1993;3(3):521-30.
 145. Pelc NJ, Bernstein MA, Shimakawa A, Glover GH. Encoding strategies for three - direction phase - contrast MR imaging of flow. *Journal of Magnetic Resonance Imaging*. 1991;1(4):405-13.
 146. Lee JH. Informing brain connectivity with optogenetic functional magnetic resonance imaging. *Neuroimage*. 2012;62(4):2244-9.
 147. Ferenczi EA, Zalocusky KA, Liston C, Grosenick L, Warden MR, Amatya D, Katovich K, Mehta H,

- Patenaude B, Ramakrishnan C. Prefrontal cortical regulation of brainwide circuit dynamics and reward-related behavior. *Science*. 2016;351(6268).
148. Marshall JD, Li JZ, Zhang Y, Gong Y, St-Pierre F, Lin MZ, Schnitzer MJ. Cell-type-specific optical recording of membrane voltage dynamics in freely moving mice. *Cell*. 2016;167(6):1650-62. e15.
149. Paxinos G, Watson C. *The rat brain in stereotaxic coordinates: hard cover edition*: Elsevier; 2006.
150. Miyagi Y, Shima F, Sasaki T. Brain shift: an error factor during implantation of deep brain stimulation electrodes. *Journal of neurosurgery*. 2007;107(5):989-97.
151. Pallavaram S, Dawant BM, Remple MS, Neimat JS, Kao C, Konrad PE, D'Haese P-F. Effect of brain shift on the creation of functional atlases for deep brain stimulation surgery. *International journal of computer assisted radiology and surgery*. 2010;5(3):221-8.
152. Liu J, Lee HJ, Weitz AJ, Fang Z, Lin P, Choy M, Fisher R, Pinskiy V, Tolpygo A, Mitra P. Frequency-selective control of cortical and subcortical networks by central thalamus. *Elife*. 2015;4:e09215.
153. Resendez SL, Jennings JH, Ung RL, Namboodiri VMK, Zhou ZC, Otis JM, Nomura H, McHenry JA, Kosyk O, Stuber GD. Visualization of cortical, subcortical and deep brain neural circuit dynamics during naturalistic mammalian behavior with head-mounted microscopes and chronically implanted lenses. *Nature protocols*. 2016;11(3):566.
154. Russell P. Photonic crystal fibers. *science*. 2003;299(5605):358-62.
155. Pautler RG, Silva AC, Koretsky AP. In vivo neuronal tract tracing using manganese - enhanced magnetic resonance imaging. *Magnetic resonance in medicine*. 1998;40(5):740-8.
156. Binnewijzend MA, Schoonheim MM, Sanz-Arigita E, Wink AM, van der Flier WM, Tolboom N, Adriaanse SM, Damoiseaux JS, Scheltens P, van Berckel BN. Resting-state fMRI changes in Alzheimer's disease and mild cognitive impairment. *Neurobiology of aging*. 2012;33(9):2018-28.
157. Pievani M, Filippini N, Van Den Heuvel MP, Cappa SF, Frisoni GB. Brain connectivity in neurodegenerative diseases—from phenotype to proteinopathy. *Nature Reviews Neurology*. 2014;10(11):620.
158. de Eulate RG, Goñi I, Galiano A, Vidorreta M, Recio M, Riverol M, Zubieta JL, Fernández-Seara MA. Reduced cerebral blood flow in mild cognitive impairment assessed using phase-contrast MRI. *Journal of Alzheimer's Disease*. 2017;58(2):585-95.

6. Acknowledgments

This work would not have been made without the support and help from a lot of people. Therefore, I would like to express my sincere gratitude to all of them.

First of all, I am deeply grateful to my supervisor Dr. Xin Yu and Prof. Dr. Hanspeter A. Mallot for allowing me to perform my Ph.D. in the Max Planck Institute for Biological Cybernetics and bringing me into the field of MRI, for their valuable guidance and constructive comments, for their constant encouragement and strong support, for their kindly evaluating my thesis.

Thanks to Prof. Dr. Klaus Scheffler and Dr. Rolf Pohmann for their great guidance, for sharing their skills and insights.

Thanks to Dr. Jörn Engelmann for giving his comments on my thesis drafts, for his great encouragement.

Thanks to Mrs. Tina Schröder, Mrs. Hildegard Schulz, Mr. Mihai Vintiloiu, for their patience, for helping me to adjust to life in Germany.

Thanks to all my colleagues and friends in Tübingen (Tina, Giuseppe, Marlon, Rosa, Filip, Kengo, Vinod), for the shared experiences, for the fun, for the wonderful memories. Also, thanks to my old friends in China (Ping Bai, Juelling Tan, Wen Fan), for their precious friendships.

Thanks to Dr. Pedro Douay, Dr. Elke Weiler, Mrs. Rebecca König, Ms. Sabrina Fischer, and Mrs. Mariana Pitscheider for animal support.

Thanks to the nice guys in the workshops for strong technical support.

Thanks to my family, my grandparents (Qingyuan Chen, Jinping Tian, Qiming Tian, Birong Zhao), my parents (Gang Chen and Jun Tian), for their love and freedom.

Thanks to my husband (Ying He), for his trust, support, and love.

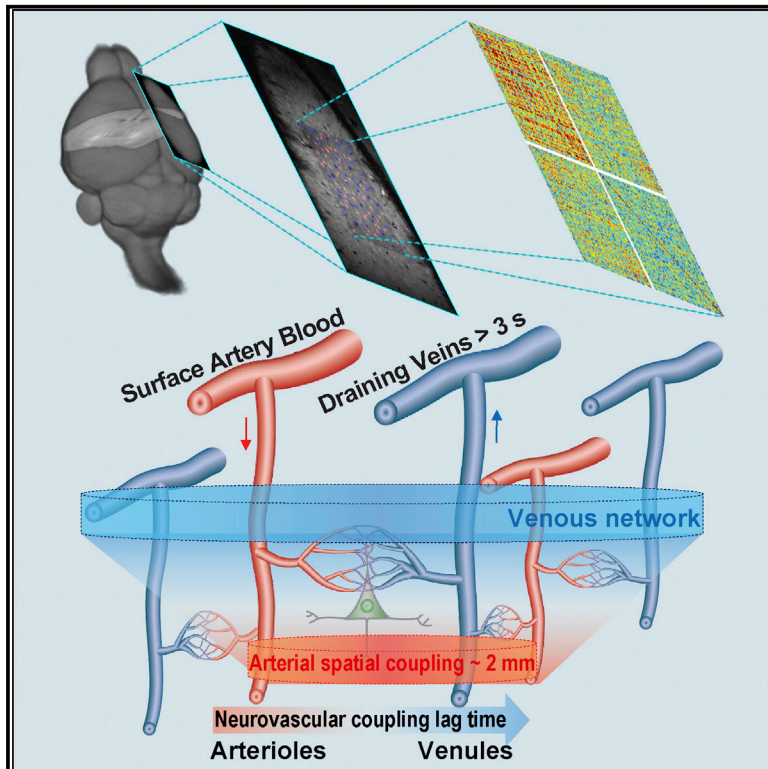
Thanks to my daughter (Penning He), for her smile, tear, hug, kiss....

7. Appendix: original manuscripts

Neuron

Ultra-Slow Single-Vessel BOLD and CBV-Based fMRI Spatiotemporal Dynamics and Their Correlation with Neuronal Intracellular Calcium Signals

Graphical Abstract



Authors

Yi He, Maosen Wang, Xuming Chen, ..., Bruce R. Rosen, David Kleinfeld, Xin Yu

Correspondence

xin.yu@tuebingen.mpg.de

In Brief

He et al. performed single-vessel fMRI in rat to map spatiotemporal correlations of ultra-slow arteriole CBV and venule BOLD fluctuations, concurrent with intracellular-calcium photometry. They find a 2 mm correlation length, which bears on the resolution of functional connectivity.

Highlights

- bSSFP-based single-vessel fMRI reveals dynamic vascular network connectivity
- Arterioles and venules showed distinct patterns of spatiotemporal correlations
- Neural Ca^{2+} ultra-slow oscillations correlate to vessel-specific fMRI fluctuations
- Human brain fMRI signal fluctuations were mapped in individual gray matter veins



Ultra-Slow Single-Vessel BOLD and CBV-Based fMRI Spatiotemporal Dynamics and Their Correlation with Neuronal Intracellular Calcium Signals

Yi He,^{1,2} Maosen Wang,^{1,2} Xuming Chen,^{1,2} Rolf Pohmann,¹ Jonathan R. Polimeni,³ Klaus Scheffler,^{1,6} Bruce R. Rosen,³ David Kleinfeld,^{4,5} and Xin Yu^{1,7,*}

¹High-Field Magnetic Resonance Department, Max Planck Institute for Biological Cybernetics, 72076 Tuebingen, Germany

²Graduate Training Centre of Neuroscience, International Max Planck Research School, University of Tuebingen, 72074 Tuebingen, Germany

³MGH/MIT/HMS Athinoula A. Martinos Center for Biomedical Imaging, Department of Radiology, Harvard Medical School, Massachusetts General Hospital, Charlestown, MA 02114, USA

⁴Department of Physics

⁵Section of Neurobiology

University of California at San Diego, La Jolla, CA 92093, USA

⁶Department of Biomedical Magnetic Resonance, University of Tübingen, 72076 Tübingen, Germany

⁷Lead Contact

*Correspondence: xin.yu@tuebingen.mpg.de

<https://doi.org/10.1016/j.neuron.2018.01.025>

SUMMARY

Functional MRI has been used to map brain activity and functional connectivity based on the strength and temporal coherence of neurovascular-coupled hemodynamic signals. Here, single-vessel fMRI reveals vessel-specific correlation patterns in both rodents and humans. In anesthetized rats, fluctuations in the vessel-specific fMRI signal are correlated with the intracellular calcium signal measured in neighboring neurons. Further, the blood-oxygen-level-dependent (BOLD) signal from individual venules and the cerebral-blood-volume signal from individual arterioles show correlations at ultra-slow (<0.1 Hz), anesthetic-modulated rhythms. These data support a model that links neuronal activity to intrinsic oscillations in the cerebral vasculature, with a spatial correlation length of ~2 mm for arterioles. In complementary data from awake human subjects, the BOLD signal is spatially correlated among sulcus veins and specified intracortical veins of the visual cortex at similar ultra-slow rhythms. These data support the use of fMRI to resolve functional connectivity at the level of single vessels.

INTRODUCTION

The cerebral vasculature is an interconnected network that supplies metabolites to the brain and mediates chemical signaling between the brain and the body. Cerebral circulation is mediated by an electrogenic vascular system, composed of interconnected endothelial cells that transmit signals between neighboring vessels to control the tone of arteriole smooth muscle (Ay-

din et al., 1991; Longden et al., 2017) in addition to forming the lumen of the vessels. The vascular system exhibits a number of rhythms of neurological and vascular origin (Obrig et al., 2000; Tak et al., 2015; Zhu et al., 2015). Respiratory- and cardiac-based rhythmic components can be regressed out of the fMRI data. Yet an ultra-low frequency (0.1 Hz) fluctuation in the diameter of arterioles, known as vasomotion (Intaglietta, 1990), remain. Far from a confounding factor (Murphy et al., 2013), these fluctuations form the basis of resting-state fMRI (Biswal et al., 1995; Fox and Raichle, 2007). Critically, vasomotion has been shown to be entrained by similarly ultra-slow oscillations in neuronal signaling (Mateo et al., 2017). It has been hypothesized that these covaried vasomotion and oscillatory neuronal patterns may contribute to the physiological basis of the resting-state fMRI connectivity mapping. This would provide the underpinning to observations of concurrent ultra-slow neuronal and hemodynamic signals, acquired optically (Schulz et al., 2012; Du et al., 2014; Ma et al., 2016) and electrophysiologically (Shmuel and Leopold, 2008; Schölvinck et al., 2010).

It is an open challenge to merge the optically acquired neuronal and vessel-specific hemodynamic signaling events with fMRI recordings to directly interpret the vascular basis of the resting-state fMRI signal (Logothetis et al., 2001). In most past work, the resting-state fMRI signal is acquired from large brain voxels (He et al., 2008; Shmuel and Leopold, 2008; Schölvinck et al., 2010). However, more recently high-resolution fMRI has allowed us to map vessel-specific hemodynamic signal from distinct vessel-dominated versus parenchyma-dominated voxels enriched with capillaries in animal brains with either cerebral blood volume (CBV) fMRI or blood-oxygen-level-dependent BOLD (fMRI) (Yu et al., 2012; Moon et al., 2013; Poplawsky et al., 2017). Using line-scanning fMRI methods, the iron oxide particle-based CBV-weighted signal is localized at penetrating arterioles (Yu et al., 2016), while the BOLD signal is detected at penetrating venules (Mansfield et al., 1976; Silva and Koretsky, 2002; Yu et al., 2012, 2014). Thus, the high-resolution fMRI will



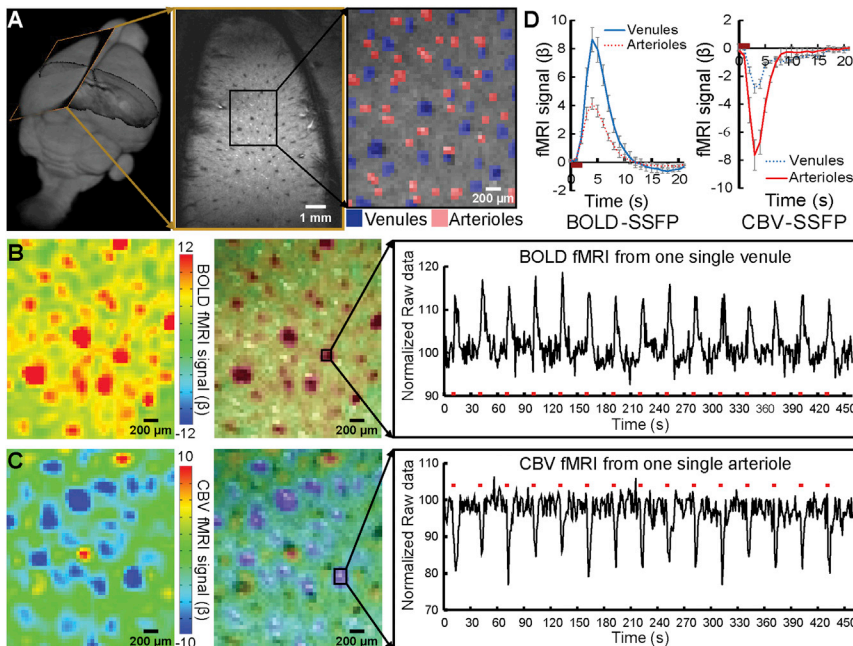


Figure 1. Balanced Steady-State Free Precession-Based Task-Related Single-Vessel BOLD and CBV fMRI

(A) An A-V map shows individual venules (dark dots, blue markers) and arterioles (bright dots, red markers) in a 2D slice.

(B) The BOLD fMRI map (left) and the semi-transparent map overlaid on the A-V map demonstrate the venule-dominated peak BOLD signal with the on/off block time series from a single venule ROI.

(C) The CBV fMRI map (left) and the semi-transparent map overlaid on the A-V map show the arteriole-dominated peak CBV signal with the on/off block time series from a single arteriole ROI.

(D) The averaged BOLD (left)/CBV (right) fMRI response function from venule (blue) and arteriole (red) voxels ($n = 5$, mean \pm SEM).

See also Figures S1 and S4 and Table S1.

permit us to follow neurovascular-coupled hemodynamic signals as they propagate from the arteriolar network, e.g., in terms of a CBV-weighted signal that will be sensitive to changes in vascular diameter, to the venous network, e.g., in terms of the BOLD signal, to gain a vascular-specific view of hemodynamic signaling with fMRI.

The technical goal of this work is 2-fold. The first is to detect the vessel-specific fluctuations in fMRI signals during the resting state. This goal must be accomplished across a plane through cortex with sufficient speed to accurately determine the magnitude and phase of correlation mediated by vasomotor fluctuations across vessels. The second is to measure these fluctuations concurrent with calcium signal recordings from neighboring neurons. Our approach builds on our ability to identify brain arterioles from venules with MRI and our line-scanning method to map the single-vessel hemodynamic signal (Yu et al., 2016). The line-scanning scheme reshuffled the k-space acquisition so that each image was reconstructed from data acquired along the entire experimental time series with a fast sampling rate, but not in real time (Silva and Koretsky, 2002; Yu et al., 2016). Here, we develop a single-vessel resting-state fMRI mapping method to specify the unique temporal dynamic features of neurovascular oscillatory signals, as well as to characterize the spatial distribution of fluctuations in the fMRI signal in both arteriolar and venous networks. We ask: (1) can the balanced steady-state free precession (bSSFP) method be used to detect vessel-specific fMRI signal fluctuations during resting state? The bSSFP method has higher SNR per time unit than the line-scanning method and presents less image distortion with reduced extravascular effect than the echo-planar imaging (EPI) method for high-field rat brain fMRI (Scheffler and Lehnardt, 2003). (2) Can both BOLD and CBV signals be detected at the scale of penetrating vessels, the finest spatial scale within the brain in

cortical vessels studied with fMRI match all or part of the fMRI signal with the context of low-frequency fluctuations in brain state (Schulz et al., 2012; Du et al., 2014; Ma et al., 2016)? (4) Lastly, can the single-vessel fMRI scheme be extended to map the vessel-specific long-range correlation patterns in the gray matter of the human brain?

RESULTS

Single-Vessel Mapping of the Evoked BOLD and CBV-Weighted Signal with bSSFP-fMRI

Balanced steady-state free precession (bSSFP) single-vessel fMRI was implemented to map the evoked BOLD and CBV-weighted fMRI signal in the forepaw region of primary sensory (S1) cortex rats under α -chloralose anesthesia. Although anesthesia will alter brain rhythms, and lower the ultra-slow fluctuations to below their awake, resting-state value of ~ 0.1 Hz (Chan et al., 2015), the use of anesthesia is currently necessary for stability in these initial single-vessel fMRI measurements. Our stimulus was transient electrical stimulation of the forepaw. To acquire a high spatial resolution 2D bSSFP image, we acquired each spin echo every 7.8 ms to shorten the total acquisition time for each 2D image, comprising a 96×128 matrix (FOV, 9.6×12.8 mm) for an in-plane resolution of $100 \times 100 \mu\text{m}$, to a TR of 1 s. As described previously (Yu et al., 2016), a multi-gradient-echo (MGE) sequence was used to distinguish among individual arterioles (bright dots, due to the inflow effect) and venules (dark dots, due to fast $T2^*$ decay of deoxygenated blood) from the anatomical single-vessel 2D images, i.e., the arteriole-venule (A-V) map (Figure 1A). Also noteworthy is that the A-V ratio is 0.85 ± 0.04 (Table S1), demonstrating more penetrating veins than arteries, which is consistent with what has been previously reported in rodents (Hirsch et al., 2012; Blinder et al., 2013).

Further, the sensory-evoked single-vessel BOLD and CBV-weighted fMRI signal was detected by the bSSFP single-vessel fMRI before and after iron oxide particle injection. The data of Figure 1B show that the peak BOLD signals are primarily located at the venule voxels with the time course of the positive BOLD signal from a selected venule (Figure S1). After an injection of iron oxide particles, the bSSFP fMRI signal was acquired in the same 2D slice and shows that the evoked CBV-weighted signal corresponds to a decreased T2*-weighted MR signal (Figure 1C). Note that the T2*-weighted signal drops since activity-evoked vasodilation leads to an increased blood volume with more iron oxide particles in a given voxel, which shortens the magnitude of T2* and diminishes the signal (Mandeville et al., 1998). The peak CBV-weighted signal was mainly located at individual arterioles with the time course of the negative CBV-weighted signal originated from a selected arteriole (Figures 1C and S1). The averaged hemodynamic time courses from regions of interest of venule and arteriole voxels showed that the positive BOLD signal is much higher in venule than arteriole voxels (Figure 1D). Similarly, the negative CBV-weighted signal is much lower in arteriole than venule voxels (Figure 1D). Interestingly, the CBV-weighted signal in arteriole voxels returned to baseline faster than that in venules. An extended temporal response for the CBV-weighted signal in venules has been previously reported for CBV-based fMRI studies (Mandeville et al., 1999; Silva et al., 2007; Drew et al., 2011) and may be inferred from optical imaging (Drew et al., 2011). These results demonstrate the feasibility of bSSFP-fMRI for real-time single-vessel hemodynamic mapping from arterioles. They complement the venule-dominated approach for the positive BOLD signal mainly in terms of oxy/deoxy-hemoglobin ratio changes.

Single-Vessel bSSFP fMRI Mapping the Resting-State BOLD and CBV-Weighted Signals

Moving beyond the evoked single-vessel fMRI mapping, the ultra-slow resting-state hemodynamic signal was directly mapped with the bSSFP single-vessel fMRI method. Individual arterioles or venules identified from the A-V map were selected as seed voxels to calculate the correlation maps of both BOLD and CBV-based fluctuations in the fMRI signal (Figure 2); the frequency range was 0.01 to 0.1 Hz. As shown in the example data of Figure 2B, venule voxels were highly correlated to each other but less correlated for arterioles in the resting-state BOLD correlation maps (Movie S1). In contrast, as shown in the example data of Figure 2C, arteriole voxels were highly correlated but venules essentially uncorrelated in the resting-state CBV-weighted correlation maps (Movie S2). The power spectral density shows that the venule-specific BOLD and arteriole-specific CBV-weighted fMRI signal fluctuate within the ultra-slow frequency range of 0.01 to 0.04 Hz (Figure 2D). Similar to the evoked fMRI maps, the significant BOLD signal correlations were primarily located at venule voxels, i.e., the venule-specific connectivity map, and the significant CBV-weighted signal correlation were primarily located at arteriole voxels, i.e., the arteriole-specific connectivity map, during the resting state.

To better characterize the spatial and temporal features of the single-vessel fMRI fluctuations, the vessels identified in

the A-V map were paired to calculate correlation coefficients (Figure 3A). First, the values of the correlation coefficient for all vessel pairs (arteriole pairs: A-A; venule pairs: V-V) were plotted as the function of inter-vessel distance. For the BOLD signal fluctuation, V-V pairs show a stronger correlation than that of A-A pairs in the large field-of-view, up to 5×5 mm. This highlights the large-scale extent of the BOLD-based venule functional connectivity (Figures 3B and 3F). In contrast to the case for BOLD, a stronger correlation was detected for the A-A pairs than the V-V pairs for the CBV-weighted signal fluctuations. These correlations diminished over a vessel separation distance of 2 mm (Figures 3C and 3G). This spatial scale is consistent with the scale for correlations in vasomotion across arterioles, as detected by two-photon imaging of vessel diameter (Mateo et al., 2017). This spatial scale also corresponds to the ~ 2 mm electrotonic length for conduction through endothelial cells (Segal and Duling, 1989). The color-coded correlation matrices showed higher BOLD values of correlation in V-V pairs than the other pairs (Figure 3D) and higher CBV-weighted values of correlation in A-A pairs than the other pairs (Figure 3E), which is quantitatively represented as the function of vessel pair distance (Figures 3F and 3G).

Next, Spectral coherence analysis from paired venules or arterioles was performed to characterize the full frequency spectrum of the vessel-specific fMRI signal fluctuation during the resting state. The coherent oscillation was mainly distributed in the 0.01–0.04 Hz frequency range for both BOLD and CBV-weighted fMRI signal fluctuation (Figures 3H and 3I, similar to the spectral power, Figure 2D). Quantitative analysis demonstrates that the coherence coefficient of venule pairs is significantly higher than that of arteriole pairs for the BOLD signal fluctuation. In contrast, for the CBV-weighted signal fluctuation, the coherence coefficient of arteriole pairs is significantly higher than that of venule pairs for the 0.01–0.04 Hz frequency bandwidth (Figures 3J and 3K). In addition to the seed-based analysis, independent component analysis (ICA) was used to determine the venule-specific dynamic connectivity for BOLD signal fluctuation and the arteriole-specific dynamic connectivity for CBV-weighted signal fluctuation (Figures S2A–S2G). One component appeared specific for vessel-specific BOLD ultra-slow oscillations and another for CBV-weighted the ultra-slow oscillations (Figures S2F and S2G). These results confirm distinct vessel-specific correlation patterns for BOLD and CBV-weighted signal fluctuation.

Vessel-specific BOLD correlation maps were detected in rats anesthetized with isoflurane ($<1.2\%$ [v/v]) (Figures S2H–S2M). The frequency range of oscillations extended to ~ 0.1 Hz with peak power levels at 0.01–0.04 Hz, similar to those observed with rats anesthetized with α -chloralose (Figure 2). This result suggests that while oscillation at frequencies above ~ 0.1 Hz may vary depending on the anesthetized or awake brain state (Obrig et al., 2000; Du et al., 2014; Ma et al., 2016; Mateo et al., 2017), the ultra-slow frequencies are fairly stable (<0.1 Hz) under uniform ventilation. It is noteworthy that blood pressure was acquired simultaneously with fMRI, but no clear ultra-slow frequency fluctuation was observed from either of the physiological parameters (Figure S3).

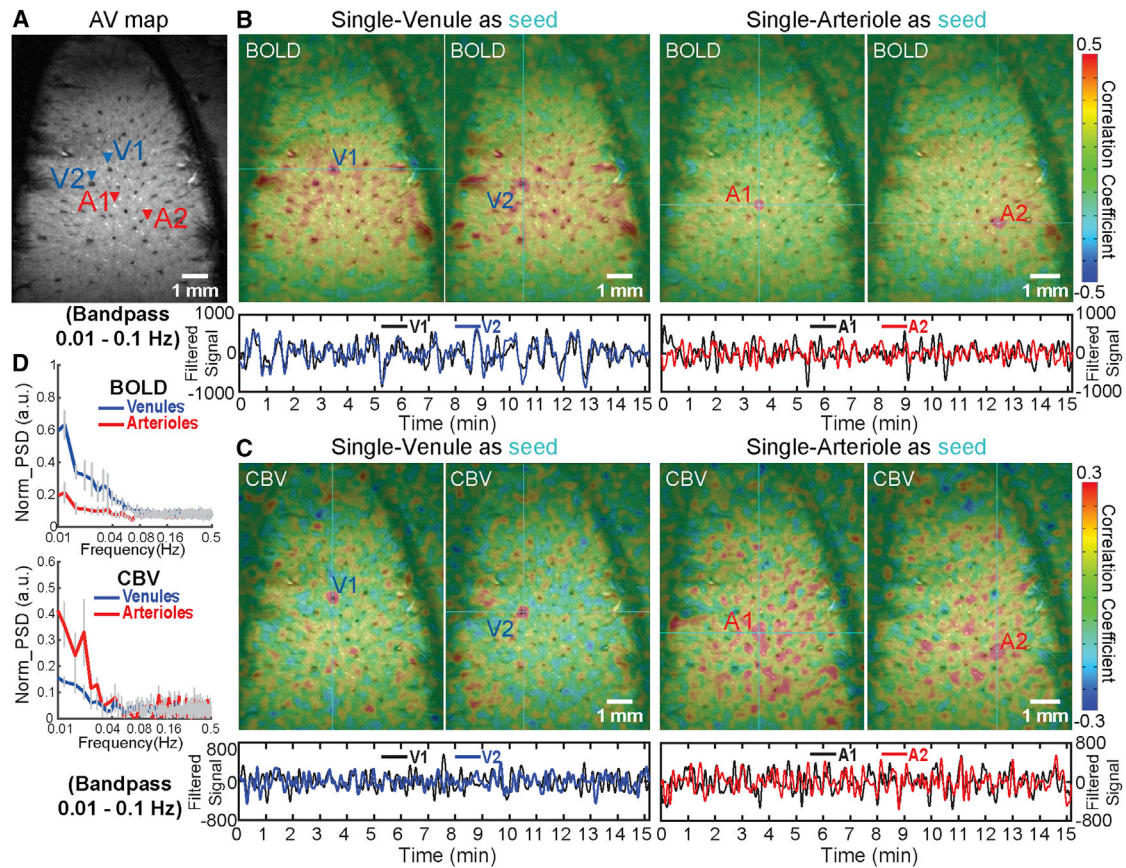


Figure 2. Using bSSFP-Based rs-fMRI to Map Vascular-Specific Correlation Patterns

(A) The A-V map shows individual penetrating arterioles and venules (blue arrowheads, venules; red arrowheads, arterioles).

(B) The seed-based BOLD rs-fMRI correlation maps (0.01–0.1 Hz; seeds: cyan crosshairs) of two venule seeds (V1 and V2; left) and CBV rs-fMRI correlation maps (0.01–0.1 Hz; seeds: cyan crosshairs) of two arteriole seeds (A1 and A2; right). The lower panel is the BOLD signal time course of the two venule seed ROIs and two arteriole seed ROIs.

(C) The seed-based CBV rs-fMRI correlation maps (0.01–0.1 Hz; seeds: cyan crosshairs) of two venule seeds (V1 and V2; left) and CBV rs-fMRI correlation maps (0.01–0.1 Hz; seeds: cyan crosshairs) of two arteriole seeds (A1 and A2; right). The lower panel is the CBV signal time course of the two venule seed ROIs and two arteriole seed ROIs.

(D) The power spectral density (PSD: arbitrary unit [a.u.]) of the venule and arteriole-specific resting-state BOLD (upper) and CBV (lower) fMRI time courses. See also Figures S2 and S3.

Comparison of Vessel-Specific BOLD and CBV fMRI Signals with Simultaneous Neuronal Calcium Recording

To characterize the potential neural correlates of the vessel-specific fMRI signal fluctuation, a genetically encoded calcium indicator, GCaMP6f, was expressed in neurons of forepaw S1 or vibrissa S1 cortex for simultaneous intracellular $[Ca^{2+}]$ recording and fMRI (Figure S4); immunostaining verified the GCaMP expression in cortical neurons (Figure S4B). Evoked and spontaneous intracellular $[Ca^{2+}]$ transients were recorded in the deep layers with fiber photometry concurrent with the local field potential (LFP) (Figures 4A and S4C–S4F). Evoked $[Ca^{2+}]$ spikes were acquired simultaneously with single-vessel bSSFP-fMRI for comparison with the venule-specific positive BOLD signal and arteriole-specific negative CBV-weighted signal (Figures S4E and S4F). These results demonstrate the feasibility of simultaneous single-vessel fMRI with intracellular $[Ca^{2+}]$ fiber optic recording.

We sought to characterize the potential neuronal origin of the vessel-specific fMRI signal fluctuation. We first considered the correlation between changes in intracellular $[Ca^{2+}]$ in the 0.01 to 0.1 Hz band and the resting-state BOLD signal. It shows vessel-specific positive correlation patterns that are similar to the venule-seed based correlation maps from rats anesthetized with α -chloralose (Figures 4B and 4C); time courses of representative venules (V1, V2), and changes in intracellular $[Ca^{2+}]$ are shown in Figure 4D. The correlation coefficient between the intracellular $[Ca^{2+}]$ and the venule BOLD signal (Ca^{2+} -V) was significantly higher than that with the arteriole BOLD signal (Ca^{2+} -A) (Figure 4F). Cross-correlation analysis between the changes in intracellular $[Ca^{2+}]$ and the venule-specific BOLD signal showed a positive peak at the averaged lag time of 2.3 ± 0.2 s (Figures 4E and 4G). The vessels at the cortical surface had the longest lag, up to 3–5 s (Figure 4C), which agrees with the lag reported previously by cross-correlation analysis of the

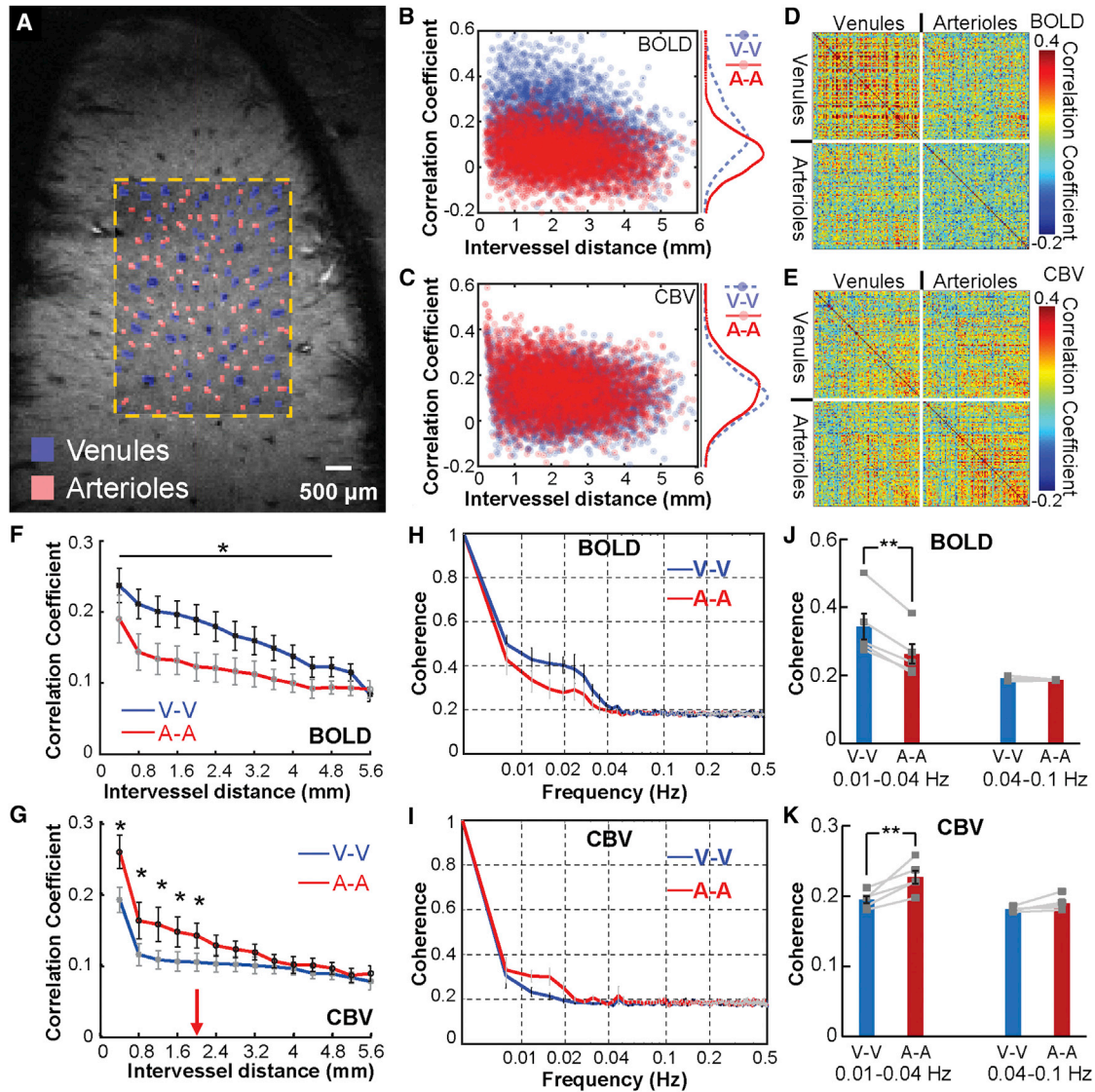


Figure 3. Vascular Dynamic Network Connectivity in Rats at 14.1T

(A) The A-V map of one representative rat (arteriole ROIs in red and venule ROIs in blue).

(B and C) Scatterplots of the correlation coefficient (CC) of BOLD (B) and CBV (C) fMRI from venule-to-venule (V-V) pairs, arteriole-to-arteriole (A-A) pairs as the function of the inter-vessel distance from one representative rat.

(D and E) The correlation matrices of all vessel pairs for the BOLD (D) and CBV (E) fMRI from one representative rat.

(F and G) The mean CC value of the BOLD signal from the venule pairs is significantly higher than that of the arteriole pairs with large spatial inter-vessel distance (>5 mm) (F, $n = 5$, mean \pm SEM, *, paired t test, $p < 0.03$). In contrast, the mean CC value of the CBV signal from the arteriole pairs is significantly higher than that of the venule pairs with small spatial inter-vessel distance (~ 2 mm) (G, $n = 5$, mean \pm SEM, *, paired t test, $p < 0.03$).

(H and I) The averaged coherence graph of paired venules and arterioles from BOLD/CBV fMRI (H), BOLD fMRI, $n = 5$, (I), CBV fMRI, $n = 5$ rats, mean \pm SEM.

(J) The mean BOLD coherence coefficient of the venule pairs is significantly higher than that of arteriole pairs at the low-frequency range (0.01–0.04 Hz) ($n = 5$, paired t test, ** $p = 0.0009$).

(K) The mean CBV coherence value of paired venules is significantly lower than that of paired arterioles at the low-frequency range (0.01–0.04 Hz) ($n = 5$ rats, paired t test, ** $p = 0.007$).

See also Figures S2 and S3.

calcium signal and hemoglobin-based intrinsic optical signal (Du et al., 2014).

We next considered the correlation of the calcium signal in the 0.01–0.1 Hz band with the single-vessel CBV-weighted fMRI signal obtained after the injection of iron oxide particles. Similar

to the arteriole-seed based CBV correlation maps (Figure 4I), the highly correlated voxels with changes in intracellular $[Ca^{2+}]$ were located mainly at arterioles, but with negative values of the correlation coefficient (Figure 4J); the time courses of representative arterioles (A1, A2) and the calcium signal are shown in Figure 4K.

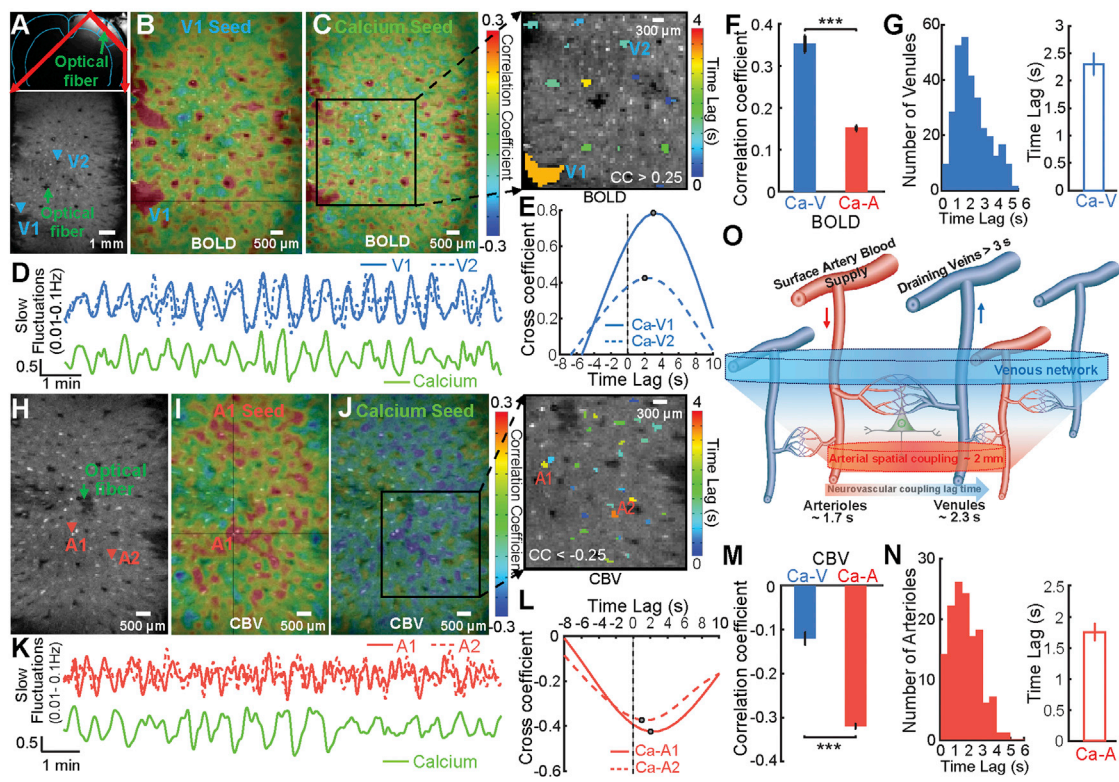


Figure 4. Correlation Analysis of the Single-Vessel BOLD/CBV fMRI with GCaMP6f-Mediated Calcium Signal

(A) The coronal view of the anatomical MR image with the optic fiber targeting the vibrissa S1 (upper). The A-V map from a 2D slice covering the deep cortical layer (lower).

(B) The seed-based BOLD correlation maps from one representative venule voxels (V1) overlaid on the A-V map.

(C) The correlation map between the BOLD fMRI signal and the calcium signal (band-pass filter: 0.01–0.1 Hz). Inset is a representative color-coded lag time map between the calcium signal with the BOLD fMRI of individual venules ($CC > 0.25$).

(D) The time courses of the BOLD fMRI signal from vessel voxels (V1: blue, solid line; V2: blue, dotted line) and the slow oscillation calcium signal (green).

(E) The cross-correlation function of the calcium signal and BOLD fMRI signal of two representative venules (Ca-V1 and Ca-V2) with positive peak coefficients at the lag time 2–3 s.

(F) The mean correlation coefficient of the calcium signal with the BOLD fMRI signal of venules is significantly higher than that of arterioles ($n = 7$ rats, mean \pm SEM, paired t test, $***p = 2.5 \times 10^{-5}$).

(G) The histogram of venules with lag times varied from 0.5 to 6 s ($CC > 0.25$) and mean lag time at 2.30 ± 0.19 s. ($n = 7$, mean \pm SEM).

(H) The A-V map with the markers of arterioles (arteriole 1: A1, arteriole 2: A2, red arrowheads) and optical fiber (green arrowhead).

(I) The seed-based correlation maps of CBV fMRI from one arterioles voxel (A1) overlaid on the A-V map.

(J) The correlation map between the CBV fMRI and calcium signal (band-pass filter: 0.01–0.1 Hz). Inset is a representative color-coded lag time map between the calcium signal and the CBV fMRI signal of individual arterioles ($CC < -0.25$).

(K) The time course of the CBV fMRI signal from arteriole voxels (red, solid and dotted lines) and the slow oscillation calcium signal (green).

(L) The cross-correlation function of the calcium signal and CBV fMRI signal of two representative arterioles (Ca-A1 and Ca-A2) with negative peak coefficients at the lag time 1–2 s.

(M) The mean correlation coefficient of the calcium signal with the CBV fMRI signal of arterioles is significantly higher than that of venules ($n = 4$, mean \pm SEM, paired t test, $***p = 0.0002$).

(N) The histogram of arterioles with lag times varied from 0.5 to 5 s ($CC < -0.25$). The mean lag time is 1.76 ± 0.14 s ($n = 4$, mean \pm SEM), which is significantly shorter than the lag times of the calcium and venule BOLD signal (BOLD, $n = 7$, CBV, $n = 4$, t test, $p = 0.025$).

(O) The schematic drawing of the spatial and temporal relation patterns of the slow oscillation signal coupling from neurons to vessels.

See also [Figures S4–S7](#) and [S10](#) and [Table S2](#)

Quantitative analysis showed that the correlation between the intracellular $[Ca^{2+}]$ and the CBV-weighted signal of arterioles (Ca²⁺-A) was significantly higher than that of venules (Ca²⁺-V) (Figure 4M). The oscillation in intracellular $[Ca^{2+}]$ also led the arteriole-specific CBV-weighted signal fluctuations, as observed by the cross-correlations of two representative arterioles as the function of lag time (Figure 4L). Different arterioles showed varied

lags with a mean value at 1.8 ± 0.2 s (Figure 4N). Cross-correlation of the intracellular $[Ca^{2+}]$ with the arteriole CBV-weighted signal showed a shorter lag time than that with the venule BOLD signal (Figures 4G and 4N). Meanwhile, the oscillation in intracellular $[Ca^{2+}]$ was found to be correlated with the CBV-weighted signal of a few venules with lag time of 5–10 s (Figure S5). This result indicates the passive venule dilation usually

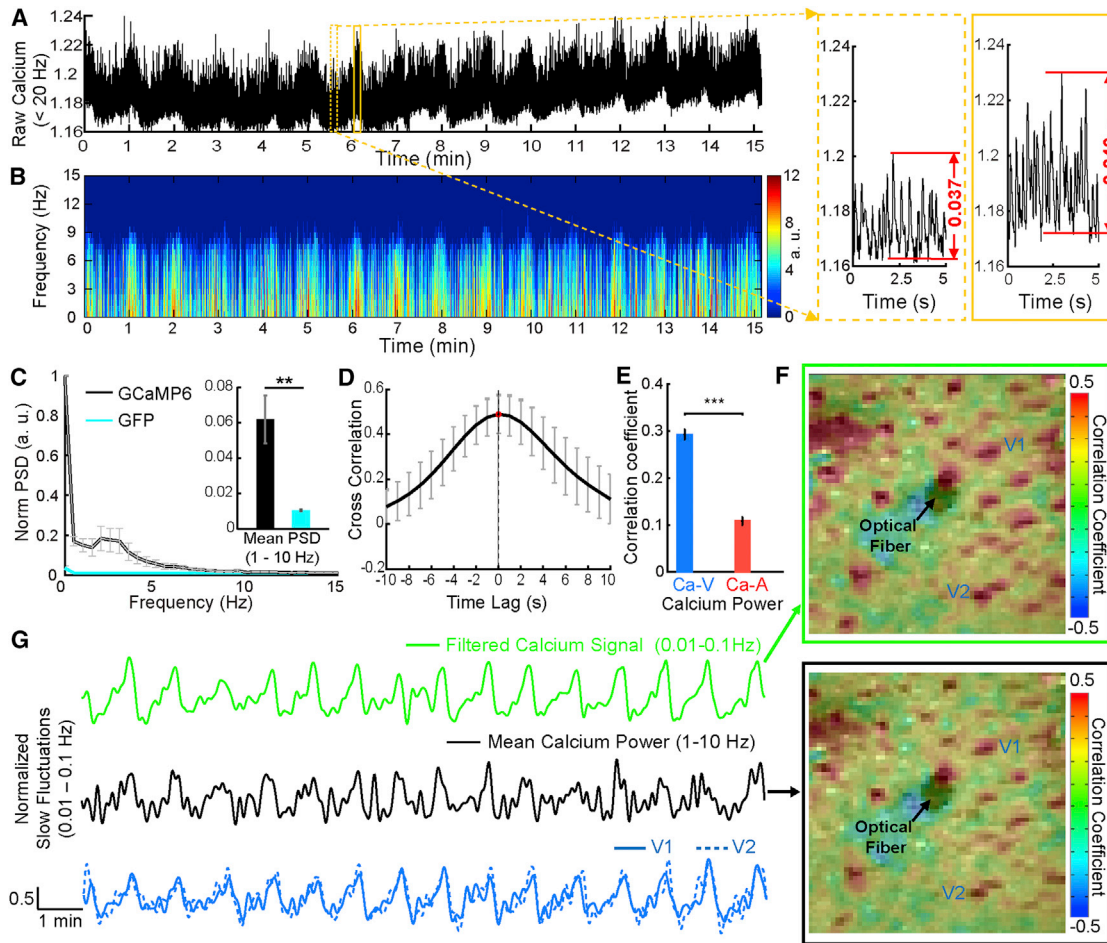


Figure 5. The Correlation between the Calcium Power Spectral Profile with Vessel-Specific fMRI Signal

(A) The time course of the calcium signal (low-pass filter: 20 Hz) from one representative rat at the resting state with enlarged 5 s windows of the calcium spikes identified at different periods (dotted and solid yellow boxes).

(B) The time-varying power spectrogram of the calcium signal is plotted as the function of time from 0.5 to 15 Hz (discrete Fourier transform in 1 s Hamming window; the sampling rate is 1 Hz to match the TR of fMRI signal).

(C) The normalized PSD from the rats with GCaMP6 (black, $n = 5$) or GFP (cyan, $n = 4$) indicates the mean PSD (1–10 Hz) of GCaMP6 is significantly higher than that of GFP (** $p = 0.001$, t test).

(D) The cross-correlation function of the calcium signal and the averaged power (1–10 Hz) profile from the calcium spectrogram (band-pass filter with 0.01–0.1 Hz) illustrates the peak cross-correlation coefficient at 0 s lag time ($n = 4$, mean \pm SEM).

(E) The mean correlation coefficients of the averaged calcium power signal with the BOLD fMRI signal of venules are significantly higher than that of arterioles (** $p = 1.9 \times 10^{-4}$, pair t test, $n = 4$, mean \pm SEM).

(F) The correlation maps between the SSFP-based BOLD fMRI signal and the slow oscillation calcium signal (band-pass filter: 0.01–0.1 Hz, upper) and the mean calcium power spectral profile (1–10 Hz, lower) show similar venule-specific correlation patterns.

(G) The time series (band-pass filter: 0.01–0.1 Hz) of the slow oscillation calcium signal (green), the mean calcium spectral power profile (1–10 Hz) (black), the BOLD fMRI signal from two venules (V1, V2; blue, solid and dotted blue lines).

See also Figure S6.

detected as the post-stimulus undershoot of the evoked BOLD signal results from increase blood flow following prolonged stimulation (Buxton et al., 1998; Silva et al., 2007; Drew et al., 2011).

Besides the ultra-slow oscillation, the GCaMP6-mediated calcium signal exhibited EEG-like rhythmic neuronal activity, showing significantly higher spectral power at the 1–10 Hz frequency range than that of the fluorescent signal detected from the GFP-expressing cortex of control rats (Figures 5A–5C). Cross-correlation of the spectral power in the 1–10 Hz and ul-

tra-slow oscillatory calcium signal fluctuation (0.1–0.01 Hz) showed peak positive correlation coefficient at zero time lag (Figure 5D). In addition, the spectral power in 1–10 Hz was correlated to the vessel-specific BOLD signal, showing the correlation coefficient of spectral power with the venule BOLD signal is significantly higher than that of the spectral power with the arteriole BOLD signal, similar to the ultra-slow oscillatory calcium signal fluctuation (Figures 4B–4D and 5E–5G). This result further demonstrates the neuronal correlates of the vessel-specific fMRI

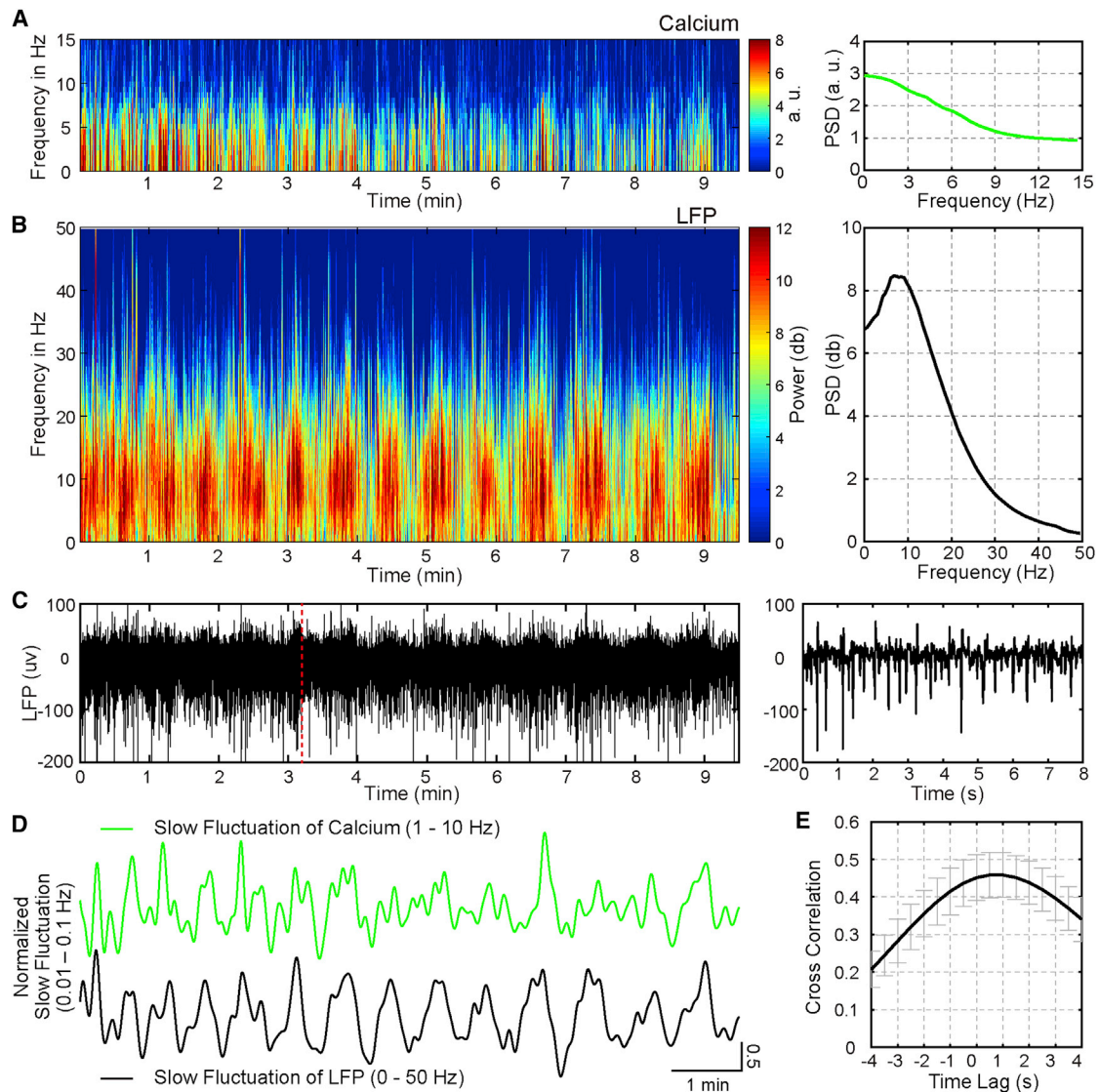


Figure 6. The Spectrogram of Simultaneous Calcium and Electrophysiological Signal under α -chloralose Anesthesia

(A) Spectrogram of calcium signal during light anesthesia.

(B) Spectrogram of local field potential (LFP) at light anesthesia from multi-taper spectral estimates (1 s sliding window with 0.1 s steps, 9 tapers). The right panel shows the averaged power spectral density (PSD).

(C) The time course of the LFP signal under light anesthesia.

(D) The mean calcium spectral power profile (band-pass filter: 0.01–0.1 Hz of 1–10 Hz, green) and the mean LFP spectral power profile (0–50 Hz, black) at light anesthesia.

(E) The cross-correlation function of the averaged LFP power (0–50 Hz) from LFP spectrogram and the averaged calcium power (1–10 Hz) profile from the calcium spectrogram (band-pass filter with 0.01–0.1 Hz) illustrates the peak cross-correlation coefficient at 0.8 s lag time at light anesthesia ($n = 4$, mean \pm SEM).

See also [Figures S5](#) and [S6](#).

signal fluctuation in the cerebrovascular network. Finally, the cartoon of [Figure 4O](#) summarizes the spatial and temporal patterns of neurovascular hemodynamic signal fluctuation from arteriolar to venous networks.

Also noteworthy is that the power spectral density shows elevated power at frequencies below 0.1 Hz for the venule BOLD and arteriole CBV-weighted signal, as well as for the simultaneously acquired calcium signal at the light anesthesia ([Figures 2D](#) and [S6](#)). In contrast, at the deep anesthesia level

with α -chloralose, the ultra-slow oscillation pattern was undetectable for both fMRI and changes in $[Ca^{2+}]$ concentration in the same rats ([Figure S6](#)), but the evoked BOLD and CBV fMRI signals and changes in $[Ca^{2+}]$ concentration remained ([Figures S4E](#) and [S4F](#)). This result further supports the neural correlates of the single-vessel fMRI signal fluctuation. Meanwhile, simultaneous LFP and intracellular $[Ca^{2+}]$ recording was performed to specify the ultra-slow oscillatory signal at different anesthesia levels ([Figures 6](#) and [S7](#)). The spectrogram of the spontaneous

LFP and intracellular $[Ca^{2+}]$ signal showed similar ultra-slow oscillation patterns in rats under the light anesthesia level (Figures 6A–6D). Cross-correlation of the LFP and intracellular $[Ca^{2+}]$ signal power profile showed positive correlation coefficients (0.46 ± 0.06) at the time lag (0.73 ± 0.13 s), showing the ultra-slow oscillatory LFP signal leads the intracellular $[Ca^{2+}]$ signal (Figure 6E). Similar to the single-vessel fMRI data, these results showed consistent correlation features at the light anesthesia level (Figure 5) but not at the deep anesthesia (Figures S7A–S7E). In addition, the ultra-slow oscillatory correlation of the LFP power profile and intracellular $[Ca^{2+}]$ fluctuations were detected in rats anesthetized with 1.2% (v/v) isoflurane (Figures S7F–S7I). These results suggest that the neuronal and vascular hemodynamic oscillations are highly correlated in the anesthetized brain and that the correlation is dampened when the neural activity is suppressed with deep anesthesia.

Mapping Vascular Network Connectivity in the Human Brain under 3T and 9.4T

The single-vessel mapping scheme was implemented to characterize the prospects for vessel-specific fMRI correlation patterns in awake human subjects. Although bSSFP shows great advantage for the high-field fMRI in the rat brain as a consequence of decreased distortion and reduced extravascular effect compared to the EPI method, the single-echo bSSFP method acquires single k-space line per echo and takes longer time than the EPI method to acquire multi-slice high-resolution images (Budde et al., 2014). We established single-vessel fMRI human brain mapping with the EPI method. First, the fMRI signal of sulcus veins in the occipital lobe was mapped using EPI-fMRI at 3T. Upon the checkerboard visual stimulation, the evoked BOLD signal was located primarily at venous voxels with a sparsely distributed patchy pattern that was previously reported (Menon et al., 1993) (Figures 7A–7C and 7F; Movie S3). Besides the task-related functional maps, the seed-based correlation maps from resting-state fMRI demonstrated vein-dominated correlation spatial patterns (Figures 7D and 7G; Movie S4). The coherence analysis of paired venous voxels showed coherent ultra-slow oscillation of the awake human subjects up to ~ 0.1 Hz (Figure 7H), which was much higher than the oscillation frequency detected in anesthetized rats (Figure 3H). The correlation coefficients of paired venous voxels were plotted as the function of the intra-hemispheric and inter-hemispheric vessel distances (Figure 7I). The values of the correlation decreased as the function of the intra-hemispheric vessel distance but showed significantly higher values for the inter-hemispheric venous voxel pairs (Figure 7J), similar to previously established spatial vasomotion correlation patterns in awake mice (Mateo et al., 2017). The low-frequency oscillation around 0.1 Hz has been previously reported in the visual cortex of the human brain with conventional resting-state fMRI method (Mittra et al., 1997). Also, when EPI images were spatially smoothed with different kernels from 1 to 5 mm, the vessel-specific spatial patterns merged to functional blobs similar to the conventional functional connectivity maps (Biswal et al., 1995; Smith et al., 2009) (Figures 7K and 7L).

The seed-based analysis was performed before and after the regression of respiration and heartbeat relevant temporal artifacts (Figures S8A–S8F), showing the little difference in the

vessel-specific spatial patterns (Figures S8G–S8M). In addition, ICA analysis specified the highly correlated venous voxels at multiple slices, showing a 3D vascular dynamic correlation structure through the main branches of cerebral vasculature (Figures S9A–S9D; Movie S5). These results demonstrate that the hemodynamic fMRI signals from central veins through sulci or at the gyrus surface are highly correlated, representing large-scale vascular dynamic network connectivity detectable with the 3T MR scanner.

To characterize the hemodynamic signal fluctuation in vessels penetrating cortical gray matter, we mapped the single vessel-based resting-state fMRI signal at 9.4T. The multiple 2D EPI images were acquired with an in-plane resolution of $500 \times 500 \mu\text{m}^2$ and $800 \mu\text{m}$ thickness at a TR of 1 s. In parallel, a single-vessel A-V map was acquired to better characterize the location of individual sulcus arteries and veins, as well as a few intracortical veins (Figures 8A–8C). Similarly, the BOLD signal was highly correlated on venous voxels, but not on artery voxels (Figures 8D and 8E). In the enlarged correlation maps, a few intracortical veins penetrating the gray matter could be spotted on the A-V map, given their unique vascular orientation through the 2D slice, showing a strong correlation to each other (Figures 8B, 8C, S9E, and S9F). Furthermore, coherence analysis of paired veins showed a coherent frequency range less than ~ 0.1 Hz, which is consistent with previous brain ultra-slow oscillation studies (Obrig et al., 2000) (Figure 8G). This result provides a good example for the illustration of vascular correlation of the selected intracortical veins penetrating cortical gray matter at 9.4T. This result shows the translational potential of high-resolution single-vessel fMRI to associate anatomical vascular biomarkers with prognostic dynamic indicators of neurovascular disease and vascular dementia in the brain.

DISCUSSION

We have demonstrated that a single-vessel fMRI mapping scheme reveals the spatial and temporal features of vessel-to-vessel hemodynamic correlations in anesthetized rats and in awake human subjects. With regard to rats, BOLD-specific venous signals and the CBV-specific arteriolar signals evolve at ultra-slow timescales, with frequency components between 0.01 and 0.04 Hz (Figure 3). Both signals show a causal relationship to the simultaneously acquired calcium signal (Figure 4). With regard to humans, the ultra-slow oscillation was observed in the BOLD signal for frequencies up to 0.1 Hz and vessel-to-vessel correlations are strong (Figure 8). This work demonstrates the feasibility to apply a multi-modal fMRI platform to measure the neuronal correlates of resting-state hemodynamic signal fluctuation from arteriolar to venous networks at the scale of individual vessels.

Technical Advances

The attainment of single-vessel imaging with high SNR was achieved based on three factors: a high magnetic field to enhance the transverse signal; a bSSFP sequence with high SNR efficiency per time unit; and a small radio frequency coil with appropriate sample loading to optimize the detection from local cortical regions. These factors ensured that the temporal

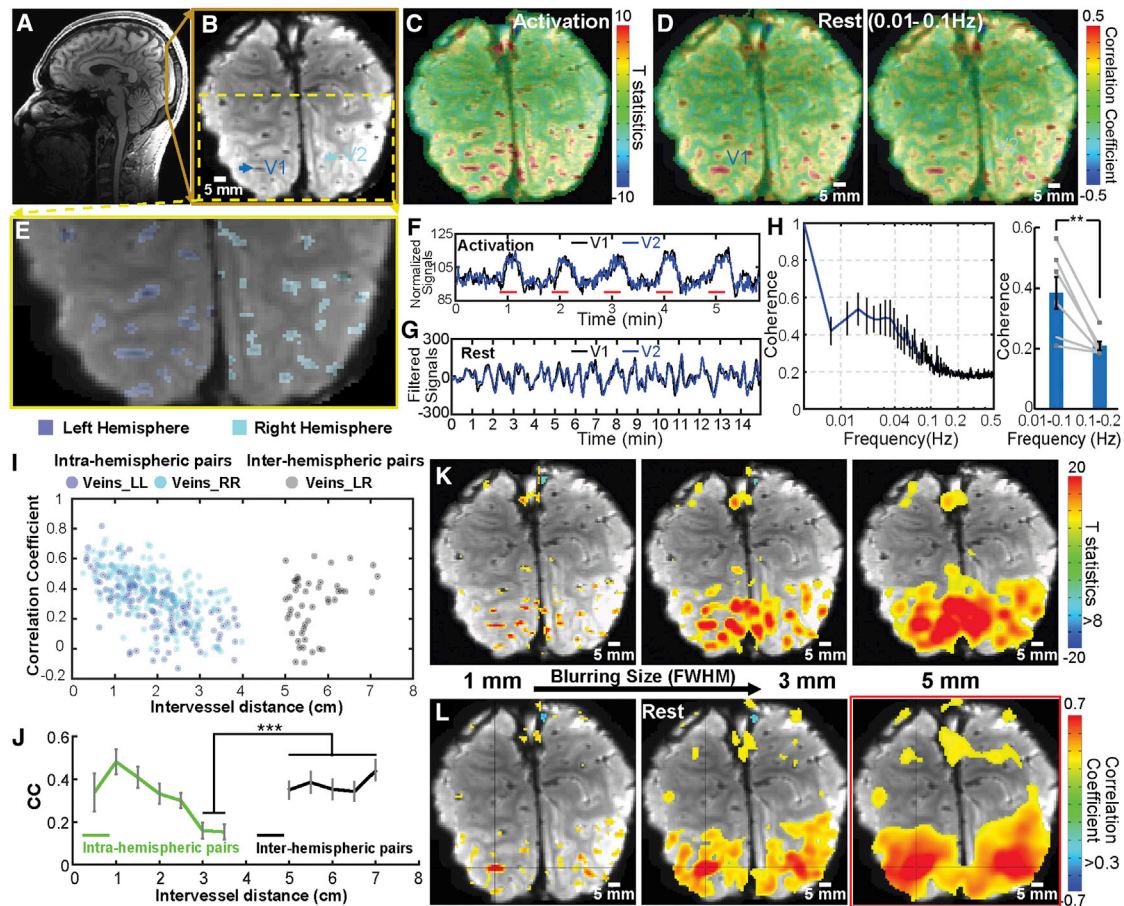


Figure 7. The Task-Related and Resting-State Single-Vessel fMRI Mapping in Awake Human Subjects at 3T

(A) A sagittal view of the human brain with a 2D EPI slice located in the occipital lobe.
 (B) An averaged EPI image shows the pial veins in sulci as dark dots.
 (C) The checkerboard visual stimulation-evoked BOLD functional map with peak BOLD signals located at pial veins.
 (D) The seed-based BOLD correlation maps (0.01–0.1 Hz; seeds: two veins [V1 and V2]) demonstrate vessel-dominated patterns.
 (E) The magnified view of the averaged EPI image from one representative subject (vein ROIs, left hemisphere, blue, right hemisphere, cyan).
 (F and G) The time courses of two veins in the task-related (F) and resting-state (G) (0.01–0.1 Hz) conditions.
 (H) The coherence graph of paired veins exhibits coherent oscillation at the frequency range of 0.01–0.1 Hz significantly higher than the higher frequency range (0.1–0.2 Hz; $n = 6$, mean \pm SEM, **, paired t test, $p = 0.008$).
 (I) The scatterplot of the correlation coefficient (CC) from intra and inter-hemispheric vein pairs.
 (J) The mean CC of inter-hemispheric vein pairs with the intervessel distance between 5–7 cm is significantly higher than that of intra-hemispheric vein pairs with distance between 3–3.5 cm. (***, $n = 6$, mean \pm SEM, t test, $p = 0.0002$).
 (K and L) The evoked functional (K) and resting-state correlation (L) maps were smoothed from 1 mm to 5 mm (FWHM).
 See also [Figures S8](#) and [S9](#).

fluctuation of the vessel-specific fMRI signal was not dominated by machine-based technical noise, but rather represented the physiological state of the brain. This issue was further verified by the anesthetic dose-dependent study, which indicated that the vessel-specific fMRI signal fluctuation could be dampened even though the SNR remained unchanged ([Figure S6](#)). Besides the technical noise, artifacts from physiological motion can be erroneously intrinsically linked to the functional connectivity ([Hu et al., 1995; Murphy et al., 2013](#)). Numerous strategies have been developed to regress out the potential artifacts, or identify the functional node-specific component using ICA analysis ([Glover et al., 2000; McKeown et al., 2003](#)). Nonetheless, a

lack of standard criteria to distinguish the contribution from brain signal fluctuation versus physiological motion artifacts limits the reliability of functional connectivity. We nominally expect that the pattern of correlations should be insensitive to global motion artifacts. Further, the enhanced correlations in the BOLD response for pairs of venules versus arterioles ([Figures 3F, 3H, 3J, and 8F](#)) and the enhanced correlations in the CBV response for arterioles versus venules ([Figures 3G, 3I, and K](#)) as a function of frequency are highly unlikely to result from known artifacts.

The detected bSSFP signal change is a mixture of intravascular and extravascular contributions. The intravascular signal is given by the steady-state contrast of passband bSSFP, which

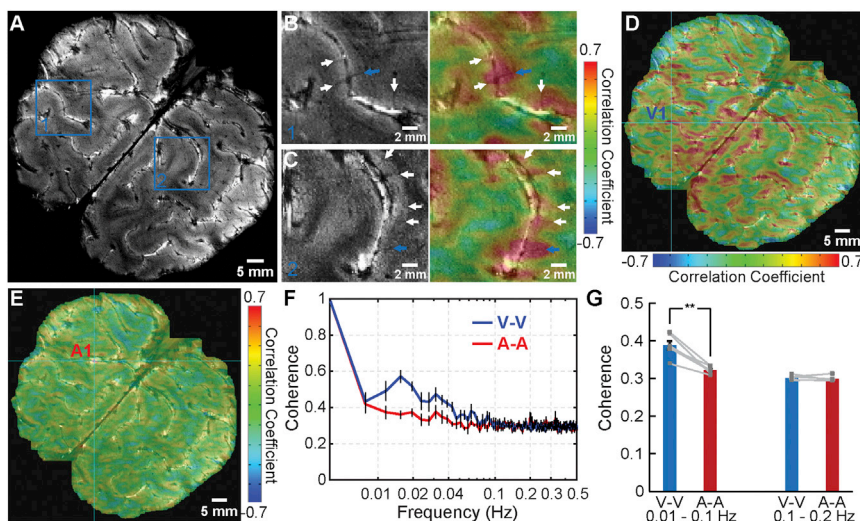


Figure 8. The Intracortical Vascular Dynamic Mapping with 9.4T

(A) The A-V map is acquired from a 2D slice across the occipital lobe.

(B and C) The intra-cortical veins (arrows) in the magnified view of region 1 and region 2 in the A-V map (left). The right panel shows the correlation map based on the selected seeds (the intra-cortical veins: blue arrows) with highly correlated voxels detected on the other intracortical veins (white arrows) in the gray matter.

(D and E) The seed-based correlation maps with vein 1 (V1), artery 1 (A1) as seeds, respectively (seeds: cyan crosshairs).

(F) The coherence graph of paired veins (blue) and arteries (red) identified by the AV map demonstrates the slow fluctuations from 0.01 to 0.1 Hz. (G) The mean coherence coefficients of the paired veins are significantly higher than that of the paired arteries at low frequency (0.01–0.1 Hz) ($n = 6$, mean \pm SEM, paired t test, $**p = 0.0009$).

See also Figure S9.

is proportional to $\sqrt{T_2/T_1}$ (Scheffler and Lehnardt, 2003). Given the high spatial resolution of the bSSFP fMRI imaging, the BOLD contrast from venules and the CBV-based contrast from arterioles of vessel voxels remained highly T2-weighted because of the fast T2 decay of deoxygenated venule blood and iron oxide enriched arteriole blood (Lee et al., 1999; Blockley et al., 2008). The extravascular contribution depends on the vessel size. As for spin echoes, the rapid refocusing in bSSFP produces dynamic averaging that reduces the extravascular effects of the cortical penetrating vessels larger than 10–20 μm (Bieri and Scheffler, 2007; Scheffler and Ehse, 2016). Therefore, the observed signal changes with high spatial resolution bSSFP were mainly intravascular. It is noteworthy that the blood flow could contribute to the BOLD fMRI signal fluctuation based on the in-flow effect, given the short TR of the bSSFP sequence at a given flip angle (Kim et al., 1994). This is especially true for arterioles. However, the BOLD signal fluctuation in arterioles showed significantly lower correlation than that of venules, indicating that the in-flow effect is not the primary contributor to the vascular dynamic correlation patterns (Figures 2 and 3).

BOLD versus CBV-Weighted fMRI Signals

In contrast to the venous BOLD signal, for the CBV signal fluctuation, the arteriole-dominated CBV-signal results from vasomotor fluctuations in vessel diameter. The vasomotion signal shows ultra-slow oscillation with a broader frequency band centered at 0.1 Hz in the anesthetized rat brain (Mayhew et al., 1996; Kleinfeld et al., 1998) and 0.1 Hz in awake mice (Drew et al., 2010). Although in the present study arteriole CBV signal fluctuations were detected at a frequency band of <0.04 Hz in α -chloralose anesthetized rats, it is likely that this hemodynamic signal corresponds to vasomotion. Further to this point, beyond the neuronal effects of anesthetics (Brown et al., 2011; Mateo et al., 2017), anesthetics may directly affect vasomotion and directly contribute to the temporal dynamic patterns detected by fMRI in anesthetized animals (Colantuoni et al., 1984; Hundley et al., 1988). In addition, future studies will compare the arteriole-

specific fMRI signal fluctuation in rat under anesthesia and wakefulness to specify the dynamic patterns driven by vasomotion. Lastly, our result is also consistent with the “bagpipe” model of active arteriole dilation with increased neuronal activity, where arteriole dynamics dominate both spontaneous and evoked blood volume changes in the brain (Drew et al., 2011). Following the net increase of the arteriole blood reservoir, venules drain the blood with a delayed passive dilation, which is consistent with undershoot of the evoked BOLD fMRI signal (Mandeville et al., 1999).

The ultra-slow passive venule dilation was detected by single-vessel CBV-bSSFP fMRI when iron oxide particles were delivered at a lower than normal dosage so that the venule fMRI signal was not completely dampened due to shortened T2* decay (Figure S5). This observation also explains the small number of venules highlighted by the arteriole-seed-based CBV correlation maps (Figure 2C), which showed much longer lag time than arterioles when analyzing the simultaneously acquired calcium ultra-slow oscillation signal via cross-correlation (Figure S5). All told, single-vessel bSSFP-fMRI detects distinct spatial and temporal patterns of vessel-specific dynamic connectivity in the anesthetized rat brain.

Correlates of Neuronal $[\text{Ca}^{2+}]$ and Single-Vessel fMRI

A key observation was the correlation of ultra-slow calcium oscillation with single-vessel fMRI signal fluctuation. Prior combined fMRI and electrophysiological studies show that the resting-state BOLD signal correlates with neuronal activity oscillation (He et al., 2008; Shmuel and Leopold, 2008; Schölvinc et al., 2010; Pan et al., 2013). The present study extends the spatial resolution of resting-state fMRI down to single vessels. The coherence of the ultra-slow oscillations from both intracellular $[\text{Ca}^{2+}]$ and vessel-specific fMRI signals demonstrates a potential link of the two events, with the calcium event leading the vascular fluctuation (Figures 4E and 4L). In particular, the BOLD signal from individual venules and the CBV-weighted signal detected primarily from arterioles showed

varied lag times, ranging from 0.5 to 6 s, relative to the calcium signal (Figures 4G and 4N).

Previous studies reported only long, i.e., 5 to 6 s, lag times by cross-correlation of the change in γ -band power and the resting-state BOLD signal (Schölvinck et al., 2010). This long lag time could be caused by signal fluctuations in large voxels, with primary weighting on surface draining veins. In the present study, the fMRI signal from draining veins also showed longer lag time, which is consistent with the lag time between the calcium and hemoglobin signal oscillation (~ 0.1 Hz) detected from the cortical surface (Du et al., 2014). In contrast to surface draining veins, penetrating vessels at the deep cortical layers showed shorter lag times of 1.8 ± 0.2 s for the arteriole CBV signal and 2.3 ± 0.2 s for the venule BOLD signal (Figure 4), which is in concordance with the signaling order of arteriole dilation followed by oxygen saturation changes in venules for neurovascular coupling (Devor et al., 2003; Iadecola, 2004).

The arterio-venous (A-V) transit time of the resting-state hemodynamic signal was calculated based on the cross-correlation lag times of the BOLD and CBV-weighted signals to the simultaneously recorded calcium signal (Figure S10 and Table S2). The resting-state A-V transit time of 0.61 s at the deep cortical layers is slightly shorter than the transit time of 0.8–1.2 s, calculated by the time to half-maximal, $t_{1/2}$, from surface arterioles to venules (Hutchinson et al., 2006). This further supports the vessel-specific hemodynamic signal propagation. Also noteworthy is that the variability of the measured resting-state transit time is relatively higher than that of the evoked A-V hemodynamic transit time (Yu et al., 2016) (Figure S10), indicating a more heterogeneous hemodynamic coupling during the resting state. Lastly, cortical calcium waves have been observed in the newborn and adult rodent brain (Adelsberger et al., 2005; Ma et al., 2016) and can propagate through the cortex at a fast speed (Stroh et al., 2013). It will be interesting to determine whether these drive propagating vascular events.

Single-Vessel Human Maps

Vascular dynamic network connectivity was directly mapped in awake human subjects to demonstrate the translational potential of single-vessel fMRI mapping. The vessel-specific ultra-slow oscillation shares a similar frequency range to that of the long-distance functional nodes detected by conventional resting-state fMRI, as well as the spontaneous oscillation of the cerebral hemodynamic signal detected by near-infrared spectroscopy (Obrig et al., 2000). In addition, the smoothed single-vessel correlation maps represented similar functional connectivity maps in the visual area as detected by the conventional resting-state fMRI (Smith et al., 2009) (Figures 7K and 7L). Together with the rat data that show highly correlated calcium and single-vessel fMRI signal fluctuation, the vascular dynamic network connectivity could represent the hemodynamic vascular correlation coupled to neuronal signal oscillation in both anesthetized and awake conditions. Interestingly, a recent resting-state fMRI study showed that the connectivity strength of a given voxel among the “default mode” and other networks is inversely proportional to its vascular volume fraction (Tak et al., 2015). This observation indicates that functional connectivity of long-range

nodes in the brain may be driven independently of the vascular-specific hemodynamic fluctuation. Given the highly correlated calcium signal to the hemodynamic signal fluctuation, one possible explanation for this discrepancy is that vascular dynamic network connectivity represents the whole brain state fluctuation with less region specificity (Chang et al., 2016), but the functional connectivity may specify the network pattern of long-distance functional nodes (Biswal et al., 1995; Smith et al., 2009). Alternatively, because the vascular volume fraction was calculated from the largest extracerebral vessels detected by MRI images, it is also possible that the reduced connectivity may be caused by the low SNR of voxels occupied by these extracerebral vessels.

Given the cerebral folds and fissures of the human brain, single-vessel EPI-fMRI mapping mainly detects the central pial veins through the sulci with diameters of a few hundred micrometers based on the T2*-weighted partial volume effect. Single-vessel fMRI with 9.4T at high spatial resolution, i.e., $500 \times 500 \times 800 \mu\text{m}^3$, showed the correlation patterns of the intracortical penetrating veins in the human brain (Duvernoy et al., 1981) (Figure 8). In contrast to studies focusing on excluding the venous BOLD signal to improve spatial specificity for brain function and connectivity mapping (Barth and Norris, 2007; Curtis et al., 2014), this work specifies the vascular network connectivity in gray matter of the human brain with the potential clinical application of illustrating hemodynamic features of vascular dementia (O’Brien et al., 2003; Iadecola, 2013). Specifically, the neural correlates of the vascular dynamic network connectivity detected in the rodent brain display great potential for clinical applications such as the diagnosis of cognitive impairments in patients with cerebral small vessel diseases or degenerative diseases such as Alzheimer’s disease (Schaefer et al., 2014). The ability to specify the direct linkage of vascular pathology to dysfunction of the neurovascular network remains elusive (Stevens et al., 2014). The ability to map the hemodynamic origin of the BOLD signal from anatomically distinguishable vessels in human gray matter provides a key step to link vascular biomarkers, e.g., microbleeds (Poels et al., 2012) or cortical microinfarcts (van Veluw et al., 2013; van Rooden et al., 2014), with dynamic indicators in patients with small vessel or Alzheimer’s disease.

Caveats Going Forward

We developed the single-vessel fMRI resting-state mapping scheme to characterize the spatial and temporal hemodynamic signals in arteriolar and venous networks, concurrent with photometric calcium recording. The high field MRI scanner, 14T for animals and 9.4T for humans, achieves sufficient SNR and high BOLD contrast for high-resolution fMRI imaging. A redesign of the radio frequency detection coil will be needed to extend the single-vessel fMRI method to broader application with lower magnetic field scanners. Toward this goal, a super-conducting coil has been developed to boost the SNR of MRI images (Ratering et al., 2008). Also, instead of the current 32- or 64-channel coils for human brain imaging, region-specific array coils can be developed to cover focal cortical areas with optimized geometry to increase the SNR. This step will help further resolve individual intracortical vessels in gray matter of normal human

subjects as well as patients with neurovascular dysfunction due to vascular dementia.

STAR★METHODS

Detailed methods are provided in the online version of this paper and include the following:

- [KEY RESOURCES TABLE](#)
- [CONTACT FOR REAGENT AND RESOURCE SHARING](#)
- [EXPERIMENTAL MODELS AND SUBJECT DETAILS](#)
 - Animals
 - Human Subjects
- [METHODS DETAILS](#)
 - Animal experiments
 - MRI image acquisition from rats (14.1T)
 - MRI image acquisition from humans (3 T)
 - MRI image acquisition from humans (9.4 T)
 - Data processing
 - Immunohistochemistry
- [QUANTIFICATION AND STATISTICAL ANALYSIS](#)

SUPPLEMENTAL INFORMATION

Supplemental Information includes ten figures, three tables, and five movies and can be found with this article online at <https://doi.org/10.1016/j.neuron.2018.01.025>.

ACKNOWLEDGMENTS

This research was supported by Germany Research Foundation (DFG) SPP-1655 and internal funding from Max Planck Society for X.Y. and NIH grants R35NS097265 for D.K. and NIMH BRAIN grant R01MH11438 for D.K. and B.R.R. We thank Dr. H. Merkle and Dr. K. Buckenmaier for technical support, Ms. H. Schulz and Ms. S. Fischer for animal maintenance support, the AFNI team for the software support, and Dr. L. Looger and the Janelia Research Campus of HHMI for kindly providing viral vectors.

AUTHOR CONTRIBUTIONS

X.Y., D.K., and B.R.R. designed the research, Y.H., X.Y., M.W., and X.C. performed animal experiments, Y.H., X.Y., and R.P. acquired data, X.Y. supervised the research, Y.H. analyzed data, K.S., R.P., J.R.P., and M.W. provided key technical support, and X.Y., D.K., and Y.H. wrote the manuscript.

DECLARATION OF INTERESTS

The authors declare no competing interests.

Received: June 26, 2017

Revised: November 14, 2017

Accepted: January 10, 2018

Published: February 1, 2018

REFERENCES

- Adelsberger, H., Garaschuk, O., and Konnerth, A. (2005). Cortical calcium waves in resting newborn mice. *Nat. Neurosci.* *8*, 988–990.
- Aydin, F., Rosenblum, W.I., and Povlishock, J.T. (1991). Myoendothelial junctions in human brain arterioles. *Stroke* *22*, 1592–1597.
- Barth, M., and Norris, D.G. (2007). Very high-resolution three-dimensional functional MRI of the human visual cortex with elimination of large venous vessels. *NMR Biomed.* *20*, 477–484.
- Bell, A.J., and Sejnowski, T.J. (1995). An information-maximization approach to blind separation and blind deconvolution. *Neural Comput.* *7*, 1129–1159.
- Bieri, O., and Scheffler, K. (2007). Effect of diffusion in inhomogeneous magnetic fields on balanced steady-state free precession. *NMR Biomed.* *20*, 1–10.
- Biswal, B., Yetkin, F.Z., Haughton, V.M., and Hyde, J.S. (1995). Functional connectivity in the motor cortex of resting human brain using echo-planar MRI. *Magn. Reson. Med.* *34*, 537–541.
- Blinder, P., Tsai, P.S., Kaufhold, J.P., Knutsen, P.M., Suhl, H., and Kleinfeld, D. (2013). The cortical angiome: an interconnected vascular network with noncolumnar patterns of blood flow. *Nat. Neurosci.* *16*, 889–897.
- Blockley, N.P., Jiang, L., Gardener, A.G., Ludman, C.N., Francis, S.T., and Gowland, P.A. (2008). Field strength dependence of R1 and R2* relaxivities of human whole blood to ProHance, Vasovist, and deoxyhemoglobin. *Magn. Reson. Med.* *60*, 1313–1320.
- Brown, E.N., Purdon, P.L., and Van Dort, C.J. (2011). General anesthesia and altered states of arousal: a systems neuroscience analysis. *Annu. Rev. Neurosci.* *34*, 601–628.
- Budde, J., Shajan, G., Zaitsev, M., Scheffler, K., and Pohmann, R. (2014). Functional MRI in human subjects with gradient-echo and spin-echo EPI at 9.4 T. *Magn. Reson. Med.* *71*, 209–218.
- Buxton, R.B., Wong, E.C., and Frank, L.R. (1998). Dynamics of blood flow and oxygenation changes during brain activation: the balloon model. *Magn. Reson. Med.* *39*, 855–864.
- Chan, A.W., Mohajerani, M.H., LeDue, J.M., Wang, Y.T., and Murphy, T.H. (2015). Mesoscale infraslow spontaneous membrane potential fluctuations recapitulate high-frequency activity cortical motifs. *Nat. Commun.* *6*, 7738.
- Chang, C., Leopold, D.A., Schölvinc, M.L., Mandelkow, H., Picchioni, D., Liu, X., Ye, F.Q., Turchi, J.N., and Duyn, J.H. (2016). Tracking brain arousal fluctuations with fMRI. *Proc. Natl. Acad. Sci. USA* *113*, 4518–4523.
- Chen, T.W., Wardill, T.J., Sun, Y., Pulver, S.R., Renninger, S.L., Baohan, A., Schreiter, E.R., Kerr, R.A., Orger, M.B., Jayaraman, V., et al. (2013). Ultrasensitive fluorescent proteins for imaging neuronal activity. *Nature* *499*, 295–300.
- Colantuoni, A., Bertuglia, S., and Intaglietta, M. (1984). Effects of anesthesia on the spontaneous activity of the microvasculature. *Int. J. Microcirc. Clin. Exp.* *3*, 13–28.
- Cox, R.W. (1996). AFNI: software for analysis and visualization of functional magnetic resonance neuroimages. *Comput. Biomed. Res.* *29*, 162–173.
- Curtis, A.T., Hutchison, R.M., and Menon, R.S. (2014). Phase based venous suppression in resting-state BOLD GE-fMRI. *Neuroimage* *100*, 51–59.
- Delorme, A., and Makeig, S. (2004). EEGLAB: an open source toolbox for analysis of single-trial EEG dynamics including independent component analysis. *J. Neurosci. Methods* *134*, 9–21.
- Devor, A., Dunn, A.K., Andermann, M.L., Ulbert, I., Boas, D.A., and Dale, A.M. (2003). Coupling of total hemoglobin concentration, oxygenation, and neural activity in rat somatosensory cortex. *Neuron* *39*, 353–359.
- Drew, P.J., Duyn, J.H., Golanov, E., and Kleinfeld, D. (2008). Finding coherence in spontaneous oscillations. *Nat. Neurosci.* *11*, 991–993.
- Drew, P.J., Shih, A.Y., Driscoll, J.D., Knutsen, P.M., Blinder, P., Davalos, D., Akassoglou, K., Tsai, P.S., and Kleinfeld, D. (2010). Chronic optical access through a polished and reinforced thinned skull. *Nat. Methods* *7*, 981–984.
- Drew, P.J., Shih, A.Y., and Kleinfeld, D. (2011). Fluctuating and sensory-induced vasodynamics in rodent cortex extend arteriole capacity. *Proc. Natl. Acad. Sci. USA* *108*, 8473–8478.
- Du, C., Volkow, N.D., Koretsky, A.P., and Pan, Y. (2014). Low-frequency calcium oscillations accompany deoxyhemoglobin oscillations in rat somatosensory cortex. *Proc. Natl. Acad. Sci. USA* *111*, E4677–E4686.
- Duvernoy, H.M., Delon, S., and Vannson, J.L. (1981). Cortical blood vessels of the human brain. *Brain Res. Bull.* *7*, 519–579.
- Fox, M.D., and Raichle, M.E. (2007). Spontaneous fluctuations in brain activity observed with functional magnetic resonance imaging. *Nat. Rev. Neurosci.* *8*, 700–711.

- Glover, G.H., Li, T.Q., and Ress, D. (2000). Image-based method for retrospective correction of physiological motion effects in fMRI: RETROICOR. *Magn. Reson. Med.* *44*, 162–167.
- He, B.J., Snyder, A.Z., Zempel, J.M., Smyth, M.D., and Raichle, M.E. (2008). Electrophysiological correlates of the brain's intrinsic large-scale functional architecture. *Proc. Natl. Acad. Sci. USA* *105*, 16039–16044.
- Hirsch, S., Reichold, J., Schneider, M., Székely, G., and Weber, B. (2012). Topology and hemodynamics of the cortical cerebrovascular system. *J. Cereb. Blood Flow Metab.* *32*, 952–967.
- Hu, X., Le, T.H., Parrish, T., and Erhard, P. (1995). Retrospective estimation and correction of physiological fluctuation in functional MRI. *Magn. Reson. Med.* *34*, 201–212.
- Hundley, W.G., Renaldo, G.J., Levasseur, J.E., and Kontos, H.A. (1988). Vasomotion in cerebral microcirculation of awake rabbits. *Am. J. Physiol.* *254*, H67–H71.
- Hutchinson, E.B., Stefanovic, B., Koretsky, A.P., and Silva, A.C. (2006). Spatial flow-volume dissociation of the cerebral microcirculatory response to mild hypercapnia. *Neuroimage* *32*, 520–530.
- Iadecola, C. (2004). Neurovascular regulation in the normal brain and in Alzheimer's disease. *Nat. Rev. Neurosci.* *5*, 347–360.
- Iadecola, C. (2013). The pathobiology of vascular dementia. *Neuron* *80*, 844–866.
- Intaglietta, M. (1990). Vasomotion and flowmotion: physiological mechanisms and clinical evidence. *Vasc. Med. Rev.* *1*, 101–112.
- Kim, S.G., Hendrich, K., Hu, X., Merkle, H., and Ugurbil, K. (1994). Potential pitfalls of functional MRI using conventional gradient-recalled echo techniques. *NMR Biomed.* *7*, 69–74.
- Kleinfeld, D., Mitra, P.P., Helmchen, F., and Denk, W. (1998). Fluctuations and stimulus-induced changes in blood flow observed in individual capillaries in layers 2 through 4 of rat neocortex. *Proc. Natl. Acad. Sci. USA* *95*, 15741–15746.
- Lee, S.P., Silva, A.C., Ugurbil, K., and Kim, S.G. (1999). Diffusion-weighted spin-echo fMRI at 9.4 T: microvascular/tissue contribution to BOLD signal changes. *Magn. Reson. Med.* *42*, 919–928.
- Logothetis, N.K., Pauls, J., Augath, M., Trinath, T., and Oeltermann, A. (2001). Neurophysiological investigation of the basis of the fMRI signal. *Nature* *412*, 150–157.
- Longden, T.A., Dabertrand, F., Koide, M., Gonzales, A.L., Tykocki, N.R., Brayden, J.E., Hill-Eubanks, D., and Nelson, M.T. (2017). Capillary K⁺-sensing initiates retrograde hyperpolarization to increase local cerebral blood flow. *Nat. Neurosci.* *20*, 717–726.
- Ma, Y., Shaik, M.A., Kozberg, M.G., Kim, S.H., Portes, J.P., Timerman, D., and Hillman, E.M. (2016). Resting-state hemodynamics are spatiotemporally coupled to synchronized and symmetric neural activity in excitatory neurons. *Proc. Natl. Acad. Sci. USA* *113*, E8463–E8471.
- Mandeville, J.B., Marota, J.J., Kosofsky, B.E., Keltner, J.R., Weissleder, R., Rosen, B.R., and Weisskoff, R.M. (1998). Dynamic functional imaging of relative cerebral blood volume during rat forepaw stimulation. *Magn. Reson. Med.* *39*, 615–624.
- Mandeville, J.B., Marota, J.J., Ayata, C., Zaharchuk, G., Moskowitz, M.A., Rosen, B.R., and Weisskoff, R.M. (1999). Evidence of a cerebrovascular post-arteriole windkessel with delayed compliance. *J. Cereb. Blood Flow Metab.* *19*, 679–689.
- Mansfield, P., Maudsley, A.A., and Baines, T. (1976). Fast Scan Proton Density Imaging by Nmr. *J. Phys. E Sci. Instrum.* *9*, 271–278.
- Mateo, C., Knutsen, P.M., Tsai, P.S., Shih, A.Y., and Kleinfeld, D. (2017). Entrainment of arteriole vasomotor fluctuations by neural activity is a basis of blood-oxygenation-level-dependent “resting-state” connectivity. *Neuron* *96*, 936–948.e3.
- Mayhew, J.E., Askew, S., Zheng, Y., Porrill, J., Westby, G.W., Redgrave, P., Rector, D.M., and Harper, R.M. (1996). Cerebral vasomotion: a 0.1-Hz oscillation in reflected light imaging of neural activity. *Neuroimage* *4*, 183–193.
- McKeown, M.J., Hansen, L.K., and Sejnowski, T.J. (2003). Independent component analysis of functional MRI: what is signal and what is noise? *Curr. Opin. Neurobiol.* *13*, 620–629.
- Menon, R.S., Ogawa, S., Tank, D.W., and Ugurbil, K. (1993). Tesla gradient recalled echo characteristics of photic stimulation-induced signal changes in the human primary visual cortex. *Magn. Reson. Med.* *30*, 380–386.
- Mitra, P.P., Ogawa, S., Hu, X., and Ugurbil, K. (1997). The nature of spatiotemporal changes in cerebral hemodynamics as manifested in functional magnetic resonance imaging. *Magn. Reson. Med.* *37*, 511–518.
- Moon, C.H., Fukuda, M., and Kim, S.G. (2013). Spatiotemporal characteristics and vascular sources of neural-specific and -nonspecific fMRI signals at sub-millimeter columnar resolution. *Neuroimage* *64*, 91–103.
- Murphy, K., Birn, R.M., and Bandettini, P.A. (2013). Resting-state fMRI confounds and cleanup. *Neuroimage* *80*, 349–359.
- O'Brien, J.T., Erkinjuntti, T., Reisberg, B., Roman, G., Sawada, T., Pantoni, L., Bowler, J.V., Ballard, C., DeCarli, C., Gorelick, P.B., et al. (2003). Vascular cognitive impairment. *Lancet Neurol.* *2*, 89–98.
- Obrig, H., Neufang, M., Wenzel, R., Kohl, M., Steinbrink, J., Einhüpl, K., and Villringer, A. (2000). Spontaneous low frequency oscillations of cerebral hemodynamics and metabolism in human adults. *Neuroimage* *12*, 623–639.
- Pan, W.J., Thompson, G.J., Magnuson, M.E., Jaeger, D., and Keilholz, S. (2013). Infralow LFP correlates to resting-state fMRI BOLD signals. *Neuroimage* *74*, 288–297.
- Poels, M.M., Ikram, M.A., van der Lugt, A., Hofman, A., Niessen, W.J., Krestin, G.P., Breteler, M.M., and Vernooij, M.W. (2012). Cerebral microbleeds are associated with worse cognitive function: the Rotterdam Scan Study. *Neurology* *78*, 326–333.
- Poplawsky, A.J., Fukuda, M., Kang, B.M., Kim, J.H., Suh, M., and Kim, S.G. (2017). Dominance of layer-specific microvessel dilation in contrast-enhanced high-resolution fMRI: Comparison between hemodynamic spread and vascular architecture with CLARITY. *NeuroImage*. Published online August 16, 2017. <https://doi.org/10.1016/j.neuroimage.2017.1008.1046>.
- Ratering, D., Baltes, C., Nordmeyer-Massner, J., Marek, D., and Rudin, M. (2008). Performance of a 200-MHz cryogenic RF probe designed for MRI and MRS of the murine brain. *Magn. Reson. Med.* *59*, 1440–1447.
- Schaefer, A., Quinque, E.M., Kipping, J.A., Arélin, K., Roggenhofer, E., Frisch, S., Villringer, A., Mueller, K., and Schroeter, M.L. (2014). Early small vessel disease affects frontoparietal and cerebellar hubs in close correlation with clinical symptoms—a resting-state fMRI study. *J. Cereb. Blood Flow Metab.* *34*, 1091–1095.
- Scheffler, K., and Ehses, P. (2016). High-resolution mapping of neuronal activation with balanced SSFP at 9.4 tesla. *Magn. Reson. Med.* *76*, 163–171.
- Scheffler, K., and Lehnardt, S. (2003). Principles and applications of balanced SSFP techniques. *Eur. Radiol.* *13*, 2409–2418.
- Schölvinck, M.L., Maier, A., Ye, F.Q., Duyn, J.H., and Leopold, D.A. (2010). Neural basis of global resting-state fMRI activity. *Proc. Natl. Acad. Sci. USA* *107*, 10238–10243.
- Schulz, K., Sydekum, E., Krueppel, R., Engelbrecht, C.J., Schlegel, F., Schröter, A., Rudin, M., and Helmchen, F. (2012). Simultaneous BOLD fMRI and fiber-optic calcium recording in rat neocortex. *Nat. Methods* *9*, 597–602.
- Segal, S.S., and Duling, B.R. (1989). Conduction of vasomotor responses in arterioles: a role for cell-to-cell coupling? *Am. J. Physiol.* *256*, H838–H845.
- Shajan, G., Kozlov, M., Hoffmann, J., Turner, R., Scheffler, K., and Pohmann, R. (2014). A 16-channel dual-row transmit array in combination with a 31-element receive array for human brain imaging at 9.4 T. *Magn. Reson. Med.* *71*, 870–879.
- Shmuel, A., and Leopold, D.A. (2008). Neuronal correlates of spontaneous fluctuations in fMRI signals in monkey visual cortex: Implications for functional connectivity at rest. *Hum. Brain Mapp.* *29*, 751–761.
- Silva, A.C., and Koretsky, A.P. (2002). Laminar specificity of functional MRI onset times during somatosensory stimulation in rat. *Proc. Natl. Acad. Sci. USA* *99*, 15182–15187.

- Silva, A.C., Koretsky, A.P., and Duyn, J.H. (2007). Functional MRI impulse response for BOLD and CBV contrast in rat somatosensory cortex. *Magn. Reson. Med.* *57*, 1110–1118.
- Smith, S.M., Fox, P.T., Miller, K.L., Glahn, D.C., Fox, P.M., Mackay, C.E., Filippini, N., Watkins, K.E., Toro, R., Laird, A.R., and Beckmann, C.F. (2009). Correspondence of the brain's functional architecture during activation and rest. *Proc. Natl. Acad. Sci. USA* *106*, 13040–13045.
- Stevens, R.D., Hannawi, Y., and Sair, H. (2014). Small vessel disease and the resting functional architecture of the brain. *J. Cereb. Blood Flow Metab.* *34*, 1089–1090.
- Stroh, A., Adelsberger, H., Groh, A., Rühlmann, C., Fischer, S., Schierloh, A., Deisseroth, K., and Konnerth, A. (2013). Making waves: initiation and propagation of corticothalamic Ca²⁺ waves in vivo. *Neuron* *77*, 1136–1150.
- Tak, S., Polimeni, J.R., Wang, D.J., Yan, L., and Chen, J.J. (2015). Associations of resting-state fMRI functional connectivity with flow-BOLD coupling and regional vasculature. *Brain Connect.* *5*, 137–146.
- van Rooden, S., Goos, J.D., van Opstal, A.M., Versluis, M.J., Webb, A.G., Blauw, G.J., van der Flier, W.M., Scheltens, P., Barkhof, F., van Buchem, M.A., and van der Grond, J. (2014). Increased number of microinfarcts in Alzheimer disease at 7-T MR imaging. *Radiology* *270*, 205–211.
- van Veluw, S.J., Zwanenburg, J.J., Engelen-Lee, J., Spliet, W.G., Hendrikse, J., Luijten, P.R., and Biessels, G.J. (2013). In vivo detection of cerebral cortical microinfarcts with high-resolution 7T MRI. *J. Cereb. Blood Flow Metab.* *33*, 322–329.
- Wang, L., Saalman, Y.B., Pinski, M.A., Arcaro, M.J., and Kastner, S. (2012). Electrophysiological low-frequency coherence and cross-frequency coupling contribute to BOLD connectivity. *Neuron* *76*, 1010–1020.
- Yu, X., Wang, S.M., Chen, D.Y., Dodd, S., Goloshevsky, A., and Koretsky, A.P. (2010). 3D mapping of somatotopic reorganization with small animal functional MRI. *NeuroImage* *49*, 1667–1676.
- Yu, X., Glen, D., Wang, S., Dodd, S., Hirano, Y., Saad, Z., Reynolds, R., Silva, A.C., and Koretsky, A.P. (2012). Direct imaging of macrovascular and microvascular contributions to BOLD fMRI in layers IV–V of the rat whisker-barrel cortex. *NeuroImage* *59*, 1451–1460.
- Yu, X., Qian, C., Chen, D.Y., Dodd, S.J., and Koretsky, A.P. (2014). Deciphering laminar-specific neural inputs with line-scanning fMRI. *Nat. Methods* *11*, 55–58.
- Yu, X., He, Y., Wang, M., Merkle, H., Dodd, S.J., Silva, A.C., and Koretsky, A.P. (2016). Sensory and optogenetically driven single-vessel fMRI. *Nat. Methods* *13*, 337–340.
- Zhu, D.C., Tarumi, T., Khan, M.A., and Zhang, R. (2015). Vascular coupling in resting-state fMRI: evidence from multiple modalities. *J. Cereb. Blood Flow Metab.* *35*, 1910–1920.

STAR★METHODS

KEY RESOURCES TABLE

REAGENT or RESOURCE	SOURCE	IDENTIFIER
Antibodies		
Anti NeuN antibody	Merck	RRID: AB_2298772, Cat# MAB377
Secondary antibody (Goat Anti-Mouse)	Abcam	RRID: AB_10680176, Cat# ab97035
Bacterial and Virus Strains		
AAV5.Syn.GCaMP6f.WPRE.SV40	PENN Vector Core	Cat# AV-5-PV2822
Chemicals, Peptides, and Recombinant Proteins		
Isoflurane	CP-Pharma	Cat# 1214
Iron oxide nanoparticle: Molday ION	BioPhysics Assay Laboratory (BioPAL)	Cat# CL-30Q02-2
α -chloralose	Sigma-Aldrich	Cat# C0128-25G;RRID
pancuronium bromide	Inresa Arzneimittel	Cat# 34409.00.00
VECTASHIELD Antifade Mounting Medium with DAPI	Vector Laboratories	RRID: AB_2336790, Cat# H-1200
Phosphate Buffered Saline (PBS)	GIBCO	Cat# 10010-023
Experimental Models: Organisms/Strains		
Rat: Sprague Dawley rat	Charles River Laboratories	N/A
Software and Algorithms		
MATLAB	MathWorks	RRID: SCR_001622, https://www.mathworks.com/
AFNI	Cox, 1996	RRID: SCR_005927, http://afni.nimh.nih.gov
EEGLAB	Delorme and Makeig, 2004	RRID: SCR_007292, https://sccn.ucsd.edu/eeglab/index.html
Group ICA Of fMRI Toolbox (GIFT)	Medical Image Analysis Lab	RRID: SCR_001953, GIFT 4.0, http://mialab.mrn.org/software/gift/
Excel 2013	Microsoft	https://products.office.com/en-us/excel
Adobe Illustrator CC	Adobe	RRID: SCR_010279, http://www.adobe.com/products/illustrator.html
Other		
Biopac MP 150 System	Biopac	RRID: SCR_014829
AcqKnowledge Software	Biopac	RRID: SCR_014279, https://www.biopac.com/product/acqknowledge-software/
Master-9	A.M.P.I	N/A
Nanoliter Injector	World Precision Instruments	Cat# NANOFIL
Laser (473 nm)	CNI	Cat# MBL-III
Dichroic mirrors	AHF Analysentechnik	Cat# F48-487
Fiber launch	Thorlabs	Cat# MBT613D/M
Optical fiber	Thorlabs	Cat# FT-200-EMT
Optical power meter	Thorlabs	Cat# PM20A
Optical filter	AHF Analysentechnik	Cat# F37-516
Silicon photomultiplier	SensL	Cat# MiniSM-10035-X08
Voltage amplifier	Femto	Cat# DHPVA-100
Tungsten Microelectrode	FHC	Cat# UEWSDDSMCN1M

CONTACT FOR REAGENT AND RESOURCE SHARING

Further information and requests for resources and reagents should be directed to and will be fulfilled by the Lead Contact, Dr. Xin Yu (xin.yu@tuebingen.mpg.de).

EXPERIMENTAL MODELS AND SUBJECT DETAILS

Animals

All experimental procedures were approved by the Animal Protection Committee of Tuebingen (Regierungspräsidium Tuebingen) and performed in accordance with the guidelines. Thirty-five male Sprague-Dawley rats were employed in all experiments. Littermates of the male rats (age: 2 - 3 months) were randomly assigned to experimental groups. Both evoked and resting-state bSSFP-fMRI data with A-V maps were acquired from five of nine rats under alpha-chloralose anesthesia, of which both BOLD and CBV signals were acquired under the same A-V map. To verify the effect of different drugs on vascular dynamic network connectivity, five rats were utilized for resting-state BOLD bSSFP-fMRI data under isoflurane anesthesia. In addition, the rats (BOLD: seven of eight, CBV: four of eight) with calcium indicator were employed for the statistics of simultaneous BOLD/CBV rsfMRI and fiber-optic calcium recording studies. Some rats were excluded from statistical analysis due to the large SSFP image distortion introduced by the optical fiber insertion. In addition, seven rats were employed to acquire simultaneous local field potential (LFP) and calcium signal.

Human Subjects

All human subject experiments follow the guidelines of the regulation procedure in the Max Planck Institute, and the informed consents were obtained from all human volunteers. For 3T MRI image acquisition, six healthy adult subjects (female, $n = 3$; male, $n = 3$; age: 20 - 35 years) were employed to obtain rsfMRI. For 9.4T MRI image acquisition, six healthy adult subjects (female, $n = 2$; male, $n = 4$; age: 20 - 35 years) were examined with Echo-planar imaging (EPI) sequence.

METHODS DETAILS

Animal experiments

Animal preparation

All procedures were described in a previous study (Yu et al., 2010). Rats were initially anesthetized with isoflurane (5% induction, 1.5% maintenance). Each rat was orally intubated and placed on a mechanical ventilator (SAR-830/AP, CWE). Plastic catheters were inserted into the right femoral artery and vein to allow monitoring of arterial blood gasses and administration of anesthetics. Two different anesthesia treatments were delivered during fMRI (Table S3). For alpha-chloralose anesthesia, after surgery, each rat was given an intravenous bolus of α -chloralose (60 mg/kg) and isoflurane was discontinued. Anesthesia was maintained with two constant infusion rates of α -chloralose (15 and 26.5 mg/kg/hr) in combination with pancuronium bromide (4 mg/kg/hr) to reduce motion artifacts. For isoflurane anesthesia, the ventilator maintained the rats breathing under isoflurane 1.2% in the magnet. The rats' rectal temperature was maintained at around 37°C. To prevent head motion, rats were secured in a head holder with a bite bar. All relevant physiological parameters (end-tidal CO₂, rectal temperature, heart rate, and arterial blood pressure) were continuously monitored during imaging (Figure S3, blood pressure and heart rate). The pulse sequence-based trigger and stimulation control were established using the BioPac system (Goleta, USA) and Master-9 A.M.P.I system (Jerusalem, Israel).

Viral vector injection and optical fiber implantation

The viral vectors (AV-1-PV2822 AAV5.Syn.GCaMP6f.WPRE.SV40) were procured from University of Pennsylvania Vector Core (Chen et al., 2013). Viral vectors were injected in the barrel cortex (BC) or the forepaw region of the primary somatosensory cortex (S1FL) of 3 to 4 week old rats. For the stereotactic injection procedure, rats were initially anesthetized with isoflurane. After exposing the skull, a small bur hole was drilled. A nanoliter injector (WPI, FL) was used to place a 35-gauge needle at the proper coordinates in the stereotactic frame. Injections were performed slowly over 5–6 min and the needle was slowly removed after being kept in the injection site for 10 min after finishing the injection. The injection sites of BC were as follows with stereotactic coordinates: AP = -2.35 mm; ML: 4.8 mm; DV = 2; injections each 400 nL at 1.2 mm and 0.7 mm. The injection sites of S1FL were as follows: AP = 0.2 mm; ML = 3.7 mm; DV = 2 injections each 400 nL at 1.2 mm and 0.7 mm. After 6–8 weeks of viral expression, a 200- μ m optical fiber (7 m length) was inserted through the burr holes on the skull into the BC (stereotactic coordinates: AP = -2.7 mm; ML = 5.1 mm; DV = 1.3 mm; tilt, 4°) or S1FL (AP = 0.2 mm; ML = 4 mm; DV = 1.3 mm). The optical fiber was fixed on the skull with glue. Then, the skin was sutured to cover the glue with the optical fiber extending outside of the rat head.

Simultaneous rsfMRI and calcium recording

The optical setup for calcium signal recording was built up based on a previous study (Schulz et al., 2012; M.W., Y.H., T.J. Sejnowski, and X.Y., unpublished data). As shown in Figure S4A, a 473 nm laser (MBC-III, CNI) was set to deliver the fluorescent excitation light. The laser beam was first aligned by a reflection mirror to a correct angle better deflect off a dichroic beam-splitting mirror (BS R488: reflection 471 - 491 nm, >94%; transmission 500 - 1200 nm, >93%; AHF Analysentechnik), which was coupled into a multimode fiber (FT200EMT: NA = 0.48, 230 μ m cladding diameter; Thorlabs) via amplifying lens (RMS4X; Thorlabs). Fluorescence excitation occurred in the vicinity of the fiber tip inside the MRI scanner and the emitted fluorescence light was collected and guided back to the optical setup through the same fiber. The emitted fluorescent signal from the fiber passed a lens, dichroic mirror, and an emission filter (Semrock RazorEdge; 488 Long Pass; AHF Analysentechnik), and was finally focused by a tube lens (AC254-030-A1-ML; Thorlabs) onto a peltier-cooled silicon photomultiplier with transimpedance preamplifier (MiniSM-10035-X08; SensL). The signal from the photomultiplier was amplified by voltage amplifier (DHPVA-100; Femto) and acquired by the analog input module of a Biopac

MP 150 system (5-K sampling rate). Triggers from the MRI scanner were also recorded by the Biopac system and used to synchronize calcium to BOLD fMRI offline. Laser intensity was measured at the fiber tip for neuronal calcium ($\sim 5 \mu\text{W}$) to avoid phototoxicity for long-term recording by optical power meters (PM20A; ThorLabs).

Simultaneous calcium with electrophysiology recording

The anesthetized rats were adapted in a stereotaxic device for *in vivo* recordings using similar anesthetics and surgical preparation to the fMRI experiments. Tungsten microelectrode (1 M Ω , $\sim 100 \mu\text{m}$, Tungsten, FHC) was bonded to an optical fiber with closely contacted fiber optic tip and electrode contacting point. The local field potential (LFP) was recorded through the EEG module of the Biopac system (gain factor, 5,000; band-pass filter, 0.02 - 100 Hz; sample rate, 5,000/s). In addition, calcium data and blood pressure were digitized and recorded with Biopac MP 150 system at a sampling rate of 5 kHz. The spectrogram of LFP was calculated through multi-taper spectral estimation. (Figure 6, and S7, 1 s sliding window with 0.1 s steps, 9 tapers)

MRI image acquisition from rats (14.1T)

All images from rats were acquired with a 14.1 T/26 cm horizontal bore magnet (Magnex) interfaced to an Avance III console (Bruker). A transmitter surface coil with a 6-mm diameter was used to acquire images.

bSSFP-fMRI

Balanced Steady-State Free Precession was implemented with the following parameters: TE, 3.9 ms; TR, 7.8 ms; flip angle (FA), 12°; matrix, 96 \times 128; FOV, 9.6 \times 12.8 mm; slice thickness = 400 μm ; in-plane resolution = 100 \times 100 μm^2 , resulting in one slice repetition time of 1 s. The block design was 2 s stimulation and 28 s inter-stimulus interval. The duration of each trial of rsfMRI was 15 min, and 2 - 5 trials of BOLD/CBV rsfMRI were acquired for each rat. CBV fMRI signals were acquired after intravenous injection of 15 - 20 mg of Fe/kg dextran-coated iron oxide (BioPAL, MA).

Single-vessel MGE imaging in rats

The imaging protocol was similar with our previous paper (Yu et al., 2016). To recognize individual arterioles and venules, we employed a 2D Multiple Gradient-Echo (MGE) sequence with the following parameters: TR = 50 ms; TE = 2.5, 5, 7.5, 10, 12.5 and 15 ms; flip angle = 40°; matrix = 192 \times 192; in-plane resolution = 50 \times 50 μm^2 ; slice thickness = 500 μm . We averaged the MGE images from the second echo to the fourth echo and created an arteriole-venule (A-V) map, where the venule voxels display as dark dots (blue marks) because of the fast T_2^* decay but arteriole voxels remain bright (red marks) owing to the in-flow effect (Figure 1A).

MRI image acquisition from humans (3 T)

All measurements were performed on a 3-T Siemens Prisma with a 20-channel receive head coil. Six healthy adult subjects (female, $n = 3$; male, $n = 3$; age: 20 - 35 years) were employed to obtain a BOLD signal using EPI with the following parameters: TR = 1,000 ms; TE = 29 ms; FA = 60°; matrix = 121 \times 119; in-plane resolution = 840 $\mu\text{m} \times$ 840 μm ; 9 slices with thicknesses of 1.5 mm. Parallel imaging (GRAPPA factor: 3) and partial Fourier (6/8) were employed to accelerate image acquisition. The visual stimulation consisted of a circular black and white checkerboard. For the resting state fMRI, the duration of each trial of rs-fMRI was 15 min with the eyes-closed condition. The Siemens physiologic Monitoring Unit (PMU) was used to monitor the respiration and pulse oximetry simultaneously. Both PMU physiological log files and EPI data contain time tags, which were utilized to synchronize the temporal profile for statistical analysis.

MRI image acquisition from humans (9.4 T)

All images were acquired with a 9.4-T MRI scanner (Siemens Healthcare, Erlangen, Germany) with a home-built 16-channel transmit/31-channel receive head coil (Shajan et al., 2014). All the imaging protocols follow those of the 3-T scanner but at a higher resolution. Six healthy subjects (female, $n = 2$; male, $n = 4$; age: 20 - 35 years) were examined with EPI sequence: TR = 1,000 ms; TE = 22 ms; FA = 50°; matrix = 300 \times 300; in-plane resolution = 500 $\mu\text{m} \times$ 500 μm ; 9 slices a thicknesses of 0.8 mm. Parallel imaging (GRAPPA factor: 4) and partial Fourier (5/8) were utilized to accelerate image acquisition.

Single-vessel MGE imaging in humans

We utilized a 2D MGE sequence with the following parameters: TR = 61 ms; TE = 5.99, 10.39, 14.79, 19.19, 23.59, 27.99, 32.39, 36.79, 41.19, 45.59 ms; flip angle = 60°; matrix = 896 \times 896; in-plane resolution = 19 \times 19 μm^2 ; slice thickness = 1,000 μm . An arteriole-venule (A-V) map was acquired by averaging of the MGE images from the second echo to the ninth echo (Figure 8A).

Data processing

All data processing was performed using Analysis of Functional NeuroImages (AFNI) software (Cox, 1996) and MATLAB. The relevant fMRI analysis source codes can be downloaded through <https://www.afni.nimh.nih.gov/afni/>. A detailed description of the processing procedure conducted is provided in a previous study (Yu et al., 2012). To register the single-vessel functional map with the A-V map, the tag-based registration method was applied, which carried out ten to twelve tags (venule voxels) of the averaged bSSFP fMRI images corresponding to those of the A-V map. No additional smoothing step was applied. For evoked fMRI analysis, images were normalized by scaling the baseline to 100. Linear regression analysis was applied to estimate the hemodynamic response function. The beta estimates were used to indicate the amplitude of the BOLD response in the beta maps.

Definition of the individual vessel

The individual vessel voxels in A-V map were identified by the following algorithm: the intensities of arteriole/artery voxels are higher than the mean signal intensities plus two times the standard deviation (s.d.) of the local area in a 5×5 kernel, while the intensities of venule/vein voxels are lower than the mean signal intensities minus two times the s.d. of local area, as shown in Figure 1A (Yu et al., 2016). The locations of individual vessel voxels defined in the A-V map were employed to extract the time courses from BOLD/CBV fMRI of individual vessels.

Resting state fMRI analysis

The preprocessing analysis was performed using a modified AFNI resting state fMRI processing protocol (afni_proc.py). The time courses of the vessel seed voxels were chosen for correlation analysis. The vessel voxels from both arteriole and venules were determined based on the A-V map. The detailed image processing procedure utilized was described previously (Yu et al., 2016). Then the 3dTCorr1D function in AFNI was employed to generate the correlation map. In addition, ICA analysis was also performed to characterize the vessel specific correlation maps with the Independent Component Analysis (ICA) Toolbox (GIFT 4.0, MIND Research Network). The ICA toolbox employed principal component analysis (PCA) to realign the data at a lower dimensionality (or reduced variance in a simplified dimensional space). ICA was utilized to generate ten independent components using Infomax algorithms, which specialize in the separation of super-Gaussian sources (Bell and Sejnowski, 1995). After the back reconstruction step, the spatial maps and time courses of components were scaled using Z-scores. Finally, a RETROICOR algorithm (Glover et al., 2000) was implemented to correct physiological motion effects (Figure S8).

Power spectrum analysis

Depending on data format, power spectrum analysis was performed in AFNI (image format) or MATLAB (text format). In AFNI, a 3dPeriodogram function was utilized to compute the power spectrum of time courses in all individual voxels. Then the averaged power spectral density was calculated in venule voxels or arteriole voxels, respectively (FFT length: 256, Figures S6B and S6D). In MATLAB, we employed Fast Fourier Transform (FFT) to calculate the power spectral density of the physiologic data (respiration/pulse oximetry) (Figure S8F) and calcium data (Figure S6F). The calcium signals under light/deep anesthesia were sampled at 1 Hz and calculated by Welch's power spectral density estimate method (FFT length: 256, the overlap: 50%).

Coherence analysis

Previously, coherence analysis was implemented to identify the functional connectivity between different brain areas (Drew et al., 2008; Wang et al., 2012). For this study, to investigate the interactions of paired vessels, coherence analysis was employed as an indicator of functional interactions and indicator of how well the seed vessel corresponds to other vessel voxels at different frequency ranges. The definition of coherence is as follows:

$$Coh_{xy}(f) = \frac{|P_{xy}(f)|^2}{P_{xx}(f)P_{yy}(f)}$$

where x indicates the fMRI signal from one seed vessel, y represents the fMRI time course from another vessel. $P_{xx}(f)$ and $P_{yy}(f)$ are the power spectral densities of x and y , respectively, and $P_{xy}(f)$ is the cross power spectral density of x and y . The coherence was calculated by using Welch's overlapped averaged periodogram method with FFT (256-point length) and a 256 s Hamming window, which divides x and y into equal overlapping sections (240-point overlap, >90% overlap). The frequency resolution of coherence is $1 / 256 \text{ s} = 0.0039 \text{ Hz}$ which provides enough resolution to observe the slow frequency range.

The calcium data analysis

The calcium signal was down-sampled to one TR per sample. Next, zero-phase digital filtering (0.01 - 0.1 Hz) was employed to obtain the slow fluctuation of the calcium signal (filtfilt function in MATLAB). In addition, a cross-correlation between the slow fluctuation of the calcium signal and individual venules was performed using the MATLAB function xcorr (Figures 4E and 4L). A 3ddelay function from the AFNI library was utilized to estimate the time lag map between the slow fluctuation of the calcium signal with BOLD fMRI of venules ($CC > 0.25$) (Figure 4C, inset) or CBV fMRI of arterioles ($CC < -0.25$) (Figure 4J, inset). For the spectrogram of the calcium signal, a function timefreq from EEGLAB (Delorme and Makeig, 2004) was employed to get the averaged power of the spontaneous calcium spikes (Figures 5B and 6A). A time-varying power spectrogram of calcium signal was computed by using the discrete Fourier transform with a sliding Humming window. The sliding window was 1000 ms without overlap to match one TR of BOLD fMRI data.

Immunohistochemistry

After the conclusion of the fMRI experiments, the rat brain tissues were perfused using a 4% paraformaldehyde fixative. The tissues were then transferred to 15% sucrose in PBS and kept overnight at 4°C. Next, the prefixed tissues were moved to 30% sucrose in PBS. After sinking, the tissues were stored at -80°C until use. The tissues were also utilized to prepare coronal sequential brain sections (30- μm thickness, -20°C using Leica CM3050S microtome). The sections were incubated overnight at 4°C with primary antibodies: mouse anti-NeuN (1:200; Merck). Afterward, sections were washed five times with PBS and incubated for 60 min with the secondary antibodies: goat anti-mouse conjugated with CY3 (1:500; Abcam). Finally, mounting medium with DAPI (VectaShield, vector) was utilized to protect the fluorescence signal and reveal nuclei. The expression position of GCaMP was confirmed by colocalization with NeuN using a fluorescence microscope (ApoTome, Zeiss).

QUANTIFICATION AND STATISTICAL ANALYSIS

A paired Student's *t* test was performed to compare the coherence values of paired venules/veins and paired arterioles/arteries in the rat and human resting-state fMRI data. The data with error bars are displayed as the means \pm SEM. The *p* values < 0.05 were considered statistically significant. The sample size for animal experiments was not previously estimated. The sample size for human experiments was estimated based on the statistical parameters derived from the animal data using G^* power analysis. No blinding and randomization design was needed in this work.

Supplementary information

Title: Determination of the single vessel spatial dynamic connectivity and its neural correlates with simultaneous fMRI and intracellular calcium recording

Authors: Yi He, Maosen Wang, Xuming Chen, Rolf Pohmann, Jonathan R. Polimeni, Klaus Scheffler, Bruce R. Rosen, David Kleinfeld and Xin Yu*

Supplementary Figures: 17

Supplementary Table: 2

Supplementary Videos: 5

Corresponding Author: Xin Yu

Email: xin.yu@tuebingen.mpg.de

Address: Spemannstr. 41, 72076 Tuebingen Germany

Phone: +49 7071 601-740

Fax: +49 7071 601-701

Supplementary Figures

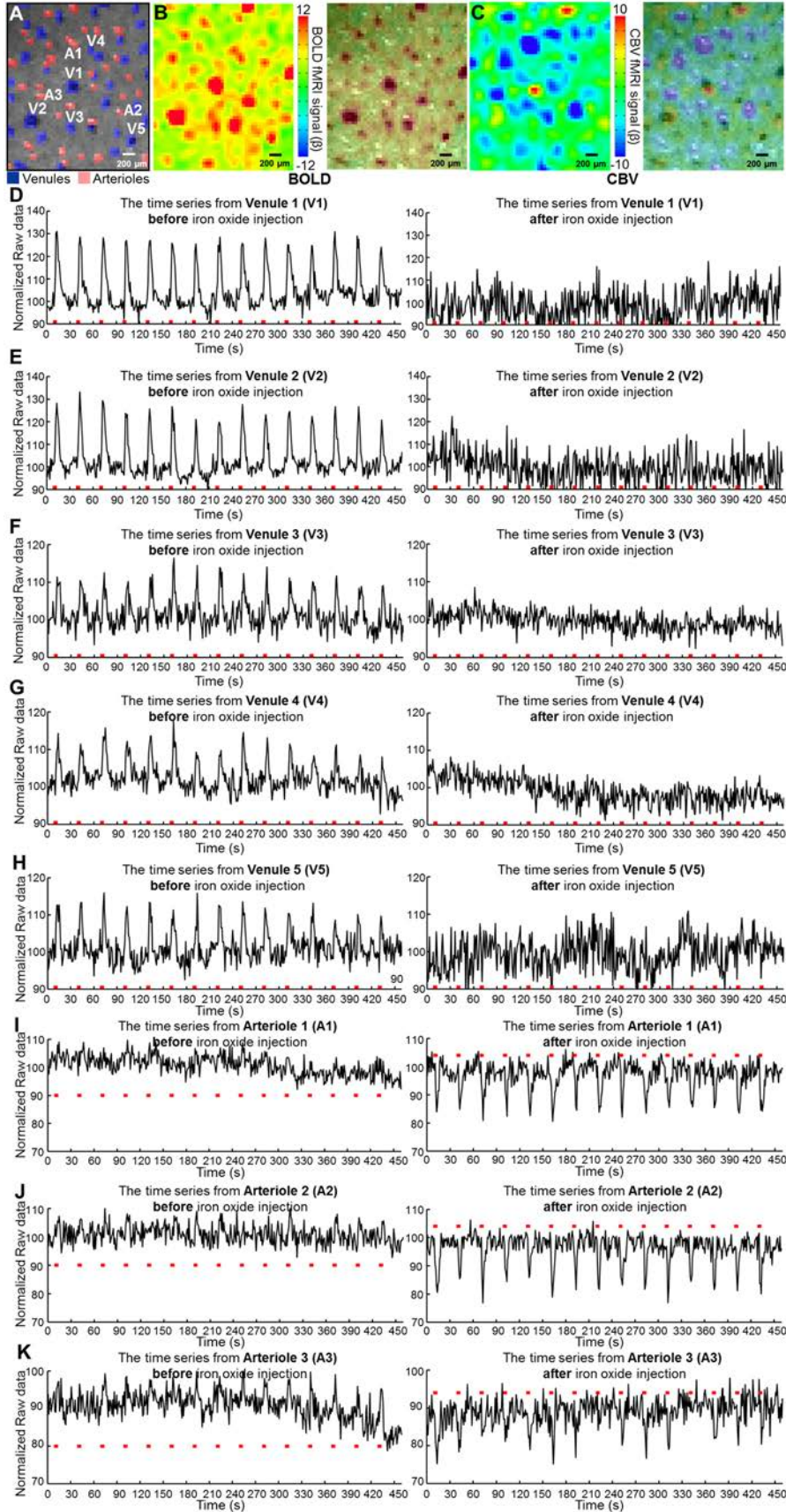


Figure S1. The bSSFP fMRI time courses of individual venules and arterioles before and after iron oxide particle injection (A) The A-V map shows the five venules and three arterioles. **(B)** The single-vessel bSSFP BOLD functional map (semi-transparent map on A-V map). **(C)** The single-vessel bSSFP CBV-weighted functional map (semi-transparent map on A-V map) **(D-H)** The time course of BOLD and CBV-weighted fMRI signal from five venules (V1-V5). **(I-K)** The time course of BOLD and CBV-weighted fMRI signal from three arterioles (A1-A3).

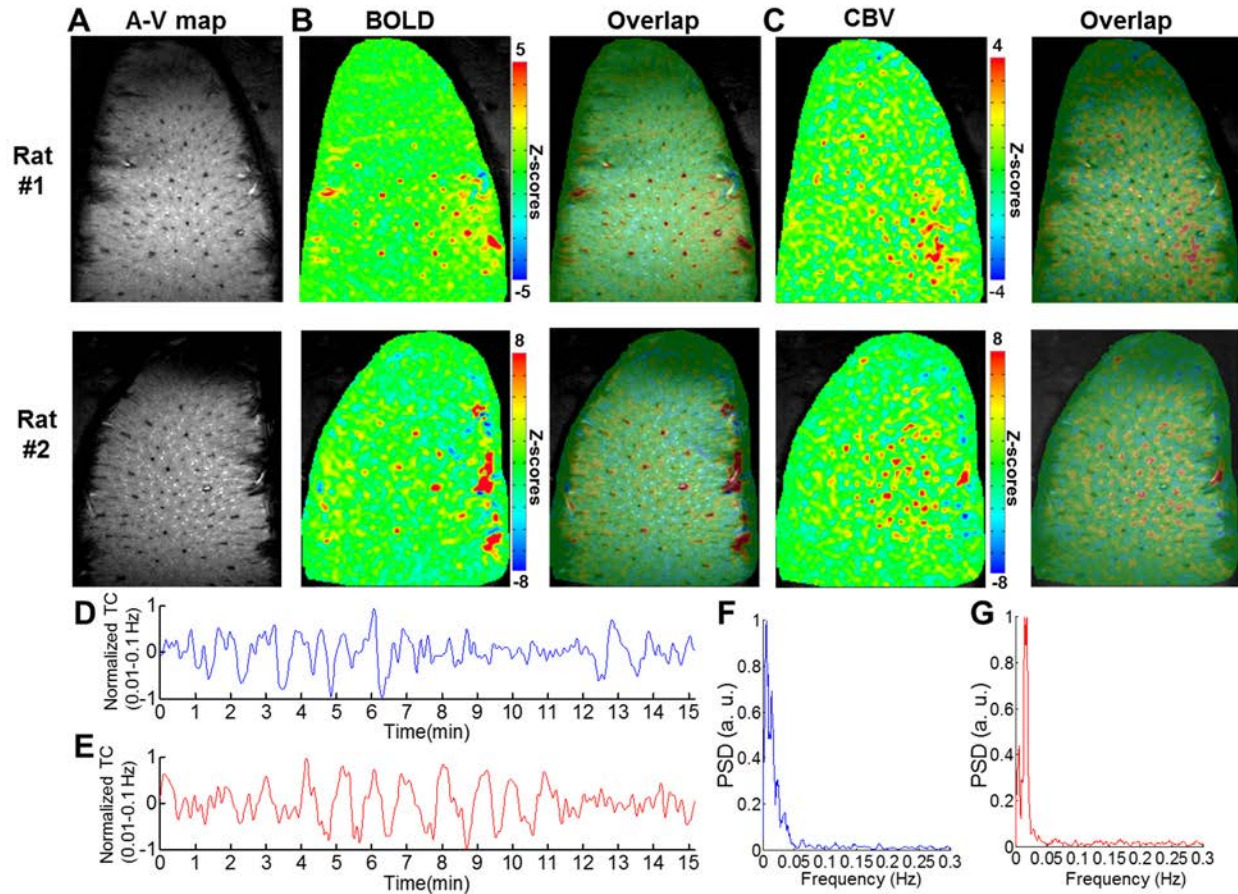


Figure S2. Vascular dynamic network connectivity using Group ICA Analysis in two representative Rats. (Related to Figure 2-3) (A) The A-V maps of two representative Rats. (B) The correlation maps based on the designated ICA component show the venule-dominated BOLD correlation pattern in both rats (right panel, the correlation map overlapped on the A-V map). (C) The correlation maps based on the designated ICA component demonstrate the arteriole-dominated CBV correlation pattern in both rats (right panel, the correlation map overlapped on the AV map). (D) The BOLD time series of the designated ICA component showing high correlation on venule voxels in the rat #2. (E) The CBV time series of the designated ICA component indicating high correlation on arteriole voxels in the rat #2. (F) The power spectrum density (PSD) of the designated ICA component for the BOLD fMRI signal from rat #2 exhibits slow fluctuations of BOLD fMRI from venule voxels vary from 0.01 to 0.04 Hz. (G) The power spectrum density of the designated ICA component for the CBV fMRI signal from rat #2.

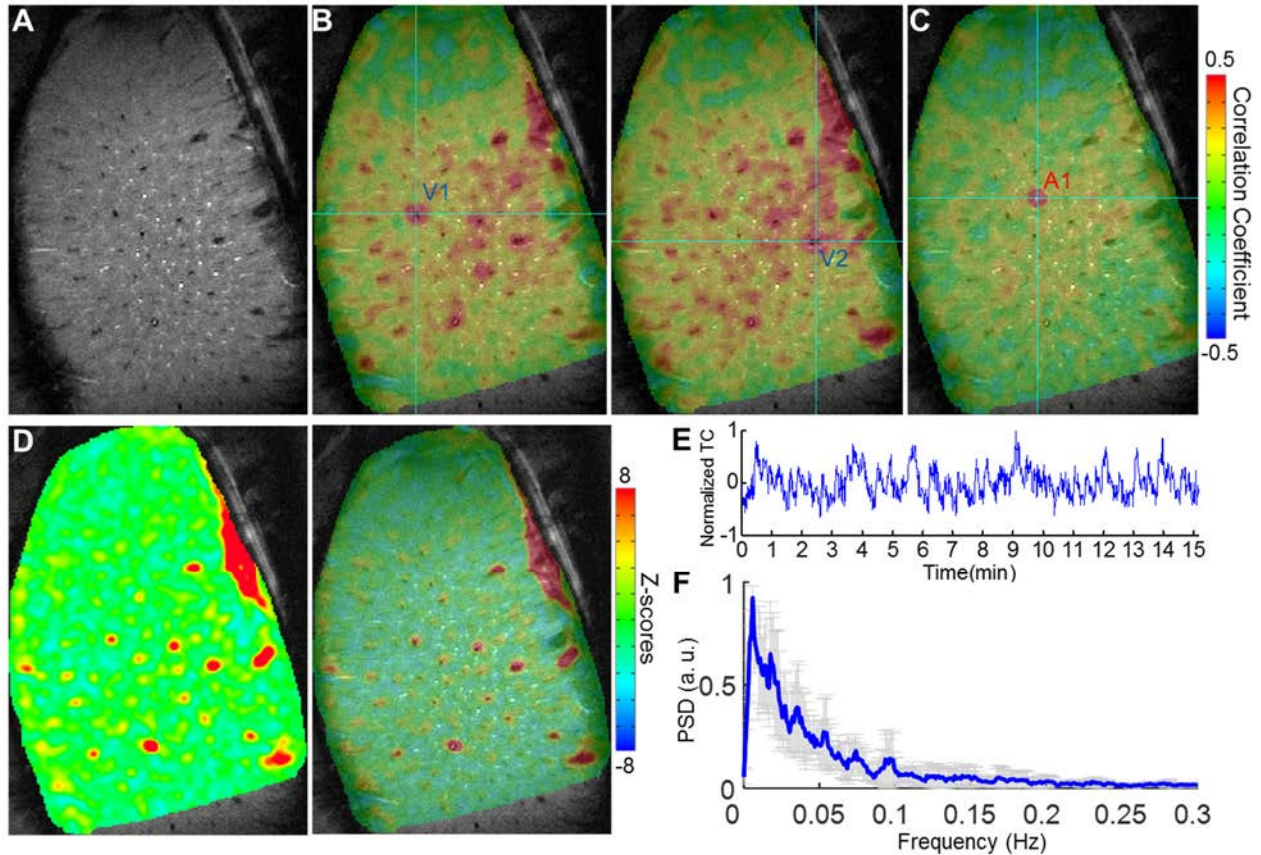


Figure S3. Mapping the Vascular dynamic network connectivity under isoflurane anesthesia. (Related to Figure 2-3) (A) The A-V map shows the individual arterioles (bright dots) and venules (dark dots). (B) The venule-seed based correlation map from two venule seed voxels (seeds: cyan crosshairs) (C) The arteriole-seed based correlation map from one arteriole seed (seed: cyan crosshair). (D) The correlation maps based on the designated ICA component show the venule-dominated BOLD correlation patterns (right panel, the correlation map overlapped on the A-V map). (E) The normalized BOLD time series of the designated ICA component. (F) The power spectrum density (PSD) of the designated ICA time series from 3 rats. ($n = 3$ rats, mean \pm s.e.m)

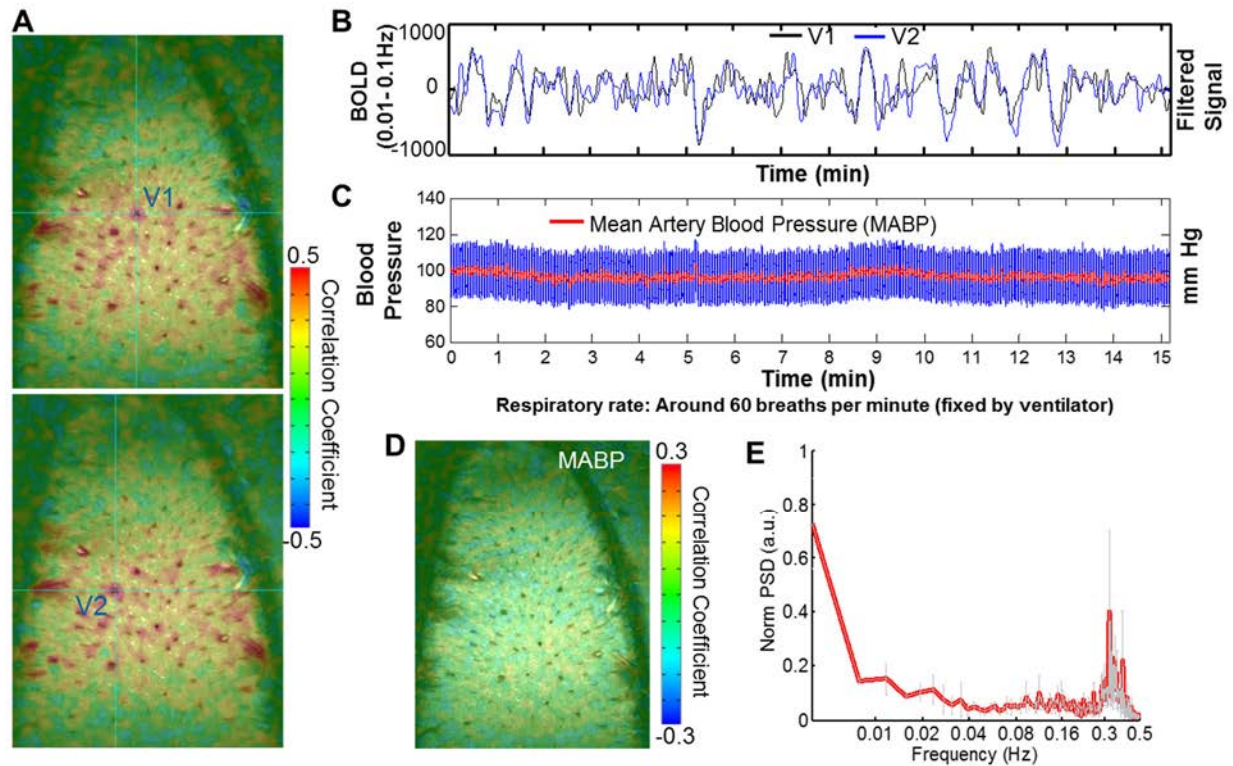


Figure S4. The simultaneously acquired physiological signals and the resting state SSFP-fMRI signal in anesthetized rats. (Related to Figure 3) (A) The venule-seeds based correlation maps from two venule seed voxels (V1 and V2). (B) The time series of the BOLD signal slow fluctuations (0.01-0.1 Hz) from the two venule seeds. (C) The blood pressure signals were acquired simultaneously with the resting state fMRI, showing no clear variation correlated to the slow-frequency oscillations of the fMRI signal. (D) The correlation map between the mean artery blood pressure (MABP) time series (0.01 - 0.1 Hz) with rs-fMRI shows little correlation. (E) The mean normalized power spectral density (PSD) of MABP ($n = 3$ rats, mean \pm s.e.m, Welch's method, FFT length = 256, the overlap: 50 %).

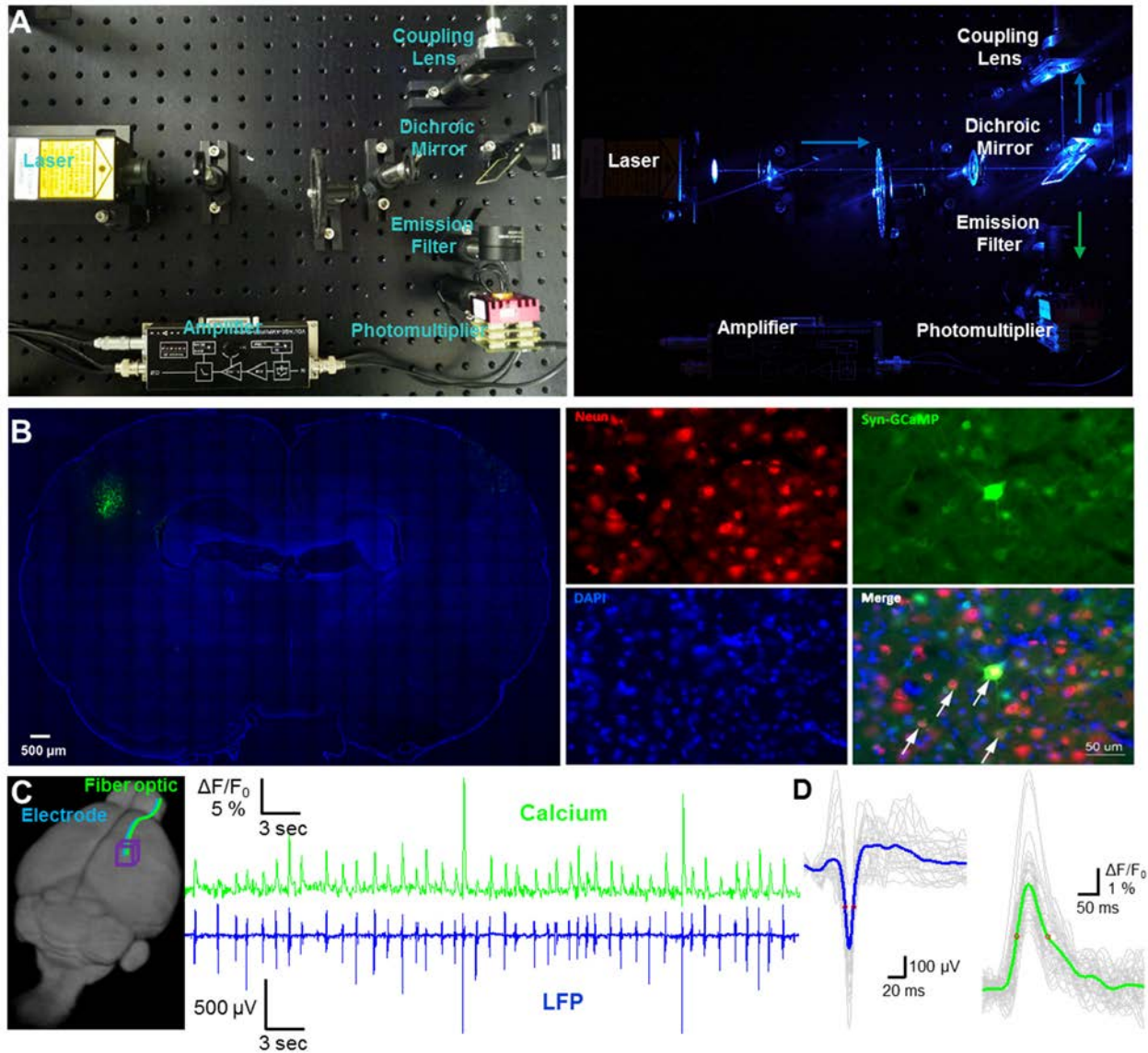


Figure S5. *In vivo* fiber optical calcium recording with simultaneous local field potential (LFP) recording. (Related to Figure 4) (A) The setup for the fiber-optic mediated fluorescent signal recording system. (B) The GCaMP6f was expressed in the deep layer of the vibrissa cortex (left panel: the green region in the coronal section of the rat brain). Right panel is the enlarged immunostaining image with the NeuN in red, DAPI in blue, and GCaMP6f in green, which were merged to show the GCaMP6f expressed in neurons with NeuN positive staining in the nuclei (white arrows). (C) The left panel is the schematic drawing to show the fiber optic and electrode targeting the barrel cortex of a reconstructed 3D rat brain. The right panel shows the simultaneous acquired calcium and LFP signal traces. There is one-to-one correspondence between spontaneous calcium (green) and LFP spikes (blue). (D) The averaged LFP spike (blue, Full width at half maximum (FWHM): 10.89 ± 0.58 ms, mean \pm s.e.m, $n = 30$) and the averaged calcium spike (green, FWHM: 78.9 ± 0.26 ms, mean \pm s.e.m, $n = 48$)

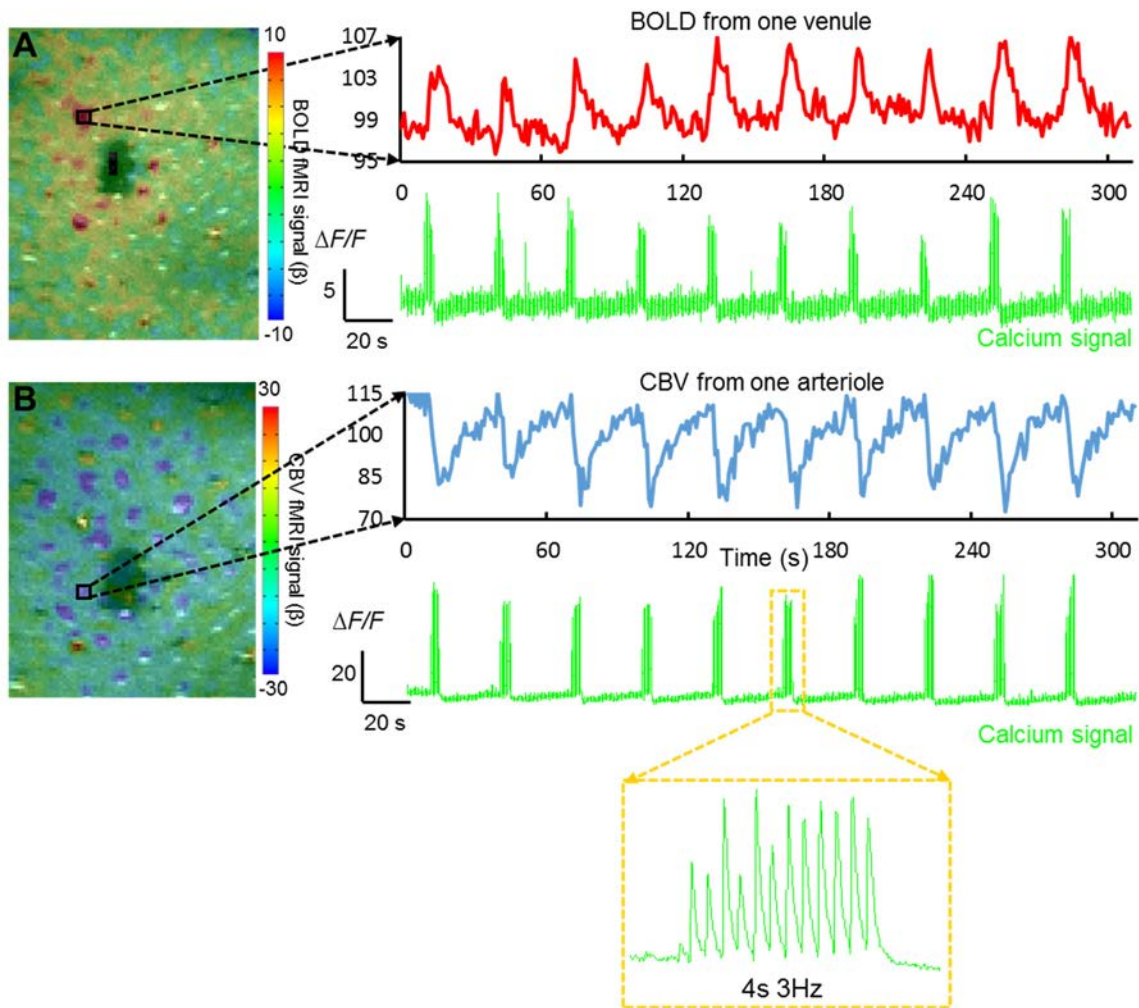


Figure S6. Map the evoked single-vessel BOLD/CBV fMRI signal with simultaneous calcium recording. (Related to Figure 1, Figure 4) (A) The BOLD fMRI map is overlaid on the A-V map, showing the venule-dominated peak BOLD signal (dark hole, fiber optic). The on/off block time series (red) of BOLD fMRI signal from one single venule ROI (marked in the left panel) and the calcium signal (green) was recorded simultaneously (forepaw stimulation: 3 Hz, 4 s, 1.5 mA). (B) The CBV fMRI map is overlaid on the A-V map, indicating the arteriole-dominated peak CBV signal. The on/off block time series (blue) of the CBV fMRI signal from one single arteriole ROI (marked in left panel). The simultaneous calcium signal was recorded with an enlarged image, showing the evoked calcium spikes upon stimulation.

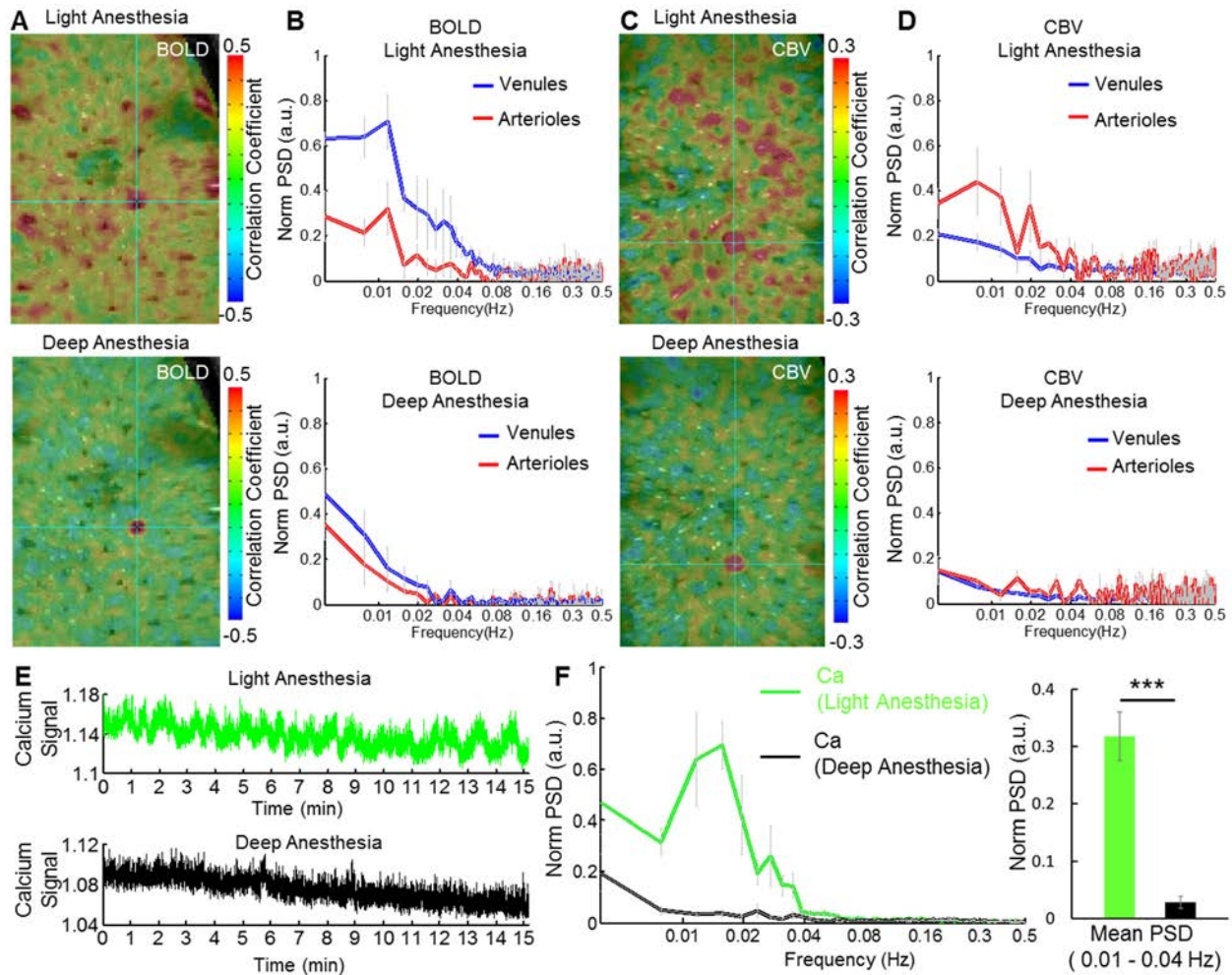


Figure S7. Mapping the vessel-specific fMRI signal fluctuation with simultaneous calcium recording at different anesthetic levels. (Related to Figure 3-4) (A) The venule-seed based BOLD correlation maps under light (upper panel) / deep (lower panel) anesthesia. (B) The normalized power spectrum density (PSD) of venule (blue) and arteriole (red) voxels of BOLD fMRI under the light (upper panel) and deep (lower panel) anesthesia. (Deep, $n = 4$ rats, light, $n = 3$ rats, mean \pm s.e.m, FFT length = 256) (C) The arteriole-seed based CBV correlation maps under light (upper panel) / deep (lower panel) anesthesia. (D) The normalized power spectrum density (PSD) of venule (blue) and arteriole (red) voxels of CBV fMRI under the light (upper panel) and deep (lower panel) anesthesia. ($n = 3$ rats, mean \pm s.e.m, FFT length = 256) (E) The raw calcium signal simultaneously acquired with the rs-fMRI signal shows slow oscillation under the light anesthesia (upper panel, green curve), but not under the deep anesthesia (lower panel, black curve). (F) The normalized PSD of the calcium signal shows elevated power at the frequency bandwidth 0.01-0.04 Hz under light anesthesia, which is significantly higher than that under deep anesthesia. (***, $p = 0.00047$, paired t-test, $n = 5$ rats, mean \pm s.e.m, Welch's method, FFT length = 256, the overlap: 50 %).

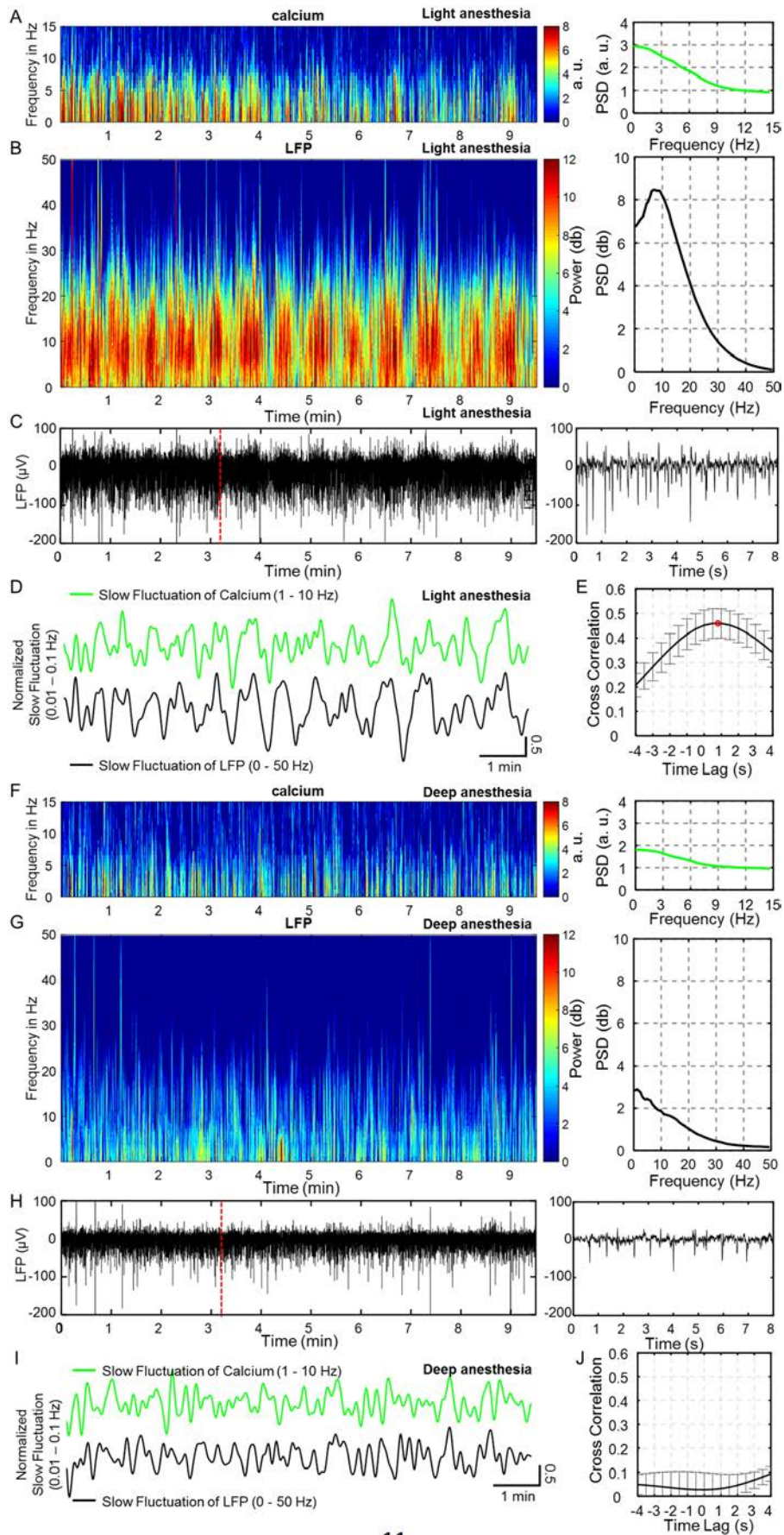


Figure S8. The Spectrogram of simultaneous calcium and electrophysiological signal under α -chloralose anesthesia (Related to Figure 4) **(A)** Spectrogram of calcium signal during light anesthesia. **(B)** Spectrogram of local field potential (LFP) at light anesthesia from multi-taper spectral estimates (1s sliding window with 0.1s steps, 9 tapers). The right panel shows the averaged power spectrum density (PSD) **(C)** The time course of the LFP signal under light anesthesia **(D)** The mean calcium spectral power profile (band-pass filter: 0.01 - 0.1 Hz of 1 - 10 Hz, green) and the mean LFP spectral power profile (0 - 50 Hz, black) at light anesthesia. **(E)** The cross-correlation function of the averaged LFP power (0 - 50 Hz) from LFP spectrogram and the averaged calcium power (1 - 10 Hz) profile from the calcium spectrogram (band-pass filter with 0.01 - 0.1 Hz) illustrates the peak cross-correlation coefficient at 0.8 s lag time at light anesthesia ($n = 4$ rats, mean \pm s.e.m). **(F)** Spectrogram of calcium signal during deep anesthesia. **(G)** Spectrogram of local field potential (LFP) at deep anesthesia from multi-taper spectral estimates (1s sliding window with 0.1s steps, 9 tapers). The right panel shows the averaged power spectrum density (PSD). **(H)** The time course of the LFP signal under deep anesthesia **(I)** The mean calcium spectral power profile (band-pass filter: 0.01 - 0.1 Hz of 1 - 10 Hz, green) and the mean LFP spectral power profile (0 - 50 Hz, black) at deep anesthesia. **(J)** The cross-correlation function of the averaged LFP power (0 - 50 Hz) from LFP spectrogram and the averaged calcium power (1 - 10 Hz) profile from the calcium spectrogram (band-pass filter with 0.01 - 0.1 Hz) show little correlation at deep anesthesia ($n = 4$ rats, mean \pm s.e.m).

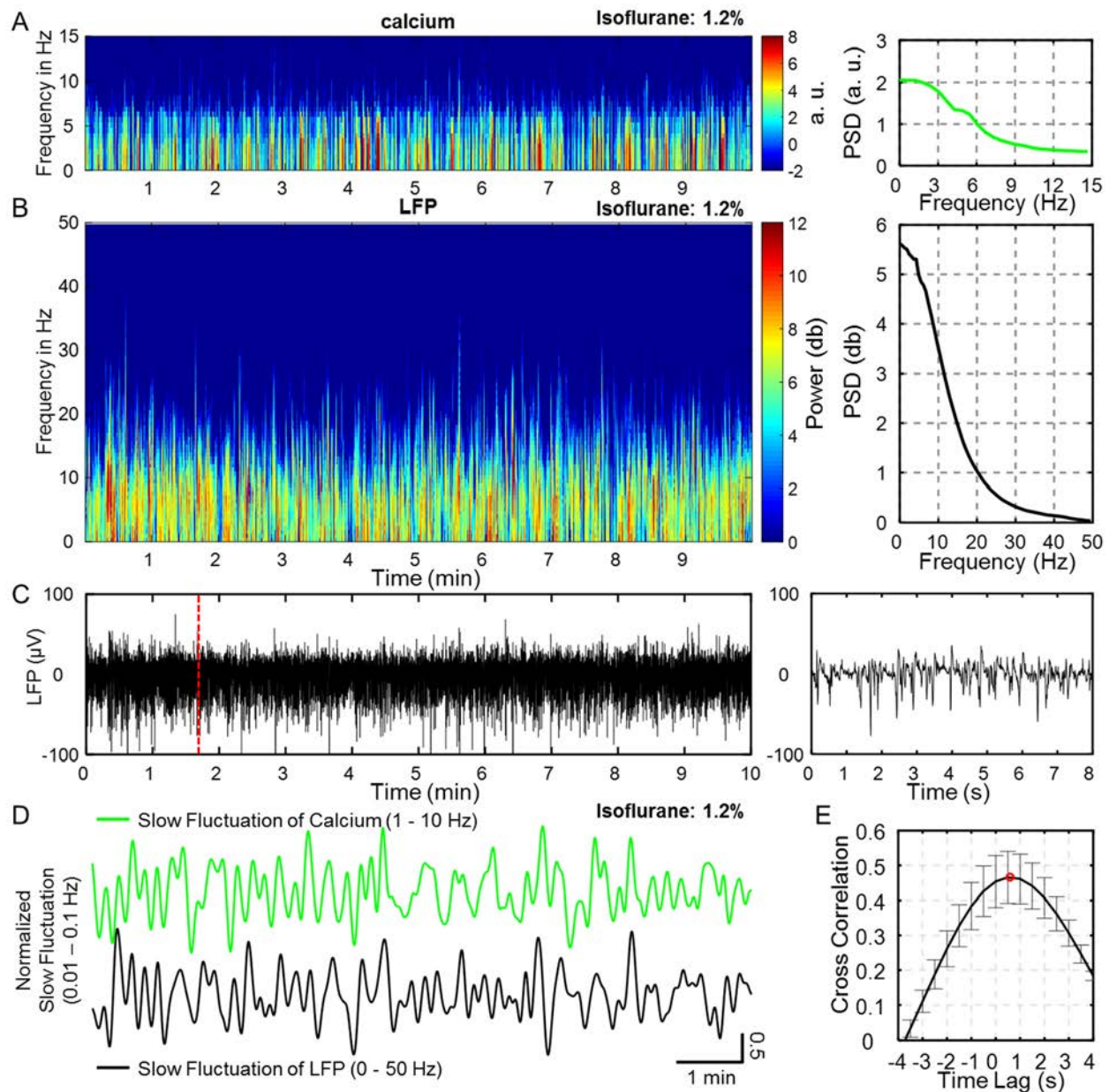


Figure S9. Figure S14. The spectrogram of simultaneous calcium and electrophysiological signal under 1.2% isoflurane anesthesia (Related to Figure 4) (A) The spectrogram of the calcium signal under isoflurane. **(B)** The spectrogram of local field potential (LFP) from multi-taper spectral estimates (1s sliding window with 0.1s steps, 9 tapers). The right panel shows the averaged power spectrum density (PSD) **(C)** The time course of the LFP signal **(D)** The mean calcium spectral power profile (band-pass filter: 0.01 - 0.1 Hz, of 1 - 10 Hz, green) and the mean LFP spectral power profile (0 - 50 Hz, black). **(E)** The cross-correlation function of the averaged LFP power (0 - 50 Hz) from LFP spectrogram and the averaged calcium power (1 - 10 Hz) profile from the calcium spectrogram (band-pass filter with 0.01 - 0.1 Hz) illustrates strong correlations during 1.2% isoflurane anesthesia ($n = 3$ rats, mean \pm s.e.m).

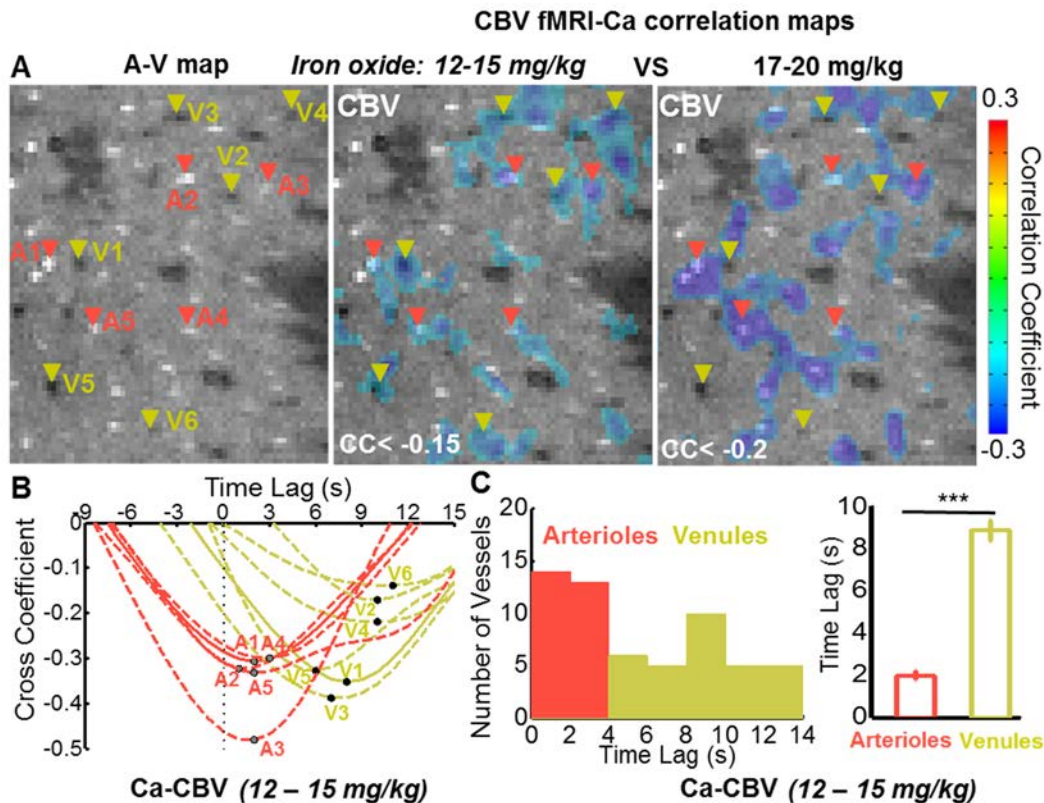


Figure S10. The correlation analysis of the venule CBV fMRI signal with the calcium signal. (Related to Figure 4) (A) The A-V map (the left panel) shows the location of five representative arterioles (A1-A5) and six representative venules (V1-V6). The correlation maps between the calcium signal and the SSFP-based CBV fMRI signal acquired at two different dosage of iron oxide particles show negative correlation in the venule voxels (V1-V6) detectable at low dose (middle panel, 12-15 mg/kg), and arteriole dominated negative correlation with increased iron particle concentration (right panel, 17-20 mg/kg). **(B)** At the lower dose of iron oxide particles, the cross-correlation function of the calcium signal and CBV fMRI signal demonstrate the negative peak of the venules (V1-V6) coefficients at the lag time 6-12 s and the negative peak of the arterioles (A1-A5) at the lag time 1-3 s. **(C)** The histogram of the number of vessels with lag times varied from 0.5 to 14 s (the threshold of the cross-correlation coefficient < -0.15). The mean lag time of arterioles are significantly lower than that of venules at the lower dose of iron oxide particles (***, $p = 5 \times 10^{-18}$, t-test, Arterioles, $n = 28$ from 4 rats, 1.96 ± 0.22 s; Venules, $n = 31$ from 4 rats, 8.88 ± 0.48 s, mean \pm s.e.m)

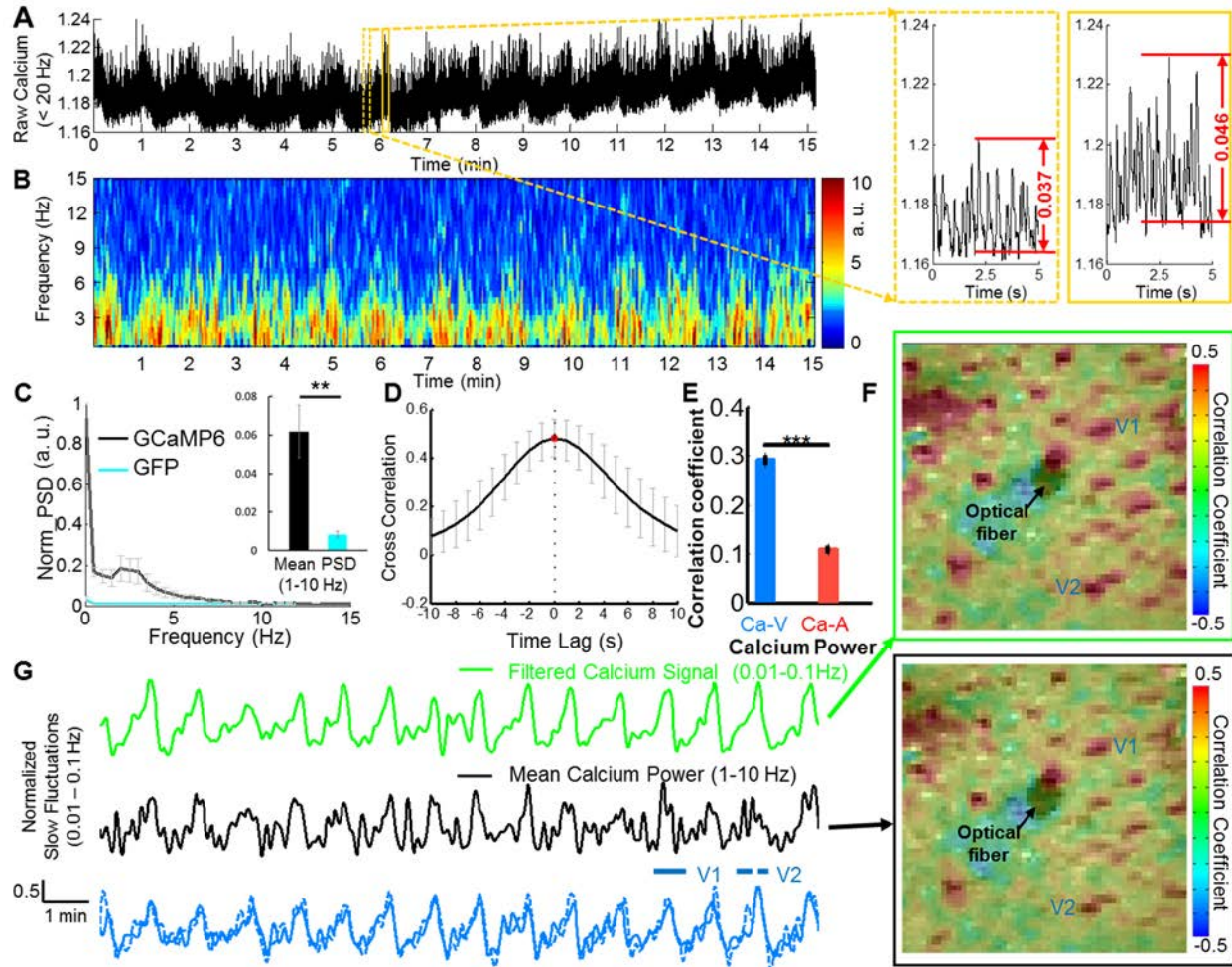


Figure S11. The correlation between the calcium spectral power (CaSP) profiles with vessel-specific fMRI signal. (Related to Figure 4) (A) The time course of the calcium signal (low pass filter: 20 Hz) from one representative rat at the resting state with enlarged 5s windows of the calcium spikes identified at different periods (dotted and solid yellow boxes). (B) The time-varying power spectrogram of the calcium signal is plotted as the function of time from 0.5 to 15 Hz (discrete Fourier transform in 1s Hamming window; the sampling rate is 1Hz to match the TR of fMRI signal). (C) The normalized power spectrum density (PSD) from the rats with GCaMP6 expression (black, $n = 5$ rats) or GFP expression (Green Fluorescent Protein, cyan, $n = 4$ rats) indicates the mean PSD (1-10Hz) of GCaMP6 is significantly higher than that of GFP (**, $p = 0.001$, t-test). (D) The cross-correlation function of the calcium signal and the averaged power (1-10 Hz) profile from the calcium spectrogram (band-pass filter with 0.01 - 0.1 Hz) illustrates the peak cross-correlation coefficient at 0 s lag time. ($n = 4$ rats, $\text{mean} \pm \text{s.e.m}$). (E) The mean correlation coefficients of the averaged calcium power signal with the BOLD fMRI signal of venules are significantly higher than that of arterioles (***, $p = 1.9 \times 10^{-4}$, pair t-test, $n = 4$ rats, $\text{mean} \pm \text{s.e.m}$). (F) The correlation maps between the SSFP-based BOLD fMRI signal and the slow oscillation calcium signal (band-pass filter: 0.01-0.1Hz, upper panel and the mean calcium power spectral profile (1 - 10 Hz, lower panel) show similar venule-specific correlation patterns. (G) The time series (band-pass filter: 0.01 - 0.1Hz) of the slow oscillation calcium signal (green), the mean calcium spectral power profile (1 - 10 Hz) (black), the BOLD fMRI signal from two venules (V1, V2; blue, solid and dotted blue lines).

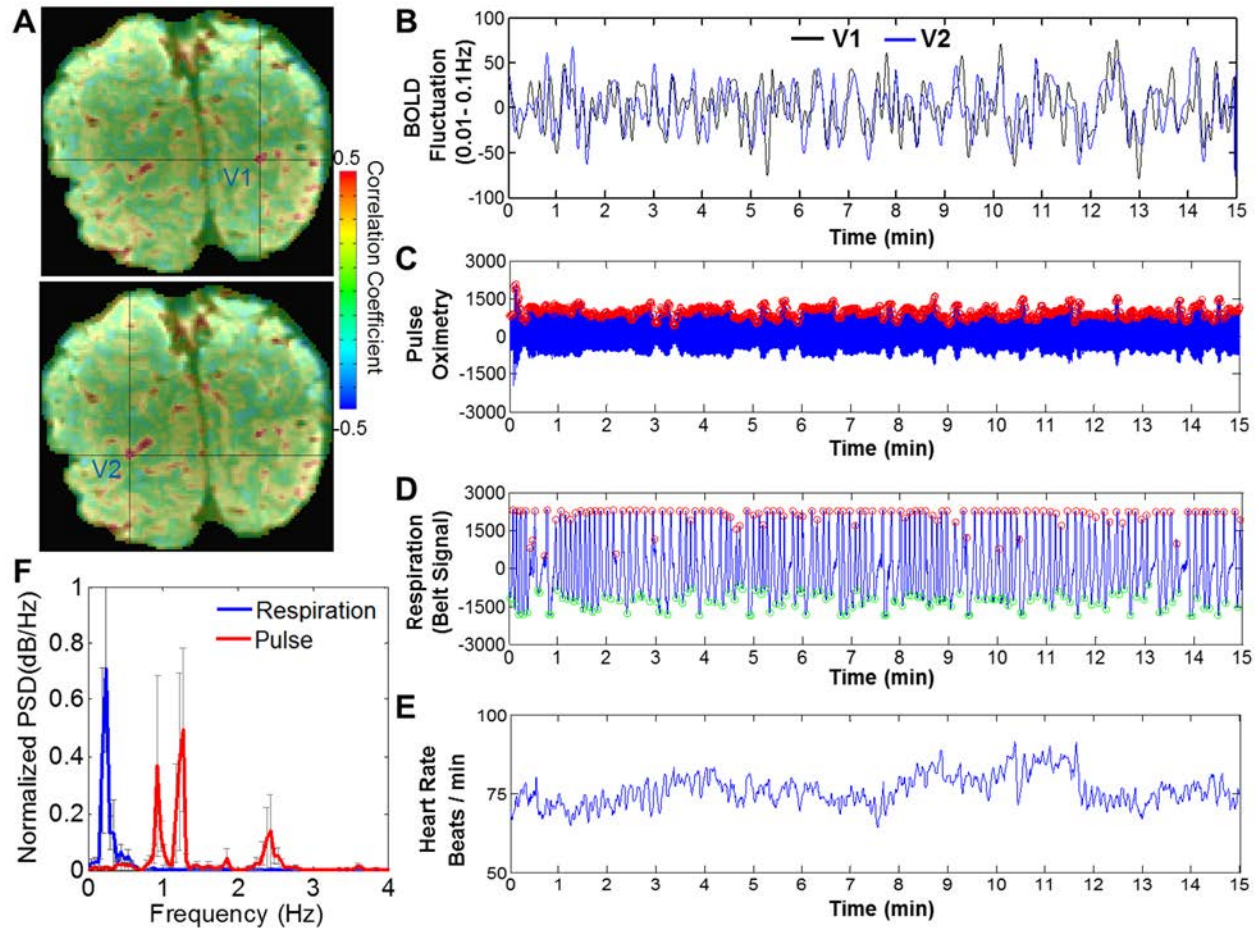


Figure S12. The simultaneously recorded physiologic parameters for the resting-state fMRI of human subjects. (Related to Figure 5) (A) The seed-based correlation maps from two vein voxels (V1 and V2). (B) The time series of BOLD signal (0.01 - 0.1 Hz) from the two representative vein seeds are highly correlative. (V1, black line; V2, blue line) (C-E) The pulse oximetry (C), respiration (D) signals were simultaneously acquired with the BOLD fMRI signal by using Siemens physiologic monitoring unit (PMU). Heart rate (E) is derived from the pulse-oximetry time series. (F) The normalized power spectral density (PSD) represents the respiration signal (blue) with peak frequency at approximately 0.18 Hz and the pulse oximetry signal (red) covering the frequency range from 0.8 to 2.5 Hz ($n = 3$ subjects, mean \pm s.e.m).

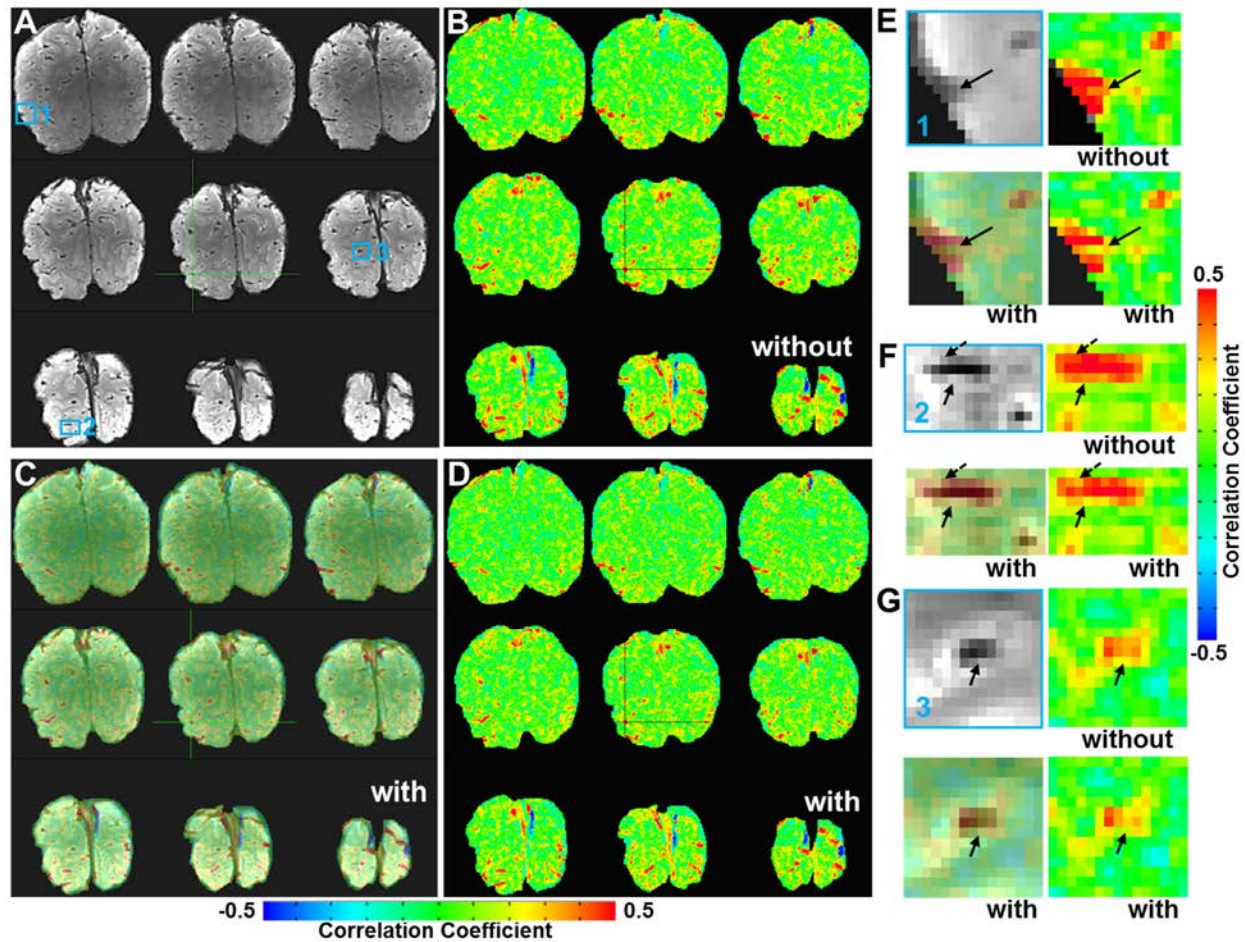


Figure S13. The correlation maps with/without the regression of the physiological parameters. (Related to Figure 5) (A) The averaged multi-slices EPI images covering the occipital lobe of the human brain. (B) The seed-based correlation maps before the physiological parameter regression (seed: black cross-point). (C-D) The seed-based correlation maps after the physiological parameter regression (seed: black cross-point; (C) is the semi-transparent map overlapped on the EPI images.) (E-G) The enlarged views of three regions in multi-slices EPI images (blue square marks in A) illustrate the similar correlation patterns with/without the regression of the physiological parameters.

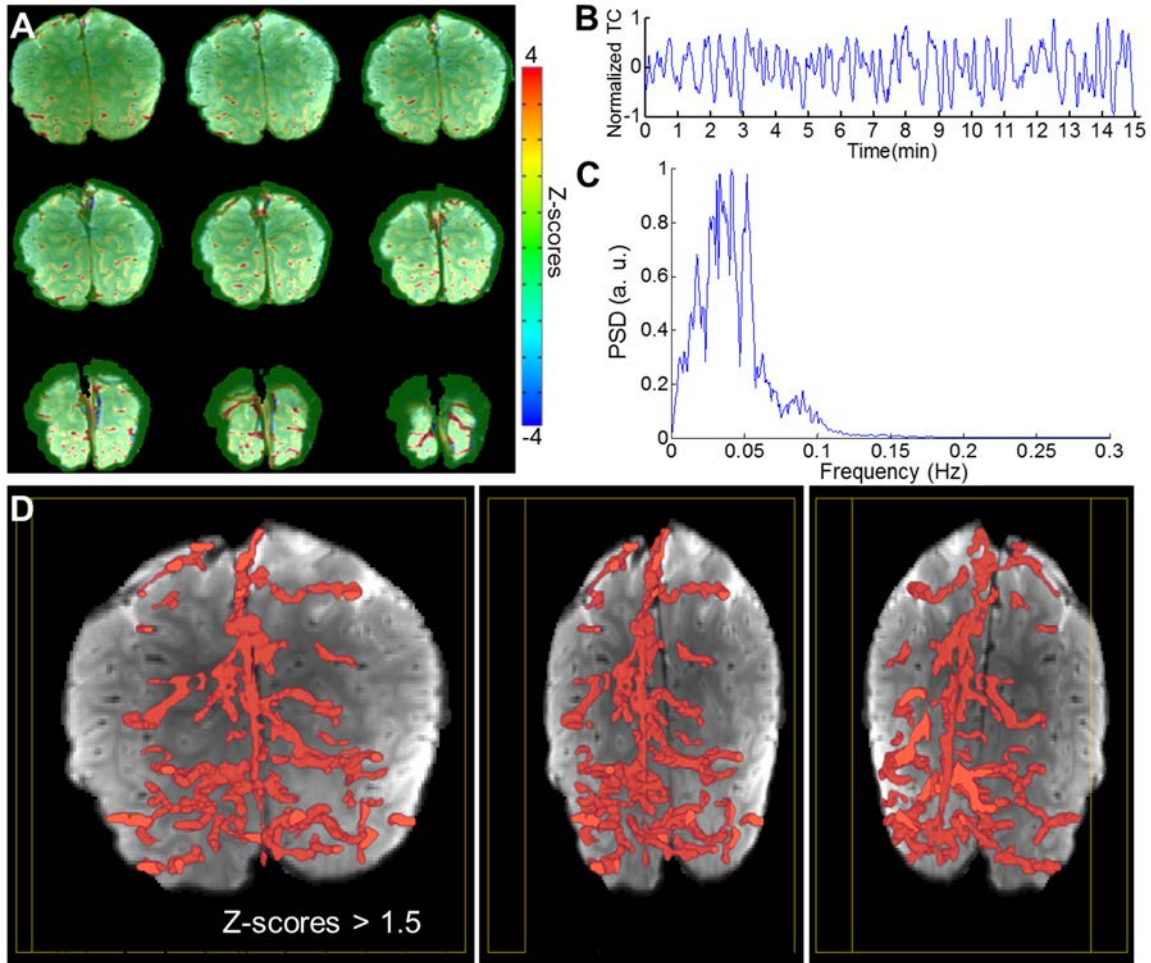


Figure S14. The ICA-based vascular dynamic network connectivity mapping. (Related to Figure 5) (A) The correlation maps of the designated ICA component demonstrate venule voxels with highest correlation at multiple slices from one representative human subject. (B) The time series of the designated ICA component displaying the slow oscillation temporal feature. (C) The power spectrum density (PSD) of the designated ICA component. (D) The 3D views of the reconstructed vascular dynamic network connectivity maps highlight the correlated cerebral vasculature at different angles ($z > 1.5$).

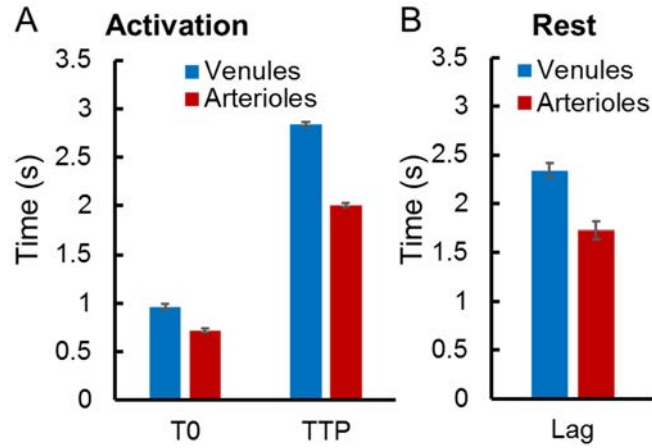


Figure S16. (Related to Figure 4) The transit time during activation and resting state A. The onset time (T0), time to peak (TTP) of BOLD from venules and CBV from arterioles during activation. (Data from the previous work (Yu et al., 2016)) **B.** The lag time of cross-correlation between the calcium signal and vessel-specific fMRI.

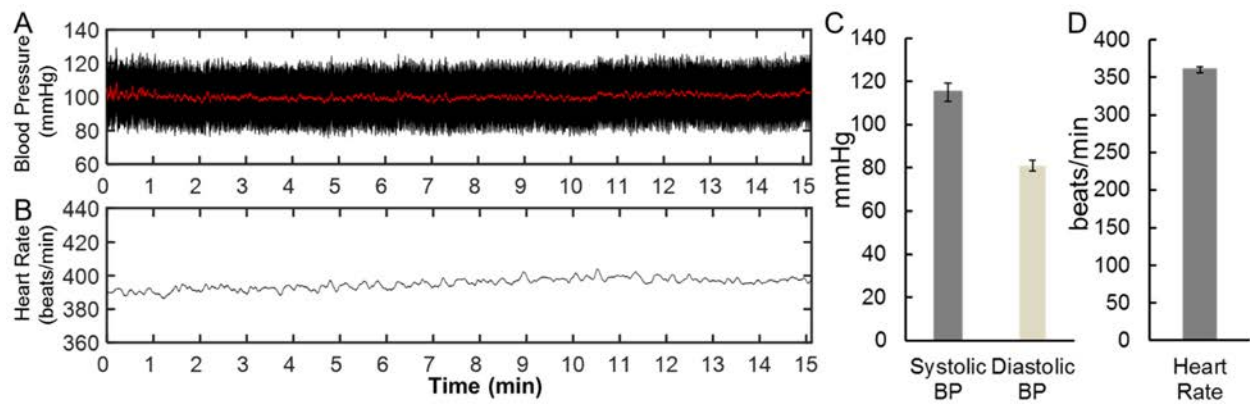


Figure S17. (Related to Method section) The blood pressure and heart beat under α -chloralose anesthesia. A-B. The blood pressure (BP) and heart rate from one representative rat **C.** The systolic BP (115.1 ± 4.2 mmHg) and the diastolic BP (81.1 ± 2.4 mmHg) from 6 rats **D.** The heart rate (360.3 ± 6.6 beats/min) from 6 rats (n = 6 rats, mean \pm s.e.m.)

Supplementary Tables

	Activation		Resting State
	T0 (s)	TTP (s)	(s)
Arterioles	0.719 ± 0.021	2.216 ± 0.048	1.727 ± 0.086
Venules	0.963 ± 0.029	2.868 ± 0.049	2.339 ± 0.073
The transit time	0.244	0.652	0.612

Table S1. (Related to Figure 4) The transit time during activation and resting state. (Activation: Arterioles, n = 61 from 5 rats, Venules, n = 69 from 5 rats; Resting State: Arterioles, n = 136 from 4 rats, Venules, n = 297 from 7 rats)

Anesthesia Type	α -chloralose anesthesia	isoflurane anesthesia
Figures	Figure 1-4, Figure S1-2, Figure S4-S8, Figure S10-11	Figure S3, Figure S9

Table S2. (Related to Figure 1-6) The anesthetic regimen in the results

Supplementary Movie Legends

Movie S1: The seed-based bSSFP BOLD rs-fMRI in the anesthetized rat brain. (Related to Figure 2)

The white arrow indicates the location of the seed (radius: 150 μm). When the seed is moved to dark dots (venule voxels), most venule voxels are highly correlated but less so for arteriole voxels.

Movie S2: The seed-based bSSFP CBV rs-fMRI in the anesthetized rat brain. (Related to Figure 2)

The white arrow indicates the position of the seed (radius: 150 μm). When the seed is moved to bright dots (arteriole voxels), most arteriole voxels are highly correlated but less so for venule voxels.

Movie S3: The evoked BOLD fMRI signal with voxel-wise time courses in the human brain. (Related to Figure 5)

With the visual stimulation (8 Hz checkerboard stimulation), the voxel-wise BOLD fMRI signal changes (left panel) are shown from 5 x 5 voxel matrix covering one individual vein through sulcus (the dark voxel in the green square, middle panel). The red cursor in the time course is corresponding to the color-coded BOLD functional movie time (right panel).

Movie S4: The seed-based rs-fMRI in the human brain. (Related to Figure 5)

The white arrow indicates the location of the seed (radius: 1 mm). The seed-based correlation maps by the resting-state fMRI demonstrates vein-dominated correlation spatial patterns.

Movie S5: Vascular dynamic network connectivity using ICA Analysis in human at resting state. (Related to Figure 5)

The left panel exhibits the ICA-based correlation maps with the averaged EPI images as the background (dark voxels as veins). The video demonstrates the highly correlated venous voxels at multiple slices, showing a 3D vascular dynamic correlation structure (Z-scores > 1.5) through the main branches of the cerebral vasculature.

ARTICLE

<https://doi.org/10.1038/s41467-019-12850-x>

OPEN

Mapping optogenetically-driven single-vessel fMRI with concurrent neuronal calcium recordings in the rat hippocampus

Xuming Chen^{1,2,3}, Filip Sobczak^{1,4}, Yi Chen^{1,4}, Yuanyuan Jiang^{1,5}, Chunqi Qian⁶, Zuneng Lu³, Cenk Ayata^{7,8}, Nikos K. Logothetis^{9,10} & Xin Yu ^{1,5*}

Extensive *in vivo* imaging studies investigate the hippocampal neural network function, mainly focusing on the dorsal CA1 region given its optical accessibility. Multi-modality fMRI with simultaneous hippocampal electrophysiological recording reveal broad cortical correlation patterns, but the detailed spatial hippocampal functional map remains lacking given the limited fMRI resolution. In particular, hemodynamic responses linked to specific neural activity are unclear at the single-vessel level across hippocampal vasculature, which hinders the deciphering of the hippocampal malfunction in animal models and the translation to critical neurovascular coupling (NVC) patterns for human fMRI. We simultaneously acquired optogenetically-driven neuronal Ca²⁺ signals with single-vessel blood-oxygen-level-dependent (BOLD) and cerebral-blood-volume (CBV)-fMRI from individual venules and arterioles. Distinct spatiotemporal patterns of hippocampal hemodynamic responses were correlated to optogenetically evoked and spreading depression-like calcium events. The calcium event-related single-vessel hemodynamic modeling revealed significantly reduced NVC efficiency upon spreading depression-like (SDL) events, providing a direct measure of the NVC function at various hippocampal states.

¹ Research Group of Translational Neuroimaging and Neural Control, High-Field Magnetic Resonance, Max Planck Institute for Biological Cybernetics, 72076 Tuebingen, Germany. ² University of Tuebingen, 72074 Tuebingen, Germany. ³ Department of Neurology, Wuhan University, Renmin Hospital, Wuhan 430060, China. ⁴ Graduate Training Centre of Neuroscience, International Max Planck Research School, University of Tuebingen, 72074 Tuebingen, Germany. ⁵ Athinoula A. Martinos Center for Biomedical Imaging, Massachusetts General Hospital and Harvard Medical School, Charlestown 02129 MA, USA. ⁶ Department of Radiology, Michigan State University, East Lansing 48824 MI, USA. ⁷ Neurovascular Research Laboratory, Department of Radiology, Massachusetts General Hospital, Harvard Medical School, Charlestown 02129 MA, USA. ⁸ Stroke Service and Neuroscience Intensive Care Unit, Department of Neurology, Massachusetts General Hospital, Harvard Medical School, 02129 Boston, USA. ⁹ Department of Physiology of Cognitive Processes, Max Planck Institute for Biological Cybernetics, Tuebingen 72076, Germany. ¹⁰ Department of Imaging Science and Biomedical Engineering, University of Manchester, Manchester M13 9PT, UK. *email: xyu9@mgh.harvard.edu

Over the past few decades the combination of behavioral and psychophysical studies with anatomical, pharmacological, and functional magnetic resonance imaging (fMRI), permitting whole-brain mapping of brain networks, has expanded our understanding of brain function and occasionally dysfunction. The blood oxygen level-dependent (BOLD) fMRI^{1–4}, in particular, is now used as a standard tool for demarcating brain states, and potentially, dynamic transitions from one state to another^{5–9}. Nonetheless, fathoming into the true and eventually detailed neural mechanisms underlying the BOLD positive and negative responses, more so at the level of cortical microcircuits and deep brain nuclei, is currently still extremely difficult if not impossible. Conventional fMRI yields surrogate signals such as continuous blood flow, volume, and oxygenation changes^{1–4,10,11}. These indirect functional mapping schemes cannot differentiate between function-specific processing and neuromodulation, between bottom-up and top-down signals, occasionally confusing even excitation and inhibition, depending on the circuit-dependent direct or indirect nature of local neural activity^{5,12–15}. The origin of such problems is not only due to the weak spatial specificity of the fMRI signal to its neural source but also to the very fact that the exact relationship between the metabolic/hemodynamic responses and the underlying neural activity patterns remains mostly elusive. Using high-resolution fMRI methods to map the animal brain, BOLD and cerebral blood volume (CBV) fMRI signals can be detected from individual venule and arteriole voxels from deep cortical layers^{16–18}. Beyond the *in vivo* penetrating depth of conventional optical imaging, single-vessel fMRI methods have enabled direct measurement of vessel-specific hemodynamic responses with fMRI in a large spatial scale to interpret better the neurovascular coupling (NVC) contribution to the fMRI signal acquired in deep brain regions.

Simultaneous fMRI and electrophysiological recordings offered the first insights into the NVC underlying the cortical fMRI signal in both task-related and resting-state conditions^{19,20}. Lately, genetically encoded Ca²⁺ indicators, for example, GCaMP, mediating Ca²⁺ imaging from neurons or astrocytes have also been combined with optical hemodynamic imaging or fMRI, demonstrating various NVC patterns across multiple scales at different cortical states^{21–28}. Besides the multi-modal correlation analysis of cortical dynamic signals, the highly varied global correlation of the fMRI signal to the concurrent hippocampal ripple activity has also demonstrated region-specific cortical NVC patterns²⁹. In contrast to extensive cortical NVC studies to interpret the fMRI signal acquired in the cortex, the linkage between subcortical NVC events to the fMRI signal, for example, in the hippocampus, has not been well elucidated. Not only has the 3D location of the hippocampus in the brain restricted its accessibility to conventional optical imaging methods but also the mesoscale hippocampal vasculature has been seldom specified for hemodynamic mapping with fMRI. Previous *in vivo* hippocampal functional imaging studies applied micro-lens/micro-prism through the cortical tissue or removed the cortex above the hippocampus^{30–33}. The optical fiber has been used to target the hippocampus for the measurement of Ca²⁺ from individual cell types or for fast dynamic recordings^{34–38}. Using long-wavelength light pulses for deeper tissue penetration, three-photon microscopy has further expanded the optical penetration depth for NVC imaging of dorsal hippocampal CA1 regions in mice with a much less invasive surgical procedure in the mouse brain^{39–41}. Nevertheless, it remains challenging to detect subcortical NVC events in animals with larger brains, such as rats and non-human primates, using multi-photon microscopic imaging methods. Although rodent hippocampal vasculature has been well described in histological studies by Coyle^{42,43} in the mid 1970s, no multi-modality neuroimaging studies have been performed to

decipher the detailed vessel-specific hemodynamic responses throughout the hippocampal vasculature with fMRI and concurrent neuronal activity measurement in the hippocampus.

Here, we developed a multi-modal fMRI platform, aiming to specify the properties of NVC across the rat hippocampus. The experiments were performed in a high magnetic field scanner (14.1 T), with customized radiofrequency (RF) coils, and the balanced steady-state free precession (bSSFP) method that permits the acquisition of the fMRI signal from individual cortical penetrating arterioles and venules²², thereby expanding the line-scanning-based method for real-time single-vessel fMRI mapping^{18,44,45}. This high spatial resolution vessel-specific fMRI mapping method allowed to directly measure mesoscale hemodynamic responses of the hippocampal vasculature. In particular, we applied the single-vessel fMRI to map the BOLD and CBV-weighted fMRI signal from interleaved arterioles and venules in the rat hippocampus, of which detailed vascular hemodynamic responses were imaged with a high spatiotemporal resolution. This has not been accomplished by other existing non-invasive global functional neuroimaging methods. This work provides direct evidence to show the deep brain large-scale hemodynamic vascular mapping with single-vessel fMRI beyond the penetration depth of conventional optical imaging methods. Using implanted optical fibers, optogenetically evoked neuronal Ca²⁺ and the spreading depression-like Ca²⁺ (SDL-Ca²⁺) events were detected with simultaneous single-vessel BOLD fMRI, demonstrating distinct spatiotemporal features of vascular hemodynamic responses. The varying NVC efficiency (NVCe) can be estimated by directly modeling single-vessel fMRI responses to concurrent Ca²⁺ events across the hippocampal vasculature. The simultaneous single-vessel hippocampal fMRI and Ca²⁺ recording not only provides a multi-modal platform for specifying the multi-scale NVC in the hippocampus but also sheds light on future pathological hippocampal NVC studies in disease animal models with stroke, epilepsy, and Alzheimer's disease.

Results

Multi-modal hippocampal fMRI and local field potential. To study the hippocampal NVC with the multi-modal fMRI platform (Fig. 1a), we co-expressed channelrhodopsin-2 (ChR2) and the genetically encoded Ca²⁺ sensor, GCaMP6f, in the rat hippocampus using adeno-associated viral (AAV) vectors (AAV5.Syn.GCaMP6f.WPRE.SV40; AAV5.CAG.hChR2-mCherry.WPRE.SV40). Figure 1b shows neurons labeled with either ChR2-mCherry or GCaMP6f in both barrel cortex (BC) and hippocampus for optogenetic fMRI with concurrent Ca²⁺ signal recording. First, optogenetically evoked local field potential (LFP) and GCaMP-mediated Ca²⁺ signals were simultaneously detected in the hippocampus of rats at varied light pulse widths, power levels, and frequencies (Fig. 1c, d, Supplementary Fig. 1). It is noteworthy that the optical light pulse introduced large artifacts for the GCaMP-mediated Ca²⁺ fluorescent signal detection. Given the specific temporal feature of optogenetically evoked Ca²⁺ transients, artifacts detected by the fast-sampling silicon photomultiplier (SiPM) can be distinguished easily from Ca²⁺ transients given its short light pulse duration. Figure 1d, e show the peak fluorescent Ca²⁺ signal at ~50–60 ms after the onset of the optogenetic light pulses with various widths from 1 to 20 ms, which is consistent with previous observations in the cortex²¹. This result demonstrates the feasibility of hippocampal optical fiber Ca²⁺ recordings with optogenetic stimulation.

Next, we aimed to verify the multi-modal fMRI platform in combination with both optogenetic stimulation and simultaneous Ca²⁺ recordings. Figure 1f demonstrates the optogenetically activated BOLD fMRI signals at the BC and the hippocampus

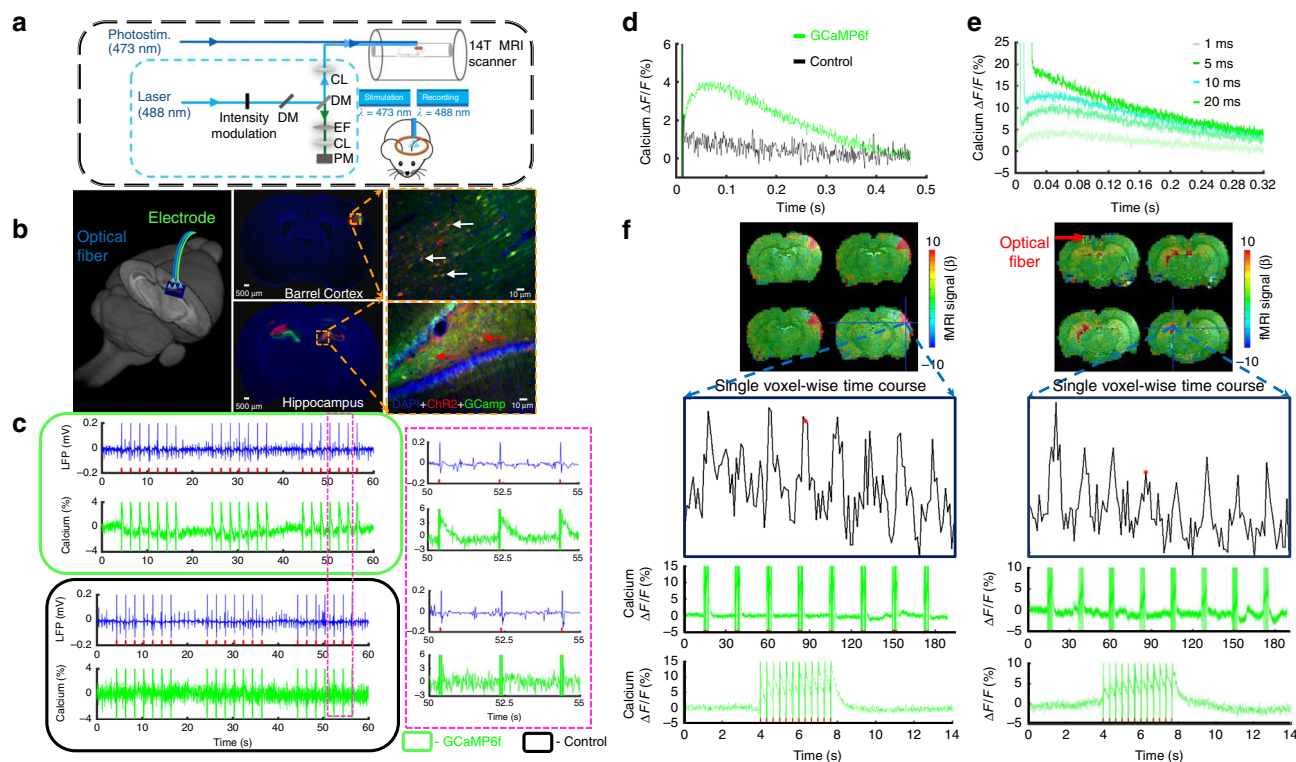


Fig. 1 Optogenetically evoked Ca^{2+} recording with LFP or fMRI. **a** Schematic drawing for the light path of optogenetic activation and calcium recordings in the multi-modal fMRI platform (PM, photomultiplier; EF, emission filter; DM, dichroic mirror; CL, coupling lens). **b** Schematic drawing of optical fibers implantation to target the rat hippocampus in a 3D view (left). Channelrhodopsin (Chr2, red) and GcaMP6f (green) were co-expressed in the barrel cortex (BC, upper, white arrows) and hippocampus (lower, red arrows) with enlarged images (dashed box, right). **c** Simultaneous LFP (blue) and neuronal Ca^{2+} (green) traces in the hippocampus following optical stimulation (10 ms light pulse, 1 Hz, 7 s, 4 mW; upper: GCaMP6f expression; lower: control; right panel, enlarged view). **d** Averaged traces of optogenetically evoked Ca^{2+} spikes in the hippocampus (green: GCaMP6f expression; black: control). **e** Averaged traces of optogenetically evoked Ca^{2+} spikes with different widths of the light pulse (1, 5, 10, and 20 ms). **f** A representative color-coded BOLD fMRI map from the BC (left) and hippocampus (optical fiber insertion trace: red arrow), together with associated fMRI time courses (lower, top) and concurrent neuronal Ca^{2+} signals (lower, middle) in the block-design paradigm (illumination: 10 ms light pulse, 3 Hz, 4 s, 5 mW, zoomed views are averaged evoked Ca^{2+} signals from one epoch)

with the 3D echo planar imaging fMRI (EPI-fMRI) method^{46,47}. Both evoked BOLD fMRI signals from activated brain voxels and concurrent Ca^{2+} transients from nearby neurons can be detected using the block-design optogenetic stimulation paradigm. These multi-modal NVC events were acquired across spatial scales from the sub-millimeter scale neuronal ensembles surrounding the fiber tip to the macroscopic vascular hemodynamic response detected by fMRI. It is important to note that direct light pulse exposure on the naive rat hippocampus did not cause detectable positive BOLD fMRI signal through hippocampal vasculature due to the local blood flow regulation, that is, cerebral blood flow changes, as previously reported by ultrasound Doppler signal measurement⁴⁸. The high power light pulse (>25 mW from 200 μm fiber tip) caused the focal negative fMRI signal near the fiber tip due to heating-induced susceptibility changes (frequency offset) (Supplementary Fig. 2)⁴⁹. In contrast, the optogenetic stimulation of rats with Chr2 expression in the hippocampus evoked the strongest signals at the choroid plexus located at the dorsal wall of the lateral ventricle across multiple slices, containing draining veins from the hippocampus in a sub-centimeter scale away from the optical fiber tip (Fig. 1f). Although these results indicate that the direct effect of light exposure on the flow regulation contributes less to the measurable BOLD signal, the widely spread hemodynamic responses in hippocampal vasculature upon optogenetic stimulation remain poorly characterized with EPI-fMRI given the limited spatial resolution. These results also led to implementing the high-resolution single-

vessel fMRI method into the multi-modal fMRI platform for hippocampal NVC mapping.

Optogenetic hippocampal fMRI with Chr2 variant (C1V1). It should be noted that in order to reduce the spectral wavelength overlap of GCaMP-based fluorescent signal excitation and optogenetic light pulse stimulation at 473 nm, we additionally applied the Chr2 variant (C1V1) to switch the optogenetic light pulse to 590 nm. Supplementary Figure 3 demonstrates similar dynamic patterns of the concurrent LFP or fMRI signal and fiber optic Ca^{2+} signal upon C1V1-mediated optogenetic activation in the rat hippocampus. These results further verify the feasibility of detecting optogenetically driven BOLD and intracellular neuronal Ca^{2+} signals in the hippocampus with the multi-modal fMRI platform.

Optogenetic single-vessel hippocampal BOLD and CBV fMRI. As shown with the magnetic resonance angiography (MRA) imaging in Fig. 2a, the hippocampal vasculature is aligned in parallel branches supplying blood to the saddle-shaped structure of the hippocampus⁵⁰ (Fig. 2a, Supplementary Movie 1). To visualize individual vessels, we applied a 2D multiple gradient echo (MGE) slice transecting the parallel hippocampal vascular branches with 40° angle to the midline (Fig. 2a). Similar to previous single-vessel MRI studies in the cortex^{18,22}, the 2D MGE images were acquired at different time of echo (TE) to distinguish

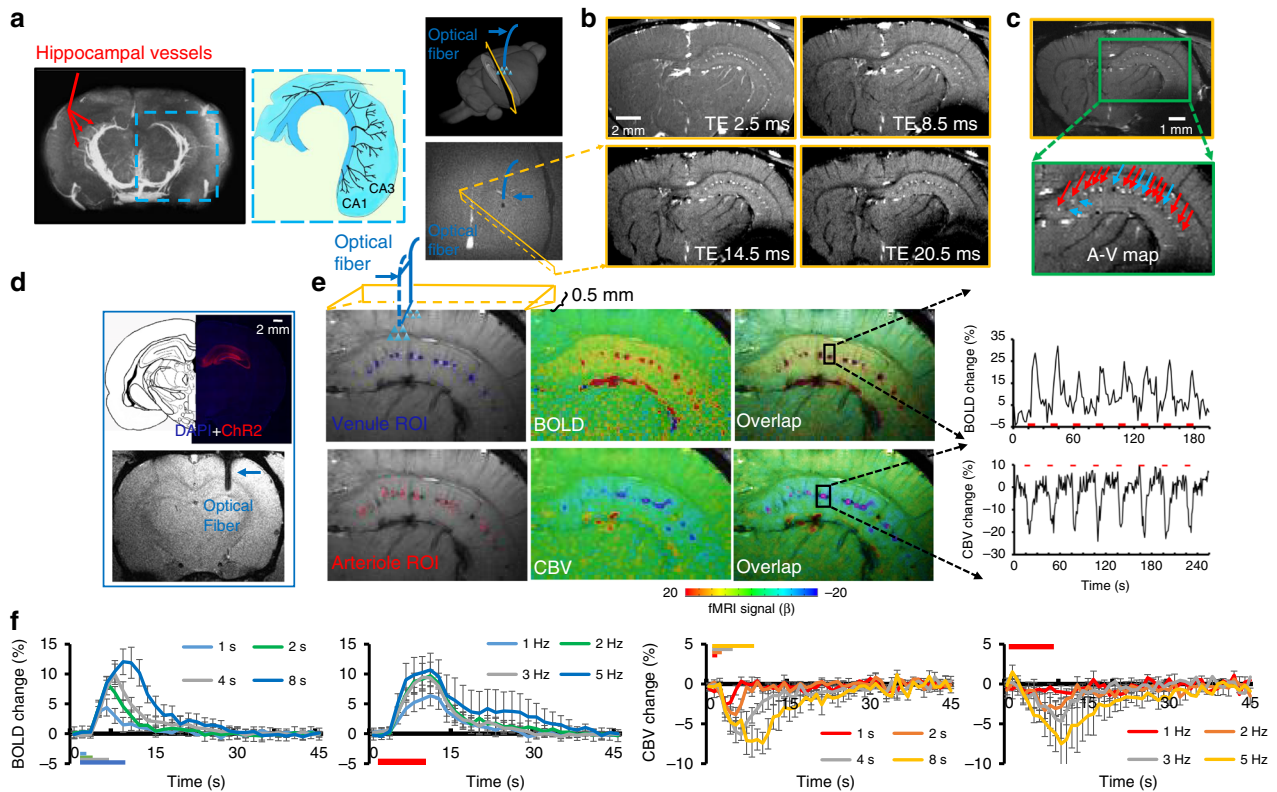


Fig. 2 Single-vessel hippocampal BOLD and CBV-weighted fMRI. **a** The magnetic resonance angiography (MRA) image shows major vascular branches penetrating the rat hippocampus (middle image is the schematic drawing of the hippocampal transverse plane of vessels aligned in parallel [modified from Peter Coyle (1976)]). The 3D view of the 2D slice alignment to cover the transverse hippocampal structure (lower image is the horizontal view to show the 2D slice with 40° to the midline to cross the penetrating vessels, dark hole: the fiber optic tip). **b** Representative images of 2D MGE slices from the hippocampus at different TEs. **c** A-V map derived from images in **b**. Arterioles and venules appear as bright and dark dots, respectively [zoomed view of hippocampal arterioles (bright dots, red arrows) and venules (dark dots, blue arrows)]. **d** A histological section shows Chr2 expressed in the hippocampus (upper). The T2*-weighted (T2*-W) image shows the optical fiber inserted into the hippocampus (lower, blue arrow). **e** Venule (blue)/arteriole (red) ROIs on A-V maps (left). Evoked BOLD (upper) and CBV-weighted (lower) fMRI maps on the same 2D slice (center) and overlap (active voxels are in purple in overlap images). Time courses of the evoked BOLD and CBV-weighted fMRI with the block-design paradigm from a representative venule (upper) and arteriole (lower) ROI (illumination: 10 ms light pulse, 3 Hz, 4 s, 5 mW). **f** Averaged BOLD (upper) and CBV-weighted (lower) fMRI responses from different stimulation durations (1, 2, 4, and 8 s) and frequencies (1, 2, 3, and 5 Hz) ($n = 4$, mean \pm SEM)

individual arteriole and venule voxels from the surrounding parenchyma voxels enriched with capillaries. At shorter TE, due to in-flow effects from vessels at the short time of repetition (TR), all vessel voxels appear brighter than the surrounding voxels based on the T1-weighted MR contrast; however, at the longer TE, the fast T2* decay of the deoxygenated blood leads to darker signal intensity in venule voxels only (Fig. 2b, Supplementary Movie 2)¹⁸. Thus, by integrating the MGE images acquired at different TEs, we could distinguish individual hippocampal arterioles (bright dots) and venules (dark dots) from the anatomical single-vessel 2D map (arteriole–venule (A–V) map), showing the interleaved arterioles and venules in the hippocampus (Fig. 2c).

One essential improvement of this work is to apply the single-vessel bSSFP-fMRI to detect the optogenetically evoked fMRI signal in the rat hippocampus, demonstrating the deep brain single-vessel hemodynamic mapping with fMRI beyond the penetration depth of conventional optical imaging methods. Following the BOLD fMRI experiment, the CBV-weighted single-vessel fMRI was performed after the intravenous MION (iron oxide particle) injection. Figure 2d shows the optical fiber targeting the hippocampal CA1 region expressing ChR2. Upon optogenetic activation, peak BOLD signals were primarily overlapping with venule voxels, showing positive BOLD signals from individual venules. Peak CBV-weighted signals were located

at arteriole voxels, showing negative CBV-weighted signals from individual arterioles in the hippocampus (Fig. 2e, Supplementary Movie 3). Besides the CBV-weighted single-vessel fMRI maps, we also calculated the CBV percentage change (%) map based on BOLD fMRI time courses acquired before the injection of MION particles⁵¹, showing positive %CBV changes from individual arterioles (Supplementary Fig. 4). Figure 2f shows vessel-specific mean hemodynamic BOLD and CBV-weighted responses upon the optogenetic stimulation at varying durations and frequencies of light pulses, demonstrating highly robust optogenetically driven single-vessel fMRI signals in the hippocampus. It is also noteworthy that the strong BOLD signal from the draining veins through the lateral ventricle can be distinguished from the hippocampal vasculature, showing a spatially more refined hemodynamic mapping than the EPI-fMRI mapping in Fig. 1f.

Optogenetic single-vessel fMRI with concurrent Ca²⁺ recording. We performed a simultaneous bSSFP-based single-vessel optogenetic fMRI and optical fiber Ca²⁺ recording. Both optical fibers were inserted to target the CA1 region, and the 2D bSSFP slice was chosen to be 500 μ m away from the optical fiber along the caudal–ventral axis (Fig. 3a), which avoided the potential focal vascular blood flow regulation by direct light exposure⁴⁸. Upon optogenetic activation, both BOLD and CBV-weighted

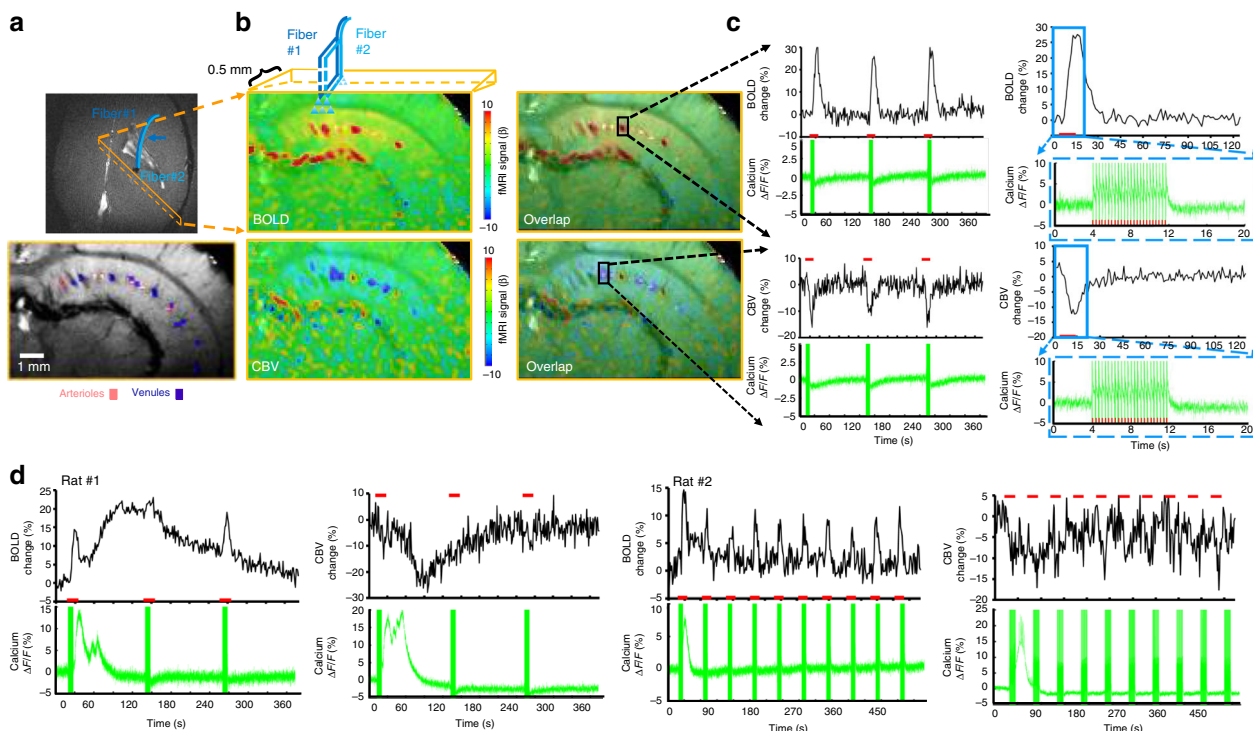


Fig. 3 Concurrent fMRI and Ca^{2+} recording in the hippocampus. **a** Schematic drawing of the hippocampal single-vessel fMRI with two optical fibers (blue arrow) for optogenetic stimulation and Ca^{2+} recordings. A representative A-V map shows individual arterioles (bright dots, red markers) and venules (dark dots, purple markers) on the same 2D slice. **b** Evoked BOLD (upper) and CBV-weighted (lower) fMRI maps and overlapping maps on the A-V map. **c** Time courses of evoked BOLD and CBV-weighted fMRI signal from a single venule (upper) or arteriole (lower) ROI with the concurrent neuronal Ca^{2+} signal (illumination: 10 ms light pulse, 3 Hz, 8 s, 5 mW). Averaged time course of the fMRI signal and the evoked Ca^{2+} spike train. **d** A representative time course of single-vessel BOLD and CBV-weighted fMRI signal changes with concurrent hippocampus SDL- Ca^{2+} responses (illumination: 10 ms light pulse, 3 Hz, 8 s, 5 mW)

fMRI signals were detected from individual hippocampal venules and arterioles with concurrent Ca^{2+} transients following each light pulse (Fig. 3a–c), showing highly correlated NVC events in the hippocampus. Similar to the previous experiment, averaged time courses of evoked BOLD and CBV-weighted signals showed robust responses with altered amplitudes and durations from individual venules and arterioles at varying durations (1, 2, 4, and 8 s) and light pulse frequencies (1, 2, 3, and 5 Hz), which were detected simultaneously with evoked neuronal Ca^{2+} transients in the hippocampus (Supplementary Fig. 5). These results demonstrate the feasibility of multi-modal imaging of NVC events in the hippocampus, linking the evoked Ca^{2+} transients from CA1 neuronal ensembles to the widely spread vessel-specific hemodynamic responses in the sub-centimeter scale hippocampal vasculature.

In contrast to the trains of Ca^{2+} transients evoked by low-frequency light pulses, the evoked Ca^{2+} signal did not return to baseline between light pulses at a higher frequency, showing an accumulative Ca^{2+} plateau response corresponding to the high-amplitude fMRI signal detected in hippocampal vessels (Fig. 3c, Supplementary Fig. 5). Interestingly, we also observed a large-scale hippocampal Ca^{2+} transient, that is, the SDL- Ca^{2+} transient, at inter-stimulus intervals following optogenetic stimulation with 3 or 5 Hz light pulses at 8 s stimulation-on duration (Fig. 3d). The SDL- Ca^{2+} transients coincided with the spreading positive BOLD and negative CBV-weighted signals during inter-stimulus intervals in the hippocampus (Fig. 3d).

As previously reported^{52,53}, the high-frequency optogenetic activation (>10 Hz) in the hippocampus leads to seizure-like events in animals. The simultaneous LFP and fiber optic Ca^{2+} recordings also detected epileptic events as a train of strong LFP

deflections and concurrent Ca^{2+} transients. These epileptic events were often accompanied by a large amplitude SDL- Ca^{2+} event in the hippocampus (Fig. 4a), which was previously reported in the cortex of both animal and human brains^{54,55}, but not with concurrent fMRI. Interestingly, the epileptic Ca^{2+} transients could be elicited concurrently with SDL- Ca^{2+} during inter-stimulus intervals even with 3 and 5 Hz light pulse stimulation, followed by the spreading positive BOLD signal from individual vessels in the hippocampus (Fig. 4b). Occasionally, after spontaneous high-amplitude Ca^{2+} events, evoked single-vessel BOLD signals were diminished in the following 5–6 min and then gradually recovered with reduced amplitude, indicating the conventional depression pattern (Fig. 4b, trial #3). We have systematically analyzed occurrence rates of the SDL and SDL with seizure (SDL + seizure) events across multiple trials recorded from rats, showing that the occurrence rate is dependent on the optogenetic light pulse frequency and stimulation duration (Fig. 4c). When the light pulse stimulation duration is longer than 8 s, the occurrence rate of the SDL events ($36.2 \pm 5.5\%$) was significantly higher than that ($12.5 \pm 3.8\%$, $p = 0.001$) of the 4 s stimulation-on duration (Fig. 4c). These results demonstrate that the multi-modal fMRI platform can detect both optogenetically evoked and spontaneous SDL- Ca^{2+} transients with specifically coupled fMRI signals, presenting a unique scheme to investigate the NVCE to varied hippocampal activities.

Vessel-specific NVCE at different forms of Ca^{2+} spikes. Different from the random incidence of epileptic events (Fig. 4c, ≤ 4 s, $2 \pm 1.1\%$, ≥ 8 s, $3.5 \pm 1.2\%$), SDL- Ca^{2+} events were often detected after the first epoch of 8 s optogenetic stimulation across multiple trials of several animals ($\geq 50\%$ induction rate, Fig. 4c,

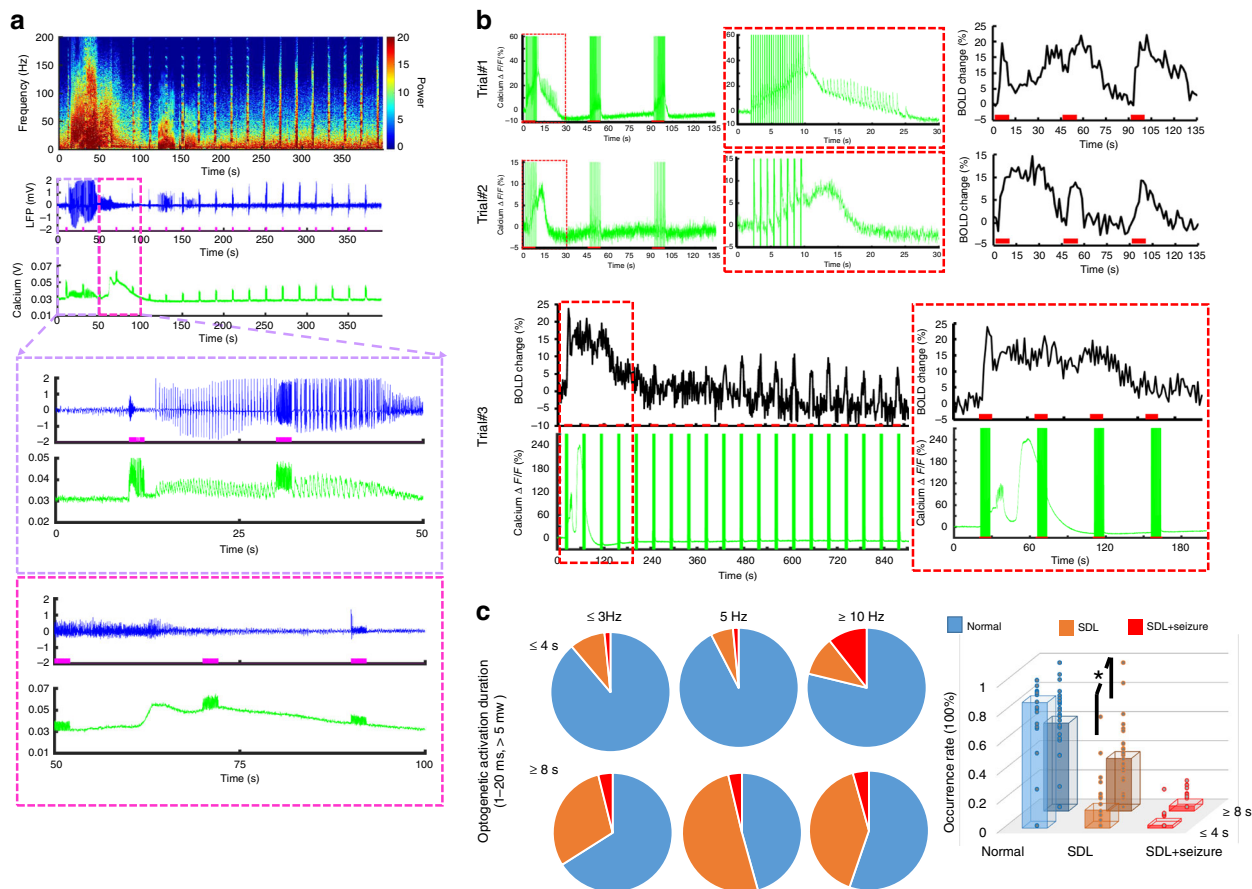


Fig. 4 SDL and seizure-based Ca^{2+} recordings with LFP or fMRI. **a** Representative traces of SD and seizure spikes in the hippocampus: power spectra of LFP (top), LFP trace (middle), and Ca^{2+} signal (bottom). Zoomed views of the area are outlined in the upper panel (purple/pink box) (illumination: 10 ms light pulse, 50 Hz, 2 s, 5.5 mW). **b** Representative trials (3 rats) of neuronal Ca^{2+} signal (green) with simultaneous single-vessel BOLD fMRI signal (black) (upper: 10 ms light pulse, 1 Hz, SDL and 3 Hz, SDL + seizure Ca^{2+} events, 8 s, 6 mW; lower: 20 ms light pulse, 5 Hz, 8 s, 5.5 mW). Zoomed views of the area are outlined in the red box. **c** Quantification of the occurrence percentage of normal, SDL and SDL + seizure Ca^{2+} events as a function of optogenetic light pulse frequency (≤ 3 Hz, 5 Hz, ≥ 10 Hz) and stimulation duration (≤ 4 s, 382 trials, ≥ 8 Hz, 448 trials, $n = 28$ rats). Induction rate of SDL- Ca^{2+} events in trials with 8 s stimulation duration is significantly higher than that of trials with 4 s stimulation ($*p = 0.001$, $n = 28$ rats, mean \pm SEM)

8 s, 5 Hz, and ≥ 10 Hz conditions). It enabled to statistically compare the spatiotemporal hemodynamic response pattern and the NVCe between the SDL and the optogenetically evoked Ca^{2+} transients in the hippocampal vasculature. The bSSFP-fMRI method was used to characterize the distinct spatiotemporal hemodynamic patterns of the single-vessel fMRI signal coupled to either optogenetically evoked or SDL- Ca^{2+} events in the hippocampus. The single-vessel hippocampal A-V map can be used to specify the relative position of individual vessels with respect to the optical fiber tip (Fig. 5a). First, BOLD fMRI signals from individual venules were extracted to show the temporal dynamics corresponding to different Ca^{2+} events. In contrast to the evoked BOLD signals that co-occurred instantaneously across different hippocampal penetrating venules upon the optogenetic stimulation, the SDL- Ca^{2+} -coupled BOLD signals presented a propagation delay from individual venules as a function of distance to the optical fiber. Figure 5b shows the early onset and time to peak (TTP) from the venule closest to the optical fiber (V_0), and the delayed onset time and TTP from hippocampal venules aligned further away from the optical fiber ($V_{-1,-2}$, $V_{1,2}$). BOLD signal propagation velocity was estimated by measuring TTP or the half-peak onset time ($t_{1/2}$) across different hippocampal venules ($v_{\text{TTP}} = 4.58 \pm 0.47$ mm/min; $v_{t_{1/2}} = 5.94 \pm 1.31$ mm/min) (Fig. 5c), which fell into the top-end SD propagation speed range (1–6 mm/s) detected in the cortex^{54–56}. In addition, time-lapsed

fMRI maps show slowly spreading BOLD signals from individual venules through the sub-centimeter scale hippocampal vasculature corresponding to SDL- Ca^{2+} events, which are different from the optogenetic activation pattern specific to evoked Ca^{2+} events (Fig. 5d, Supplementary Movie 4). Also noteworthy is the fact that although peak BOLD amplitudes were similar between the two different forms of Ca^{2+} events, the evoked Ca^{2+} transient amplitude was significantly lower than that of the SDL- Ca^{2+} event across different trials from the same animal and among different animals (Fig. 5e). These results suggested that varied NVc events are coupled to the optogenetically evoked and SDL- Ca^{2+} signal, and can be directly measured with the multi-modal single-vessel fMRI method in the hippocampus from the same experimental trials.

Concurrent single-vessel fMRI and Ca^{2+} signals can be used to estimate the efficiency of the vessel-specific NVc according to the different forms of neuronal activity. In contrast to the conventional general linear model (GLM) that fits the fMRI signal with the ideal time course, describing the hemodynamic function derived from the stimulation paradigm, we analyzed the concurrent Ca^{2+} signal amplitude and applied an amplitude modulated (AM) response model to calculate β -coefficients, as estimates of the NVc to the optogenetically evoked and SDL- Ca^{2+} events (Supplementary Fig. 6, see Methods section for details)²¹. Figure 5f demonstrates NVc β maps of the two forms

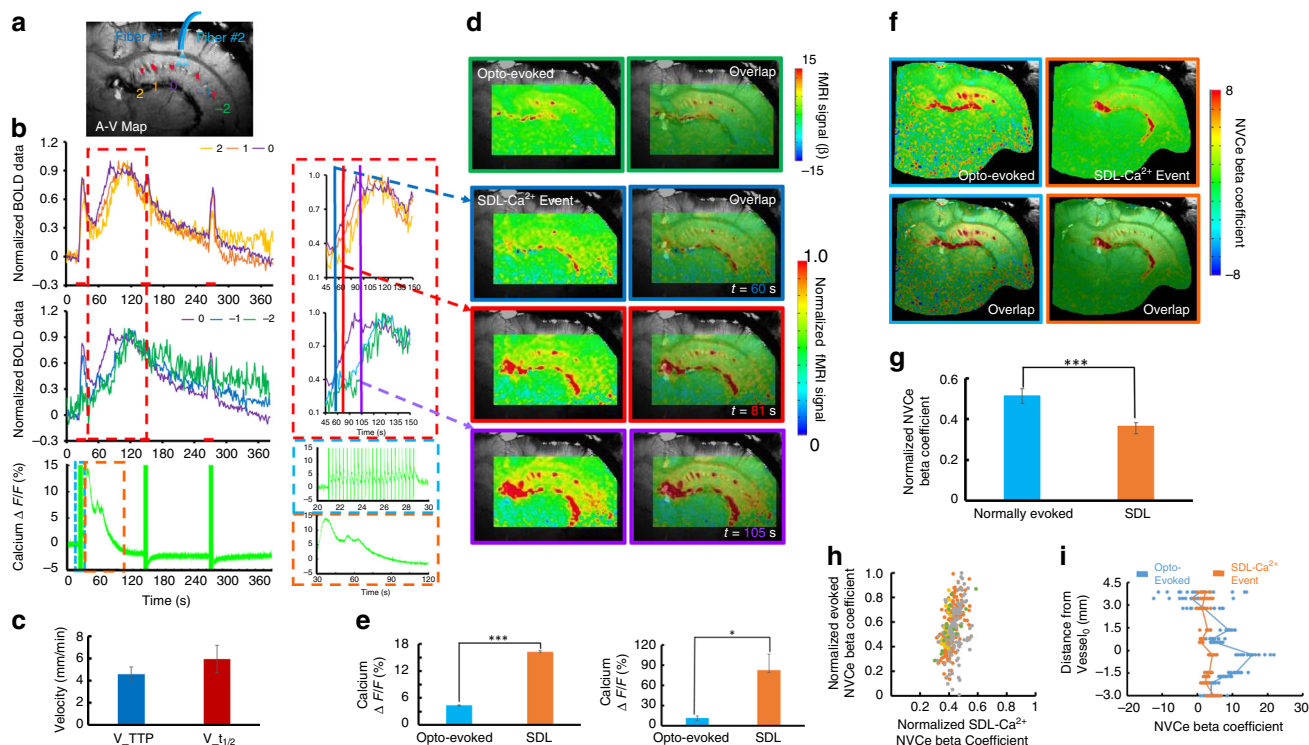


Fig. 5 Ca^{2+} -based NVCe mapping. **a** Numbered venules on the A–V map. Venule 0 (purple) is the one closest to the optical fiber tip, venules 1, 2 and –2 are vessels with different directions in the hippocampal structure. **b** Time courses of normalized single-vessel BOLD fMRI signal from individual venules, as shown in Fig. 4a, are plotted (top) with the concurrent neuronal Ca^{2+} signal (bottom). Insets are the magnified figures of the dashed box in the left to highlight the SDL- Ca^{2+} events and coupled single-vessel BOLD responses (illumination: 10 ms light pulse, 3 Hz, 8 s, 5 mW). **c** Velocity of SDL- Ca^{2+} events spreading between different hippocampal venules with different time to peak (TTP) and $t_{1/2}$ (18 vessels from 3 rats, mean \pm SEM). **d** Representative color-coded BOLD fMRI map (optogenetically evoked) from the hippocampus (upper). Time-lapsed function maps and semi-transparent overlapping images on the A–V map at 60 s (blue box), 81 s (red box), and 105 s (purple box) during the trial. **e** Amplitude of optogenetically evoked Ca^{2+} signals is significantly lower than that of SDL- Ca^{2+} spikes in the hippocampus (left: $*p = 6.22e - 11$, 10 trials from a representative rat; right: $*p = 0.028$, $n = 4$ rats). **f** NVCe coefficient map for both optogenetically evoked and SDL- Ca^{2+} events. **g** Z-score normalized NVCe coefficients of optogenetically evoked events are significantly higher than those of SDL- Ca^{2+} events ($n = 4$ rats, $*p = 0.003$). **h** Scatter plot of z-score normalized NVCe coefficients from optogenetically evoked vs. SDL- Ca^{2+} events from each trial in four representative rats. **i** Z-score normalized NVCe coefficients from individual vessels were plotted as a function of vessel distance for both optogenetically evoked and SDL- Ca^{2+} events in a representative rat

of Ca^{2+} events, showing peak NVCe β values on individual hippocampal venules. Mean vessel-specific NVCe β values of optogenetically evoked Ca^{2+} events were significantly higher than those of SDL- Ca^{2+} events (Fig. 5g). To better quantify the spatial distribution of the NVCe across hippocampal vasculature, we plotted β -coefficients from individual venules as a function of the relative distance to V_0 (Fig. 5i). Despite the fact that the SDL- Ca^{2+} events were elicited in the hippocampal structure close to V_0 , the NVCe β values were found to be similar and evenly distributed across the hippocampal vasculature, whereas NVCe β values of optogenetically evoked Ca^{2+} events showed a distance-dependent distribution (Fig. 5h, i, scatter plot of NVCe β values from all hippocampal vessels through multiple trials of four animals). These results demonstrate altered NVCe linking to normal and SDL hippocampal activity detected by the multi-modal fMRI platform.

Discussion

Here, we developed a multi-modal fMRI platform to investigate detailed, spatiotemporally resolved NVC events in rat hippocampus. By implementing simultaneous optogenetic single-vessel fMRI and optical fiber Ca^{2+} recordings, distinct hemodynamic spatiotemporal patterns across the sub-centimeter hippocampal vasculature could be directly characterized based on concurrent

neuronal Ca^{2+} signals, for example, optogenetically evoked or SDL- Ca^{2+} events, for the first time. We believe that this method provides a unique multi-modal/cross-scale mapping scheme for the study of neurovascular activity in the hippocampus in both normal and pathological conditions.

Despite extensive imaging studies on hippocampal neural activity, the actual information flow from neuronal activity to the hippocampal neurovascular system, the modulation of which provides the vast majority of fMRI signals, has seldom been taken into account in investigations attempting to relate behavior to the function or dysfunction of this structure^{30,33,57}. One major barrier is our ability to access large-scale hippocampal vascular dynamics in vivo with minimally invasive procedures, preserving NVC function. Three critical features needed to be solved for existing neuroimaging methods: large field of view (FOV), high resolution to detect the vessel-specific hemodynamic signal with sufficient signal-to-noise ratio (SNR), and accessibility to deep brain nuclei. Although wide-field two-photon or the newly developed three-photon microscopy has significantly enlarged the FOV and the penetration depth for in vivo brain optical imaging with cellular resolution^{39–41,58}, it remains challenging to acquire vascular hemodynamic signaling through the sub-centimeter hippocampal structure in rats and higher mammals.

The fMRI signal directly represents vascular hemodynamic responses to indicate large-scale brain function. Our work and

other animal fMRI studies have demonstrated the optogenetically evoked hippocampal BOLD signal in the context of whole-brain functional mapping^{52,59}. By improving the spatial resolution of the fMRI image, it is possible to detect fMRI signals from individual penetrating vessels through the cortex^{17,18,60,61}. The real power of single-vessel fMRI can be further released when targeting large deep brain regions beyond the penetration depth of conventional optical methods. To achieve sufficient SNR, the bSSFP-based single-vessel fMRI method was applied with an implanted surface RF coil²². The RF coil implantation could be merged with the optical fiber targeting the hippocampus during the surgical procedure. The RF coil implanted to the skull substantially increased *B1* field sensitivity and prevented additional signal loss due to the extra space occupied for fiber fixation between the surface coil and the brain, which can be readily implemented by MRI users with 7 to 11.7 T scanners. This optimized multi-modal fMRI platform employed optogenetic single-vessel fMRI mapping to detect venule-specific BOLD and arteriole-specific CBV-weighted signals from individual vessels aligned in parallel through the hippocampal structure (Fig. 2), which have been previously described only by histological studies^{42,43}. We delivered optical fiber-mediated optogenetic stimulation using light pulses with varied frequencies and power levels to specify BOLD and CBV-weighted fMRI signals from individual hippocampal vessels (Supplementary Fig. 4), as well as evoked LFP spikes and Ca²⁺ transients (Supplementary Fig. 1), representing highly correlated NVC features in the hippocampus. Single-vessel fMRI provides a unique mapping scheme to identify large-spread hemodynamic response patterns in the hippocampal vasculature.

Optogenetic light exposure may contribute directly to hemodynamic responses in the hippocampus. As reported by Rungta et al.⁴⁸, direct light exposure can directly regulate blood flow through arteriole dilation following the reduced Ca²⁺ signal from smooth muscle cells, similar to NVC events but independent of neuroglial activity. Our work and a previous optogenetic fMRI study⁴⁹ on naive animals mainly detect the susceptibility-based non-physiological MRI signal changes sensitive to the light-induced heating effect, which can shadow the MRI signal relevant to blood flow changes as detected by ultrasound Doppler measurement. In addition, the direct heating effect through light illumination can alter the spiking activity in the animal brain⁶². To avoid the confounding effects of light exposure-induced blood flow regulation, we have aligned the single-vessel 2D slice at least 500 μm away from the optical fiber tip. Also, both two-photon and single-vessel fMRI studies have shown that the spatial scale of the hemodynamic coherence in the arteriole network is <2 mm spatial scale in the cortex^{22,58}. The spatial distribution of light exposure-induced flow regulation can be controlled using light pulses with low frequency and power, which could further reduce direct light-exposure contribution to the sub-centimeter scale hippocampal vascular hemodynamic responses and heating-induced neuronal activity modulation.

Using GCaMP6f, optogenetically evoked hippocampal neuronal Ca²⁺ transients showed similar temporal dynamics to cortical Ca²⁺ transients detected by the optical fiber in anesthetized rats upon sensory stimulation²¹. This temporal feature makes it possible to distinguish individual Ca²⁺ transients from light pulse-induced artifacts, which has been previously reported in the Opto-fMRI with Ca²⁺ dye (OGB-1) sensing-based optical fiber measurements²⁸. To reduce the spectral signal cross-talk, we applied a red-shifted ChR2 variant (C1V1) to alter the optogenetic light pulse up to 590 nm (Supplementary Fig. 3). Although the artifacts can be significantly reduced, the remaining light pulse signals detected by the photomultiplier can be caused by imperfect filtering of the dichroic filter. It is noteworthy that the

optogenetic light pulses were delivered at 1–5 mW from the 200 μm optical fiber tip, which is significantly higher than the power used for GCaMP fluorescent excitation (5–10 μW)²¹. Since the optical excitation was delivered at a low power level for continuous Ca²⁺ signal recording, its effect on optogenetic activation is negligible.

To better validate hippocampal Ca²⁺ transients free of optogenetic light pulse artifacts, we also observed individual Ca²⁺ transients coinciding with interictal LFP spikes during seizure induction following high-frequency optogenetic activation (Fig. 4). These interictal spikes paired with the train of spontaneous Ca²⁺ transients have also been observed in the mouse cortex with an optogenetically induced seizure⁶³. Also, we observed robust SDL-Ca²⁺ events during inter-stimulus intervals in the hippocampus following 8 s (≥ 5 Hz) optogenetic stimulation (Fig. 4). These SDL-Ca²⁺ events were recently reported to follow trains of interictal spikes during the optogenetically induced seizure⁶³ in the mouse cortex, which could be reliably detected in the hippocampus following optogenetic stimulation with fMRI. In our study, the number of seizure events detected by calcium recordings is much smaller than that of the SDL events, which might be due to the lack of sensitivity of calcium recording to detect interictal spikes through the 8-m optical fiber. The multi-modal fMRI mapping scheme allows us to specify unique NVC patterns according to different formats of hippocampal activity.

The hippocampal CA1 region has been considered as a key component in the framework of epilepsy induction and treatment^{53,57,64}. Previous hippocampal Opto-fMRI studies have also shown the seizure behavior in animals following high-frequency light exposure, demonstrating broad hippocampal BOLD fMRI spatial patterns and global hemodynamic effects concurrent with epileptic events^{52,65}, which are different from the evoked hippocampal activity with Opto-fMRI^{59,66}. Epileptic events observed in the cortex are usually accompanied by cortical spreading depression^{54,55,63}, which is typically studied with fMRI by direct KCl topical treatment or focal ischemia in animal brains⁶⁷. In the hippocampus, we detected robust SDL-Ca²⁺ events independent of epileptic activity in inter-stimulus intervals when 3–5 Hz optogenetic light pulses were used (Fig. 3d, Supplementary Fig. 5B), which have dominated the random incidence of epileptic events using similar stimulation paradigm in the hippocampus. The optogenetically induced cortical spreading depression has been reported in the mouse cortex without seizure induction⁶⁸. These SDL-Ca²⁺ events link to specific spatio-temporal patterns of hippocampal vascular hemodynamic responses. Intermediate characteristics of SDL-Ca²⁺-specific NVC events can be quantitatively examined to bridge the normal condition to the typical spreading depression, as well as hippocampal epileptic events despite their scarce occurrence in normal animals.

Coupled to SDL-Ca²⁺ events, the BOLD signal propagation through individual hippocampal vessels has a 4–6 mm/min velocity in a ~ 6 –8 mm spatial scale (Fig. 5c). This speed falls to the relatively top-end propagation speed range of cortical SD detected from the neuronal network^{54–56,68,69}. This observation might be because of intrinsic architectural differences between the cortex and the hippocampus; the latter is highly susceptible to SD and may sustain faster SD propagation speed^{70,71}. Kunkler et al.⁷² have observed Ca²⁺ waves occurring in neurons (~ 6 mm/min) and astrocytes (~ 4 mm/min) during SD initiation and propagation in hippocampal organ cultures. Meanwhile, in contrast to astrocytic Ca²⁺ waves propagation speed of (2–3.3 mm/min) related to cortical SD in both rat and mouse neocortex^{69,73,74}, Heuser et al.⁷⁵ also reported a 6–8 mm/min propagation speed of SD Ca²⁺ waves from both neurons and astrocytes in the hippocampal CA1 region. Interestingly, unique, spontaneous astrocytic

Ca²⁺ waves, which have been reported to propagate at ~4 mm/min in the hippocampus, do not show the long-term spreading depression features⁷⁶. It is noteworthy that the neuronal Ca²⁺ signal was only acquired through the single optical fiber inserted into the hippocampus with limited coverage of neuronal activation in comparison to the large-scale hippocampal vascular dynamic mapping with single-vessel fMRI. To better characterize neuron–glial–vascular interaction at various brain states in the hippocampus, we will apply the multiple fiber insertion with single-vessel fMRI to image transgenic mice expressing GCaMP specifically in astrocytes⁷⁷, as well as the right-shifted calcium indicator in neurons⁷⁸, with a multi-slice single-vessel fMRI method to cover the three-dimensional hippocampal structure.

Besides the similarity of the propagation speed of SDL-Ca²⁺-specific hemodynamic responses to SD events reported in the hippocampus, the baseline Ca²⁺ signal was reduced following the SDL-Ca²⁺ event for 5–6 min (Fig. 3d). Nevertheless, we only detected the correlated BOLD signal increase and CBV-weighted signal decrease (due to vasodilation), but no clear sign of vasoconstriction-based fMRI signal change was detected. Also, suppressed fMRI signals recovered in 3–6 min in most of the SDL-Ca²⁺ events (except for one dramatic case showing a long-term depression over 10 min, which was shown in Fig. 4b). Interestingly, although no clear vasoconstriction-based fMRI signal was detected following the SDL-Ca²⁺ event, significantly reduced NVCe was detected when comparing to the optogenetically evoked Ca²⁺ transients (Fig. 5). Consistent with impaired NVC during cortical SD^{54,79}, we provide a multi-modal fMRI platform to directly measure altered NVCe directly linked to concurrent SDL-Ca²⁺ events in the hippocampus.

In summary, we have developed a multi-modal fMRI platform to acquire concurrent neuronal Ca²⁺ and single-vessel fMRI signal in a subcortical brain region, for example, the hippocampus. This method allows for detecting hemodynamic fMRI responses from individual vessels through the sub-centimeter hippocampal vasculature. In particular, when neuronal activation is elicited in the hippocampus, large-scale vascular hemodynamic responses can be represented based on the estimated NVCe. This multi-modal fMRI platform will possibly be used to specify distinct NVC events through the hippocampal structure in animal models at various disease states.

Methods

Animal preparation and instrument setup. All surgical and experimental procedures reported in this paper were approved by local authorities (Regierung-spraesidium, Tübingen Referat 35, Veterinärwesen, Leiter Dr. Maas) and were in full compliance with guidelines of the European Community (EUVD 86/609/EEC) for the care and use of laboratory animals. Experimental animals were rodents, specifically Sprague–Dawley male rats, ~3 to 4 weeks old, or ~90 g, provided by Charles River Laboratories in Germany. The rats were housed in transparent Plexiglass cages (381 × 513 × 256 mm³) under conditions of well-controlled humidity and temperature. A 12–12 h on/off lighting cycle was maintained to assure an undisturbed circadian rhythm. Food and water were obtainable ad libitum. A total of 37 male Sprague–Dawley rats were used at 2–3 months of age. Five rats were imaged under 14 T at the Max Planck Institute (both BOLD and CBV-weighted fMRI data with A–V maps were acquired from four of five rats). In 12 rats, optogenetically driven neuronal calcium signals were concurrently recorded with BOLD/CBV-weighted signals (in 4 of these 12 rats optogenetically evoked responses and SDL-Ca²⁺ events were acquired). Twenty rats were used for concurrent optogenetically driven electrophysiological and neuronal calcium recordings. For the SDL and seizure induction rate calculation, 4 of the 32 rats were not included due to a failed calcium signal detection from hippocampal neurons. If the optical fiber insertion caused severe micro-bleeding in the hippocampus, which led to poor calcium recording and optogenetic activation, the data acquired from that rat was not included in the statistical analysis.

Viral injection. After 1 week habitation, rats were injected with the non-replicating AAV vectors into BC and hippocampus (AAV5.Syn.GCaMP6f.WPRE.SV40: Addgene100837-AAV5; AAV5.CAG.hChR2 (H134R)-mCherry.WPRE.SV40: Addgene100054-AAV5; AAV9-CaMKIIa-C1V1 (t/t)-TS-EYFP: Addgene35499-

AAV9). Viral vectors were procured from the University of Pennsylvania Vector Core. The injection process was carried out under isoflurane anesthesia with an induction concentration of 5.0% and a maintenance concentration of 1.5–2.0% in an oxygen-enhanced gas (30% oxygen). Following their stabilization, the rats were secured in a stereotaxic apparatus (Model 900, David Kopf Instruments). Eyes of the rats were protected with an ophthalmic ointment (Puralube), and the level of anesthesia was regularly checked by testing toe and tail pinch reflexes. With a midline incision, one small craniotomy (1–2 mm) was performed above the region of interest by using a dissecting microscope (Leica) and a pneumatic drill (Ideal Micro Drill, Harvard Apparatus). A 10 µL syringe (NanoFil, World Precision Instruments Inc.) with a 35 gauge beveled metal needle (World Precision Instruments Inc.) were placed in the stereotaxic frame and slowly lowered towards target sites (BC: caudal, 2.5 mm, lateral, 5.0 mm, and ventral, 1.5–0.9 mm; hippocampus: caudal, 4.2 mm, lateral, 2.8 mm, and ventral, 2.75–2.65 mm, respectively, from bregma). The flow rate of the virus injection was controlled by an infusion pump (Pump11 Elite, Harvard Apparatus) at a speed of 0.1 µL/min. The total injection volume was around 0.2–0.6 µL (ChR2)/0.6–1 µL (GCaMP6f). After the injection, the syringe needle was kept in place for an additional 10 min before being slowly withdrawn. The hole was sealed by bone wax (W31G, Ethicon), and the incision was sutured. Ketoprofen [5 mg/kg, q.d. (once/day)] was subcutaneously injected to relieve postoperative pain for 3 days after surgery. fMRI experiments were performed 4–8 weeks after the injection to ensure the expression of the AAV viral vectors.

Optical fiber/electrode preparation and implantation. Optical stimulation and electrophysiological recordings were performed with a 2 m (bench experiment) or 8 m (fMRI experiment) optical fiber (FT200-EMT, NA = 0.39, 200 µm, Thorlabs). The coating of both ends of the optical fiber was stripped off. One end was glued into an FC/PC connector (Thorlabs), and the other end was carefully polished by using polishing sand papers with appropriately selected grit size (LF1P/3P/5P, Thorlabs). Optical quality of the polishing interface was confirmed by using a fiber inspection microscope (FS200, Thorlabs). For simultaneous Ca²⁺ recording and fMRI, two fibers (one for optical stimulation, the other for Ca²⁺ recording) were closely glued (454, Loctite) together. For simultaneous Ca²⁺ and electrophysiological recording, a Tungsten electrode (1 MΩ, ~100 µm, FHC) was closely glued to the optical fiber tips. The dura was carefully removed, the optical fibers with the electrode were slowly inserted into either the BC or the hippocampus. The reference and ground were placed on the screws, which were fixed above the cerebellum. After implantation, the fibers with the electrode were glued to the skull for acute terminal experiments.

Animal preparation for fMRI. The experiments were described in the previous studies^{18,45}. Briefly, after induction of anesthesia, animals were endotracheally intubated with a mechanical ventilator (SAR-830, CWE). Plastic catheters (PE50, INSTECH) were carefully implanted into the right femoral artery/vein of rats to administer drugs and monitor arterial blood gases. After catheterization, the rats were secured into a stereotaxic apparatus. One small craniotomy (1–2 mm) was performed just above the regions of the virus injection and the dura was carefully removed. Two optical fibers were slowly inserted into the virus expression regions in the hippocampus, and the fibers together with a custom-made coil were fixed above the skull by using super glue (454, Loctite). Around 30 min for fixation, after the injection of a bolus of α-chloralose (60 mg/kg, intravenously (i.v.)), the rats were transferred into the MR scanner (14T, Bruker). Maintenance anesthesia was switched from isoflurane to continuous infusion of α-chloralose (infusion rate: 26.5 mg/kg/h). Throughout the whole experiment, the rectal temperature of the rat was monitored and maintained at around 37 °C by using a feedback heating system. All relevant physiological parameters were continuously monitored, including rectal temperature, arterial blood pressure (Biopac 150, Biopac Systems Inc.), pressure of the tidal ventilation (SAR-830, CWE), and end-tidal CO₂ (capnometer, Novamatrix). Arterial blood gas was measured regularly to guide physiological status adjustments by changing the respiratory volume or administering the sodium bicarbonate (8.4%, Braun) to maintain normal pH levels. For α-chloralose anesthetized animals, a muscle relaxant (pancuronium bromide, 1 mg/kg/h) was intravenously injected to minimize motion artifacts. Dextran-coated iron oxide (15 mg of Fe/kg, BioPAL, MA, i.v.) was additionally injected for obtaining high SNR CBV-weighted signal.

Optogenetic-driven Ca²⁺ with electrophysiological recording. Around 4–8 weeks after virus injection, LFP signal and Ca²⁺ signal were simultaneously recorded in a terminal experiment. Virus injection coordinates were first confirmed by a FLASH (fast low angle shot) anatomical MRI image before surgery. Anesthetics and surgical preparation procedures were similar to those of the fMRI experiments. After insertion, the LFP signal was amplified using a BioPac EEG100C module (gain factor, 5000, bandpass filter, 0.02–100 Hz, sampling rate, 5000/s). The GCaMP6f-mediated Ca²⁺ signal was recorded by the analog input module of the BioPac 150 system. For electrical stimulation, electrodes were placed into rat whisker pads and later delivered electrical pulse sequences (1.0–2.0 mA, 330 µs duration repeated at 1–5 Hz) by using a high voltage stimulator (A360LA, WPI). Stimulation was controlled by the Master-9 AMPI system (Jerusalem, Israel)

based on the stimulus paradigm, and triggering pulses were recorded by the analog input module of the BioPac 150 system (sampling rate, 5000/s). For optical stimulation, light pulses were delivered through the 473 nm laser (CNI, China). An analog module was applied to trigger the light pulse to give the optical stimulation with different pulse durations (1, 2, 4, and 8 s). Light intensity from the fiber tip was measured by using fiber optical power meters (PM20A, Thorlabs), which were controlled from 1 to 36 mW (light power higher than 40 mW was beyond the measurement range).

Perfusion, section, and microscope. In all terminal experiments, after completion of the data acquisition, rats were euthanized under deep anesthesia with isoflurane (5%). They were subsequently transcardially perfused with 0.1 M ice-cold phosphate-buffered saline (PBS, Gibco) and 4% paraformaldehyde (PFA). Brains were carefully removed from the skulls and placed into 4% PFA for post fixation (4 °C, overnight). Then, they were cryoprotected in 30% sucrose in PBS at 4 °C for 2–3 days before being flash frozen in OCT on dry ice and finally stored at –80 °C. Brain slices were sectioned in 30 μm thickness using a cryostat (CM1860, Leica). Brain slices were mounted on glass slides (Super-frost, Fisherbrand) and covered with coverslips. A mounting medium with DAPI (4',6-diamidino-2-phenylindole; VectaShield, Vector) was used to protect the fluorescence signal and to stain nuclei. Wide-field images were acquired to assess the expression of ChR2/GCaMP in the BC and the hippocampus with a microscope (Zeiss). The images were minimally processed by ImageJ to enhance the brightness for visualization purposes.

The optical setup for optical fiber Ca²⁺ recordings. The light path was built based on a previous report (Fig. 1a)^{21,22}. The light source comes from a 488 nm laser (MBL-III, CNI). Light beams were first reflected through a dichroic mirror (F48-487, reflection 471–491 nm, >94%, transmission 500–1200 nm, >93%, AHF). Then, by using an objective lens fixed on the fiber launch (MBT613D/M, Thorlabs), the light beam was focused on the optical fiber (FT200-EMT, NA = 0.39, 200 μm, Thorlabs). The laser intensity was measured at the optical fiber tip (5 μW for neuronal calcium recording) by an optical power meter (PM20A, Thorlabs). The same optical fiber guided the emitted fluorescent signal back to the light path. The light beam was successively passed through a dichroic mirror and an optical filter (F37-516, 500–550 nm bandpass, AHF). By using a tube lens (AC254-030-A1-ML, Thorlabs), the GCaMP6-mediated fluorescent signal was coupled to a Peltier-cooled SiPM with a transimpedance preamplifier (MiniSM-10035-X08, SensL). Before being recorded by the analog input module of the Biopac 150 system, the signal from the photomultiplier was amplified by a voltage amplifier (DHPVA-100, Femto).

MRI and fMRI procedures. All images were obtained by using a 14T/26 cm horizontal-bore magnet (Magnex Scientific) interfaced through the Bruker Avance III (Bruker). The scanner has a 12 cm Magnet gradient set with a strength of 100 Gauss per cm (G/cm), and a 150 μs rise time (Resonance Research Inc.). Home-made surface transceiver RF coils with an internal diameter of 7.5 and 21 mm, respectively, were used for fMRI image acquisition.

Echo planar imaging fMRI. EPI image acquisition was preceded by FASTMAP shimming (i.e., measuring *B*₀ field plots along projections instead of mapping whole imaging planes). By adjustments of echo spacing, symmetry, and setting up the *B*₀ compensation, it considerably increases the speed and performance. By using the custom-made single surface coil, parameters of the 3D gradient echo sequence were as below: volume TR = 1.5 s; TE = 14 ms; bandwidth: 170 kHz; flip angle: 12°; matrix: 64 × 64 × 16; in-plane resolution: 300 × 300 μm²; slice thickness: 500 μm. The paradigm consisted of 360 dummy scans enabling the emergence of reaching the steady state, 10 pre-stimulation scans, 3 scans during stimulation, and 12 post-stimulation scans with 8 epochs for each run or 5 scans during stimulation and 25 post-stimulation scans for 10 epochs. For anatomical images, the RARE (rapid imaging with refocused echoes) sequence was implemented to acquire images with the same geometry of the fMRI images.

Balanced steady-state free precession fMRI. The bSSFP-fMRI method was applied to acquire evoked fMRI signals using the following parameters: TR: 11.7 ms; TE: 5.85 ms; matrix: 128 × 128; FOV: 12.8 × 12.8 mm²; in-plane resolution: 100 × 100 μm²; flip angle: 22° (BOLD); TR: 10.4 ms; TE: 5.2 ms; matrix: 96 × 96; FOV: 12.8 × 12.8 mm²; in-plane resolution: 130 × 130 μm²; flip angle: 17° (CBV); slice thickness: 500 μm. The paradigm consisted of 300 dummy scans to reach the steady state, 25 pre-stimulation scans, 1 scan during stimulation, and 14 post-stimulation scans with a total of 8 epochs for each run, 1 scan during stimulation, and 29 post-stimulation scans with a total of 10 epochs for each run, and 1 scan during stimulation and 79 post-stimulation scans with a total of 3 epochs for each run. CBV-weighted fMRI signals were acquired after intravenous injection of dextran-coated iron oxide (BioPAL, MA, i.v.).

Single-vessel MGE Imaging. For the detection of the individual arterioles and venules in rat hippocampus, a 2D MGE sequence was applied with the following parameters: TR: 50 ms; TE: 2.5, 5.5, 11.5, 14.5, 17.5, 17.5, 20.5, 23.5 ms; flip angle: 58°; matrix: 256 × 192; in-plane resolution: 67 × 67 μm²; slice thickness: 500 μm.

The MGE images were averaged from the 2nd echo to the 5th/6th echo to get the A–V map (Fig. 2c).

Data analysis and statistics. Preprocessing and analysis of functional imaging data were carried out by using the software package, Analysis of Functional NeuroImages (AFNI) (NIH, Bethesda, MD). Evoked calcium signals were processed in Matlab (MATLAB, MathWorks, USA).

For calcium data analysis, neuronal calcium signals were low-pass filtered (100 Hz) by zero-phase shift digital filtering. The relative percentage change of the calcium fluorescence ($\Delta F/F$) was defined as $(F - F_0)/F_0$, where F_0 is the baseline fluorescent signal.

For the EPI-fMRI analysis, EPI images were aligned to anatomical datasets, which were registered to template images across the trials. Baselines of EPI images were normalized to 100 for multiple trials of block-design statistical analysis of EPI time courses.

For bSSFP-fMRI analysis, the tag-based registration method was used to register the single-vessel functional map with the A–V map. We normalized time courses of bSSFP-fMRI signals from SDL-Ca²⁺ events by scaling the maximum to 1 (Fig. 5b). GLM analysis was applied to estimate evoked and SDL-Ca²⁺ NVCe β -coefficients. β Estimates were used to indicate the amplitude of the BOLD and CBV-weighted responses in β maps. For the CBV percentage (%) map, the %CBV was estimated based on the equation: %CBV = $\ln(S_{Fe-base}/S_{stim})/\ln(S_{Fe-pre}/S_{Fe-base})$. The $S_{Fe-base}$ is the baseline level fMRI signal after iron oxide particle injection, and S_{Fe-pre} is the baseline level fMRI signal before iron oxide particle injection⁵¹.

For the analysis of fMRI signals recorded simultaneously with hippocampal SDL-Ca²⁺ transients, an AM response model based on an AFNI script was implemented to perform GLM analysis.

The AM response model is given by:

$$r_{AM1}(t) = \sum_{k=1}^K h(t - \tau_k) a_k,$$

where a_k is the value of *k*th amplitude of hippocampal SDL Ca²⁺ transient. $h(t)$ is the hemodynamic response function based on the γ variate function implemented by the AFNI BLOCK function:

$$h(t) = \int_0^{\min(t,L)} s^4 e^{-s} / [4^4 e^{-4}] ds,$$

where *L* is the duration of the response. A varied duration (*L*) was applied to test the goodness of fit for the general linear model with *t* statistics reported in Supplementary Fig. 6. Both NVCe β -coefficients were estimated simultaneously, using GLM analysis implemented in the AFNI 3dDeconvolve function. The response regressors are shown in the equation:

$$Y(t) = \beta_1 h(t) + \beta_2 r_{AM1}(t) + \epsilon,$$

where β_1 is the optogenetically evoked coefficient and β_2 is the SDL-Ca²⁺ coefficient. ϵ is the error term. Polynomial terms regressing the baseline drift are not shown. The calculated β -coefficient was represented in a voxel-wise manner, as a β map, which can be overlapped on the A–V map of the 2D hippocampal slice in Fig. 5f or Supplementary Fig. 6D.

Evoked NVCe β -coefficients and SDL-Ca²⁺ NVCe β -coefficients were normalized within each trial to have zero mean and unit variance. Coefficients were scaled to the range 0–1 using the minimal and maximal values (Fig. 5g, h). Student's *t* test (two-tailed) was performed for group analysis, to compare the calcium $\Delta F/F$ (Fig. 5e) or the normalized NVCe β -coefficient (Fig. 5g) between optogenetically evoked responses and SDL-Ca²⁺ events in calcium and fMRI data. Also, one-way analysis of variance was performed to examine the goodness of fit for the hemodynamic function with varied duration. Data with error bars were displayed as means \pm SEM. *P* values <0.05 were considered statistically significant. No blinding and randomization design was needed in this work.

Reporting summary. Further information on research design is available in the Nature Research Reporting Summary linked to this article.

Data availability

Raw data can be provided upon email request to the corresponding author. Excel files are included for each quantitative plot included in main figures. Source data underlying Figs. 2f, 4c, 5c, e, g–i are provided as a Source Data file. The data presented in the figures and other summary level data are contained within the Supplementary Files. Further information on research design is available in the Nature Research Reporting Summary linked to this article.

Code availability

AFNI software (NIH, USA) and Matlab (MATLAB, MathWorks, USA) were used to process fMRI and simultaneously acquired calcium signals, respectively. Relevant source codes can be downloaded through <https://afni.nimh.nih.gov/afni/>. Related image processing codes can be provided upon direct email request to the corresponding author.

Received: 11 April 2019; Accepted: 1 October 2019;

Published online: 20 November 2019

References

- Ogawa, S. et al. Intrinsic signal changes accompanying sensory stimulation: functional brain mapping with magnetic resonance imaging. *Proc. Natl. Acad. Sci. USA* **89**, 5951–5955 (1992).
- Kwong, K. K. et al. Dynamic magnetic resonance imaging of human brain activity during primary sensory stimulation. *Proc. Natl. Acad. Sci. USA* **89**, 5675–5679 (1992).
- Bandettini, P. A., Wong, E. C., Hinks, R. S., Tikofsky, R. S. & Hyde, J. S. Time course EPI of human brain function during task activation. *Magn. Reson. Med.* **25**, 390–397 (1992).
- Kim, S. G. & Ogawa, S. Biophysical and physiological origins of blood oxygenation level-dependent fMRI signals. *J. Cereb. Blood Flow Metab.* **32**, 1188–1206 (2012).
- Logothetis, N. K. What we can do and what we cannot do with fMRI. *Nature* **453**, 869–878 (2008).
- Fox, M. D. & Raichle, M. E. Spontaneous fluctuations in brain activity observed with functional magnetic resonance imaging. *Nat. Rev. Neurosci.* **8**, 700–711 (2007).
- Biswal, B., Yetkin, F. Z., Haughton, V. M. & Hyde, J. S. Functional connectivity in the motor cortex of resting human brain using echo-planar MRI. *Magn. Reson. Med.* **34**, 537–541 (1995).
- Chang, C. et al. Tracking brain arousal fluctuations with fMRI. *Proc. Natl. Acad. Sci. USA* **113**, 4518–4523 (2016).
- Drew, P. J., Duyen, J. H., Golanov, E. & Kleinfeld, D. Finding coherence in spontaneous oscillations. *Nat. Neurosci.* **11**, 991–993 (2008).
- Belliveau, J. W. et al. Functional mapping of the human visual cortex by magnetic resonance imaging. *Science* **254**, 716–719 (1991).
- Detre, J. A., Leigh, J. S., Williams, D. S. & Koretsky, A. P. Perfusion imaging. *Magn. Reson. Med.* **23**, 37–45 (1992).
- Lauritzen, M. On the neural basis of fMRI signals. *Clin. Neurophysiol.* **119**, 729–730 (2008).
- Devor, A. et al. Suppressed neuronal activity and concurrent arteriolar vasoconstriction may explain negative blood oxygenation level-dependent signal. *J. Neurosci.* **27**, 4452–4459 (2007).
- Chaigneau, E. et al. The relationship between blood flow and neuronal activity in the rodent olfactory bulb. *J. Neurosci.* **27**, 6452–6460 (2007).
- Anenberg, E., Chan, A. W., Xie, Y., LeDue, J. M. & Murphy, T. H. Optogenetic stimulation of GABA neurons can decrease local neuronal activity while increasing cortical blood flow. *J. Cereb. Blood Flow Metab.* **35**, 1579–1586 (2015).
- Yu, X. et al. Direct imaging of macrovascular and microvascular contributions to BOLD fMRI in layers IV–V of the rat whisker-barrel cortex. *Neuroimage* **59**, 1451–1460 (2012).
- Moon, C. H., Fukuda, M. & Kim, S. G. Spatiotemporal characteristics and vascular sources of neural-specific and -nonspecific fMRI signals at submillimeter columnar resolution. *Neuroimage* **64**, 91–103 (2013).
- Yu, X. et al. Sensory and optogenetically driven single-vessel fMRI. *Nat. Methods* **13**, 337–340 (2016).
- Logothetis, N. K., Pauls, J., Augath, M., Trinath, T. & Oeltermann, A. Neurophysiological investigation of the basis of the fMRI signal. *Nature* **412**, 150–157 (2001).
- Scholvinck, M. L., Maier, A., Ye, F. Q., Duyen, J. H. & Leopold, D. A. Neural basis of global resting-state fMRI activity. *Proc. Natl. Acad. Sci. USA* **107**, 10238–10243 (2010).
- Wang, M., He, Y., Sejnowski, T. J. & Yu, X. Brain-state dependent astrocytic Ca(2+) signals are coupled to both positive and negative BOLD-fMRI signals. *Proc. Natl. Acad. Sci. USA* **115**, E1647–E1656 (2018).
- He, Y. et al. Ultra-slow single-vessel BOLD and CBV-based fMRI spatiotemporal dynamics and their correlation with neuronal intracellular calcium signals. *Neuron* **97**, 925–939 (2018). e925.
- Lind, B. L. et al. Fast Ca(2+) responses in astrocyte end-feet and neurovascular coupling in mice. *Glia* **66**, 348–358 (2018).
- Otsu, Y. et al. Calcium dynamics in astrocyte processes during neurovascular coupling. *Nat. Neurosci.* **18**, 210–218 (2015).
- Ma, Y. et al. Resting-state hemodynamics are spatiotemporally coupled to synchronized and symmetric neural activity in excitatory neurons. *Proc. Natl. Acad. Sci. USA* **113**, E8463–E8471 (2016).
- Albers, F., Wachsmuth, L., van Alst, T. M. & Faber, C. Multimodal functional neuroimaging by simultaneous BOLD fMRI and fiber-optic calcium recordings and optogenetic control. *Mol. Imaging Biol.* **20**, 171–182 (2018).
- Schwalm, M. et al. Cortex-wide BOLD fMRI activity reflects locally-recorded slow oscillation-associated calcium waves. *Elife* **6**, <https://doi.org/10.7554/eLife.27602> (2017).
- Schmid, F. et al. Assessing sensory versus optogenetic network activation by combining (o)fMRI with optical Ca²⁺ recordings. *J. Cereb. Blood Flow Metab.* **36**, 1885–1900 (2016).
- Logothetis, N. K. et al. Hippocampal-cortical interaction during periods of subcortical silence. *Nature* **491**, 547–553 (2012).
- Dombeck, D. A., Harvey, C. D., Tian, L., Looger, L. L. & Tank, D. W. Functional imaging of hippocampal place cells at cellular resolution during virtual navigation. *Nat. Neurosci.* **13**, 1433–1440 (2010).
- Low, R. J., Gu, Y. & Tank, D. W. Cellular resolution optical access to brain regions in fissures: imaging medial prefrontal cortex and grid cells in entorhinal cortex. *Proc. Natl. Acad. Sci. USA* **111**, 18739–18744 (2014).
- Attardo, A., Fitzgerald, J. E. & Schnitzer, M. J. Impermanence of dendritic spines in live adult CA1 hippocampus. *Nature* **523**, 592–596 (2015).
- Lovett-Barron, M. et al. Dendritic inhibition in the hippocampus supports fear learning. *Science* **343**, 857–863 (2014).
- Sawinski, J. et al. Visually evoked activity in cortical cells imaged in freely moving animals. *Proc. Natl. Acad. Sci. USA* **106**, 19557–19562 (2009).
- Hirano, M., Yamashita, Y. & Miyakawa, A. In vivo visualization of hippocampal cells and dynamics of Ca²⁺ concentration during anoxia: feasibility of a fiber-optic plate microscope system for in vivo experiments. *Brain Res.* **732**, 61–68 (1996).
- Doronina-Amitonova, L. V. et al. Implantable fiber-optic interface for parallel multisite long-term optical dynamic brain interrogation in freely moving mice. *Sci. Rep.* **3**, 3265 (2013).
- Kudo, Y. et al. A single optical fiber fluorometric device for measurement of intracellular Ca²⁺ concentration: its application to hippocampal neurons in vitro and in vivo. *Neuroscience* **50**, 619–625 (1992).
- Miyamoto, D. & Murayama, M. The fiber-optic imaging and manipulation of neural activity during animal behavior. *Neurosci. Res.* **103**, 1–9 (2016).
- Kobat, D., Horton, N. G. & Xu, C. In vivo two-photon microscopy to 1.6-mm depth in mouse cortex. *J. Biomed. Opt.* **16**, 106014 (2011).
- Wang, T. et al. Three-photon imaging of mouse brain structure and function through the intact skull. *Nat. Methods* **15**, 789–792 (2018).
- Ouzounov, D. G. et al. In vivo three-photon imaging of activity of GCaMP6-labeled neurons deep in intact mouse brain. *Nat. Methods* **14**, 388–390 (2017).
- Coyle, P. Vascular patterns of the rat hippocampal formation. *Exp. Neurol.* **52**, 447–458 (1976).
- Coyle, P. Spatial features of the rat hippocampal vascular system. *Exp. Neurol.* **58**, 549–561 (1978).
- Silva, A. C. & Koretsky, A. P. Laminar specificity of functional MRI onset times during somatosensory stimulation in rat. *Proc. Natl. Acad. Sci. USA* **99**, 15182–15187 (2002).
- Yu, X., Qian, C., Chen, D. Y., Dodd, S. J. & Koretsky, A. P. Deciphering laminar-specific neural inputs with line-scanning fMRI. *Nat. Methods* **11**, 55–58 (2014).
- Turner, R., Le Bihan, D., Moonen, C. T., Despres, D. & Frank, J. Echo-planar time course MRI of cat brain oxygenation changes. *Magn. Reson. Med.* **22**, 159–166 (1991).
- Mansfield, P. Multi-planar image-formation using NMR spin echoes. *J. Phys. C* **10**, L55–L58 (1977).
- Rungta, R. L., Osmani, B. F., Boido, D., Tanter, M. & Chrapak, S. Light controls cerebral blood flow in naive animals. *Nat. Commun.* **8**, 14191 (2017).
- Christie, I. N. et al. fMRI response to blue light delivery in the naive brain: implications for combined optogenetic fMRI studies. *NeuroImage* **66**, 634–641 (2013).
- Dorr, A., Sled, J. G. & Kabani, N. Three-dimensional cerebral vasculature of the CBA mouse brain: a magnetic resonance imaging and micro computed tomography study. *Neuroimage* **35**, 1409–1423 (2007).
- Shih, Y. Y., Wey, H. Y., De La Garza, B. H. & Duong, T. Q. Striatal and cortical BOLD, blood flow, blood volume, oxygen consumption, and glucose consumption changes in noxious forepaw electrical stimulation. *J. Cereb. Blood Flow Metab.* **31**, 832–841 (2011).
- Weitz, A. J. et al. Optogenetic fMRI reveals distinct, frequency-dependent networks recruited by dorsal and intermediate hippocampus stimulations. *Neuroimage* **107**, 229–241 (2015).
- Osawa, S. et al. Optogenetically induced seizure and the longitudinal hippocampal network dynamics. *PLoS ONE* **8**, e60928 (2013).
- Ayata, C. & Lauritzen, M. Spreading depression, spreading depolarizations, and the cerebral vasculature. *Physiol. Rev.* **95**, 953–993 (2015).
- Fabricius, M. et al. Association of seizures with cortical spreading depression and peri-infarct depolarisations in the acutely injured human brain. *Clin. Neurophysiol.* **119**, 1973–1984 (2008).
- Fabricius, M. et al. Cortical spreading depression and peri-infarct depolarization in acutely injured human cerebral cortex. *Brain* **129**, 778–790 (2006).
- Muldoon, S. F. et al. GABAergic inhibition shapes interictal dynamics in awake epileptic mice. *Brain* **138**, 2875–2890 (2015).

58. Mateo, C., Knutsen, P. M., Tsai, P. S., Shih, A. Y. & Kleinfeld, D. Entrainment of arteriole vasomotor fluctuations by neural activity is a basis of blood-oxygenation-level-dependent “resting-state” connectivity. *Neuron* **96**, 936–948 (2017). e933.
59. Chan, R. W. et al. Low-frequency hippocampal–cortical activity drives brain-wide resting-state functional MRI connectivity. *Proc. Natl. Acad. Sci. USA* **114**, E6972–E6981 (2017).
60. Poplawsky, A. J. et al. Dominance of layer-specific microvessel dilation in contrast-enhanced high-resolution fMRI: comparison between hemodynamic spread and vascular architecture with CLARITY. *Neuroimage* <https://doi.org/10.1016/j.neuroimage.2017.08.046> (2017).
61. Xue, F. S., Wang, Q., Liao, X., Yuan, Y. J. & Xiong, J. Can a model of graded difficulty in Laerdal SimMan exactly compare performances of direct and indirect laryngoscopes? *Eur. J. Anaesthesiol.* **29**, 53–54 (2012); author reply 54–55.
62. Owen, S. F., Liu, M. H. & Kreitzer, A. C. Thermal constraints on in vivo optogenetic manipulations. *Nat. Neurosci.* **22**, 1061–1065 (2019).
63. Khoshkhoo, S., Vogt, D. & Sohal, V. S. Dynamic, cell-type-specific roles for GABAergic interneurons in a mouse model of optogenetically inducible seizures. *Neuron* **93**, 291–298 (2017).
64. Bernard, C. et al. Acquired dendritic channelopathy in temporal lobe epilepsy. *Science* **305**, 532–535 (2004).
65. Duffy, B. A., Choy, M., Chuapoco, M. R., Madsen, M. & Lee, J. H. MRI compatible optrodes for simultaneous LFP and optogenetic fMRI investigation of seizure-like afterdischarges. *Neuroimage* **123**, 173–184 (2015).
66. Takata, N. et al. Optogenetic activation of CA1 pyramidal neurons at the dorsal and ventral hippocampus evokes distinct brain-wide responses revealed by mouse fMRI. *PLoS ONE* **10**, e0121417 (2015).
67. Kao, Y. C. et al. Dynamic perfusion and diffusion MRI of cortical spreading depolarization in photothrombotic ischemia. *Neurobiol. Dis.* **71**, 131–139 (2014).
68. Chung, D. Y. et al. Determinants of optogenetic cortical spreading depolarizations. *Cereb. Cortex* <https://doi.org/10.1093/cercor/bhy021> (2018).
69. Enger, R. et al. Dynamics of ionic shifts in cortical spreading depression. *Cereb. Cortex* **25**, 4469–4476 (2015).
70. Dani, J. W., Chernjavsky, A. & Smith, S. J. Neuronal activity triggers calcium waves in hippocampal astrocyte networks. *Neuron* **8**, 429–440 (1992).
71. Nedergaard, M., Cooper, A. J. & Goldman, S. A. Gap junctions are required for the propagation of spreading depression. *J. Neurobiol.* **28**, 433–444 (1995).
72. Kunkler, P. E. & Kraig, R. P. Calcium waves precede electrophysiological changes of spreading depression in hippocampal organ cultures. *J. Neurosci.* **18**, 3416–3425 (1998).
73. Peters, O., Schipke, C. G., Hashimoto, Y. & Kettenmann, H. Different mechanisms promote astrocyte Ca^{2+} waves and spreading depression in the mouse neocortex. *J. Neurosci.* **23**, 9888–9896 (2003).
74. Chuquet, J., Hollender, L. & Nimchinsky, E. A. High-resolution in vivo imaging of the neurovascular unit during spreading depression. *J. Neurosci.* **27**, 4036–4044 (2007).
75. Heuser, K. et al. Ca^{2+} signals in astrocytes facilitate spread of epileptiform activity. *Cereb. Cortex* **28**, 4036–4048 (2018).
76. Kuga, N., Sasaki, T., Takahara, Y., Matsuki, N. & Ikegaya, Y. Large-scale calcium waves traveling through astrocytic networks in vivo. *J. Neurosci.* **31**, 2607–2614 (2011).
77. Srinivasan, R. et al. New transgenic mouse lines for selectively targeting astrocytes and studying calcium signals in astrocyte processes in situ and in vivo. *Neuron* **92**, 1181–1195 (2016).
78. Dana, H. et al. Sensitive red protein calcium indicators for imaging neural activity. *Elife* **5**, <https://doi.org/10.7554/eLife.12727> (2016).
79. Dreier, J. P. The role of spreading depression, spreading depolarization and spreading ischemia in neurological disease. *Nat. Med.* **17**, 439–447 (2011).

Acknowledgements

This research was supported by NIH Brain Initiative funding (RF1NS113278-01), German Research Foundation (DFG) SPP-1655 and Yu215/3-1, BMBF 01GQ1702, internal funding from Max Planck Society, and the Ph.D. support from the Chinese Scholarship Council (for X.C., Y.C.). We thank Dr. R. Pohmann and Dr. K. Buckenmaier for technical support; Dr. E. Weiler, Dr. P. Douay, Mrs. R. König, Ms. S. Fischer, and Ms. H. Schulz for animal/lab maintenance and support; the AFNI team for software support.

Author contributions

X.Y., N.K. and X.C. designed the research; X.C. and X.Y. performed animal experiments; X.C., Y.J. and F.S. performed data analysis; Y. C., C.Q., C.A. and Z.L. provided technical support; X.Y., N.K., C.A. and X.C. wrote the paper.

Competing interests

The authors declare no competing interests.

Additional information

Supplementary information is available for this paper at <https://doi.org/10.1038/s41467-019-12850-x>.

Correspondence and requests for materials should be addressed to X.Y.

Peer review information *Nature Communications* thanks Cornelius Faber, Yen-Yu Ian Shih and the other, anonymous, reviewer(s) for their contribution to the peer review of this work.

Reprints and permission information is available at <http://www.nature.com/reprints>

Publisher's note Springer Nature remains neutral with regard to jurisdictional claims in published maps and institutional affiliations.



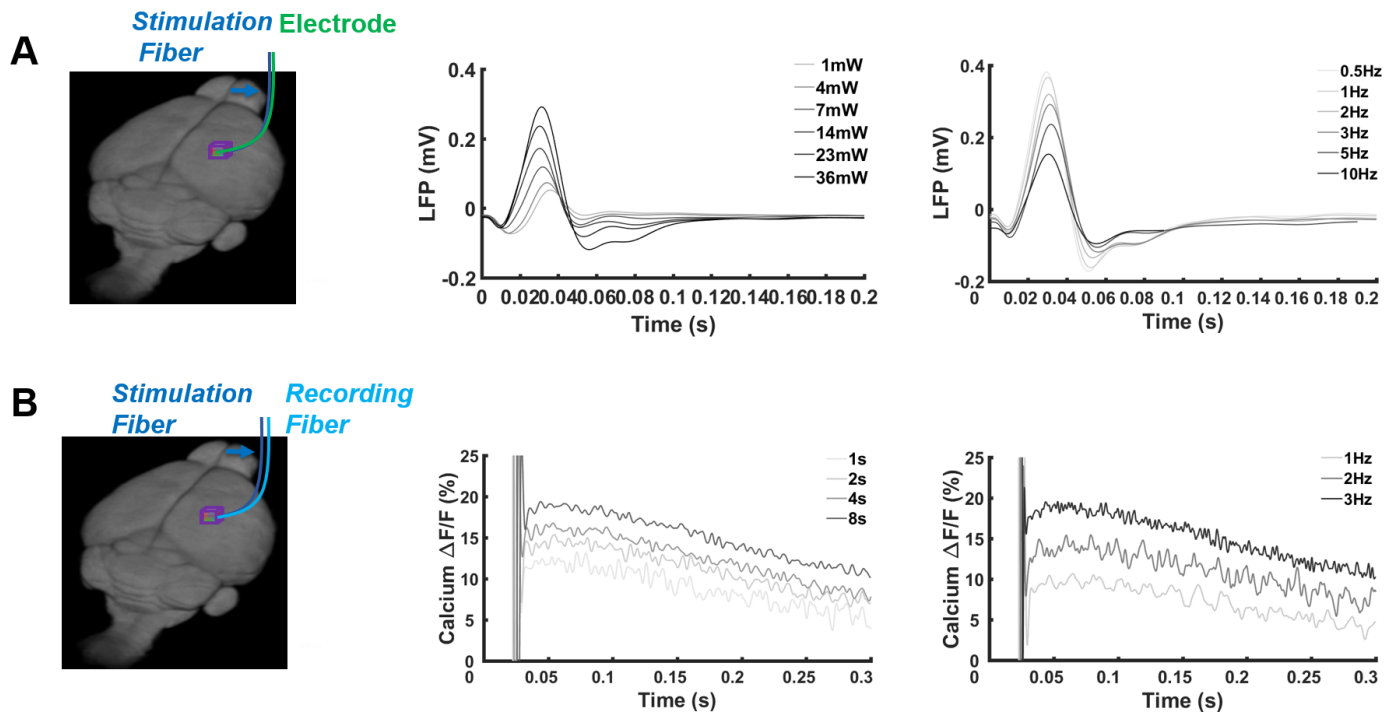
Open Access This article is licensed under a Creative Commons Attribution 4.0 International License, which permits use, sharing, adaptation, distribution and reproduction in any medium or format, as long as you give appropriate credit to the original author(s) and the source, provide a link to the Creative Commons license, and indicate if changes were made. The images or other third party material in this article are included in the article's Creative Commons license, unless indicated otherwise in a credit line to the material. If material is not included in the article's Creative Commons license and your intended use is not permitted by statutory regulation or exceeds the permitted use, you will need to obtain permission directly from the copyright holder. To view a copy of this license, visit <http://creativecommons.org/licenses/by/4.0/>.

© The Author(s) 2019

Supplementary information

Mapping optogenetically-driven single-vessel fMRI with concurrent neuronal calcium recordings in the rat hippocampus

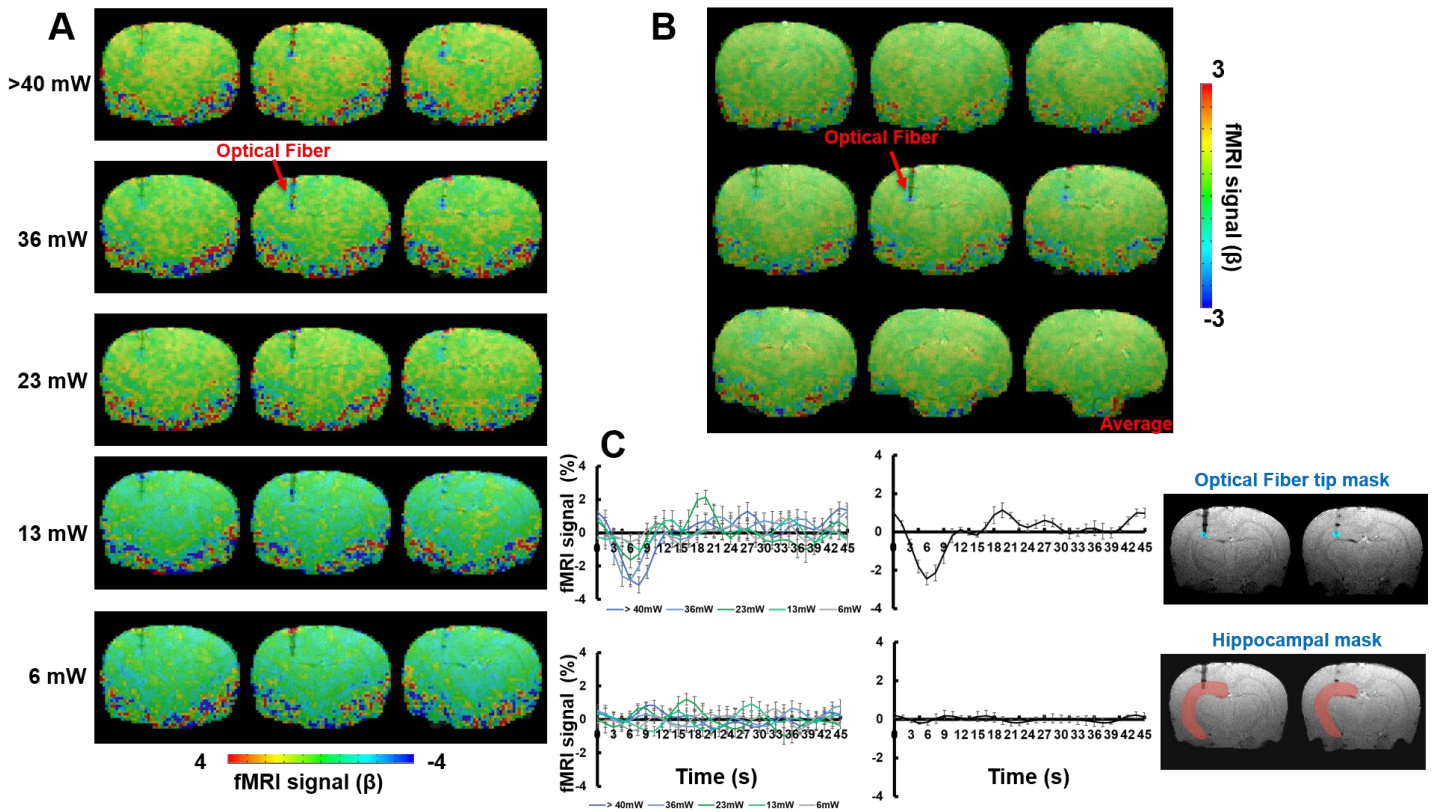
Chen et al.



Supplementary Figure 1. Optogenetically evoked LFP and GCamp6f-mediated Ca^{2+} recording in the hippocampus.

A. Optogenetically evoked LFP traces with 10 ms light pulse stimulation at different powers (1-36 mW) averaged from trails with 3 Hz light pulse stimulation paradigm and frequencies (0.5-10 Hz) averaged from trails with 14 mW power of the light pulse (4 s on with 16 s off repeated for 20 times).

B. Optogenetically evoked neuronal Ca^{2+} traces with 10 ms light pulse stimulation at different stimulation on durations (1, 2, 4, 8 s) and frequencies (1-3 Hz) from experimental trails with each epoch in 20 s (1-4s on) and 45 s (8s on) repeated for 20 times.

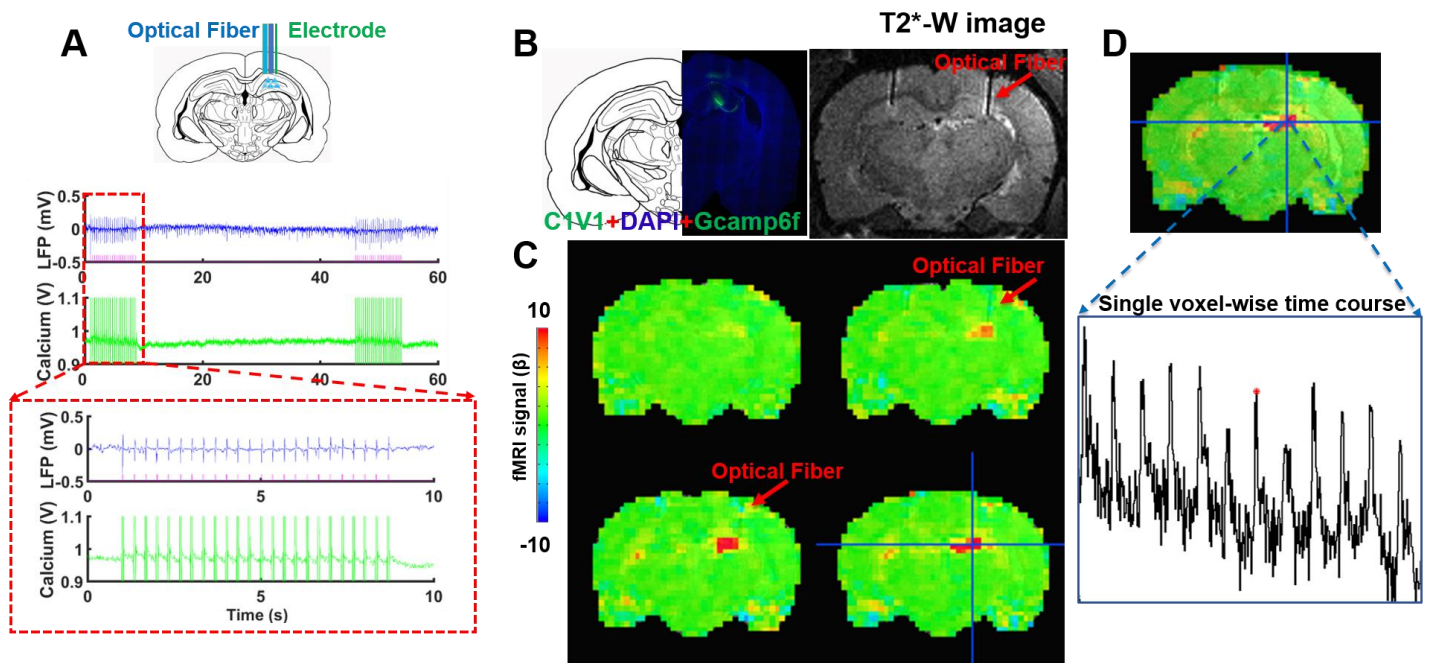


Supplementary Figure 2. Blue light-evoked B0 offset-induced MRI signal changes close to the fiber tip in the naive rat hippocampus.

A. Representative color-coded EPI-fMRI maps at different powers (6->40 mW) (illumination: 10 ms light pulse, 10 Hz, 8 s).

B. Averaged color-coded EPI-fMRI map from different powers (13, 23, 36, >40 mW) (illumination: 10 ms light pulse, 10 Hz, 8 s).

C. Averaged EPI-fMRI time courses from optical fiber tip (upper) and hippocampus (lower) at different stimulation powers (6->40 mW), averaged EPI-fMRI time courses from all the different powers (23, 36, >40 mW) (middle), and ROIs in blue contour (optic fiber tip) and red contour (hippocampus) of the MRI images (right).



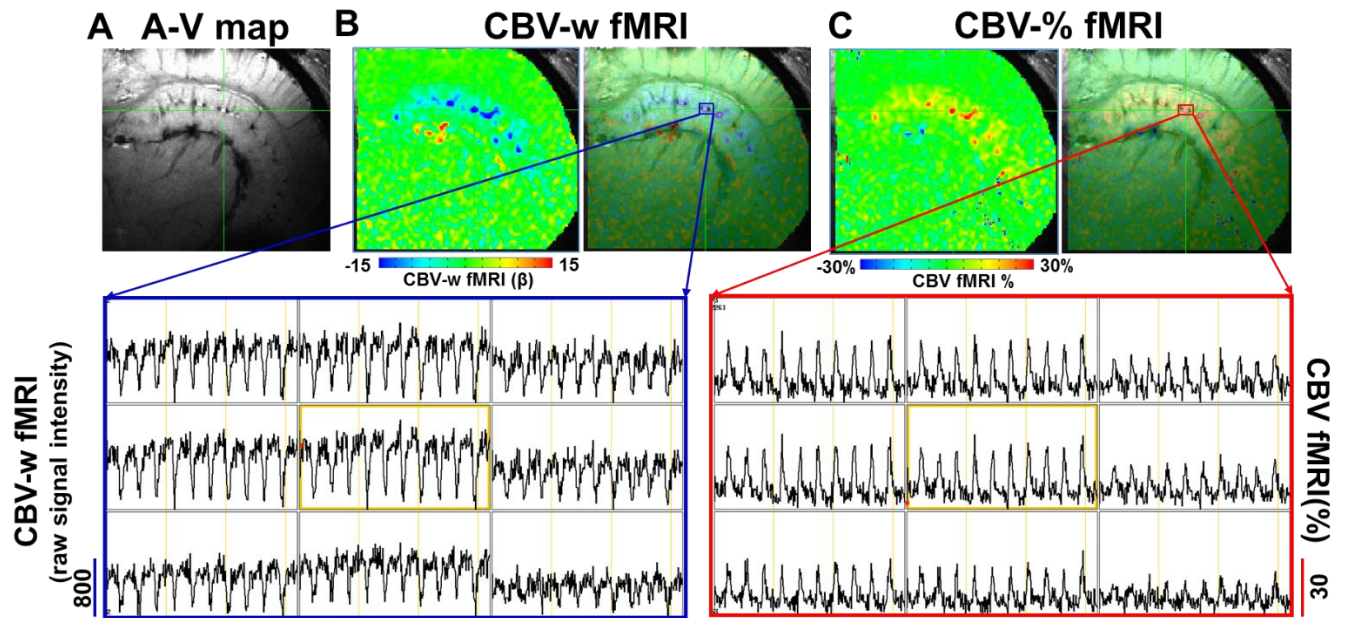
Supplementary Figure 3. Simultaneous C1V1-evoked GCaMP6f-mediated Ca²⁺ recording with LFP or EPI-fMRI in the hippocampus.

A. Simultaneous LFP (blue) and Ca²⁺ signal (green) traces from neurons expressing C1V1 in the hippocampus with optogenetic stimulation (illumination: 10 ms light pulse, 3 Hz, 8 s, 5 mW, 590 nm) with enlarged view outlined in the red box.

B. Immunohistological staining of C1V1 and Gcamp6f co-expressed in the hippocampus (left), and the T2*-weighted (T2*-W) image shows the optical fiber (red arrow) inserted into the hippocampus.

C. A representative color-coded BOLD-fMRI map shows the optogenetically activated hippocampus through C1V1 (illumination: 10 ms light pulse, 3 Hz, 8 s, 5 mW, 590 nm).

D. The BOLD-fMRI time course from a single voxel in hippocampus is plotted in a block-design paradigm (12 epochs).

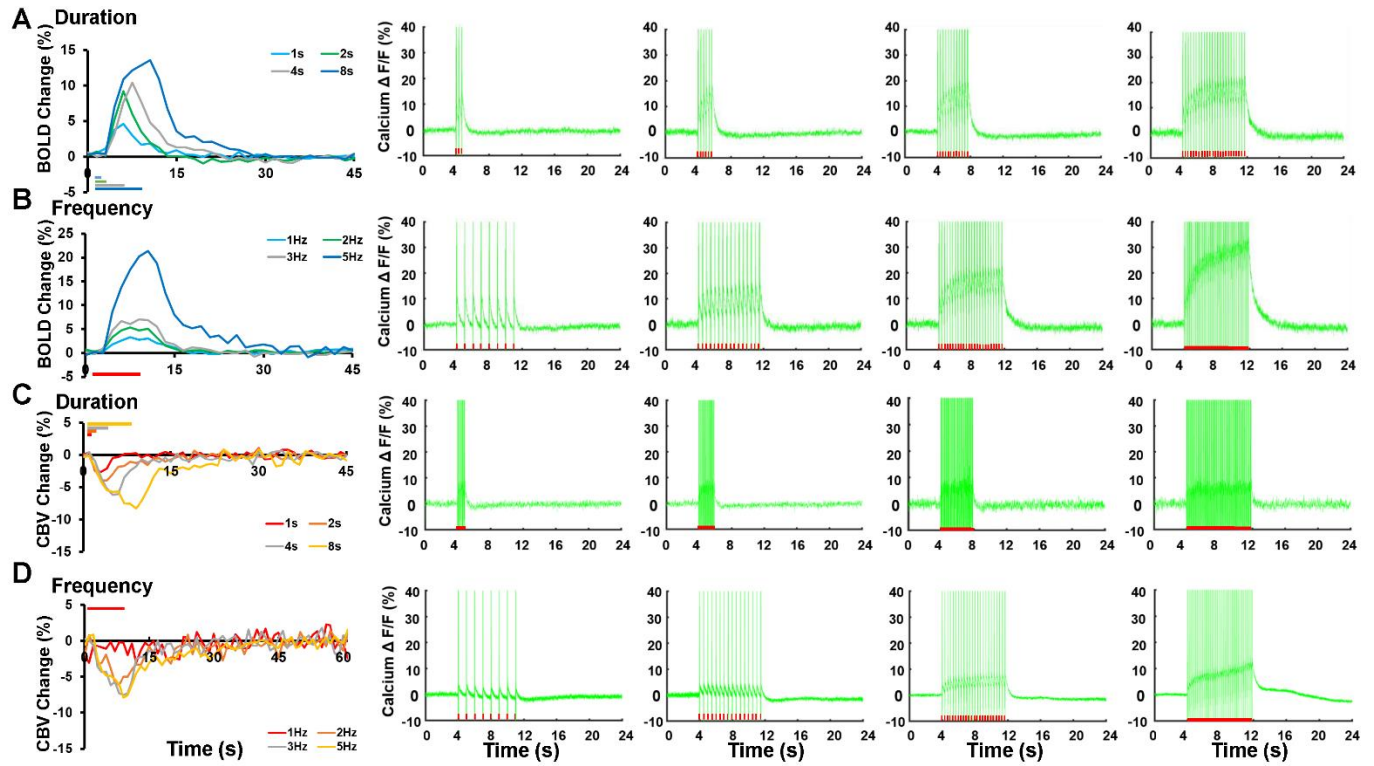


Supplementary Figure 4. The Optogenetically driven hippocampal single-vessel CBV % map.

A. Representative 2D A-V map of the hippocampal vasculature.

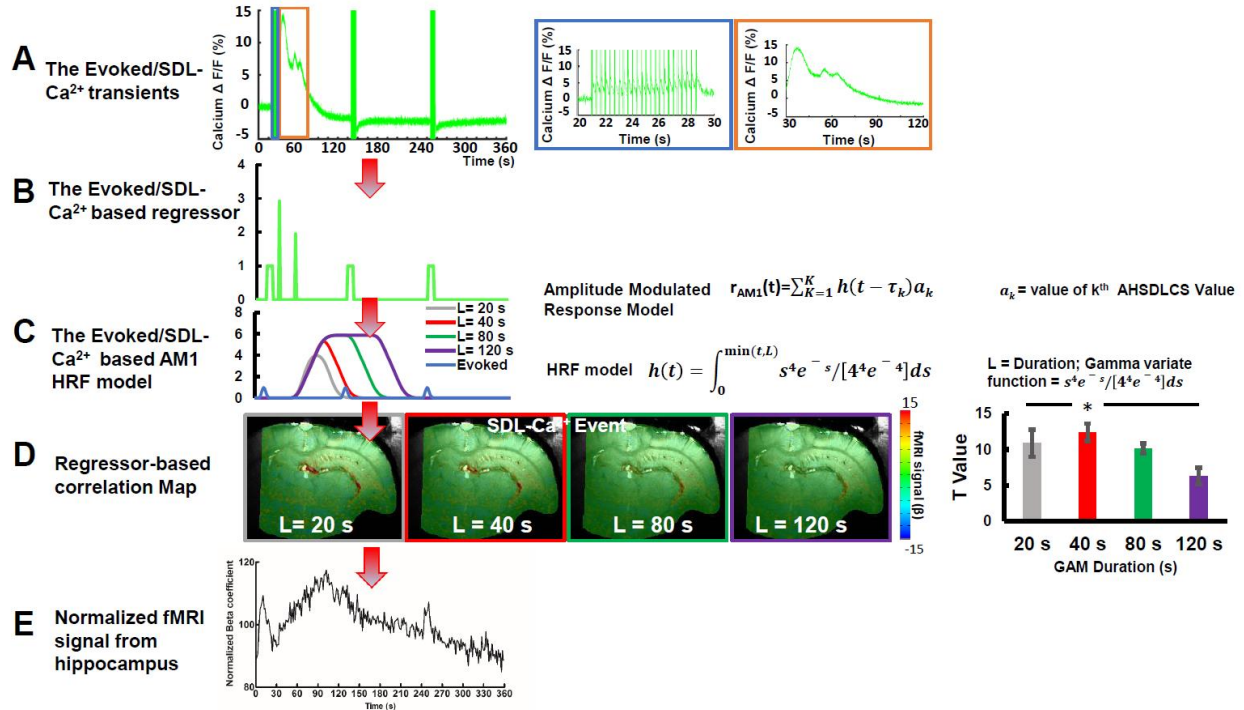
B. The CBV-weighted fMRI map shows the T2*-weighted signal changes from the individual hippocampal arterioles (bright dots). The time courses of the CBV-w signal from arterioles voxels (3x3 windows, blue box) show the negative signal changes per epoch of the stimulation paradigm.

C. The CBV % fMRI map shows the percent CBV signal changes from the individual hippocampal arterioles (bright dots). The time courses of the CBV % signal from arterioles voxels (3x3 windows, red box) show the positive signal changes per epoch of the stimulation paradigm.



Supplementary Figure 5. Simultaneous single-vessel BOLD/CBV fMRI and Ca^{2+} recordings in the hippocampus with different optogenetic stimulation paradigms.

- A.** Stimulation duration-dependent BOLD-fMRI with concurrent Ca^{2+} recordings (1, 2, 4, 8 s).
- B.** Stimulation frequency-dependent BOLD-fMRI with concurrent Ca^{2+} recordings (1, 2, 3, 5 Hz).
- C.** Stimulation duration-dependent CBV-fMRI with concurrent Ca^{2+} recordings (1, 2, 4, 8 s).
- D.** Stimulation frequency-dependent CBV-fMRI with concurrent Ca^{2+} recordings (1, 2, 3, 5 Hz).



Supplementary Figure 6. The flow diagram to calculate the SDL- Ca^{2+} signal-based single-vessel BOLD fMRI correlation map.

A. Neuronal Ca^{2+} signals and single-vessel BOLD fMRI signals were acquired simultaneously during SDL- Ca^{2+} events. A representative time course of the neuronal Ca^{2+} signal shows the optogenetically evoked Ca^{2+} signal and the SDL- Ca^{2+} signal with enlarged views of these two events (blue and orange box).

B. Peak timing and amplitudes of the optogenetically evoked and SDL- Ca^{2+} events were used to create the regressors for the single-vessel BOLD fMRI correlation.

C. Amplitude modulated BOLD response models are generated base on the Evoked/SDL- Ca^{2+} -based regressors. The ideal functions (HRF models) of the representative time course of Evoked/SDL- Ca^{2+} signal are represented with varied duration (L).

D. Voxel-wise correlation maps of the single-vessel BOLD fMRI signal with the simultaneously acquired neuronal Ca^{2+} signal with the HRF models at varied duration (L), showing t statistic values at L=40 s (ANOVA, one way, $F=4.93$, $p=0.013$, $n=5$).

E. A representative time course of the single-vessel BOLD fMRI signal from the hippocampus shows the positive fMRI signal correlated to the occurrence of the SDL- Ca^{2+} signal.

1 **Single-vessel cerebral blood flow fMRI to map blood velocity by phase-contrast**
2 **imaging**

3

4 Xuming Chen^{1,2}, Yuanyuan Jiang³, Sangcheon Choi^{1,4}, Rolf Pohmann¹,
5 Klaus Scheffler^{1,5}, David Kleinfeld^{6,7} and Xin Yu^{1,3,8,*}

6 ¹High-Field Magnetic Resonance, Max Planck Institute for Biological Cybernetics, 72076
7 Tübingen, Germany.

8 ²Department of Neurology, Wuhan University, Renmin Hospital, Wuhan 430060, China.

9 ³Athinoula A. Martinos Center for Biomedical Imaging, Massachusetts General Hospital and
10 Harvard Medical School, Charlestown 02129 MA, USA.

11 ⁴Graduate Training Centre of Neuroscience, International Max Planck Research School,
12 University of Tübingen, 72074 Tübingen, Germany.

13 ⁵Department for Biomedical Magnetic Resonance, University of Tübingen, Tübingen, Germany.

14 ⁶Department of Physics, University of California at San Diego, La Jolla, CA, 92093 USA.

15 ⁷Section of Neurobiology, University of California at San Diego, La Jolla, CA, 92093 USA.

16

17

18

19

20

21

22

23

24

25

26

27 ⁸Lead Contact:

28 Address: Max-Planck-Ring. 11, 72076, Tübingen, Germany

29 Phone: +49 7071 601-740

30 Fax: +49 7071 601-701

31 *Correspondence: xin.yu@tuebingen.mpg.de; xyu9@mgh.harvard.edu

32

33 **Abstract**

34 Current approaches to high-field fMRI provide two means to map hemodynamics at the
35 level of single vessels in the brain. One is through changes in deoxyhemoglobin in
36 venules, i.e., blood oxygenation level-dependent (BOLD) fMRI, while the second is
37 through changes in arteriole diameter, i.e., cerebral blood volume (CBV) fMRI. Here we
38 introduce cerebral blood flow (CBF)-fMRI, which uses high-resolution phase-contrast MRI
39 to form velocity measurements of flow and demonstrate CBF-fMRI in single penetrating
40 microvessels across rat parietal cortex. In contrast to the venule-dominated BOLD and
41 arteriole-dominated CBV fMRI signal, the phase-contrast -based CBF signal changes are
42 highly comparable from both arterioles and venules. Thus, we have developed a single-
43 vessel fMRI platform to map the BOLD, CBV, and CBF from penetrating microvessels
44 throughout the cortex. This high-resolution single-vessel fMRI mapping scheme not only
45 enables the vessel-specific hemodynamic mapping in diseased animal models but also
46 presents a translational potential to map vascular dementia in diseased or injured human
47 brains with ultra-high field fMRI.

48

49

50

51

52

53

54

55 **Summary**

56 We established a high-resolution PC-based single-vessel velocity mapping method using
57 the high field MRI. This PC-based micro-vessel velocity measurement enables the
58 development of the single-vessel CBF-fMRI method. In particular, in contrast to the
59 arteriole-dominated CBV and venule-dominated BOLD responses, the CBF-fMRI shows
60 similar velocity changes in penetrating arterioles and venules in activated brain regions.
61 Thus, we have built a noninvasive single-vessel fMRI mapping scheme for BOLD, CBV,
62 and CBF hemodynamic parameter measurements in animals.

63

64

65 **Keywords: Phase contrast, cerebral blood flow, velocity, single vessel, fMRI, blood**
66 **oxygen level-dependent, cerebral blood volume**

67 **Introduction**

68 Cerebral blood flow (CBF) is a key readout of neuronal processing and viability in normal
69 and diseased brain states¹. Changes in CBF may be monitored directly within individual
70 blood vessels through the use of optical-based particle tracking techniques². A variety of
71 imaging methods have been developed to measure CBF across multiple spatial scales
72 from capillary beds to the vascular network in animal brains, including multi-photon
73 microscopy³, near-infrared spectroscopy (NIRS)⁴, optical coherence tomography⁵,
74 optoacoustic imaging⁶, or laser doppler and speckle imaging^{7, 8}. In particular, the doppler-
75 based functional ultrasound imaging method provides a unique advantage to detect the
76 CBF in the brain with a high spatiotemporal resolution, which can be readily applied for
77 awake animal imaging⁹⁻¹¹. However, these methods share a common barrier that the
78 spectrum-specific signal transmission cannot effectively pass the skull of animals without
79 significant loss of the signal-to-noise ratio (SNR). Typically, a craniotomy or procedure to
80 thin the skull is needed to detect the hemodynamic signal². While current techniques
81 support transcranial imaging into the superficial layers of the cortex, only functional MRI
82 (fMRI) provides a noninvasive approach for measuring hemodynamic signals throughout
83 the brain.

84 Changes in CBF may be detected by fMRI based on arterial spin labeling (ASL),
85 in which water protons in a major upstream vessel are spin-polarized with an external
86 field¹²⁻¹⁴. Two other fMRI-based techniques provide indirect information about changes in
87 CBF. Blood oxygenation level-dependent (BOLD) fMRI is used to determine changes in
88 the ratio of deoxy- to oxyhemoglobin in the blood and is a measure of changes in brain
89 metabolism^{12, 15, 16}. Cerebral blood volume (CBV) fMRI is used to measure changes in

90 blood volume, i.e., essentially changes the diameter of arterioles, based on the use of
91 exogenous or endogenous contrast agents to differentiate blood from brain tissue^{12, 17}.

92 Phase-contrast (PC) MRI relies on gradient-oriented dephasing of magnetized
93 protons to map the velocity, i.e., direction and speed, of blood flow^{18, 19}. The ASL-based
94 CBF fMRI technique detects local changes in the flow of blood through brain tissue but
95 does not show orientation-specific information related to the alignment of vessels²⁰. Past
96 works with 7 T MR scanning showed that PC-MRI can be used to measure flow in the
97 perforating arteries through the white matter or the lenticulostriate arteries in the basal
98 ganglia of human brains²¹⁻²⁴. However, the SNR was insufficient in these prior studies to
99 map changes in flow, and thus changes in CBF.

100 Here, we report on a PC-MRI method to detect the vessel-specific changes in
101 blood velocity in single trials. Compared with past implementations of PC-MRI^{21, 25-28}, we
102 have implemented a small surface radio frequency (RF) coil with the high field MRI, i.e.,
103 14.1 T for improved SNR. This further allows us to map the BOLD- and CBV-fMRI from
104 individual penetrating venules and arterioles, which span 20 to 70 μm diameter, with high
105 spatial resolution²⁹⁻³¹.

106 **Results**

107 **Phantom validation of high-resolution PC-based flow velocity measurement**

108 For calibration, we constructed an *in vitro* capillary tubing circulatory system to mimic
109 penetrating vessels, with flow rates from 1 to 10 mm/s (**Figure 1A**). A 2D PC-MRI slice is
110 aligned perpendicular to the capillary tubing (**Figure 1A, B**) and provides a voxel-specific
111 measurement of the flow velocity through two tubes with the upward flow (positive sign,
112 bright dots in **Figure 1B**) and two tubes with the downward flow (negative sign, dark dots
113 in **Figure 1B**), as well as a control tube. We observe a monotonic and near-linear relation

114 between the velocity measured by PC-MRI and the true velocity: $V_{\text{meas}} =$
115 $(0.67 \pm 0.01) v_{\text{pump}} + (0.02 \pm 0.11)$ mm/s at echo time (TE) = 5.0 ms (**Figure 1C**). The
116 small offset could be caused by eddy current effects and other gradient-related scaling
117 errors of the PC-MRI sequence³²⁻³⁴. We further observe that the measured velocities are
118 relatively insensitive to the value of TE (**Figure 1C**).

119 We implemented the high-resolution PC-MRI for *in vivo* measurement of blood flow
120 from individual penetrating arterioles and venules through the infragranular cortex, i.e.,
121 layer V, of the anesthetized rats with 14.1 T MR scanning. To improve the SNR of PC-
122 MRI images as well as multi-gradient echo (MGE) images used for arteriole-venule (A-V)
123 mapping^{29, 31}, a surface RF transceiver coil with 6 mm diameter was constructed and
124 attached to the rat skull (**Supplemental Figure 1**). This was essential for the high-
125 resolution mapping with a fast sampling rate of the single-vessel flow velocity over a
126 complete hemisphere of the rat brain (**Figure 2A and Supplemental Figure 1E**).

127 ***In vivo* PC-based flow velocity mapping of penetrating microvessels**

128 We first acquired the single-vessel A-V map by aligning a 500 μm thick 2D MRI slice
129 perpendicular to the penetrating vessels through layer V of one hemisphere (**Figure 2A,**
130 **B**). We designed the pulse sequence for PC-MRI to achieve the same slice geometry of
131 the A-V map so that the CBF deduced from PC-MRI signals could be overlaid with
132 individual penetrating arterioles and venules in the single-vessel flow velocity map
133 (**Figure 2A, C**). The arteriole blood flows down into the cortex while the venule blood
134 flows upward, which determines the sign of the flow velocity. Vessel-specific velocities
135 were plotted as a function of the normalized signal intensity in the A-V map and
136 corroborated our ability to determine flow velocity specific to arterioles and venules
137 (**Figure 2C, D**). The measured flow velocities range from 1 to 10 mm/s, as previously

138 measured with optical methods³⁵. To probe the reliability of the single-vessel MR-based
139 flow velocity method, we compared the velocities detected by PC-MRI methods with
140 different TEs and flip angles (FAs) and observed comparable results across a range of
141 parameters (**Supplemental Figure 2**). All told, these data demonstrate the feasibility of
142 *in vivo* single-vessel blood velocity mapping with the PC-based MRI method.

143 **PC-based CBF-fMRI from individual arterioles and venules**

144 We contrasted the complementary capabilities of PC-based CBF-fMRI against the signals
145 observed with the balanced steady-state free precession (bSSFP)-based single- vessel
146 BOLD- and CBV-fMRI mapping method²⁹ (**Figure 3**). We first created an A-V map
147 through the deep layers of the forepaw region of the primary somatosensory cortex
148 (**Figure 3Ai**), followed by 2D-bSSFP to detect stimulus-induced changes in the single-
149 vessel BOLD-fMRI signal (**Figure 3Aii**). We next performed single-vessel PC-MRI flow
150 velocity measurements with 100 x100 μm^2 in-plane resolution, a sampling rate of 4 s
151 repetition time (TR) per image, and the same geometry as the 2D-bSSFP method to
152 measure baseline flow in penetrating arterioles and venules (**Figure 3Aiii**). Changes in
153 CBF upon stimulation overlapped with individual penetrating vessels in the A-V map
154 (**Figure 3Aiv**). Lastly, we performed 2D-bSSFP for single-vessel CBV-fMRI mapping by
155 intravenous injection of iron particles into the blood in the same rats (**Figure 3Av**). The
156 BOLD-fMRI signal is primarily detected from individual penetrating venules while the
157 CBV-weighted signal is mainly located at the individual penetrating arterioles (dark dots
158 in **Figure 3Aii** with bright dots in **Figure 3Av**). In contrast, the CBF-fMRI signal is
159 observed in both penetrating arterioles and venules (**Figure 3Aiv**).

160 The stimulus-evoked responses of all three fMRI signals were studied with an
161 on/off block design (**Figures 3B-E**). Group analysis shows that the positive BOLD signal
162 from venule voxels is significantly higher than the arteriole-specific BOLD signal
163 (**Figure 3C**). In contrast, the arteriole dilation leads to an earlier CBV-weighted negative
164 fMRI signal, which is much stronger and faster than the signal from passive venule-
165 dilation (**Figure 3C**), as expected^{36, 37}. Group analysis shows the similar temporal
166 dynamics of CBF changes appearing as a ramp in both arterioles and venules
167 (**Figure 3E**). The CBF-fMRI signal appears as the integral of the stimulus, i.e., a triangular
168 ramp (**Figure 3E**), compared to the saturation-like BOLD and CBV responses
169 (**Figure 3C**). The voxel-wise hemodynamic changes of BOLD, CBV, and CBF are
170 illustrated in **Supplementary Figure 3** and **movie 1**.

171 **Discussion**

172 Despite the existing tools developed for CBF measurement in both animal and human
173 brains, it remains challenging to detect the flow dynamics of intracortical micro-vessels
174 non-invasively. Here, we not only optimized the PC-MRI to map the vectorized single-
175 vessel flow velocity of penetrating arterioles and venules but also developed the single-
176 vessel CBF-fMRI based on the direct flow velocity measurement in rat brains. By
177 combining with previously established single-vessel BOLD- and CBV-fMRI methods, the
178 PC-based single-vessel CBF-fMRI method complements the scheme to map the vessel-
179 specific hemodynamic responses with high-resolution fMRI.

180 In contrast to the conventional ASL methods, PC-based MRI mapping allows
181 arterioles and venules to be distinguished for simultaneous velocity measurements
182 through a 2D plane. Also, ASL has less vascular specificity because water exchange

183 through the blood-brain barrier of capillary beds increases the weighting of the ASL-based
184 flow signal for parenchyma voxels^{38, 39}. Furthermore, there is significant variability in the
185 transit time to flow from arterioles to venules through the capillary bed⁴⁰, which
186 complicates the distinction of arterioles and venules by simple ASL-based CBF mapping.
187 We detected the velocity from penetrating microvessels in the deep cortical layers with
188 PC-MRI, showing velocity values from 1 to 5 mm/s (Fig 2). Single-digit velocity (mm/s) of
189 red blood cells from cortical surface microvessels has been detected in the anesthetized
190 rats using two-photon microscopy^{2, 35}. It is noteworthy that the PC-based vessel velocity
191 measurement is based on measuring water protons in blood but not limited to the flow of
192 red blood cells. Still, the PC-based velocity from microvessels matches well with the
193 previous optical measurement. We conclude that high-resolution PC-MRI is ideal for
194 noninvasive single-vessel CBF-fMRI mapping.

195 A remaining complication with PC-MRI mapping is the presence of small offsets in
196 velocity from the phantom capillary tubing with circulating flow under different conditions.
197 The phase-dependent velocity encoding depends on the quality of the magnetic field
198 gradients, and mismatched eddy currents of multiple gradients with opposite polarities,
199 as well as the nonlinear and distorted gradient fields, could contribute to distortions in
200 gradients³²⁻³⁴. In particular, the high-resolution PC-MRI method is a high-duty cycle
201 sequence and slight heating of the gradient coil during scanning may alter the gradient
202 performance, consistent with the baseline-drift of the CBF-fMRI signal in the first 5
203 minutes of scanning (**Figure 3D**). Nevertheless, it should be noted that the percentage
204 velocity changes from individual arterioles and venules can be readily detected with the
205 PC-based CBF-fMRI measurement regardless of the gradient-heating related baseline

206 drift. Another factor that contributes to the phase-dependent velocity error originated from
207 the limited spatial resolution of the PC-MRI images compared to the diameters of small
208 vessels²⁷, although corrections are possible^{21, 28}. Despite the potential partial volume
209 contribution to the single-vessel BOLD, CBV, and CBF-fMRI, the vessel-specific mapping
210 scheme presents a translational potential to identify vascular dementia in diseased or
211 injured brains with ultra-high field fMRI.

212 **ACKNOWLEDGMENTS**

213 We thank Dr. E. Weiler, Ms. H. Schulz, and Ms. S. Fischer for animal/lab maintenance and
214 support, Dr. K. Buckenmaier and Dr. N. Avdievitch for technical support, and the Analysis of
215 Functional NeuroImages (AFNI) team for their software support. This research was supported by
216 NIH BRAIN grants R01 1NS113278 and R01 MH111438, NIH NINDS grant R35 NS097265, NIH
217 instrument grant S10 RR023009 to the Massachusetts General Hospital/Harvard-MIT Program in
218 Health Sciences and Technology Martinos Center, Deutsche Forschungsgemeinschaft (DFG,
219 Germany Research Foundation) grant YU 215/3-1, SCHE 658/15, SCHE 658/12, the
220 Bundesministerium fuer bildung und forschung (BMBF, Federal Ministry of Education and
221 Research) grant 01GQ1702, and the Chinese Scholarship Council for the doctoral support of
222 X. Chen.

223 **AUTHOR CONTRIBUTIONS**

224 X.Y. and D.K. initiated the concept; X.Y. designed the research; X.C. and X.Y. performed animal
225 experiments; X.C., Y.J. performed data analysis; P.R., K.S., S.C. provided technical support; X.Y.,
226 D.K., X.C., Y.J. wrote the paper.

227

228

229 **Methods**

230 **Design of a phantom capillary tubing flow system**

231 In order to validate the PC-MRI sequence, a plastic circulatory flow phantom composed
232 of the capillary tubing (PE-10, Instech Laboratories, inner diameter 210 μm) was
233 constructed to mimic the geometries of cortical blood vessels (**Figure 1A**). The capillary
234 tube was connected to a programmable syringe infusion/withdraw pump (Pump Elite 11,
235 Harvard Apparatus) with an infusion rate of 0.25, 0.5, 1.0, 1.5, 2.0 ml/h, which were
236 transferred to the flow velocity of the capillary tubing as shown in **Figure 1**. The flowing
237 medium is a manganese solution (50 mM MnCl_2 , Sigma-Aldrich). The phantom tube was
238 cast with Fomblin (Sigma-Aldrich) to avoid the potential air interface artifacts.

239 **Animal preparation for fMRI**

240 All surgical and experimental procedures were approved by the local authorities
241 (Regierungspraesidium, Tübingen Referat 35, Veterinärwesen, Leiter Dr. Maas) and
242 were in full compliance with the guidelines of the European Community (EUVD
243 86/609/EEC) for the care and use of laboratory animals. The experimental animals were
244 Sprague-Dawley male rats, ~ 250 g, provided by the Charles River Laboratories in
245 Germany. Fifteen rats were used in all experiments (the evoked bSSFP-BOLD/CBV and
246 PC-MRI signals were acquired from five of these fifteen rats).

247 Detailed descriptions of the surgery are given in previous publications^{29, 30}. Briefly,
248 rats were first anesthetized with isoflurane (5% induction, 1~2% maintenance), each rat
249 was orally intubated with a mechanical ventilator (SAR-830, CWE). The femoral artery
250 and vein were catheterized with plastic catheters (PE-50, Instech Laboratories) to monitor
251 the arterial blood gas, administrate drugs, and constantly measure the blood pressure.

252 After catheterization, rats were secured in a stereotaxic apparatus, a custom-made RF
253 coil was fixed above the skull with cyanoacrylate glue (454, Loctite). After surgery,
254 isoflurane was switched off and a bolus of α -chloralose (80 mg/kg, Sigma-Aldrich) was
255 intravenously injected. A mixture of α -chloralose (26.5 mg/kg/h) and the muscle relaxant
256 (pancuronium bromide, 2 mg/kg/h) was continuously infused to maintain the anesthesia
257 and minimize the motion artifacts. Throughout the whole experiment, the rectal
258 temperature of rats was maintained at 37°C by using a feedback heating system. All
259 relevant physiological parameters were constantly monitored during imaging, including
260 heart rate, rectal temperature, arterial blood pressure, the pressure of the tidal ventilation,
261 and end-tidal CO₂. Arterial blood gases were checked to guide the physiological status
262 adjustments by changing the respiratory volume or administering sodium bicarbonate
263 (NaBic 8.4 %, Braun) to maintain normal pH levels. Dextran-coated iron oxide particles
264 (15 ~ 20 mg of Fe/kg, BioPAL, MA) were intravenously injected for CBV-weighted signal
265 acquisition.

266 **fMRI setup**

267 All images were acquired with a 14.1 T, 26 cm horizontal bore magnet (MagneX Scientific)
268 interfaced through the Bruker Advance III console (Bruker Corporation). The scanner is
269 equipped with a 12 cm magnet gradient set capable of providing a strength of 100 G/cm
270 and a 150 μ s rise time (Resonance Research Inc.). A custom-made transceiver coil with
271 an internal diameter of 6 mm was used for fMRI images acquisition. For the electrical
272 stimulation, two custom-made needle electrodes were placed on the forepaw area of the
273 rats to deliver the electrical pulse sequences (330 μ s duration at 1.0 ~ 2.0 mA. The pulses
274 repeated at 3 Hz for 10 s) by using a stimulus isolator (A365, WPI). The stimulation
275 duration and frequency were triggered directly through the MRI scanner which controlled

276 by Master-9 A.M.P.I system (Jerusalem, Israel). The triggering pulses from the MRI
277 scanner were also recorded by the Biopac system (MP150, Biopac Systems, USA).

278 **Single-vessel multi-gradient echo (MGE) imaging**

279 To anatomically map the individual arterioles and venules penetrating the deep cortical
280 layers of the somatosensory cortex, a 2D MGE sequence was applied with the following
281 parameters: TR = 50 ms; TE = 2.5, 5.0, 7.5, 10.0, 12.5 and 15.0 ms; flip angle (FA) = 55°;
282 matrix = 192 x 192; in-plane resolution = 50 x 50 μm^2 ; slice thickness = 500 μm . The A-V
283 map was made by averaging the MGE images from the second TE echo to the fifth TE
284 echo. In the A-V map, the arteriole voxels show bright (red marks) due to the in-flow effect
285 and venule voxels show as dark dots (blue marks) because of the fast T_2^* decay
286 **(Figure 2B)**.

287 **Balanced steady-state free precession (bSSFP) BOLD- and CBV-fMRI**

288 The bSSFP sequence was applied to acquire the evoked BOLD signals by using the
289 following parameters: TR = 15.6 ms; TE = 7.8 ms; flip angle = 15°; matrix = 96 x 96; FOV
290 = 9.6 x 9.6 mm; in-plane resolution = 100 x 100 μm^2 ; slice thickness = 500 μm . For the
291 bSSFP CBV-fMRI, the parameters were adjusted with TR = 10.4 ms and TE = 5.2 ms.
292 The total TR to acquire each image is 1 s. To reach the steady-state, 300 dummy scans
293 were used, followed by 25 pre-stimulation scans, one scan during stimulation, and 44
294 post-stimulation scans with 10 epochs for each trial. The fMRI stimuli block design of each
295 trial consisted of 10 s stimulation and 35 s inter-stimulus interval. The total acquisition
296 duration of each trial was 7 min 55 s. CBV-weighted fMRI signals were acquired after
297 intravenous injection of dextran-coated iron oxide particles (15 ~ 20 mg of Fe/kg, BioPAL,
298 MA).

299 **Phase Contrast (PC)-MRI**

300 To measure the flow velocity of individual arterioles and venules, the PC-MRI sequence
301 was applied with the following parameters. For the *in vitro* phantom measurement: TR =
302 15.6 ms; TE = 4.2, 4.5, 5.0, 6.0 ms; flip angle = 25°; FOV = 6.4 x 6.4 mm; matrix =
303 128 x 128; in-plane resolution = 50 x 50 μm^2 ; slice thickness = 500 μm ; maximum velocity
304 (Venc) = 1.56 or 0.66 cm/s (based on the flow values); number of averages = 172. The
305 total acquisition time was 11 min 28 s. For the *in vivo* measurements: TR = 15.6 ms; TE
306 = 5 ms; flip angle = 30°; FOV = 6.4 x 6.4 mm; matrix = 64 x 64; in-plane resolution = 100
307 x 100 μm^2 ; slice thickness = 500 μm . A total TR for each image is 4 s. The total acquisition
308 duration of each trial was 16 min. To measure the blood flow velocity, bipolar flow
309 encoding gradients were applied along the slice encoding direction. The slice position
310 was anatomically identical with the slice position of the MGE imaging.

311 **Data analysis and statistics**

312 All data preprocessing and analysis were performed by using the software package,
313 Analysis of Functional NeuroImages (AFNI) (NIH, Bethesda). All relevant fMRI analysis
314 source codes can be downloaded from <https://www.afni.nimh.nih.gov/afni/>.

315 **Definition of the individual vessels**

316 The individual arteriole/venule voxels were defined by the signal intensity of the A-V
317 map³¹. The arterioles are determined if the voxel intensities are higher than the mean
318 signal intensities plus two times the standard deviation of the local area in a 5 x 5 kernel.
319 The venules are determined if the voxel intensities are lower than the mean signal
320 intensities minus two times the standard deviation of the local area²⁹⁻³¹. The locations of
321 individual arteriole/venule voxels defined in A-V map were used to extract the time
322 courses of BOLD/CBV-fMRI for individual vessels.

323 **BOLD/CBV-fMRI and PC-MRI data analysis**

324 To register the evoked bSSFP-fMRI images and evoked PC-MRI images with the 2D
325 anatomical A-V map, the tag-based registration method was applied. Twelve to fifteen
326 tags were selected from the averaged bSSFP-fMRI images or the averaged PC-fMRI
327 images to register those selected from A-V map. We used a 3dLocalstat AFNI function to
328 normalize the signal intensity of the single-vessel maps. This process allowed us to plot
329 the PC-based velocity values of individual vessel voxels to the normalized signal intensity
330 of A-V maps. For the evoked signals, the bSSFP-fMRI images and PC-MRI images were
331 normalized by scaling the baseline to 100. Multiple trials of block-design time courses
332 were averaged for each animal. No additional smoothing step was applied. The β -value
333 was calculated to measure the amplitude of the fMRI responses at each TR. The voxel-
334 wise β -map was illustrated with the spatial pattern of the fMRI responses corresponding
335 to the different time points after the stimulus onset. After registration (tag-based
336 registration) and region of interest extraction (3dLocalstat function, mask shown in
337 **Figure 2B**), we extracted the PC-based flow velocity values from individual vessel voxels,
338 which were identified based on the algorithm as described in the previous section.

339 The hemodynamic response function is based on the “block function” of 3dDeconvolve
340 module developed in AFNI. The HRF model is defined as follows:

$$341 \quad h(t) = \int_0^{\min(t,L)} s^4 e^{-s} / [4^4 e^{-4}] ds$$

342 Gamma variate function = $s^4 e^{-s} / 4^4 e^{-4}$. L was the duration of the response. BLOCK (L, 1)
343 is a convolution of a square wave of duration L, makes a peak amplitude of block
344 response = 1.

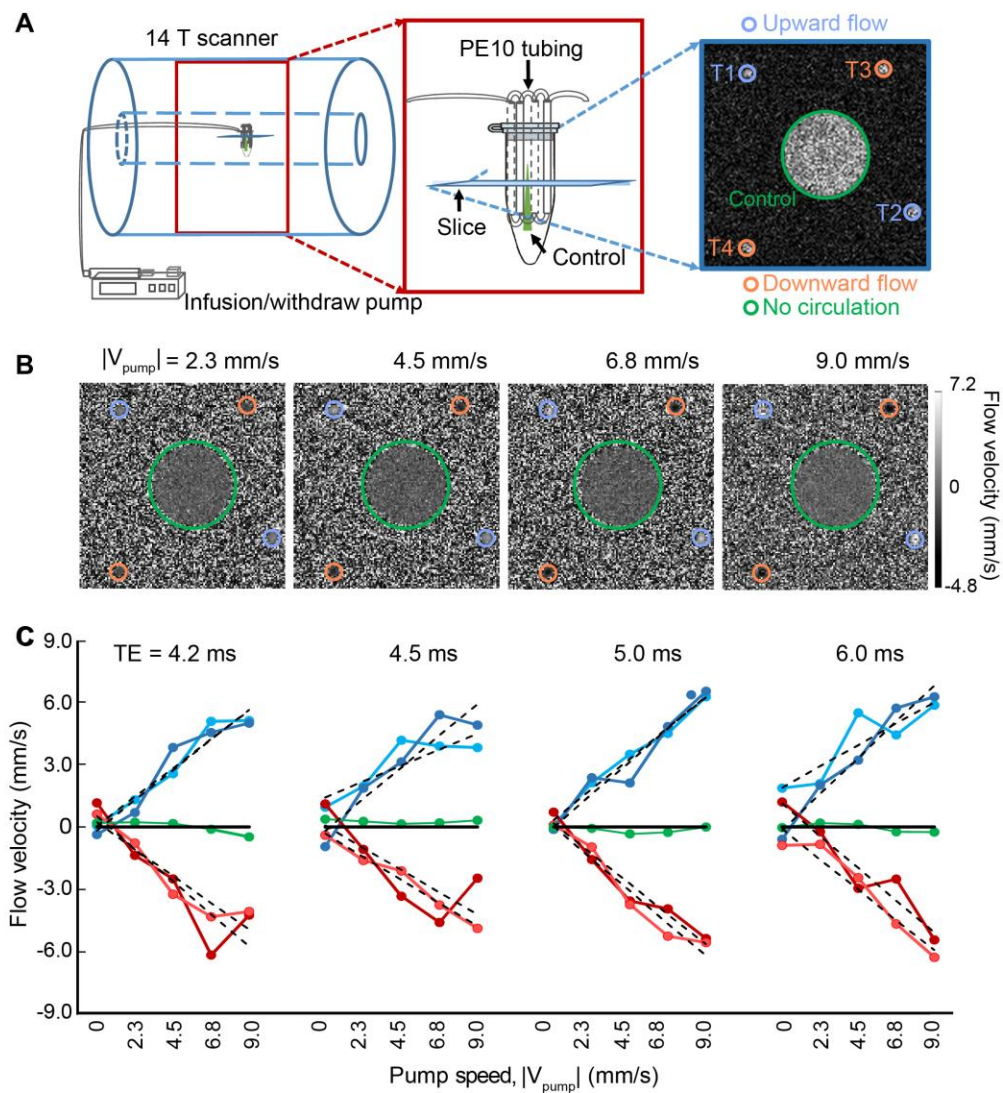
345 For the group analysis, Student's t-test was performed, error bars are displayed as the
346 means \pm SEM. The p values < 0.05 were considered statistically significant. The sample
347 size of animal experiments is not previously estimated. No blinding and randomization
348 design was needed in this work.

349 References

- 350 1. Attwell, D. et al. Glial and neuronal control of brain blood flow. *Nature* **468**, 232-243 (2010).
- 351 2. Shih, A.Y. et al. Two-photon microscopy as a tool to study blood flow and neurovascular
352 coupling in the rodent brain. *J Cereb Blood Flow Metab* **32**, 1277-1309 (2012).
- 353 3. Kleinfeld, D., Mitra, P.P., Helmchen, F. & Denk, W. Fluctuations and stimulus-induced
354 changes in blood flow observed in individual capillaries in layers 2 through 4 of rat
355 neocortex. *Proceedings of the National Academy of Sciences of the United States of
356 America* **95**, 15741-15746 (1998).
- 357 4. Jobsis, F.F. Noninvasive, infrared monitoring of cerebral and myocardial oxygen
358 sufficiency and circulatory parameters. *Science* **198**, 1264-1267 (1977).
- 359 5. Srinivasan, V.J. et al. Depth-resolved microscopy of cortical hemodynamics with optical
360 coherence tomography. *Optics letters* **34**, 3086-3088 (2009).
- 361 6. Yao, J., Maslov, K.I., Shi, Y., Taber, L.A. & Wang, L.V. In vivo photoacoustic imaging of
362 transverse blood flow by using Doppler broadening of bandwidth. *Optics letters* **35**, 1419-
363 1421 (2010).
- 364 7. Ances, B.M., Greenberg, J.H. & Detre, J.A. Laser doppler imaging of activation-flow
365 coupling in the rat somatosensory cortex. *NeuroImage* **10**, 716-723 (1999).
- 366 8. Dunn, A.K., Bolay, H., Moskowitz, M.A. & Boas, D.A. Dynamic imaging of cerebral blood
367 flow using laser speckle. *Journal of cerebral blood flow and metabolism : official journal of
368 the International Society of Cerebral Blood Flow and Metabolism* **21**, 195-201 (2001).
- 369 9. Mace, E. et al. Functional ultrasound imaging of the brain. *Nature methods* **8**, 662-664
370 (2011).
- 371 10. Sieu, L.A. et al. EEG and functional ultrasound imaging in mobile rats. *Nature methods*
372 **12**, 831-834 (2015).
- 373 11. Rungta, R.L., Osmanski, B.F., Boido, D., Tanter, M. & Charpak, S. Light controls cerebral
374 blood flow in naive animals. *Nature communications* **8**, 14191 (2017).
- 375 12. Kwong, K.K. et al. Dynamic magnetic resonance imaging of human brain activity during
376 primary sensory stimulation. *Proceedings of the National Academy of Sciences of the
377 United States of America* **89**, 5675-5679 (1992).
- 378 13. Detre, J.A., Leigh, J.S., Williams, D.S. & Koretsky, A.P. Perfusion imaging. *Magnetic
379 resonance in medicine : official journal of the Society of Magnetic Resonance in Medicine
380 / Society of Magnetic Resonance in Medicine* **23**, 37-45 (1992).
- 381 14. Williams, D.S., Detre, J.A., Leigh, J.S. & Koretsky, A.P. Magnetic resonance imaging of
382 perfusion using spin inversion of arterial water. *Proceedings of the National Academy of
383 Sciences of the United States of America* **89**, 212-216 (1992).
- 384 15. Ogawa, S., Lee, T.M., Kay, A.R. & Tank, D.W. Brain magnetic resonance imaging with
385 contrast dependent on blood oxygenation. *Proceedings of the National Academy of
386 Sciences of the United States of America* **87**, 9868-9872 (1990).
- 387 16. Ogawa, S. et al. Intrinsic signal changes accompanying sensory stimulation: functional
388 brain mapping with magnetic resonance imaging. *Proceedings of the National Academy
389 of Sciences of the United States of America* **89**, 5951-5955 (1992).

- 390 17. Belliveau, J.W. et al. Functional mapping of the human visual cortex by magnetic
391 resonance imaging. *Science* **254**, 716-719 (1991).
- 392 18. Moran, P.R. A flow velocity zeugmatographic interlace for NMR imaging in humans.
393 *Magnetic resonance imaging* **1**, 197-203 (1982).
- 394 19. Bryant, D.J., Payne, J.A., Firmin, D.N. & Longmore, D.B. Measurement of flow with NMR
395 imaging using a gradient pulse and phase difference technique. *Journal of computer*
396 *assisted tomography* **8**, 588-593 (1984).
- 397 20. Detre, J.A. & Wang, J. Technical aspects and utility of fMRI using BOLD and ASL. *Clin*
398 *Neurophysiol* **113**, 621-634 (2002).
- 399 21. Zong, X. & Lin, W. Quantitative phase contrast MRI of penetrating arteries in centrum
400 semiovale at 7T. *NeuroImage* **195**, 463-474 (2019).
- 401 22. Bouvy, W.H. et al. Assessment of blood flow velocity and pulsatility in cerebral perforating
402 arteries with 7-T quantitative flow MRI. *NMR in biomedicine* **29**, 1295-1304 (2016).
- 403 23. Kang, C.K. et al. Velocity measurement of microvessels using phase-contrast magnetic
404 resonance angiography at 7 Tesla MRI. *Magnetic resonance in medicine : official journal*
405 *of the Society of Magnetic Resonance in Medicine / Society of Magnetic Resonance in*
406 *Medicine* **75**, 1640-1646 (2016).
- 407 24. Schnerr, R.S. et al. Pulsatility of Lenticulostriate Arteries Assessed by 7 Tesla Flow MRI-
408 Measurement, Reproducibility, and Applicability to Aging Effect. *Front Physiol* **8**, 961
409 (2017).
- 410 25. Wei, Z. et al. Optimization of phase-contrast MRI for the estimation of global cerebral blood
411 flow of mice at 11.7T. *Magnetic resonance in medicine : official journal of the Society of*
412 *Magnetic Resonance in Medicine / Society of Magnetic Resonance in Medicine* **81**, 2566-
413 2575 (2019).
- 414 26. Dolui, S. et al. Comparison of non-invasive MRI measurements of cerebral blood flow in
415 a large multisite cohort. *Journal of cerebral blood flow and metabolism : official journal of*
416 *the International Society of Cerebral Blood Flow and Metabolism* **36**, 1244-1256 (2016).
- 417 27. Geurts, L.J. et al. Vascular reactivity in small cerebral perforating arteries with 7T phase
418 contrast MRI - A proof of concept study. *NeuroImage* **172**, 470-477 (2018).
- 419 28. Hoogeveen, R.M., Bakker, C.J. & Viergever, M.A. MR phase-contrast flow measurement
420 with limited spatial resolution in small vessels: value of model-based image analysis.
421 *Magnetic resonance in medicine : official journal of the Society of Magnetic Resonance in*
422 *Medicine / Society of Magnetic Resonance in Medicine* **41**, 520-528 (1999).
- 423 29. He, Y. et al. Ultra-Slow Single-Vessel BOLD and CBV-Based fMRI Spatiotemporal
424 Dynamics and Their Correlation with Neuronal Intracellular Calcium Signals. *Neuron* **97**,
425 925-939 e925 (2018).
- 426 30. Chen, X. et al. Mapping optogenetically-driven single-vessel fMRI with concurrent
427 neuronal calcium recordings in the rat hippocampus. *Nature communications* **10**, 5239
428 (2019).
- 429 31. Yu, X. et al. Sensory and optogenetically driven single-vessel fMRI. *Nature methods* **13**,
430 337-340 (2016).
- 431 32. Walker, P.G. et al. Semiautomated method for noise reduction and background phase
432 error correction in MR phase velocity data. *Journal of magnetic resonance imaging : JMIR*
433 **3**, 521-530 (1993).
- 434 33. Peeters, J.M., Bos, C. & Bakker, C.J. Analysis and correction of gradient nonlinearity and
435 B0 inhomogeneity related scaling errors in two-dimensional phase contrast flow
436 measurements. *Magnetic resonance in medicine : official journal of the Society of*
437 *Magnetic Resonance in Medicine / Society of Magnetic Resonance in Medicine* **53**, 126-
438 133 (2005).

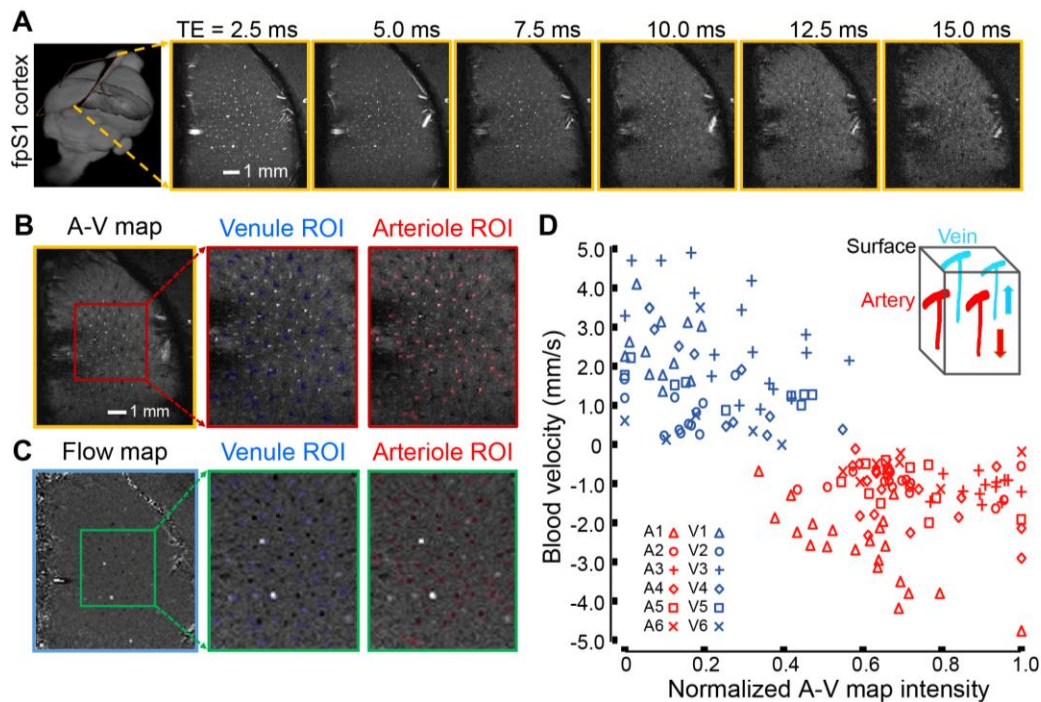
- 439 34. Bernstein, M.A. et al. Concomitant gradient terms in phase contrast MR: analysis and
440 correction. *Magnetic resonance in medicine : official journal of the Society of Magnetic*
441 *Resonance in Medicine / Society of Magnetic Resonance in Medicine* **39**, 300-308 (1998).
442 35. Schaffer, C.B. et al. Two-photon imaging of cortical surface microvessels reveals a robust
443 redistribution in blood flow after vascular occlusion. *PLoS Biol* **4**, e22 (2006).
444 36. Silva, A.C., Koretsky, A.P. & Duyn, J.H. Functional MRI impulse response for BOLD and
445 CBV contrast in rat somatosensory cortex. *Magnet Reson Med* **57**, 1110-1118 (2007).
446 37. Drew, P.J., Shih, A.Y. & Kleinfeld, D. Fluctuating and sensory-induced vasodynamics in
447 rodent cortex extend arteriole capacity. *Proc. Natl. Acad. Sci. USA* **108**, 8473-8478 (2011).
448 38. Koretsky, A.P. Early development of arterial spin labeling to measure regional brain blood
449 flow by MRI. *NeuroImage* **62**, 602-607 (2012).
450 39. Wang, J., Fernandez-Seara, M.A., Wang, S. & St Lawrence, K.S. When perfusion meets
451 diffusion: in vivo measurement of water permeability in human brain. *Journal of cerebral*
452 *blood flow and metabolism : official journal of the International Society of Cerebral Blood*
453 *Flow and Metabolism* **27**, 839-849 (2007).
454 40. Hutchinson, E.B., Stefanovic, B., Koretsky, A.P. & Silva, A.C. Spatial flow-volume
455 dissociation of the cerebral microcirculatory response to mild hypercapnia. *NeuroImage*
456 **32**, 520-530 (2006).



474 **Figure 1. *In vitro* flow velocity measurements with phase-contrast (PC)-MRI.** A. Schematic
 475 drawing of the phantom experimental flow chamber in the 14.1 T scanner. An expanded image
 476 (red box) shows the circulatory system constructed of capillary tubes. A representative fast low
 477 angle shot (FLASH) MRI image (blue box), 500 μm in thickness, shows the capillary positions.
 478 regions of interest (ROIs) T1 and T2, contoured in purple, indicate the upward flow. ROIs T3 and
 479 T4, in orange contour, indicate the downward flow. The green contour indicates the stagnant fluid.
 480 **B.** Representative images with different flow velocity in the capillaries T1 to T4 in panel A. (echo
 481 time) TE = 5.0 ms for all panels. **C.** The plot of flow velocity estimates from the five ROIs with
 482 different TEs, as marked, and different pump rates, as indicated and marked in panel B. The
 483 dotted lines correspond to a linear fitting for velocity measurements of different ROIs.

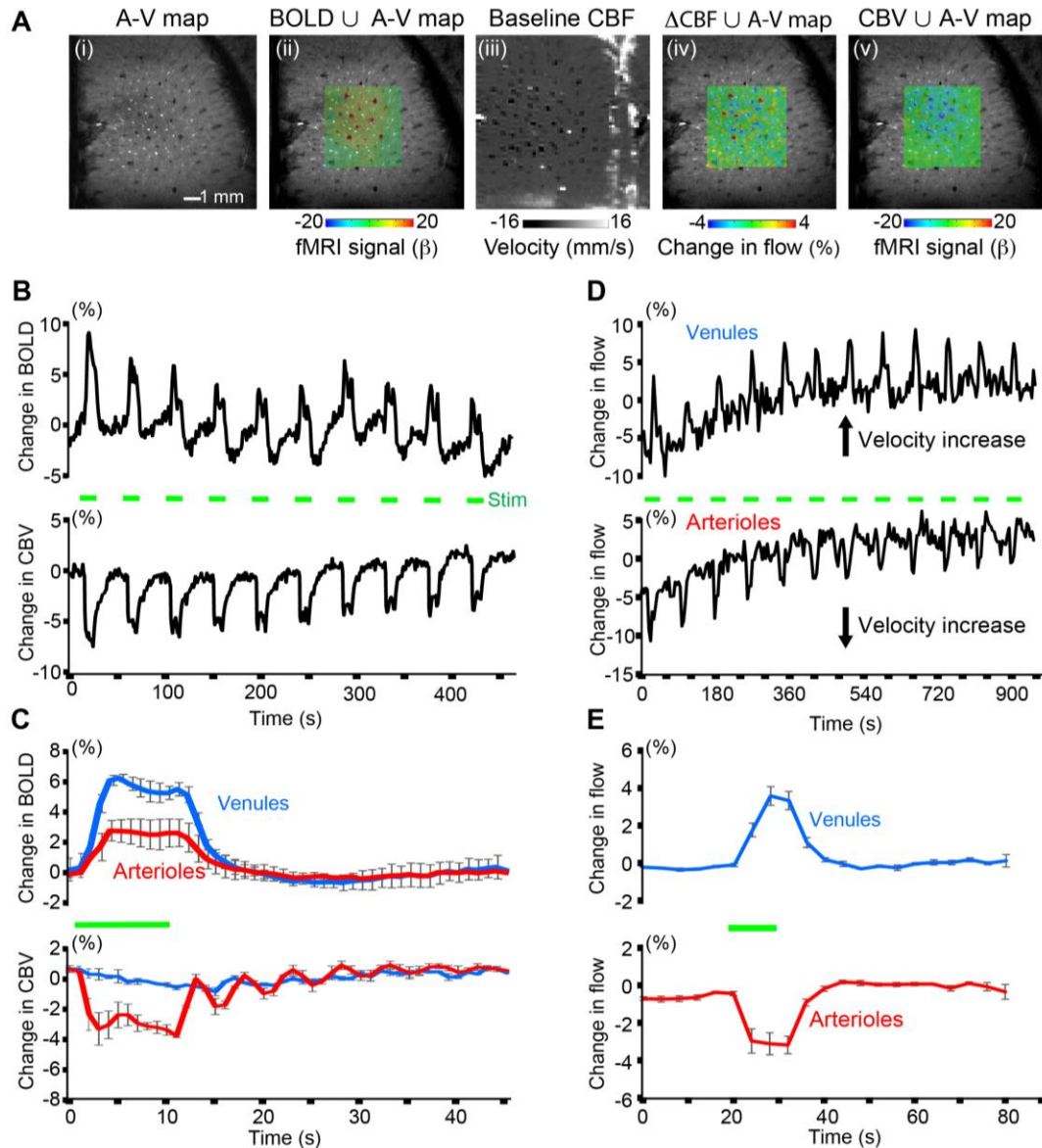
484

485



486

487 **Figure 2. Single-vessel flow velocity measurement.** **A.** Representative 2D multi-gradient echo
488 (MGE) slices (yellow boxes) from a deep layer of the primary forepaw somatosensory cortex (first
489 frame) at different TEs, as indicated. **B.** The 2D arteriole-venule (A-V) map (yellow box) derived
490 from the images with different TEs in panel A, arterioles and venules appear as bright and dark
491 voxels, respectively. The expanded views (red boxes) show individual venules, i.e., black voxels
492 marked in blue, and arterioles, i.e., white voxels marked in red. **C.** The vectorized flow velocity
493 map (blue box) from the same 2D MGE slice in panel B. The expanded views (green boxes) show
494 the individual venules, i.e., white dots with positive velocity, and arterioles, i.e., black dots with
495 negative velocity. Note that 2 bright dots are caused by the “over-flowed” velocity beyond the
496 maximal velocity, i.e., the velocity encoding (V_{enc}) parameter, defined in the PC-MRI sequence,
497 which could be not correctly estimated. **D.** Scatter plot of the flow velocities from individual
498 arterioles and venules as the function of the normalized signal intensities of each vessel in the A-
499 V map of panel B, data from 6 rats as indicated. Insert shows the blood flow direction of arterioles
500 and venules in the forepaw somatosensory cortical region.



501
 502 **Figure 3. Maps of task-related hemodynamic signals with BOLD, CBV, and CBF-fMRI. A.**
 503 Different MRI measurement strategies on the same 2D slice. From left to right: (i) The single-
 504 vessel A-V map acquired with the MGE method; (ii) The evoked balanced steady-state free
 505 precession (bSSFP)-based BOLD-fMRI signal, within the green subregion, on top of the A-V map;
 506 (iii) the PC-MRI map of baseline CBF; (iv) the change in CBF on top of the A-V map with an
 507 increased flow velocity corresponding to brighter voxels for venules and darker voxels for
 508 arterioles; and (v) the evoked bSSFP-based CBV-fMRI signal on top of the A-V map. **B.** The time
 509 courses of the evoked bSSFP-BOLD and CBV-fMRI with the block-design paradigm from the
 510 venules and arterioles shown in panel A. Forepaw stimulation pulse of 330 μ s in width and 1 mA
 511 in amplitude delivered at 3 Hz for 10 s. **C.** The averaged time courses of the fractional change for

512 the evoked BOLD and CBV signals from the venule and arteriole ROIs from different rats (mean
513 \pm SEM, the green bar shows stimulation duration). The peak BOLD values of venule are
514 significantly higher than those of arteriole (5 rats, $p = 0.009$), while the peak CBV values of
515 arteriole are significantly higher than those of venule (3 rats, $p = 0.028$). **D.** The time courses of
516 the evoked CBF changes from the arteriole and venule ROIs show increased velocity from both
517 arterioles and venules with the block–design, 10 s duration stimulation paradigm. **E.** The
518 averaged time courses of the evoked CBF changes show the velocity increase from both arteriole
519 and venule ROIs with the block–design stimulation paradigm from 4 rats (mean \pm SEM, the green
520 bar shows stimulation duration).

521
522
524
525
526
527
528
529

Supporting information

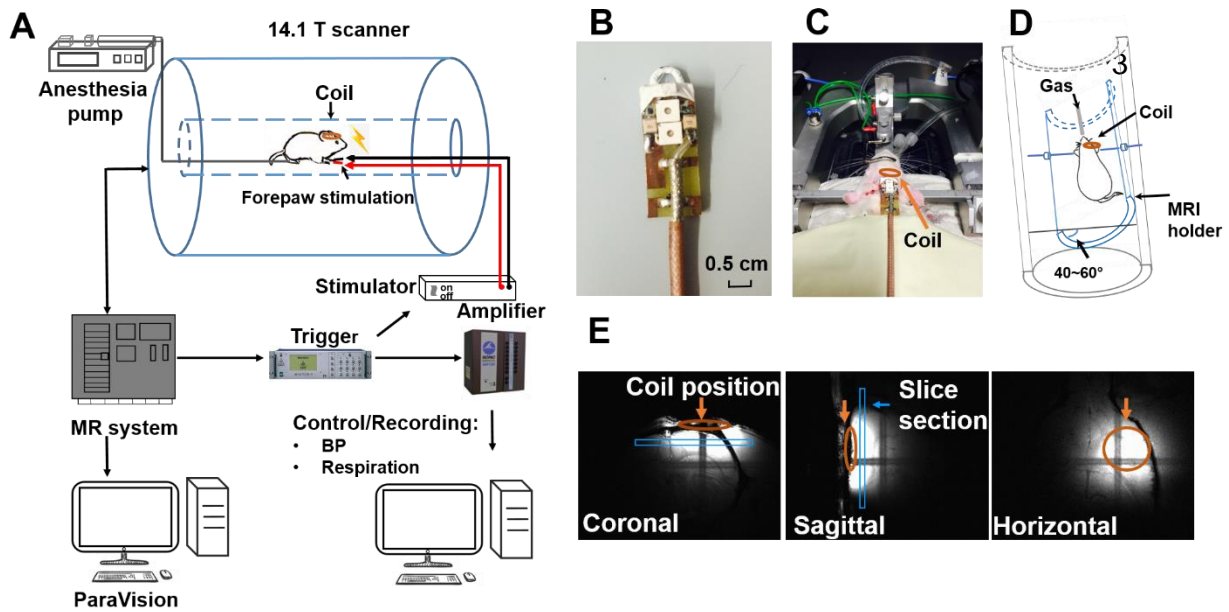


Figure S1. The preparation of *in vivo* experiment for the PC-MRI in 14.1 T.

- A.** The flow chart of the *in vivo* experiment in the 14.1 T scanner.
- B.** Photograph of the custom-made transceiver surface RF coil.
- C.** Photograph of the coil position: the coil is glued to the rat skull.
- D.** The schematic drawing of the rat position inside the MRI holder.
- E.** Representative images from different views of the FLASH MRI show the ideal coil position.

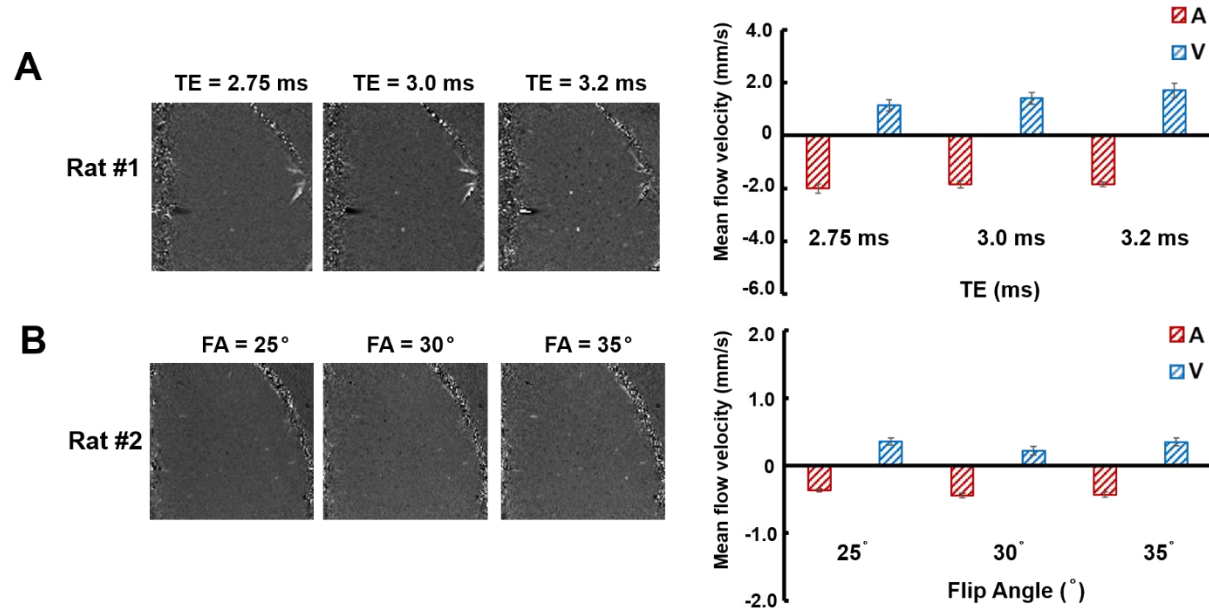


Figure S2. Phase images from the different representative rats with different TEs and flip angles.

A. Phase images from a representative rat with different TEs, i.e., 2.75, 3.0, and 3.2 ms. The right panel shows the mean blood flow velocity (mean \pm SEM) from left images with $N_{\text{Arteriole}} = 48$ and $N_{\text{Venule}} = 22$.

B. Phase images from a representative rat with different flip angles, i.e., 25°, 30°, and 35°. The right panel shows the mean blood flow velocity from left images with $N_{\text{Arteriole}} = 38$ and $N_{\text{Venule}} = 14$.

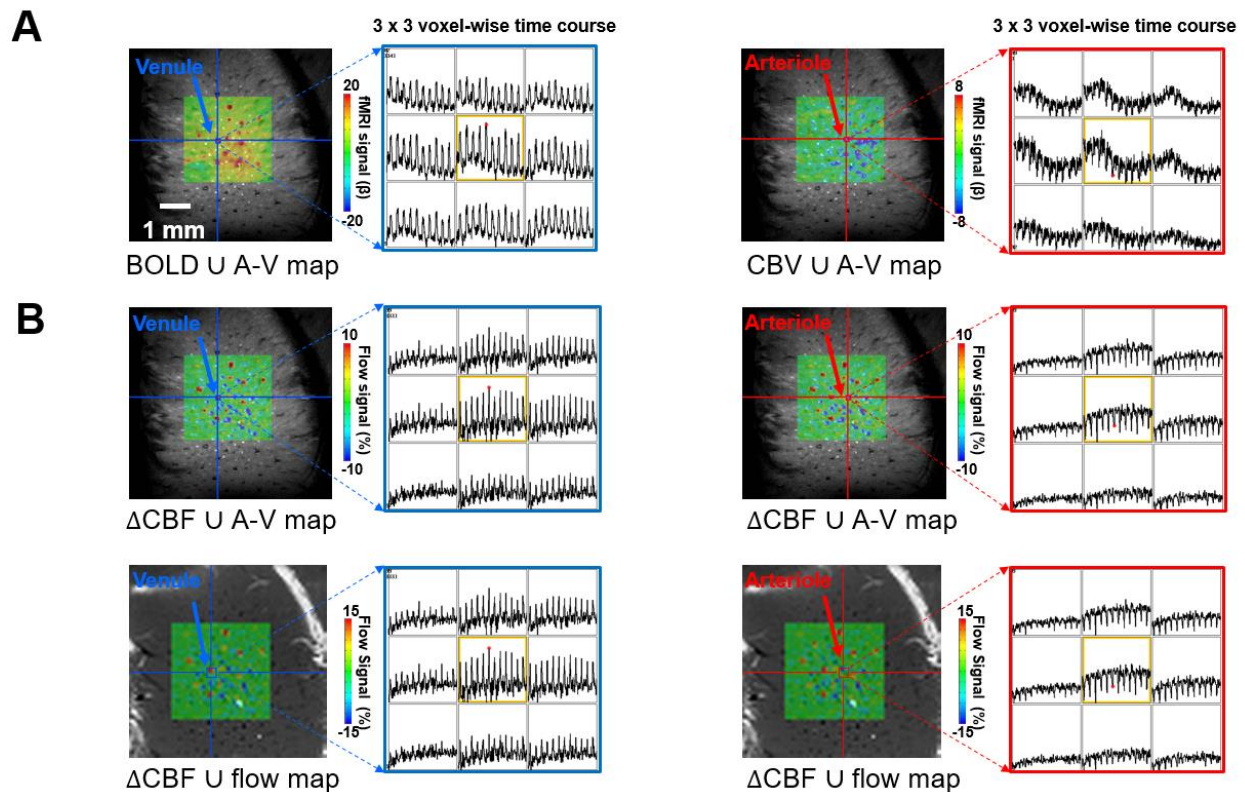


Figure S3. The bSSFP-based single-vessel BOLD/CBV-fMRI and the PC-MRI based single-vessel dynamic flow measurement from a representative rat.

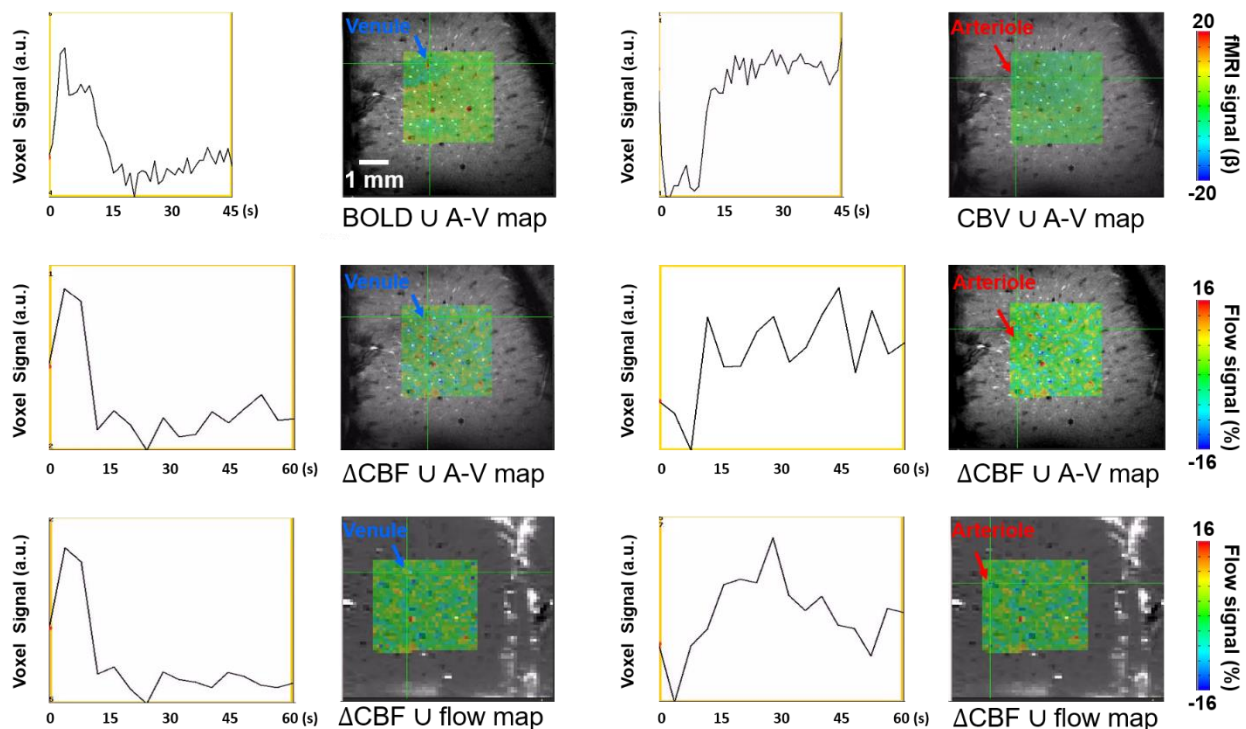
A. The evoked bSSFP-based BOLD- (left) and CBV- (right) fMRI maps overlaid on the same A-V map from a representative rat, with the voxel-wise time courses from the ROIs of individual venule (blue arrow) and arteriole (red arrow) (10 s on and 35 s off for 10 epochs plotted in a 3 x 3 matrix).

B. The evoked CBF maps overlaid on both A-V map (upper panel) and PC-based flow map (lower panel) from the same representative rat. The voxel-wise time courses of CBF changes from the same ROIs of individual venule (blue arrow) and arteriole (red arrow) (10 s on and 50 s off for 12 epochs plotted in a 3 x 3 matrix).

Supplementary Movie Legends

Movie 1. The bSSFP-based single-vessel BOLD/CBV-fMRI and the PC-MRI based single-vessel dynamic flow measurement in the rat cortex.

The upper panel shows the evoked bSSFP-based BOLD- (left) and CBV- (right) fMRI maps overlaid on the 2D A-V map with $50 \times 50 \mu\text{m}^2$ in-plane and the time course from a single voxel located at a representative venule (blue arrow) and arteriole (red arrow) (10 s on and 35 s off for a total of 45 s time window with $\text{TR} = 1$ s). The middle panel shows the evoked CBF maps overlaid on the same 2D A-V map from the same individual venule (left) and arteriole (right), of which the CBF-fMRI maps were registered to match the 2D A-V map at the $50 \times 50 \mu\text{m}^2$ resolution, as well as the time courses of the PC-based flow velocity dynamic changes from same voxels identified as the upper panel (10 s on and 50 s off for a total of 60 s time window with $\text{TR} = 4$ s). The lower panel shows the evoked CBF maps overlaid on the PC-based flow map with $100 \times 100 \mu\text{m}^2$ resolution and the time course from the voxels located at the representative venule (left) and arteriole (right). Note that the venule is a bright voxel and arteriole is a dark voxel in the flow map, which is opposite to the A-V map and also the slightly different time course due to the altered spatial resolution.



ARTICLE

<https://doi.org/10.1038/s41467-019-10450-3>

OPEN

MRI-guided robotic arm drives optogenetic fMRI with concurrent Ca^{2+} recording

Yi Chen^{1,2}, Patricia Pais-Roldan^{1,2}, Xuming Chen^{1,3}, Michael H. Frosz ⁴ & Xin Yu ^{1,5}

Optical fiber-mediated optogenetic activation and neuronal Ca^{2+} recording in combination with fMRI provide a multi-modal fMRI platform. Here, we developed an MRI-guided robotic arm (MgRA) as a flexible positioning system with high precision to real-time assist optical fiber brain intervention for multi-modal animal fMRI. Besides the ex vivo precision evaluation, we present the highly reliable brain activity patterns in the projected basal forebrain regions upon MgRA-driven optogenetic stimulation in the lateral hypothalamus. Also, we show the step-wise optical fiber targeting thalamic nuclei and map the region-specific functional connectivity with whole-brain fMRI accompanied by simultaneous calcium recordings to specify its circuit-specificity. The MgRA also guides the real-time microinjection to specific deep brain nuclei, which is demonstrated by an Mn-enhanced MRI method. The MgRA represents a clear advantage over the standard stereotaxic-based fiber implantation and opens a broad avenue to investigate the circuit-specific functional brain mapping with the multi-modal fMRI platform.

¹Research Group of Translational Neuroimaging and Neural Control, High-Field Magnetic Resonance, Max Planck Institute for Biological Cybernetics, 72076 Tuebingen, Germany. ²Graduate Training Centre of Neuroscience, University of Tuebingen, 72076 Tuebingen, Germany. ³Department of Neurology, Renmin Hospital of Wuhan University, Wuhan University, 430060 Wuhan, China. ⁴Max Planck Institute for the Science of Light, 91058 Erlangen, Germany. ⁵Athinoula A. Martinos Center for Biomedical Imaging, Massachusetts General Hospital and Harvard Medical School, Charlestown, MA 02129, USA. Correspondence and requests for materials should be addressed to X.Y. (email: xin.yu@tuebingen.mpg.de)

A multi-modal brain mapping platform for animals has been established by merging the fiber optic-mediated optogenetic activation and neuronal Ca^{2+} recording with functional magnetic resonance imaging (fMRI)^{1–5}. Given its non-magnetic properties, the optical fiber can be used in combination with fMRI brain mapping without electromagnetic interference with the radio frequency (RF) transmission and magnetic gradient switching of the MR scanner^{2,3,6,7}. The increased cellular specificity of genetic labeling reassures the advantageous usage of optical fiber recording/imaging to track neural spiking activity in the deep brain regions^{8–13}. However, one emerged challenge is how to precisely target specific functional nuclei in the animal brain^{8,14}. The procedure of fiber optic implantation in rodent studies has been commonly performed with conventional stereotaxic devices^{2,3,7–11,14,15}, but the success rate to precisely target the deep brain nuclei remains low, especially for the functional nuclei that cover only a few hundred microns space in the animal brain, e.g., the central thalamic nuclei⁸. A solution to precisely target the genetically labeled neuronal tracts or subdivisions of functional nuclei could significantly improve the reproducibility of basic scientific discoveries. Here, we report an MRI-guided robotic arm (MgRA) positioning device to maneuver the real-time fiber optic implantation into the animal brain inside a high-field MR scanner (14.1 T), intended for parallel optogenetics and/or calcium imaging and fMRI studies.

The genetic expression of channelrhodopsins (ChR2) has been extensively applied to target-specific cell types in the deep brain nuclei, such as the dopaminergic neurons in the midbrain⁹, the orexin in the lateral hypothalamus (LH)^{16,17} or noradrenergic neurons in the locus coeruleus¹⁸. The cell-type specific genetic labeling ensures the optogenetic activation on neuronal ensembles of interest assuming that the optical fiber is precisely located at the functional nuclei. However, the stereotaxic device-driven fiber optic implantation scheme shows little flexibility after the fiber tips are fixed in the brain for either fMRI mapping, electrophysiological recordings, or behavioral studies^{8,19}. The precise coordinates of a certain functional brain nucleus can vary between different animals, and incorrect positioning may result in largely altered functional activation and behavioral outcomes. This systematic error, which is intrinsic to the blind optical fiber

placement, can potentially conceal important discoveries and lead to inappropriate conclusions in causality analysis. Using MgRA assisted fiber-optic insertion in combination with real-time fMRI, we can provide a step-wise optogenetic activation scheme to allow multi-site targeting through a fiber insertion trajectory during the fMRI study. This strategy can not only improve the precision, but also provide a thorough view to examine the subtle differences in the whole brain activation patterns when targeting the sub-regions of the functional nuclei of interest.

Numerous efforts have been made to develop robotic positioning systems inside the MRI scanner for translational application from animals to the clinical practice, e.g., deep brain stimulation or brain tumor ablation^{20–26}. In contrast to the growing access to robotic manipulation strategies inside large-bore MRI scanners (e.g., 1.5 or 3 T human scanner), there are only a handful of works that have implemented remote controlling systems inside high field MRI scanners with smaller bore (>7 T, <12 cm gradient bore size), which have been applied to adjust sample orientation within the B_0 field²⁷ or to tune RF coil arrays²⁸. To the best of our knowledge, there is currently no MRI-compatible robotic control system to assist fiber optic insertion in small bore high field MRI scanners (>9.4 T) for optogenetic fMRI studies. Hence, as a proof-of-concept, we developed an MgRA to provide a flexible positioning system inside a 14.1 T MRI scanner which assists fiber optical brain intervention in animals. Besides an ex vivo precision evaluation, we present a series of in vivo studies showing the whole brain activity patterns upon optogenetic stimulation of MgRA-targeted nuclei in the LH or thalamus in a step-wise manner and with simultaneous fiber-optic calcium recordings to specify the region-specific optogenetic activation patterns. In addition, the MgRA system can be applied for region-specific deep brain microinjection. Here, we demonstrate a series of high precision brain interventional applications in the context of multi-modal neuroimaging using the MgRA system.

Results

Mechanical design of the MgRA with ex vivo operation. A stepper motor-driven MgRA was designed for real-time control of the insertion of an optical fiber into animal brains inside a 14.1

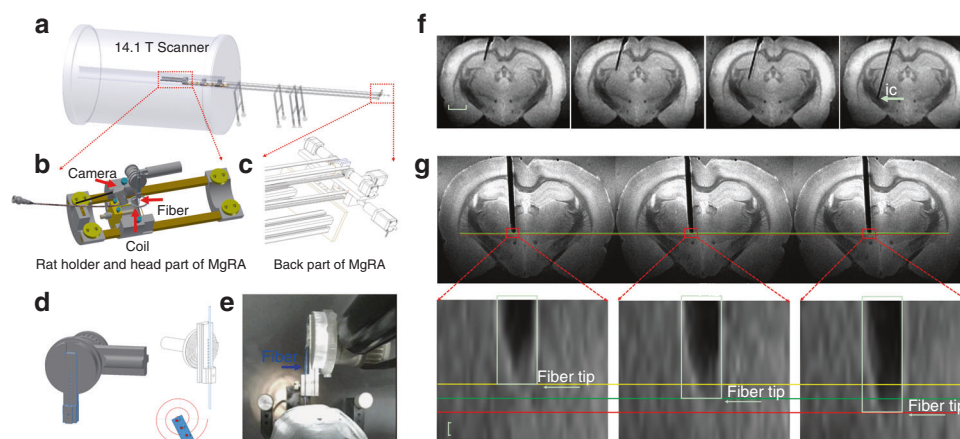


Fig. 1 3D view of the MgRA and its application in ex vivo studies. **a** Overview of the MgRA inside the 14.1 T MR scanner. **b** Schematic of the customized animal holder and head part of the MgRA. Both MR compatible camera and surface transceiver coil are included for monitoring the fiber optic insertion inside the MR scanner. **c** Stepper motors implemented at the back part of the MgRA to control up to four degrees-of-freedom movement. The long arm reaching 4.7 m away from the magnetic center point excludes the influence by the ultra-high magnetic field. **d** Schematic drawing of the Archimedean spiral design to transmit the dorsal-ventral movement. **e** Snapshot of the mechanically controlled fiber optic movement videotaped by the built-in camera. **f** Time-lapsed images showing the optical fiber targeting the hippocampus, thalamus, and internal capsule along the insertion trajectory. Scale bar, 2 mm. **g** Three continuous MRI anatomical images with step distance 50 μm (the MRI in-plane resolution is $50 \times 50 \mu\text{m}^2$, thus it can be seen that the distance moved in each step is approximately 50 μm). Scale bar, 50 μm

T scanner (Fig. 1a, 3D schematic view in Supplementary Movie 1, Supplementary Fig. 1). The MgRA contains two key parts: the front part (head of the MgRA) includes the driving pieces and a customized rat holder (Fig. 1b), and the back part accommodates the stepper motors to fulfill the optical fiber movement with multi-degree of freedom (Fig. 1c). The coupling of the actuator (back part) to the matching toothed pulley in the head was achieved by a synchronous belt drive (Fig. 1c) in a form-fit manner, without slippage and run at constant speed. Insertion of the optical fiber in the dorsal-ventral direction into the rat brain is executed using an Archimedean spiral mechanism to achieve high precision and accuracy (Fig. 1d). With a built-in MRI compatible camera, the insertion of the optical fiber could be monitored outside of the scanner to verify the effectiveness, safety, and feasibility of the MgRA (Fig. 1e and Supplementary Movie 2), simultaneously tracked with anatomical MRI. The assembly of all components provides the MgRA unique features in a portable frame that can be easily located inside the MRI room substituting the conventional subject table. A more detailed description of MgRA can be found in Methods and Supplementary Figs. 11–13.

The MgRA was first evaluated in perfused brains embedded in agarose (Fig. 1f), in order to simulate the procedure of intracerebral fiber insertion in the living animal. The optical fiber was first inserted into the agarose-embedded brain preparation in a 100 μm step-wise manner, and real-time MRI images were acquired to monitor the movement trajectory and to identify the location of the fiber tip (Supplementary Movie 3). Precision of the MgRA was determined as the smallest step in the dorsal-ventral direction that could be maneuvered based on the remote stepper motor controlling. Figure 1g shows the step-wise movement of the fiber inside the rat brain at 50 μm per step with high-resolution MRI time-lapsed 2D images (Supplementary Movie 4). It is worth noting that fiber insertion trajectories can be optimized with special angles to target specific deep brain nuclei or fiber bundles while avoiding disturbance of neural circuits, projection pathways of interest or certain brain vessels. For instance, an angled fiber optic insertion can be implemented to target the internal capsule to preserve the ascending pathway of the thalamocortical circuits (Fig. 1f and Supplementary Fig. 2). In summary, MgRA-based fiber optic insertion in the *ex vivo* brain verifies its functionality and demonstrates the stability in terms of remote motor control.

In vivo MgRA-driven fiber insertion with optogenetic fMRI.

MgRA allows the insertion of optical fibers *in vivo* inside the 14 T MRI scanner, which induces great advantages for optogenetic fMRI studies^{3,29,30}. To locate the fiber tip prior to intracerebral insertion inside the MRI scanner, two procedures were followed. First, we implemented two MRI-compatible cameras to visually locate the fiber tip, as well as the craniotomy on the animal skull (Fig. 2a and Supplementary Movie 5). Second, a prior application of a manganese-treated agarose gel was applied over the skull and the sequential lowering of the fiber was monitored with real-time anatomical MRI to locate the fiber tip as well as the craniotomy hole on the skull to guide the fiber targeting inside the brain (Supplementary Fig. 3). A more detailed description can be found in Methods, Supplementary Fig. 3. Figure 2b shows snapshots of the fiber tip outside the brain during the MgRA-driven fiber insertion. Figure 2c demonstrates an example of the *in vivo* fiber targeting of subcortical thalamic regions. Also noteworthy is the bleeding-induced T2-weighted signal drop when the fiber was inserted through the lateral ventricle (Fig. 2c). When a fiber tip first reaches a ventricle, its pushing force causes deformation of the surrounding ependyma, which can induce minor bleeding from the choroid plexus. This observation should raise a note of

caution to target deep brain regions. The damage could be reduced by decreasing the insertion speed, which can be accomplished at approximately 20 $\mu\text{m}/\text{s}$ with the MgRA (Supplementary Movie 5 and Supplementary Fig. 4).

Fiber optic insertions with customized angles can also be applied with MgRA for the *in vivo* animal fMRI environment. Figure 2d shows the step-wise fiber tip targeting to the hippocampus and ventral posteromedial nucleus (VPM) of the thalamus by inserting the optical fiber with a 40° angle from the midline. Figure 2e demonstrates the whole brain BOLD fMRI map upon optogenetic activation of either the hippocampus or the VPM, based on the MgRA-driven step-wise fiber tip localization. Thus, the implementation of MgRA in standard opto-fMRI workflows provides flexibility to guide an optical fiber along a certain insertion trajectory, allowing to target different nuclei in a single fMRI experiment, and hence, to study whole brain responses upon deliberate region-specific stimulation.

Whole brain fMRI with LH optogenetic activation. The MgRA can be used to target the deep brain nuclei with much higher precision for fiber optic-mediated optogenetic activation than the conventional stereotaxic-based fiber implantation on bench. For example, the LH is a heterogeneous nucleus with highly varied cell types across a few millimeter space in the ventral brain³¹. The MgRA-driven fiber optic positioning provides a reliable and precise targeting scheme for the LH optogenetic activation during fMRI. Figure 3a shows ChR2 expression with the AAV viral vector AVV9.CaMKII.ChR2.eYFP into the LH and the fiber optic trace to target the LH in the histological slice, as well as the MR image showing how the fiber tip coincides with the traced site of viral injection. The whole brain activation pattern upon the LH optogenetic activation is presented in Fig. 3b, showing the blood oxygen level dependent (BOLD) signal along the ascending projection to the basal forebrain from the LH. Figure 3c shows the temporal evolution of the optogenetically evoked BOLD signals in both LH and its projected basal forebrain regions with the mean time courses acquired at different stimulation durations. Figure 3d shows the mean BOLD signal time courses from both nuclei with varied optical light pulse frequencies and pulse widths (whole brain functional patterns at varied pulse width are shown in Supplementary Fig. 5). The BOLD amplitude dependency on the light pulse parameters provides strong evidence for reliable detection of the functional projections from the LH with optogenetic fMRI. It is also noteworthy that MgRA-driven fiber optic implantation ensures highly comparable activation patterns in the LH across different animals (results from 5 individual rats, Fig. 3b), as well as the activation of areas in the basal forebrain including the lateral preoptic area (LPO), medial preoptic area (MPA), and the strial part of the preoptic area (StA) (the co-registered brain atlas to the individual rat functional map, Fig. 3b). Additionally, the evoked calcium and BOLD signals in the barrel cortex (BC) were observed in these animals upon somatosensory whisker stimulation (Supplementary Fig. 6), which indicates a stable physiological state of the animal and therefore validates the biological data acquired from these experiments. These results indicate that MgRA provides high targeting accuracy and effectiveness to target deep brain circuits and produce optogenetically-driven brain activation in a highly reliable manner.

Step-wise optogenetically driven fMRI and calcium recording.

The flexibility and high precision of MgRA-driven fiber optic targeting was further verified in a series of experiments that combined optogenetic activation with concurrent fMRI and calcium fiber optic recording (Fig. 4a). This multi-modal fMRI

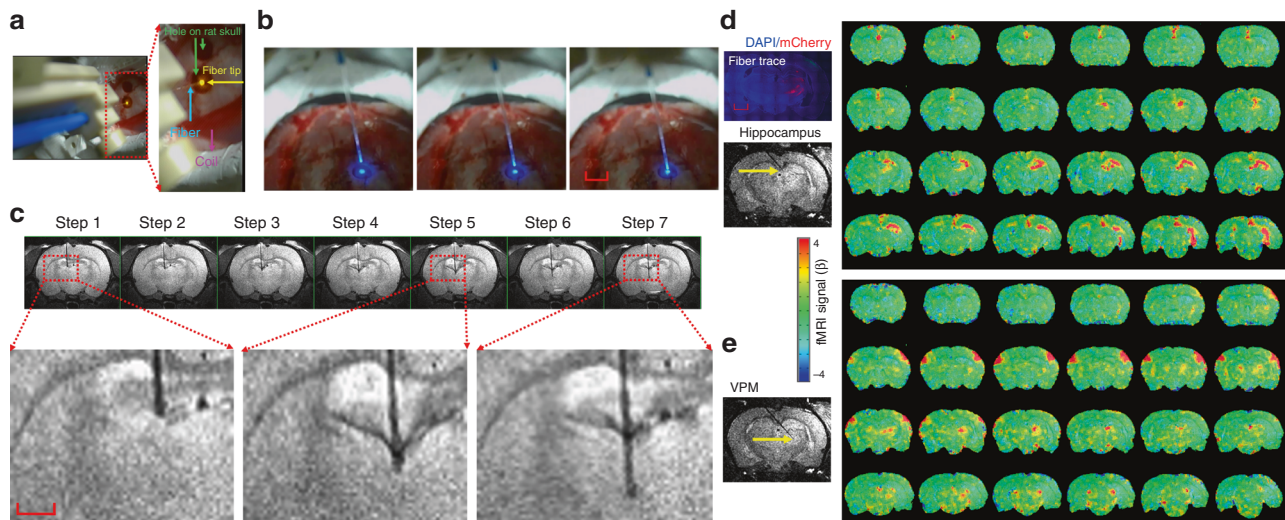


Fig. 2 Evaluation of MgRA for in vivo studies and brain-wide opto-fMRI patterns in multiple targets. **a** Snapshot of the optical fiber (tip with 589 nm wavelength laser light, yellow arrow) positioned above the burr hole (green arrow) on the skull of an anesthetized rat with the driving piece of the head part. **b** Camera-based fiber optic movement for three steps outside the rat brain. The fiber tip delivers blue laser light (473 nm wavelength). The bright ring-structure above the rat skull is the RF surface coil. Scale bar, 2 mm. **c** Potential collateral damage from the choroid plexus when the fiber was lowered to pass through the lateral ventricles, shown as a dark signal below the hippocampus. The step size was 300 μm . Scale bar, 1 mm. **d** Left, histological image demonstrates Chr2-mCherry expression in most of the thalamus and part of hippocampus. Red, Chr2-mCherry; blue, 4',6-Diamidino-2-phenylindole (DAPI). Right, the fiber tip targets the hippocampal area and the BOLD fMRI map shows the activated area primarily located in the ipsilateral hippocampal structure. Scale bar, 2 mm. **e** The fiber tip targets the ventral postero-medial (VPM) thalamus and map of BOLD activity was detected in bilateral vibrissal S1 cortex in response to blue light stimulation. (For both (**d**) and (**e**), 3D whole brain EPI: 400 μm isotropic resolution, 1.5 s repetition time; stimulation block design: 8 s on 37 s off; laser pulse: 10 ms, 5 Hz, 3.7 mW/200 μm core diameter of fiber tip)

scheme with MgRA enables real-time feedback at the level of the whole brain (via fMRI) and specifically from the fiber tip (via optical fiber) regarding the activation of the projection structures upon region-specific stimulation. Here, calcium imaging was acquired from the neurons in the BC that received afferents from the subcortical thalamic region by using the calcium reporter GCaMP6^{4,5,12}; optogenetic stimulation was performed on the VPM thalamic nuclei, after expression of the light-sensitive protein Chr2 (Fig. 4b–d)^{2,3,32}. The recording fiber was directly implanted to record the GCaMP6f-mediated calcium signal in the BC, while the optogenetic activation fiber was controlled by the MgRA inside the scanner with real-time anatomical and functional MRI to track the insertion trajectory. The MgRA guided the fiber tip to deliver the optogenetic activation at multiple sites along the insertion trajectory (Fig. 4e and Supplementary Movie 6). Evoked calcium and BOLD signals from the somatosensory cortex ipsilateral to the targeted thalamic nucleus increased in a stepwise manner as the optical fiber was moved closer to the VPM region, while, after the fiber bypassed the VPM region, BOLD and calcium signal decreased accordingly (Fig. 4f–i). There was a slightly different stepwise fMRI response from the contralateral somatosensory cortex as well (Fig. 4h, i), which has been previously reported with electrical stimulation^{33,34}. To further demonstrate the reliability of MgRA, five power levels of light pulses were used to trigger increased BOLD and simultaneous calcium signals (Supplementary Fig. 7). Moreover, by altering the frequency of the light from 0.5 to 5 Hz, we could observe a fully recovered evoked calcium baseline signal at 0.5 Hz and elevated calcium signals from 1 to 3 Hz, while at 5 Hz, the overall plateau amplitude was not further increased (Supplementary Fig. 8). The BOLD signal increased with higher frequency, but not at 5 Hz, which was consistent with the calcium signal dynamics (Supplementary Fig. 8). Results from two additional rats with different or similar insertion trajectories

confirmed the reliability of the stepwise optogenetic activated fMRI and calcium signals acquired using the MgRA (Supplementary Figs. 9 and 10). These experiments further demonstrate the unique capability of the MgRA to specifically target subcortical nuclei, which, combined with cortical recordings in the projection area, allow unequivocal stimulation of the target sites.

MgRA-driven Mn-injection into CL and LH. The MgRA can also be used to guide the real-time microinjection with high precision inside the MRI scanner. MnCl₂ solution was used as the MR contrast agent and a modified MPRAGE sequence³⁵ (Mdef, ~4 min) was implemented to detect the manganese-enhanced T1-weighted MRI signal^{15,36–38}. As shown in Fig. 5a, a hollow core optical fiber^{39–41} was used to target the central lateral thalamic nucleus (CL) and Mn solution was delivered in two consecutive steps. The initial stop was introduced to target the corpus callosum with a small dosage of Mn delivery (Fig. 5b), illustrating the real-time guided injection to target the callosal fibers with a few hundred micron thickness. When the fiber tip as located at the CL (position was verified with a T2-weighted MR image (RARE) overlapped with the brain atlas), Mn solution was injected for three times to show dose-dependent signal changes in the T1-weighted Mdef images acquired before and after Mn injection (Fig. 5b). This result demonstrates the real-time injection capabilities of the MgRA.

Besides the multiple stops along the single trail of injection trajectory, the MgRA can be used to drive multi-trial microinjection, e.g., to the lateral hypothalamic nucleus from the same rat, inside the MRI scanner. As shown in Fig. 5c, the fiber tip was guided to target the LH. The Mdef images were acquired before and after the injection (3 times, Fig. 5d, e), showing clear effective Mn delivery to the LH. In addition, we continuously acquired the Mdef images within the first ~1 h following the injection, showing highly robust and confined Mn-enhanced signal of the

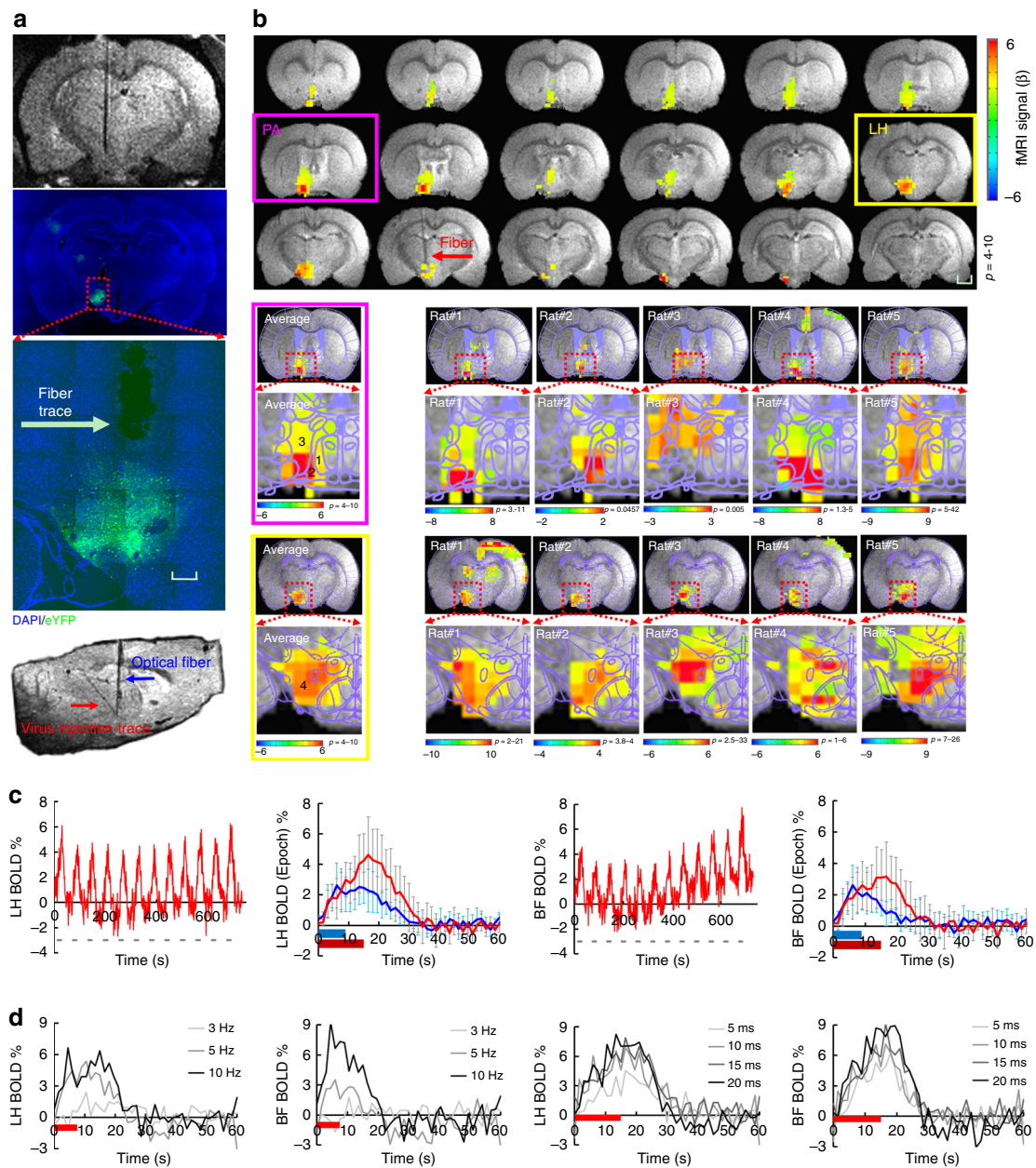


Fig. 3 MgRA-driven fiber optic targeting of the lateral hypothalamic nuclei with optogenetic fMRI. **a** Top: representative RARE anatomical image used to clarify the optical fiber location driven by MgRA for optical stimulation in LH. Middle: representative wide-field fluorescence image illustrating robust ChR2-eYFP expression focused on LH. Fiber optic insertion trace marked with white arrow. Scale bar, 200 μ m. Bottom: sagittal RARE anatomical image showing the fiber optic trace (blue arrow) and virus injection trace (red arrow). **b** Top: average fMRI map of brain-wide activity during optogenetic stimulation of LH neurons at 5 Hz, 20 ms pulse width, 15 s duration. Middle: averaged evoked BOLD map (left) and the same map from 5 individual rats (right) zoomed in on the basal forebrain (BF) showing activation of the lateral preoptic nucleus (LPO) and medial preoptic area (MPA), overlaid with the brain atlas. Bottom: average evoked BOLD map (left) and 5 individual rats (right) in lateral hypothalamic region, overlaid with the brain atlas. GLM-based *t*-statistics in AFNI is used. Scale bar, 2 mm. **c** Average time courses of significantly modulated voxels showing fMRI signal changes within the ipsilateral LH and BF (*n* = 5 animals) upon optogenetic stimulation of block design: 15 s on/45 s off, 12 epoch, 20 ms light pulse, 5 Hz, 18.9 mW. The individual hemodynamic response shows the average BOLD signal upon different stimulation durations (8 s in blue, 15 s in red). Error bars represent mean \pm SD across 5 animals. **d** Average stimulation duration-locked time evolution for both LH and BF depicting the frequency-dependent hemodynamic responses at 3, 5, and 10 Hz with 8 s stimulus duration, as well as pulse-width-dependent hemodynamic responses at 5, 10, 15, and 20 ms with 15 s stimulus duration, from one representative rat

targeted regions with limited diffusion (Fig. 5f and Supplementary Movie 7). The MgRA-driven microinjection was reproduced in multiple animals, suggesting a highly robust performance of the MgRA to target deep brain nuclei for injection purposes, as quantified in Fig. 5g. The high spatial specificity of MgRA-driven

microinjection can be used to improve the tract-tracing studies with MEMRI^{15,36–38}, as well as to optimize the real-time *in vivo* neuromodulation or molecular MRI by direct intracranial injection of drugs^{42–44} and MRI contrast sensors for neurotransmitters^{45–49}.

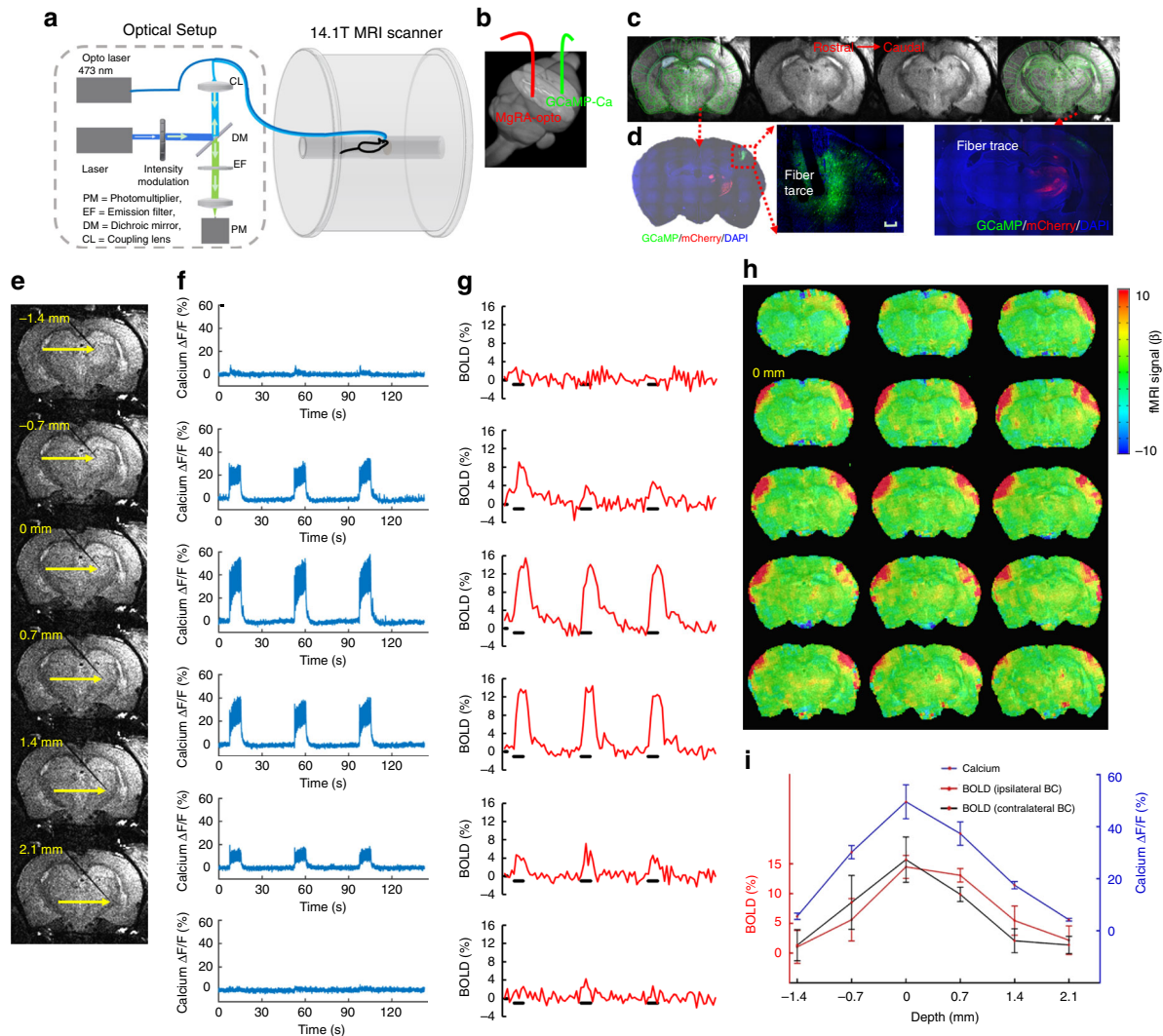


Fig. 4 MgRA-driven stepwise optogenetic activation of the thalamic nuclei with simultaneous fMRI and neuronal Ca^{2+} recordings. **a** Schematic drawing of the experimental setup to conduct optogenetic fMRI with simultaneous fiber optic calcium recording. The optical setup was placed outside the 14.1 T scanner. Opto Laser: laser for optogenetics. **b** Schematic of the fiber optic insertion inside the rat brain (3D view) with MgRA-controlled optical fiber for optogenetic activation (red) and a second optical fiber for calcium recording (green) in the barrel cortex. **c** The anatomical MRI images confirm the location of the recording fiber and the stimulation fiber targeting the VPM thalamic region. The brain atlas is superimposed on the anatomical image (green). **d** The immunostaining images show the ChR2 expression in the thalamic region (ChR2-mCherry marked in red), as well as the GCaMP6f expression (green) in the vibrissal S1 cortical neurons (BC) with the fiber trace. Scale bar, 200 μm . **e** Anatomical RARE MR images illustrate the fiber tip location at 6 steps, at a step-size of 700 μm . **f** Percentage changes of the evoked calcium signal for 3 epochs upon light stimulation (3 Hz, 10 ms pulse width, 3.7 mW laser power, 8 s on 37 s off block design). **g** Simultaneous BOLD signals for 3 epochs within the ipsilateral somatosensory cortex (see (h)). **h** Evoked BOLD fMRI map when the fiber tip was positioned at 0 mm along the insertion trajectory (zero considered as the position that leads to the peak fMRI and calcium signals). **i** Average amplitudes of the ipsilateral evoked calcium and BOLD signals of both hemispheres as a function of the fiber tip locations. Error bars represent mean \pm SD

Discussion

This work presents an MRI compatible robotic arm as the navigation technique for accurate placement of optical fibers in multi-modal fMRI studies in animals using ultra high-field MRI (14.1 T scanner). The MgRA was first developed and improved with a series of phantom tests and was posteriorly evaluated in vivo for deep brain optical fiber placement. MgRA-driven optogenetic activation at subcortical nuclei, e.g., LH and VPM, in a stepwise manner not only demonstrates the high precision of MgRA to target subcortical brain nuclei as deep as 8–9 mm from the skull surface, but also increases the reproducibility of the region-specific optogenetic activation for the whole-brain fMRI mapping in combination with the concurrent fiber optic calcium recordings. Also noted is that the mobility range of the MgRA (10 mm

in the rostral–caudal and medial–lateral directions) is sufficient to reach any brain structure in small animals for optogenetic fMRI and intracellular calcium recording. In addition, the MgRA was applied for real-time microinjection to specific deep brain nuclei, as demonstrated with an Mn-enhanced MRI method, demonstrating its microinjection capabilities for contrast agent or drug delivery with high precision inside the MRI scanner.

The main challenge when targeting deep brain structures is the potential error that appears between the actual and the calculated coordinates due to the variability in bregma location, skull thickness/angles, and potential shift of brain structures within the cranium after dura removal^{50–52}. This potential error is particularly problematic when targeting some functional nuclei or neuronal fiber tracts of the rat brain that are less than 2–300 μm in

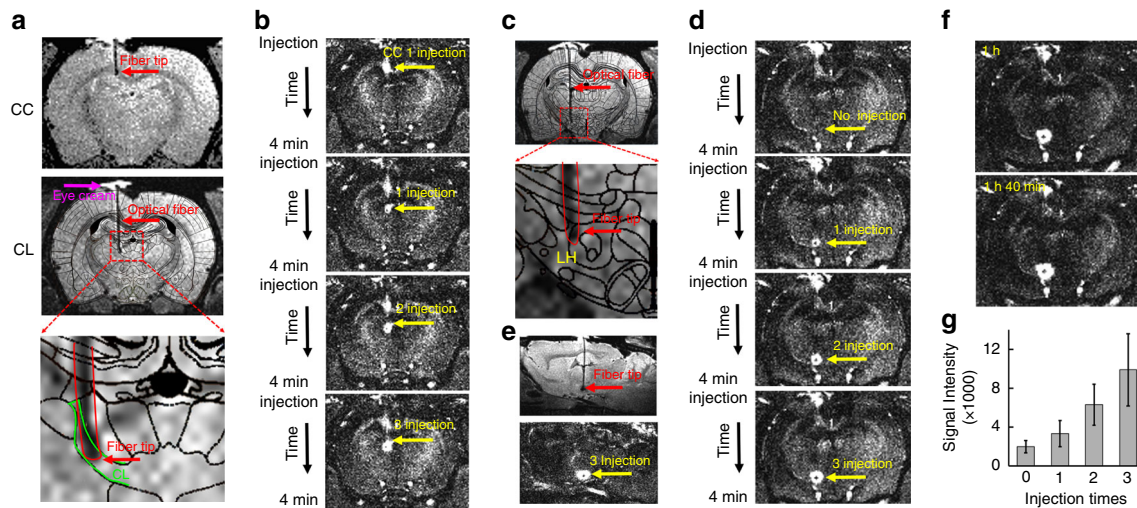


Fig. 5 MgRA-driven Mn-injection into CL and LH. **a** Top: the representative RARE anatomical image used to clarify the optical fiber location driven by MgRA for Mn injection in CC. Middle: the atlas overlapped RARE images to illustrate the fiber tip location at the CL. Eye cream is covering the craniotomy (magenta arrow). Bottom: enlarged image of fiber location. **b** T1-weighted MPRAGE image (Mdeft) showing enhanced signal from Mn injection site in the CC and CL with dose-dependency. **c** Top: the atlas overlapped RARE images to illustrate the fiber tip location at the LH, Bottom: enlarged image of fiber location. **d** T1-weighted MPRAGE image showing enhanced signal from Mn injection site in the LH with dose-dependency. **e** Sagittal view of RARE anatomical image and MPRAGE image after MnCl_2 solution injection. **f** T1-weighted MPRAGE image at 1 h and 1 h 40 min after the injection. **g** The analysis of MEMRI signal at no injection, 1 injection, 2 injection, and 3 injection times, as shown in (b, d) ($n = 5$ injection points from 3 animals). Error bars represent mean \pm SD

one of their dimensions, such as the central thalamic nuclei or corpus callosal fibers^{38,53}. This problem can produce high variability when we try to target the deeper brain nuclei, e.g., LH, since longer trajectories are subjected to larger errors^{8,14}. In order to optimize the positioning of the optical fiber into precise coordinates of the rat brain, we propose to avoid the atlas-base blind implantation by using a real-time feedback strategy that allows visualization of the whole brain with MRI during fiber insertion. We designed an MRI-compatible robotic arm which allows lowering the optical fiber inside the rat brain with real-time MRI scanning. By combining MRI guidance with the precise control of four stereotactic parameters (radial angle, rostral-caudal, dorsal-ventral, medial-lateral), the MgRA can fine-tune the fiber positioning to conduct highly reproducible and stepwise optogenetic fMRI studies.

The number of applications for robotic arms in animal research is considerably increased as a result of their potential combination with MRI. Examples include an MR image-guided mini-DBS system for BOLD activation during subthalamic nucleus DBS in nonhuman primates in a 3 T scanner²⁶, an angle positioning system to increase the image signal intensity of fibrous microstructure in a 9.4 T 12 cm-bore scanner²⁷, an integrated system, driven by piezoelectric actuators, for auto-tuning of a multichannel transceiver array at 7 T²⁸ or MRI-compatible systems for focused ultrasound experiments in rodents in 3 T scanners^{54,55}. Here, we developed a stepper motor-controlled compacted MgRA system in a 14.1 T horizontal MRI scanner with built-in MRI compatible cameras and RF surface coils to drive fiber optic insertion for optogenetic fMRI studies with concurrent intracellular calcium recordings. To our knowledge, this is the first time to combine the multi-modal fMRI neuroimaging platform with the MRI-guided robotic controlling system for in vivo rodent brain functional mapping.

There are two key advantages that need to be highlighted from the mechanical design of the MgRA system. In high-field MRI scanners, the open space inside the magnetic bore above the animal brain is usually less than 3–4 cm, which significantly limits the kinematic design options for mechanical movement. Also, the

ultra-high field (>11.7 T) also limits the commercially available motor supplies that avoid the electromagnetic interference with the MR scanning. We designed the MgRA head-probe based on an Archimedean spiral mechanism to achieve high precision and accuracy to maneuver the optical fiber insertion at less than 50 μm step-size along the dorsal-ventral axis (Fig. 1g, Supplementary Fig. 11, and Supplementary Movie 4). This head-probe is controlled by a synchronous belt drive, which can carry up to 4 degree-of-freedom movements inside the horizontal bore of the 14.1 T MRI scanner (Supplementary Fig. 12), and only occupies 1.5–2 cm space.

To deal with the MRI compatibility, in addition to hydraulic^{56,57} or pneumatic^{27,58–60} actuators, other types such as ultrasonic or piezoelectric motors, which have been the favorite so far due to their non-magnetic core, short response time and small size^{61,62}, could have been utilized. However, no commercially available piezo motors are available for the 14.1 T MRI scanner and it has been recently shown that piezo motors could induce geometric distortions in MR images even at a lower magnetic field strength^{63,64}. Also, different MRI sequences could have effects on the behavior of ultrasonic motors⁶⁵. To address the compatibility issue, remotely actuated MR-compatible manipulators were implemented using drive shafts, belts, chain drive, and linkages to transfer the motion to the distant actuated points^{66–68}. We have applied the long robotic arm to allow us to apply the regular stepper motor to control the optical fiber insertion. As shown in the Supplementary Movies 2–5, the mechanical control of the optical fiber insertion remains highly precise and reliable in both ex vivo and in vivo tests. Our MgRA design not only provides a highly robust mechanical controlling system, but also solves the MRI compatibility issue with a reliable and economically affordable solution. We will further optimize our MgRA system by shortening the robotic arm and implementing the piezo motors with a safe distance to avoid electromagnetic interference.

Besides fulfilling the role of accurately placing the fiber tip at the desired coordinates, the MgRA provides a flexible platform (Fig. 1g) to identify, de novo, the ideal targets for deep brain

stimulation in pre-clinical studies. This could be easily investigated with the MgRA by moving the stimulating fiber and running opto-fMRI at different locations in one single study, particularly for “hypothesis-free” brain activity mapping studies. This application will be critical to optimize and specify the ideal subcortical targets aiming at controlling pathological tremor or searching for more reliable treatment for depression in animal models^{69–71}. Importantly, certain effects inherent in the insertion of electrodes or optical fiber into the brain can be visualized and avoided using the MgRA strategy. One example is the case of the potential collateral damage to the choroid plexus (Fig. 2c) or other blood vessels, which could be well monitored by real-time imaging and avoided by changing the trajectory of the fiber. This is a particularly relevant feature of the MgRA, as it contributes to the maintenance of certain integrity of the surrounding tissue, which is beyond the capabilities of the standard implantation techniques with stereotactic devices and is crucial for potentially translational studies, as raised in a report showing MRI-guided cell transplantation into the brain⁷².

Several limitations pertaining to the first version of the MgRA should be considered when interpreting the results of this study and for future optimization of the MgRA in high field MRI scanner for animal imaging. Firstly, the angle/direction of the optical fiber cannot be changed once that it has been placed inside the brain parenchyma, as this would lead to excessive tissue damage and/or bleeding. Instead, in case needed, the optical fiber should be withdrawn and reinserted; thus it is crucial to improve the algorithm to calculate the trajectory based on the location of the optical fiber tip in the agarose covering the craniotomy outside of the brain parenchyma. Secondly, it is noteworthy that, because of the long arm to keep the stepper motors work properly outside of the MRI scanner, the most precise movement occurs along the ventral–dorsal direction (Fig. 1g and Supplementary Movie 4). It will be an important step forward to implement the piezo motors with a safe distance to avoid electromagnetic interference, which would allow to dramatically shorten the robotic arm and, consequently, to optimize of the precision in all the axis. Thirdly, although we acquired the 3D anatomical images of the rat brain, the major registration procedure between atlas and MRI images is still based on a 2D registration algorithm, which is applied to control the fiber tip movement along the dorsal–ventral direction. In the future development, we will provide a real-time 3D registration system to take advantage of the full motor control movement capability of the MgRA system to achieve a fully automatic performance. Lastly, the precision measurement of the MgRA can be directly evaluated based on the real-time anatomical MRI images. However, the best resolution acquired so far in our MRI scanner is $50 \times 50 \mu\text{m}$ in-plane. The MRI spatial resolution is much lower than the mechanistic movement precision provided by the MgRA system. For future piezo-based micron-resolution motor control system, the implementation of an optical encoder inside the ultra-high magnetic field will be needed for the close-loop feedback.

In summary, the real-time MRI-guidance in a robotic controlling system is verified and practiced for the optical fiber brain intervention in animals using the high field MRI scanner (>14 T). This MgRA positioning system serves as a key component for the future multi-modal fMRI platform merging concurrent fMRI with optogenetics, fiber optic-mediated optical imaging, micro-injection, and even electrophysiological recordings. The high flexibility and precision of MgRA to target the deep brain nuclei with neural circuit-specificity expands the brain functional mapping studies from the cellular levels, to the neural circuit levels, and eventually to the systems' levels in combination with behavioral tests in animals.

Methods

MgRA system. The MgRA was manufactured by the Fine Mechanical and Electrical Workshop in the Max Planck Institute for Biological Cybernetics, Tuebingen, Germany. This system consists of a positioning module, the head of the MgRA, and a custom-designed user interface. The positioning module (back part) accommodates the stepper motors (ST4118D1804-B, Nanotec, Germany) to fulfill the optical fiber movement with multi-degree of freedom, and the head of the MgRA (front part) includes the driving pieces, cameras, and a customized rat holder (Fig. 1b). The coupling of the actuators (back part) to the matching toothed pulley in the head was achieved by a synchronous belt (Optibelt OMEGA 3M, OPTI-BELT, Germany) drive in a form-fit manner. The driving pieces with Archimedean spiral mechanism were manufactured manually or with a 3D printer (Form 2, Formlabs, Germany). The detailed design and components are shown in Fig. 1a–c, Supplementary Figs. 11–13, with a table of all components and the European patent as the following link: <https://patentscope.wipo.int/search/en/detail.jsf?docId=EP215319263&tab=PCTDESCRIPTION&maxRec=1000>. The movements include three dimensions like conventional stereotactic devices, as well as pitch and yaw (manually). With MRI-compatible cameras (RS-OV7949-1818, Conrad Electronic, Germany), the user can watch the fiber insertion in real time, while the robot is executing a maneuver. If any movement needs to be modified, the user can start, stop, change, or resume the fiber movement at any time from the user-interface. Most of the other components are constructed from fully MRI-compatible materials like plastic, carbon fiber, and a minimal amount of non-ferrous metals like brass and anodized aluminum to avoid eddy currents and deterioration of magnetic field homogeneity. The MRI-compatible arm including the head part and aluminum holder were placed inside the MRI scanner room. Digital components including stepper motors (ST4118D1804-B, Nanotec, Germany), the motor controller (SMC133-1, Nanotec, Germany) and motor power supply (NTS-24V-40A, Nanotec, Germany), were placed outside the scanner room (Supplementary Fig. 1).

Viral injection. The study was performed in accordance with the German Animal Welfare Act (TierSchG) and Animal Welfare Laboratory Animal Ordinance (TierSchVersV). This is in full compliance with the guidelines of the EU Directive on the protection of animals used for scientific purposes (2010/63/EU). The study was reviewed by the ethics commission (§15 TierSchG) and approved by the state authority (Regierungspräsidium, Tübingen, Baden-Württemberg, Germany). A total of 21 male Sprague–Dawley rats were used in this study.

Intracerebral viral injection was performed in 3–4-week-old male Sprague–Dawley to express the viral vectors containing the calcium-sensitive protein (GCaMP for calcium recording) or the light-sensitive protein channelrhodopsin-2 (ChR2 for optogenetics) in neurons. The construct AAV5.Syn.GCaMP6f.WPRE.SV40 (2.818e13 genome copies per milliliter) was used to express GCaMP in the BC and the constructs AAV9.CAG.hChR2(H134R)-mCherry.WPRE.SV40 (2.918e13 genome copies per milliliter) and AAV9.CaMKII.hChR2(E123A)-eYFP.WPRE.hGH (1.19e13 genome copies per milliliter) were used to express ChR2 in the thalamus and LH, respectively. Rats were anesthetized with 1.5–2% isoflurane via nose cone and placed on a stereotaxic frame, an incision was made on the scalp and the skull was exposed. Craniotomies were performed with a pneumatic drill so as to cause minimal damage to cortical tissue. For optogenetics, a volume of 0.6–1 μL was injected using a 10 μL syringe and 33-gauge needle. The injection rate was controlled by an infusion pump (Pump 11 Elite, Harvard Apparatus, USA). The stereotaxic coordinates of the injections were 2.5 mm posterior to Bregma, 5.0 mm lateral to the midline, 0.8–1.4 mm below the cortical surface to target the BC; 2.6–2.7 mm posterior to Bregma, 2.8 mm lateral to the midline, 5.5–6.0 mm below the cortical surface for the ventral posterior medial nucleus of thalamus (VPM); and 2.75–2.85 mm posterior to Bregma, 1.1 mm lateral to the midline, 7.5–7.9 mm below the cortical surface for LH. After injection, the needle was left in place for approximately 5 min before being slowly withdrawn. The craniotomies were sealed with the bone wax and the skin around the wound was sutured. Rats were subcutaneously injected with antibiotic and painkiller for 3 consecutive days to prevent bacterial infections and relieve postoperative pain.

Animal preparation for fMRI. Anesthesia was first induced in the animal with 5% isoflurane in chamber. The anesthetized rat was intubated using a tracheal tube and a mechanical ventilator (SAR-830, CWE, USA) was used to ventilate animals throughout the whole experiment. Femoral arterial and venous catheterization was performed with polyethylene tubing for blood sampling, drug administration, and constant blood pressure measurements. After the surgery, isoflurane was switched off and a bolus of the anesthetic alpha-chloralose (80 mg/kg) was infused intravenously. A mixture of Alpha-Chloralose (26.5 mg/kg/h) and pancuronium (2 mg/kg/h) was constantly infused to maintain the anesthesia/keep the animal anesthetized and reduce motion artifacts.

Fiber optic implantation and optogenetic stimulation. Before transferring the animal to the MRI scanner, 2 craniotomies were performed. Briefly, the animal was placed on a stereotaxic frame, the scalp was opened and two ~1.5 mm diameter burr holes were drilled on the skull. The dura was carefully removed and an optical fiber with 200 μm core diameter (FT200EMT, Thorlabs, Germany) was inserted

into the BC, at coordinates: 2.75–3.3 mm posterior to Bregma, 5.0 mm lateral to the midline, 1.2–1.4 mm below the cortical surface. An adhesive gel was used to secure the calcium recording fiber to the skull. The craniotomy for optogenetics (in VPM or LH) was covered by agarose gel for robotic arm-driven fiber insertion inside the MRI scanner. Toothpaste was applied within the ears to minimize MR susceptibility artifacts for the whole brain fMRI mapping. The eyes of the rats were covered to prevent stimulation of the visual system during the light-driven fMRI.

For optogenetic stimulation, square pulses of blue light (473 nm) were delivered using a laser (MBL-III, CNI, China) connected to the 200 μm core optical fiber (FT200EMT, Thorlabs, Germany) and controlled by Master 9 (Master-9, A.M.P.I., Israel). The light intensity was tested before each experiment, and was calibrated with a power meter (PM20A, Thorlabs, Germany) to emit 0.6–40 mW from the tip of the optical fiber for LH and thalamus. The power levels used for light-driven fMRI studies did not induce pseudo-BOLD signal due to heating effects, by testing in regions of interest both with and without ChR2 expression.

Immunohistochemistry. To verify the phenotype of the transfected cells, opsin localization, and optical fiber placement, perfused rat brains were fixed overnight in 4% paraformaldehyde and then equilibrated in 15 and 30% sucrose in 0.1 M PBS at 4 °C. 30 μm -thick coronal sections were cut on a cryotome (CM3050S, Leica, Germany). Free-floating sections were washed in PBS, mounted on microscope slides, and incubated with DAPI (VectaShield, Vector Laboratories, USA) for 30 min at room temperature. Wide-field fluorescent images were acquired using a microscope (Zeiss, Germany) for assessment of GCaMP expression in BC, ChR2 in LH and VPM. Digital images were minimally processed using ImageJ to enhance brightness and contrast for visualization purposes.

Optical setup. An OBIS laser was used as excitation light source (OBIS 488LS, Coherent, Germany) with a heat sink to enable laser operation throughout the entire specified temperature range from 10 to 40 °C. The light passed through a continuously variable neutral density filter (NDC-50C-2M-B, Thorlabs, Germany) and was reflected on a dichroic beam splitter (F48-487, AHF analysentechnik AG, Germany). The beam was collected into an AR coated achromatic lens (AC254-030-A, Thorlabs, Germany) fixed on a threaded flexure stage (HCS013, Thorlabs, Germany) mounted on an extension platform (AMA009/M, Thorlabs, Germany) of a fiber launch system (MAX350D/M, Thorlabs, Germany). The laser beam was injected into the fiber and propagated to the tip. The emitted fluorescence was collected through the fiber tip, propagated back and collimated by the achromatic lens, passed through the dichroic beam splitter and filtered by a band-pass filter (ET525/50M, Chroma, USA) and focused by an AR coated achromatic lens (AC254-030-A, Thorlabs, Germany). A silicon photomultiplier module (MiniSiM 10035, SensL, Germany) was applied to detect the emitted fluorescence. The entire optical system was enclosed in a light isolator box. The photomultiplier output was amplified (gain = 100) by a voltage amplifier (DLPVA-100-BLN-S, Femto, Germany), digitized and detected by Biopac system (MP150 System, BIOPAC Systems, USA).

MRI image acquisition. All images were acquired with a 14.1 T/26 cm horizontal bore magnet interfaced to an Avance III console and equipped with a 12 cm gradient set capable of providing 100 G/cm over a time of 150 μs . A transceiver single-loop surface coil with an inner diameter of 22 mm was placed directly over the rat head to acquire anatomical and fMRI images. Magnetic field homogeneity was optimized first by global shimming for anatomical images and followed by FASTMAP shimming protocol for EPI sequence.

Anatomical images were acquired for approximate fiber location using 3D FLASH MRA sequence with the following parameters: repetition time, 20 ms; echo time, 2.82 ms; FOV: 2.28 cm \times 2.28 cm \times 2.28 cm, matrix = 114 \times 114 \times 114, spatial resolution = 0.2 mm \times 0.2 mm \times 0.2 mm. A high-resolution RARE sequence was used accurately identify the optical fiber in the coronal plane, with the following parameters: repetition time, 1200 ms; echo time, 7 ms; FOV: 1.92 cm \times 1.68 cm, matrix = 128 \times 112, resolution = 0.15 mm \times 0.15 mm, slice thickness = 0.5 mm, RARE factor = 8, averages = 16.

Higher resolution (50 μm) RARE sequence, specifically for Fig. 1f, g, to accurately identify the optical fiber in the coronal plane, with the following parameters: repetition time, 1500 ms; echo time, 11.0428 ms; FOV: 1.92 cm \times 1.56 cm, matrix = 384 \times 312, resolution = 50 μm \times 50 μm , slice thickness = 0.75 mm, RARE factor = 6, averages = 6.

For Mn injections and Mn tracing studies, rats received 150 nL of 5 mM MnCl₂ (MnCl₂, Sigma-Aldrich, Germany) solution for three times delivered by a hollow core photonic crystal fiber (diameter: ~240 μm)^{39–41}, manufactured by the Division of Photonic Crystal Fibre Science at Max-Planck Institute for the Science of Light, Erlangen, Germany. A magnetization prepared rapid gradient echo (MP-RAGE) sequence³⁵ was used. Eight coronal slices with FOV = 1.92 \times 1.92 cm, matrix 128 \times 128, thickness = 0.7 mm, (TR = 4000 ms, echo TR/TE = 15/1.7 ms, TI = 1000 ms, number of segments = 4, averages = 2), were used to cover the area of interest at 150 μm in-plane resolution with total imaging time 4 min 16 s. A same field of view T2-weighted RARE sequence was used with the following parameters: repetition time, 3000 ms; echo time, 8.3333 ms; FOV: 1.92 cm \times 1.92 cm, matrix = 128 \times 128,

resolution = 150 μm \times 150 μm , slice thickness = 0.7 mm, RARE factor = 6, averages = 4.

Functional MRI acquisition. Adjustments to echo spacing and symmetry, and B₀ compensation were set up first. Functional images were acquired with a 3D gradient-echo EPI sequence with the following parameters: echo time 12.5 ms, repetition time 1.5 s, FOV 1.92 cm \times 1.92 cm \times 1.92 cm, 48 \times 48 \times 48 matrix size, spatial resolution = 0.4 mm \times 0.4 mm \times 0.4 mm. To reach steady state 10 dummy scans were used. For anatomical reference, the RARE sequence was applied to acquire 48 coronal slices with the same geometry of the fMRI images.

For fMRI studies, needle electrodes were placed on the forepaw or whisker pads of the rats, and electric pulses (333 μs duration at 1.5 mA repeated at 3 Hz for 4 s) were first used as stimulation to serve as positive control for the evoked BOLD signal. Once that reliable fMRI signals were observed in response to electrical stimulation, optical stimulation was performed. An optical fiber of 200 μm core diameter (FT200EMT, Thorlabs, Germany) was connected to a 473 nm laser source (MBL-III, CNI, China) using a built-in FC/PC coupler to deliver blue light pulses at 3–10 Hz, 5–20 ms pulse width with different durations. To reach steady state 10 dummy scans were used and followed by 10 pre-stimulation scans, 5 scans during stimulation, and 25 inter-stimulation scans for 10 epochs and 5 scans during stimulation and 35 inter-stimulation scans for 12 epochs for thalamus and LH, respectively. The stimulation control was established using the BIOPAC system (MP150 System, BIOPAC Systems, USA) and Master 9 (Master-9, A.M.P.I., Israel).

Data analysis. For evoked fMRI analysis, EPI images were first aligned to anatomical images acquired in the same orientation with the same geometry. The anatomical MRI images were registered to a template across animals, as well as EPI datasets. The baseline signal of EPI images was normalized to 100 for statistical analysis of the multiple runs of EPI time courses. The hemodynamic response function (HRF) used the block function of the linear program 3dDeconvolve in AFNI. BLOCK (*L*, 1) is a convolution of a square wave of duration *L*, makes a peak amplitude of block response = 1, with the $g(t) = t^4 e^{-t}/[4^4 e^{-4}]$ (peak value = 1). The HRF model is defined as follows:

$$\text{HRF}(t) = \text{int}(g(t-s), s = 0.. \text{min}(t, L))$$

In this case, each beta weight represents the peak height of the corresponding BLOCK curve for that class, i.e., the beta weight is the magnitude of the response to the entire stimulus block.

The fiber optical neuronal calcium signals were low-pass filtered at 100 Hz using zero-phase shift digital filtering. The relative percentage change of fluorescence ($\Delta F/F$) was defined as $(F - F_0)/F_0$, where F_0 is the baseline, that is to say, the average fluorescent signal in a 2 s pre-stimulation window. The amplitudes of the neuronal fluorescent signal in response to 4 s optogenetic stimulus (Fig. 4f) were calculated as the average of difference in $\Delta F/F$ in a time window 300 ms after stimulus. Error bars in Figs. 3c, 4i, 5g, and Supplementary Fig. 10f represent standard deviation.

Reporting summary. Further information on research design is available in the Nature Research Reporting Summary linked to this article.

Data availability

The raw data can be provided upon email request to the corresponding author. Excel files containing raw data and each quantitative plot included in the main figures can be found in the Source Data File. For the design of the robotic arm, detailed information can be directly downloaded through the official link of World Intellectual Property Organization (WIPO): <https://patentscope.wipo.int/search/en/detail.jsf?docId=EP215319263&tab=NATIONALBIBLIO&maxRec=1000>.

Code availability

The Analysis of Functional NeuroImages software (AFNI, NIH, USA) and Matlab (MATLAB, MathWorks, USA) were used to process the fMRI and simultaneously acquired calcium signals, respectively. The relevant source codes can be downloaded through <https://afni.nimh.nih.gov/afni/>. The related image processing codes can be provided upon direct email request to the corresponding author.

Received: 11 August 2018 Accepted: 11 May 2019

Published online: 10 June 2019

References

1. Yu, X.: When Photons Meet Protons: Optogenetics, Calcium Signal Detection, and fMRI in Small Animals. In: Small Animal Imaging: Basics and Practical Guide, pp. 773 – 791 (Eds Kiessling, F., Pichler, B.J. & Hauff, P.). (Springer, Cham, Switzerland 2017).

2. Lee, J. H. et al. Global and local fMRI signals driven by neurons defined optogenetically by type and wiring. *Nature* **465**, 788–792 (2010).
3. Yu, X. et al. Sensory and optogenetically driven single-vessel fMRI. *Nat. Methods* **13**, 337–340 (2016).
4. Wang, M., He, Y., Sejnowski, T. J. & Yu, X. Brain-state dependent astrocytic Ca(2+) signals are coupled to both positive and negative BOLD-fMRI signals. *Proc. Natl. Acad. Sci. USA* **115**, E1647–E1656 (2018).
5. He, Y. et al. Ultra-slow single-vessel BOLD and CBV-based fMRI spatiotemporal dynamics and their correlation with neuronal intracellular calcium signals. *Neuron* **97**, 925–939 (2018).
6. Logothetis, N. K., Pauls, J., Augath, M., Trinath, T. & Oeltermann, A. Neurophysiological investigation of the basis of the fMRI signal. *Nature* **412**, 150–157 (2001).
7. Schulz, K. et al. Simultaneous BOLD fMRI and fiber-optic calcium recording in rat neocortex. *Nat. Methods* **9**, 597–602 (2012).
8. Liu, J. et al. Frequency-selective control of cortical and subcortical networks by central thalamus. *eLife* **4**, e09215 (2015).
9. Ferenczi, E. A. et al. Prefrontal cortical regulation of brainwide circuit dynamics and reward-related behavior. *Science* **351**, aac9698 (2016).
10. Kim, C. K. et al. Simultaneous fast measurement of circuit dynamics at multiple sites across the mammalian brain. *Nat. Methods* **13**, 325–328 (2016).
11. Marshall, J. D. et al. Cell-type-specific optical recording of membrane voltage dynamics in freely moving mice. *Cell* **167**, 1650–1662 (2016).
12. Tian, L. et al. Imaging neural activity in worms, flies and mice with improved GCaMP calcium indicators. *Nat. Methods* **6**, 875–881 (2009).
13. Chen, T. W. et al. Ultrasensitive fluorescent proteins for imaging neuronal activity. *Nature* **499**, 295–300 (2013).
14. Resendez, S. L. et al. Visualization of cortical, subcortical and deep brain neural circuit dynamics during naturalistic mammalian behavior with head-mounted microscopes and chronically implanted lenses. *Nat. Protoc.* **11**, 566–597 (2016).
15. Yu, X., Qian, C., Chen, D. Y., Dodd, S. J. & Koretsky, A. P. Deciphering laminar-specific neural inputs with line-scanning fMRI. *Nat. Methods* **11**, 55–58 (2014).
16. Dergacheva, O., Yamanaka, A., Schwartz, A. R., Polotsky, V. Y. & Mendelowitz, D. Optogenetic identification of hypothalamic orexin neuron projections to paraventricular spinally projecting neurons. *Am. J. Physiol. Heart Circ. Physiol.* **312**, H808–H817 (2017).
17. Kosse, C., Schone, C., Bracey, E. & Burdakov, D. Orexin-driven GAD65 network of the lateral hypothalamus sets physical activity in mice. *Proc. Natl. Acad. Sci. USA* **114**, 4525–4530 (2017).
18. Carter, M. E. et al. Tuning arousal with optogenetic modulation of locus coeruleus neurons. *Nat. Neurosci.* **13**, 1526–1533 (2010).
19. Sparta, D. R. et al. Construction of implantable optical fibers for long-term optogenetic manipulation of neural circuits. *Nat. Protoc.* **7**, 12–23 (2011).
20. Li, G. et al. Robotic system for MRI-guided stereotactic neurosurgery. *IEEE Trans. Biomed. Eng.* **62**, 1077–1088 (2015).
21. MacDonell, J. et al. Robotic assisted MRI-guided interventional interstitial MR guided focused ultrasound ablation in a swine model. *Neurosurgery* **84**, 1138–1148 (2018).
22. MacDonell, J. et al. Magnetic resonance-guided interstitial high-intensity focused ultrasound for brain tumor ablation. *Neurosurg. Focus* **44**, E11 (2018).
23. Starr, P. A. et al. Subthalamic nucleus deep brain stimulator placement using high-field interventional magnetic resonance imaging and a skull-mounted aiming device: technique and application accuracy. *J. Neurosurg.* **112**, 479–490 (2010).
24. Stoianovici, D. et al. Multi-imager compatible, MR safe, remote center of motion needle-guide robot. *IEEE Trans. Biomed. Eng.* **65**, 165–177 (2018).
25. Gassert, R., Moser, R., Burdet, E. & Bleuler, H. MRI/fMRI-compatible robotic system with force feedback for interaction with human motion. *IEEE/ASME Trans. Mech.* **11**, 216–224 (2006).
26. Min, H. K. et al. Subthalamic nucleus deep brain stimulation induces motor network BOLD activation: use of a high precision MRI guided stereotactic system for nonhuman primates. *Brain Stimul.* **7**, 603–607 (2014).
27. Squires, A. et al. MAPS—a magic angle positioning system for enhanced imaging in high-field small-bore MRI. *J. Med. Robot. Res.* **1**, 1640004 (2016).
28. Keith, G. A. et al. Automated tuning of an eight-channel cardiac transceiver array at 7 Tesla using piezoelectric actuators. *Magn. Reson. Med.* **73**, 2390–2397 (2015).
29. Ryali, S. et al. Combining optogenetic stimulation and fMRI to validate a multivariate dynamical systems model for estimating causal brain interactions. *NeuroImage* **132**, 398–405 (2016).
30. Lin, P., Fang, Z., Liu, J., Lee, J. H. Optogenetic Functional MRI. *J. Vis. Exp.* **110**, e53346, (2016). <https://doi.org/10.3791/53346>.
31. Bonnavion, P., Mickelsen, L. E., Fujita, A., de Lecea, L. & Jackson, A. C. Hubs and spokes of the lateral hypothalamus: cell types, circuits and behaviour. *J. Physiol.* **594**, 6443–6462 (2016).
32. Boyden, E. S., Zhang, F., Bamberg, E., Nagel, G. & Deisseroth, K. Millisecond-timescale, genetically targeted optical control of neural activity. *Nat. Neurosci.* **8**, 1263–1268 (2005).
33. Liu, J. V. et al. fMRI in the awake marmoset: somatosensory-evoked responses, functional connectivity, and comparison with propofol anesthesia. *NeuroImage* **78**, 186–195 (2013).
34. Yen, C. C., Papoti, D. & Silva, A. C. Investigating the spatiotemporal characteristics of the deoxyhemoglobin-related and deoxyhemoglobin-unrelated functional hemodynamic response across cortical layers in awake marmosets. *NeuroImage* **164**, 121–130 (2018).
35. Mugler, J. P. 3rd & Brookeman, J. R. Three-dimensional magnetization-prepared rapid gradient-echo imaging (3D MP RAGE). *Magn. Reson. Med.* **15**, 152–157 (1990).
36. Pautler, R. G., Silva, A. C. & Koretsky, A. P. In vivo neuronal tract tracing using manganese-enhanced magnetic resonance imaging. *Magn. Reson. Med.* **40**, 740–748 (1998).
37. Pautler, R. G. & Koretsky, A. P. Tracing odor-induced activation in the olfactory bulbs of mice using manganese-enhanced magnetic resonance imaging. *NeuroImage* **16**, 441–448 (2002).
38. Yu, X. et al. Thalamocortical inputs show post-critical-period plasticity. *Neuron* **74**, 731–742 (2012).
39. Cregan, R. F. et al. Single-mode photonic band gap guidance of light in air. *Science* **285**, 1537–1539 (1999).
40. Russell, P. Photonic crystal fibers. *Science* **299**, 358–362 (2003).
41. Knight, J. C., Birks, T. A., Russell, P. S. & Atkin, D. M. All-silica single-mode optical fiber with photonic crystal cladding. *Opt. Lett.* **21**, 1547–1549 (1996).
42. Turchi, J. et al. The basal forebrain regulates global resting-state fMRI fluctuations. *Neuron* **97**, 940–952 (2018).
43. Saleem, K. S. et al. Magnetic resonance imaging of neuronal connections in the macaque monkey. *Neuron* **34**, 685–700 (2002).
44. Schmid, M. C. et al. Blindsight depends on the lateral geniculate nucleus. *Nature* **466**, 373–377 (2010).
45. Okada, S. et al. Calcium-dependent molecular fMRI using a magnetic nanosensor. *Nat. Nanotechnol.* **13**, 473–477 (2018).
46. Ghosh, S., Harvey, P., Simon, J. C. & Jasanoff, A. Probing the brain with molecular fMRI. *Curr. Opin. Neurobiol.* **50**, 201–210 (2018).
47. Hai, A., Cai, L. X., Lee, T., Lelyveld, V. S. & Jasanoff, A. Molecular fMRI of serotonin transport. *Neuron* **92**, 754–765 (2016).
48. Lee, T., Cai, L. X., Lelyveld, V. S., Hai, A. & Jasanoff, A. Molecular-level functional magnetic resonance imaging of dopaminergic signaling. *Science* **344**, 533–535 (2014).
49. Barandov, A. et al. Sensing intracellular calcium ions using a manganese-based MRI contrast agent. *Nat. Commun.* **10**, 897 (2019).
50. Miyagi, Y., Shima, F. & Sasaki, T. Brain shift: an error factor during implantation of deep brain stimulation electrodes. *J. Neurosurg.* **107**, 989–997 (2007).
51. Kramer, D. R., Halpern, C. H., Danish, S. F., Jaggi, J. L. & Baltuch, G. H. The effect of intraventricular trajectory on brain shift in deep brain stimulation. *Stereotact. Funct. Neurosurg.* **90**, 20–24 (2012).
52. Pallavaram, S. et al. Effect of brain shift on the creation of functional atlases for deep brain stimulation surgery. *Int. J. Comput. Assist. Radiol. Surg.* **5**, 221–228 (2010).
53. Paxinos, G., Watson, C., Calabrese, E., Badaea, A. & Johnson, G. A. *MRI/DTI Atlas of the Rat Brain* (Elsevier, Academic Press, London, San Diego, 2015).
54. Chopra, R., Curiel, L., Staruch, R., Morrison, L. & Hynynen, K. An MRI-compatible system for focused ultrasound experiments in small animal models. *Med. Phys.* **36**, 1867–1874 (2009).
55. Yiannakou, M., Menikou, G., Yiallouras, C., Ioannides, C. & Damianou, C. MRI guided focused ultrasound robotic system for animal experiments. *Int. J. Med. Robot.* **13**, e1804 (2017). <https://doi.org/10.1002/rcs.1804>
56. Kim, D., Kobayashi, E., Dohi, T. & Sakuma, I. A new, compact MR-compatible surgical manipulator for minimally invasive liver surgery. *Lect. Notes Comput. Sci.* **2488**, 99–106 (2002).
57. Moser, R. et al. An MR compatible robot technology. *IEEE International Conference on Robotics and Automation*, 670–675 (2003).
58. Chen, Y. et al. Robotic system for MRI-guided focal laser ablation in the prostate. *IEEE/ASME Trans. Mech.* **22**, 107–114 (2017).
59. Franco, E., Ristic, M., Rea, M. & Gedroyc, W. M. Robot-assistant for MRI-guided liver ablation: a pilot study. *Med. Phys.* **43**, 5347 (2016).
60. Yoon, H. et al. Metabolomics of breast cancer using high-resolution magic angle spinning magnetic resonance spectroscopy: correlations with 18F-FDG positron emission tomography-computed tomography, dynamic contrast-enhanced and diffusion-weighted imaging MRI. *PLoS One* **11**, e0159949 (2016).
61. Su, H. et al. Piezoelectrically actuated robotic system for MRI-guided prostate percutaneous therapy. *IEEE/ASME Trans. Mech.* **20**, 1920–1932 (2015).
62. Tsekos, N. V., Khanicheh, A., Christoforou, E. & Mavroidis, C. Magnetic resonance-compatible robotic and mechatronics systems for image-guided

- interventions and rehabilitation: a review study. *Annu. Rev. Biomed. Eng.* **9**, 351–387 (2007).
63. Shokrollahi, P., Drake, J. M. & Goldenberg, A. A. Signal-to-noise ratio evaluation of magnetic resonance images in the presence of an ultrasonic motor. *Biomed. Eng. Online* **16**, 45 (2017).
 64. Shokrollahi, P., Drake, J. M. & Goldenberg, A. A. Ultrasonic motor-induced geometric distortions in magnetic resonance images. *Med. Biol. Eng. Comput.* **56**, 61–70 (2018).
 65. Shokrollahi, P., Drake, J. M. & Goldenberg, A. A. Comparing the effects of three MRI RF sequences on ultrasonic motors. *IFMBE Proc.* **51**, 846–849 (2015).
 66. Chinzei, K., Hata, N., Jolesz, F. A. & Kikinis, R. MR compatible surgical assist robot: system integration and preliminary feasibility study. *Medical Image Computing and Computer-Assisted Intervention—MICCAI 2000*, 921–930 (2000).
 67. Tajima, F. et al. A prototype master-slave system consisting of two MR-compatible manipulators with interchangeable surgical tools—part of a unified support system for diagnosis and treatment. *IEEE International Conference on Robotics and Automation Proceedings*, Vols. 1–5, 2505–2510 (2004).
 68. Tsekos, N. V., Ozcan, A. & Christoforou, E. A prototype manipulator for magnetic resonance-guided interventions inside standard cylindrical magnetic resonance imaging scanners. *J. Biomech. Eng. Trans. ASME* **127**, 972–980 (2005).
 69. Gradinaru, V., Mogri, M., Thompson, K. R., Henderson, J. M. & Deisseroth, K. Optical deconstruction of parkinsonian neural circuitry. *Science* **324**, 354–359 (2009).
 70. Plaha, P., Khan, S. & Gill, S. S. Bilateral stimulation of the caudal zona incerta nucleus for tremor control. *J. Neurol. Neurosurg. Psychiatry* **79**, 504–513 (2008).
 71. Ondo, W. G., Silay, Y., Almaguer, M. & Jankovic, J. Subthalamic deep brain stimulation in patients with a previous pallidotomy. *Mov. Disord.* **21**, 1252–1254 (2006).
 72. Silvestrini, M. T. et al. Interventional magnetic resonance imaging-guided cell transplantation into the brain with radially branched deployment. *Mol. Ther.* **23**, 119–129 (2015).

Acknowledgements

The authors thank Mr. S. Yu for building up the first prototype of the robotic arm and Fine Mechanic and Electronic Workshop at MPI for Biological Cybernetics for MgRA system automation. The financial support of the Max-Planck-Society, the Sino-Germany joint grant by DFG (YU215/3-1645423), and the China Scholarship Council (Ph.D. fellowship to Y. Chen) are gratefully acknowledged. We thank the collaborative support from Dr. G.A. Johnson to provide the original 3D MRI/DTI dataset for image processing and Dr. G. Paxinos for the support of brain atlas (the permission was issued by Elsevier). The authors thank Dr. N. Avdievitch, Ms. H. Schulz, Mr. F.

Sobczak, Mr. J.K. Schlüsener, and Mr. H. Huang for technical support, Dr. P. Douay, Dr. E. Weiler, Ms. S. Fischer, and Mrs. M. Pitscheider for animal support, the AFNI team for the software support, the Genetically-Encoded Neuronal Indicator and Effector (GENIE) Program and the Janelia Farm Research Campus for kindly providing viral plasmids.

Author contributions

X.Y. designed and supervised the research. Y.C., X.Y., P.P.-R., and X.C. performed animal experiments. Y.C., X.Y., and P.P.-R. acquired data. Y.C. analyzed data. X.C. and M.H.F. provided key technical support. X.Y. and Y.C. wrote the manuscript.

Additional information

Supplementary Information accompanies this paper at <https://doi.org/10.1038/s41467-019-10450-3>.

Competing interests: X.Y. and Y.C. are co-authors of a patent that describes the mechanical design of the MRI-guided robotic arm (EP3315064). The other authors declare no competing interests.

Reprints and permission information is available online at <http://npg.nature.com/reprintsandpermissions/>

Journal peer review information: *Nature Communications* thanks Cornelius Faber, Gregory Fischer, and other anonymous reviewer(s) for their contribution to the peer review of this work. Peer reviewer reports are available.

Publisher's note: Springer Nature remains neutral with regard to jurisdictional claims in published maps and institutional affiliations.



Open Access This article is licensed under a Creative Commons Attribution 4.0 International License, which permits use, sharing, adaptation, distribution and reproduction in any medium or format, as long as you give appropriate credit to the original author(s) and the source, provide a link to the Creative Commons license, and indicate if changes were made. The images or other third party material in this article are included in the article's Creative Commons license, unless indicated otherwise in a credit line to the material. If material is not included in the article's Creative Commons license and your intended use is not permitted by statutory regulation or exceeds the permitted use, you will need to obtain permission directly from the copyright holder. To view a copy of this license, visit <http://creativecommons.org/licenses/by/4.0/>.

© The Author(s) 2019

Supplementary Information

MRI-guided robotic arm drives optogenetic fMRI with concurrent Ca²⁺ recording

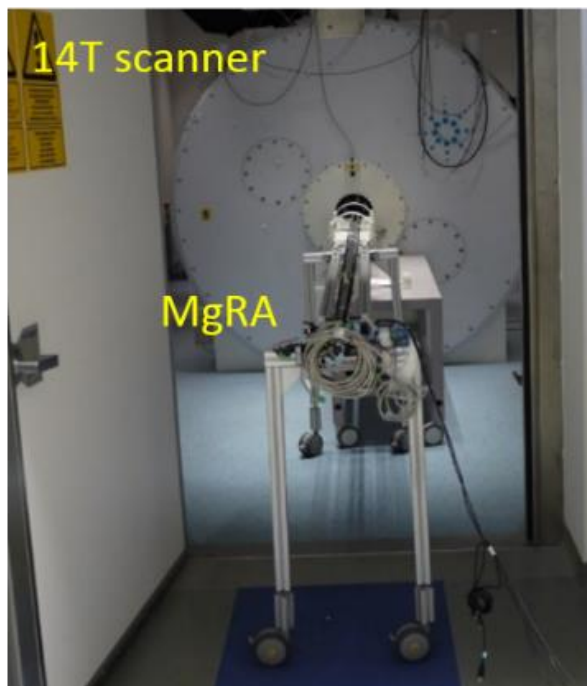
Chen et al.

Supplementary Table (1)

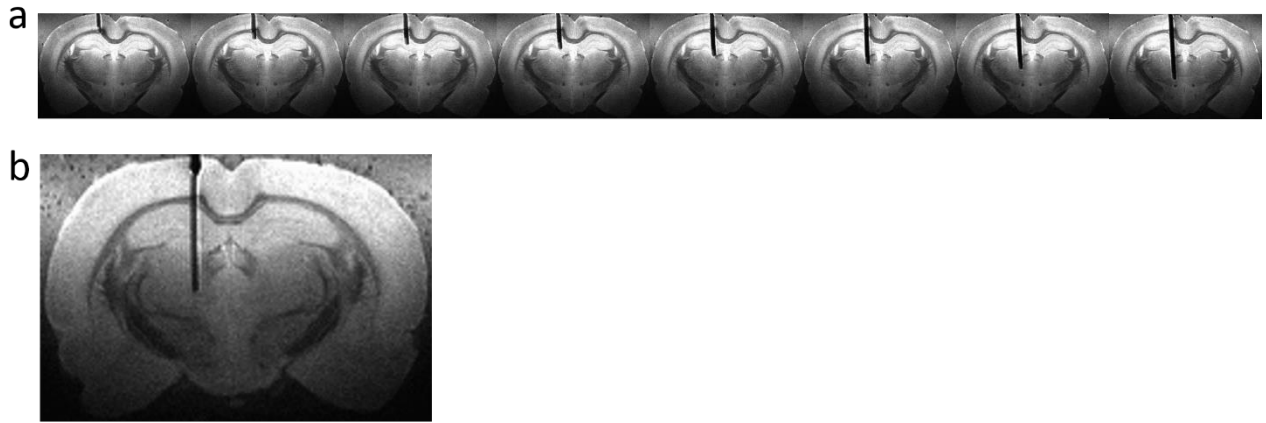
Supplementary Table 1. List of Components of MgRA

Name	Information
Archimedean spiral driving design	Custom-designed, MPI for BC Mechanic Workshop
Bearings for back/forward	JSM-2022-20, Igus, Germany
Bearings for left/right	BB-625-B180-10-GL, Igus, Germany
Belts	Optibelt OMEGA 3M, OPTIBELT, Germany
Camera	RS-OV7949-1818, Conrad Electronic, Germany
Carbon fiber tube (1)	7420182, R&G, Germany
Carbon fiber tube (2)	7420173, R&G, Germany
Charging condenser	Z-K4700/50, Nanotec, Germany
Cross table	Custom-designed, MPI for BC Mechanic Workshop
Encoder cable	ZK-NOE1-10-20000-S, Nanotec, Germany
Encoders	NOE2-05-B14, Nanotec, Germany
Gearbox	GPLE22-2S-12, Nanotec, Germany
Matching toothed pulley	Custom-designed, MPI for BC Mechanic Workshop
Motor controller	SMCI33-1, Nanotec, Germany
Platform for MgRA	Custom-designed, MPI for BC Mechanic Workshop
Power supply	NTS-24V-40A, Nanotec, Germany
Rat holder	Custom-designed, MPI for BC Mechanic Workshop
Robotic arm holder	Custom-designed, MPI for BC Mechanic Workshop
Stepper motor	ST4118D1804-B, Nanotec, Germany
USB cable for motor controller	ZK-USB, Nanotec, Germany
Cable lengthening	Custom-designed, MPI for BC Electronic Workshop
Other pieces of MgRA	Custom-designed, MPI for BC Mechanic Workshop

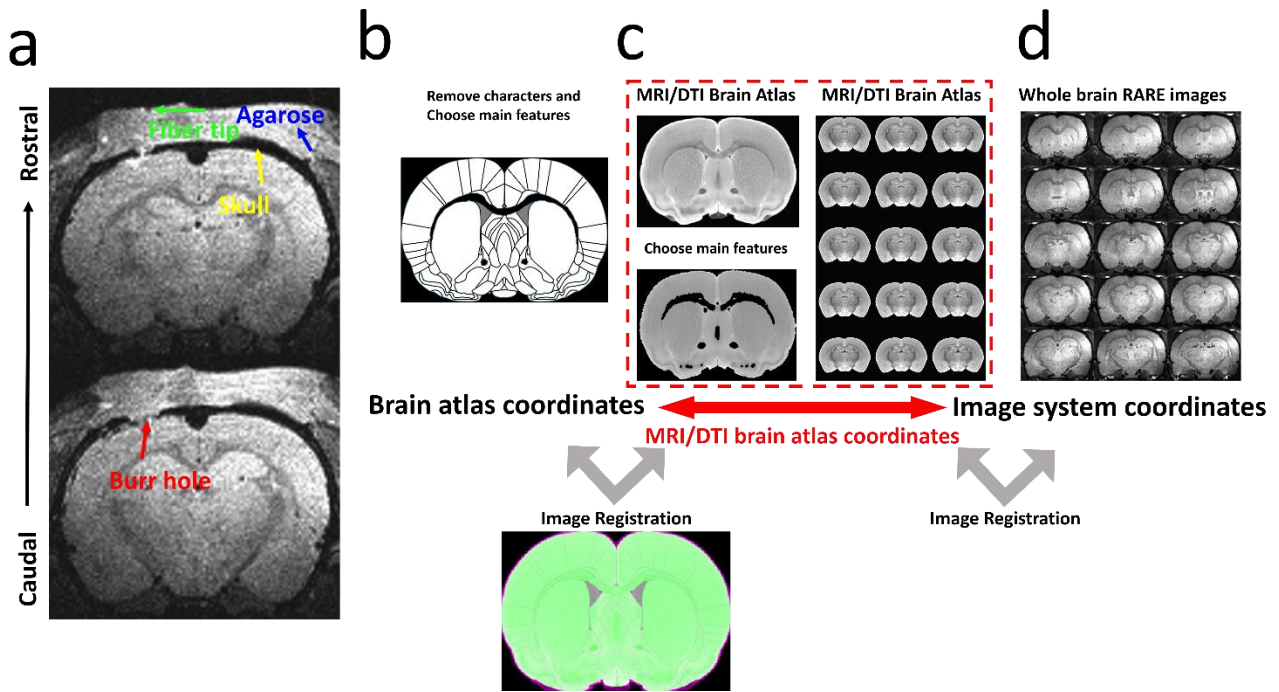
Supplementary Figures (13)



Supplementary Figure 1. MRI compatible MgRA mounted inside the 14T MRI scanner (picture taken from the control room).

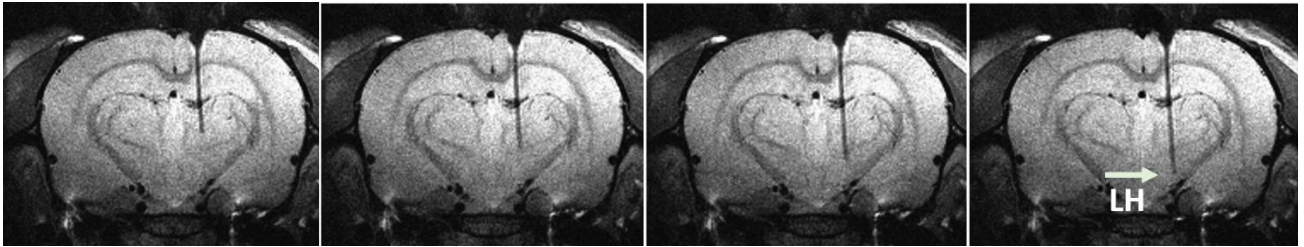


Supplementary Figure 2. Examples of optical fibers with different core diameters driven by MgRA for *in vitro* evaluation. **a** The T2-weighted MRI images show 8 different locations of the optical fiber (400 μm core diameter, black stripe) along the insertion trajectory in a perfused rat brain embedded in the soft agarose with manganese. **b** Optical fiber (200 μm core diameter, black stripe) was inserted vertically into the perfused rat brain.

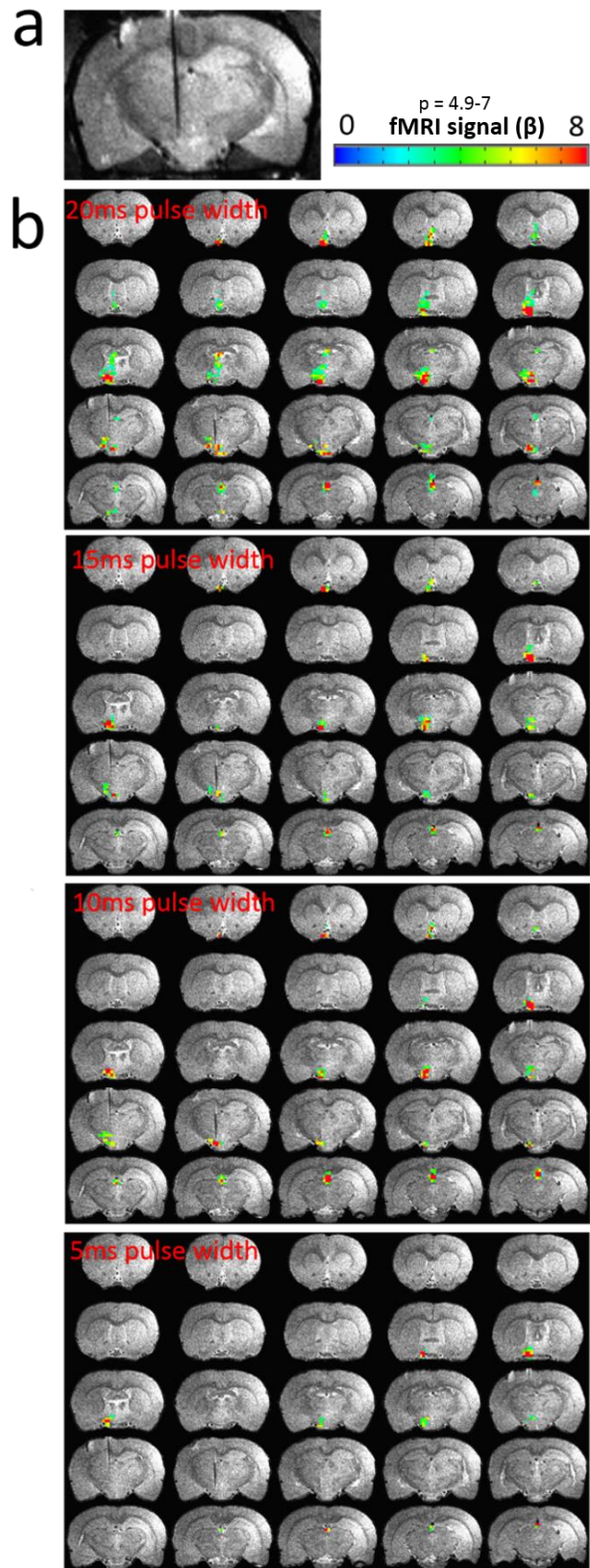


Supplementary Figure 3. MRI-based relocation outside of the rat brain and the registration of coordinates. **a** Agarose with manganese was applied to cover the skull (yellow arrow). By lowering the fiber into the agarose, we could calculate the distance between fiber tip (green arrow) and burr hole (red arrow) from the anatomical images. The burr hole is filled with agarose as well. **b** Atlas coordinates (Co1). **c** MRI/DTI Atlas of the Rat Brain (Co2, provided by Dr. G. Allen Johnson). **d** 3D anatomical images of an individual rat.

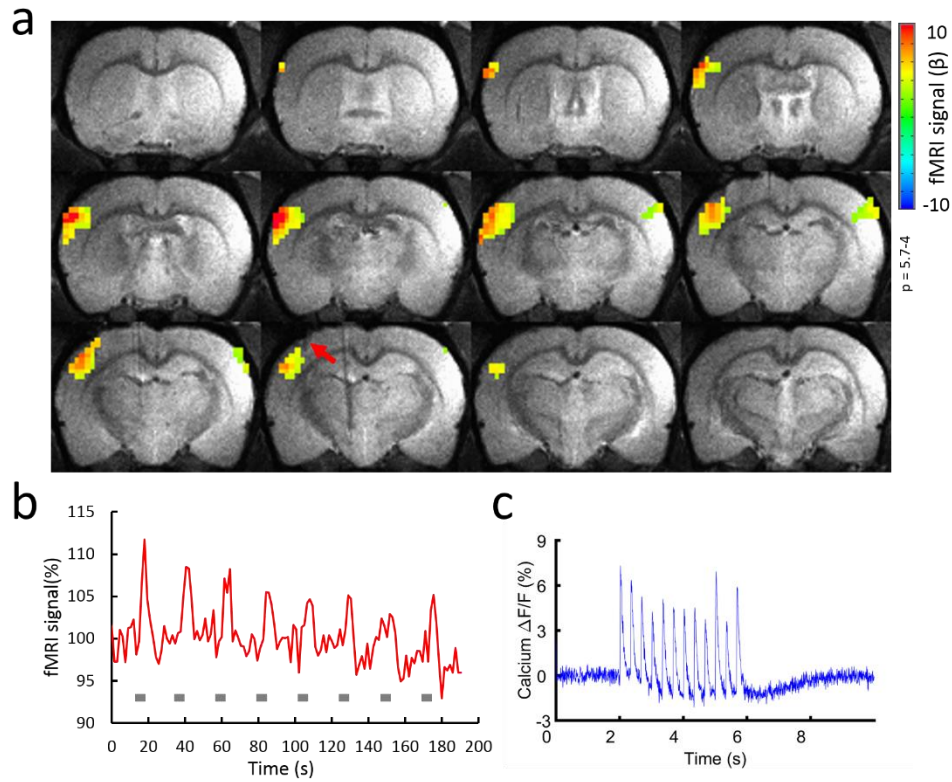
For coordinates registration, agarose has been previously applied above the burr hole of the skull and the fiber tip (previously positioned above the burr hole using the MgRA system under the guidance of the build-in camera inside the MR scanner) can be directly imaged to determine its coordinates in the MRI images (Supplementary Figure 3a). Then, an algorithm was designed to register a four coordinate system for the fiber tip position: atlas coordinate (Co1), MRI/DTI rat brain atlas (Co2, provided by Dr. G. Allen Johnson), MRI coordinate (Co3) and robotic arm coordinate (Co4). In short, the Co1 is first transferred to the Co2 by the algorithm (Supplementary Figure 3b, c). By registering the 2D anatomical images of individual rat (Co3) to the MRI/DTI brain atlas (Co2), the transformation between the Co1 and Co3 is settled (Red arrow in Supplementary Figure 3c). Since the fiber tip position is directly detected in the MRI images above the craniotomy, the related coordinate offset from the fiber tip to the targeted function nuclei can be calculated based on the multiple transformation matrices.



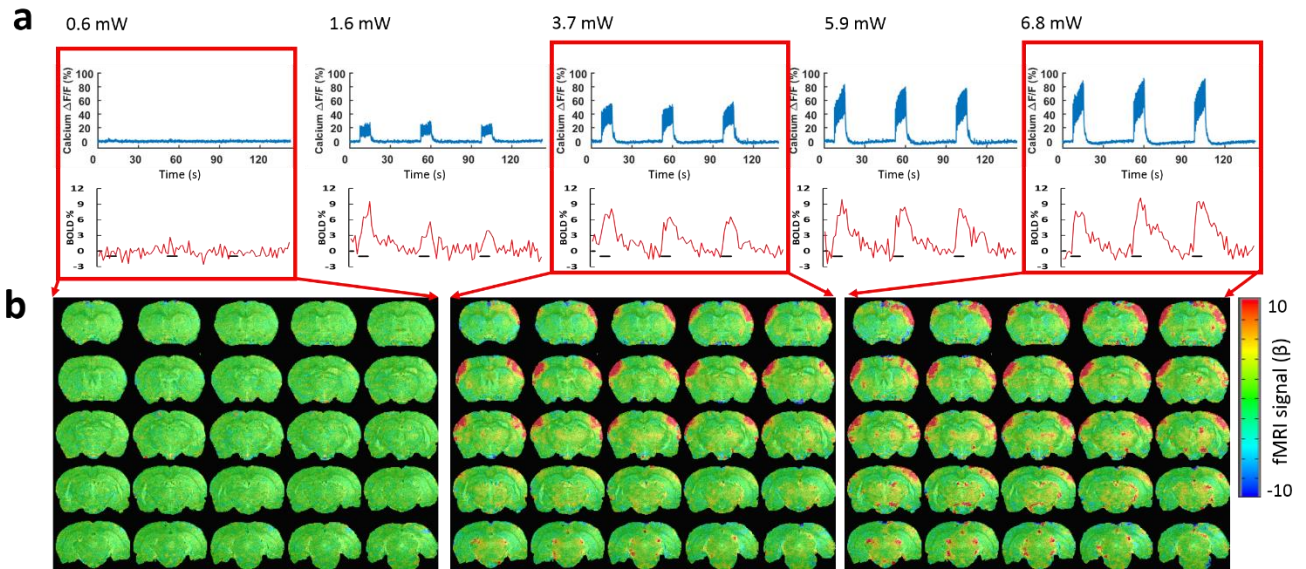
Supplementary Figure 4. The time-lapsed anatomical images to illustrate the optical fiber targeting the Lateral Hypothalamus for opto-fMRI studies.



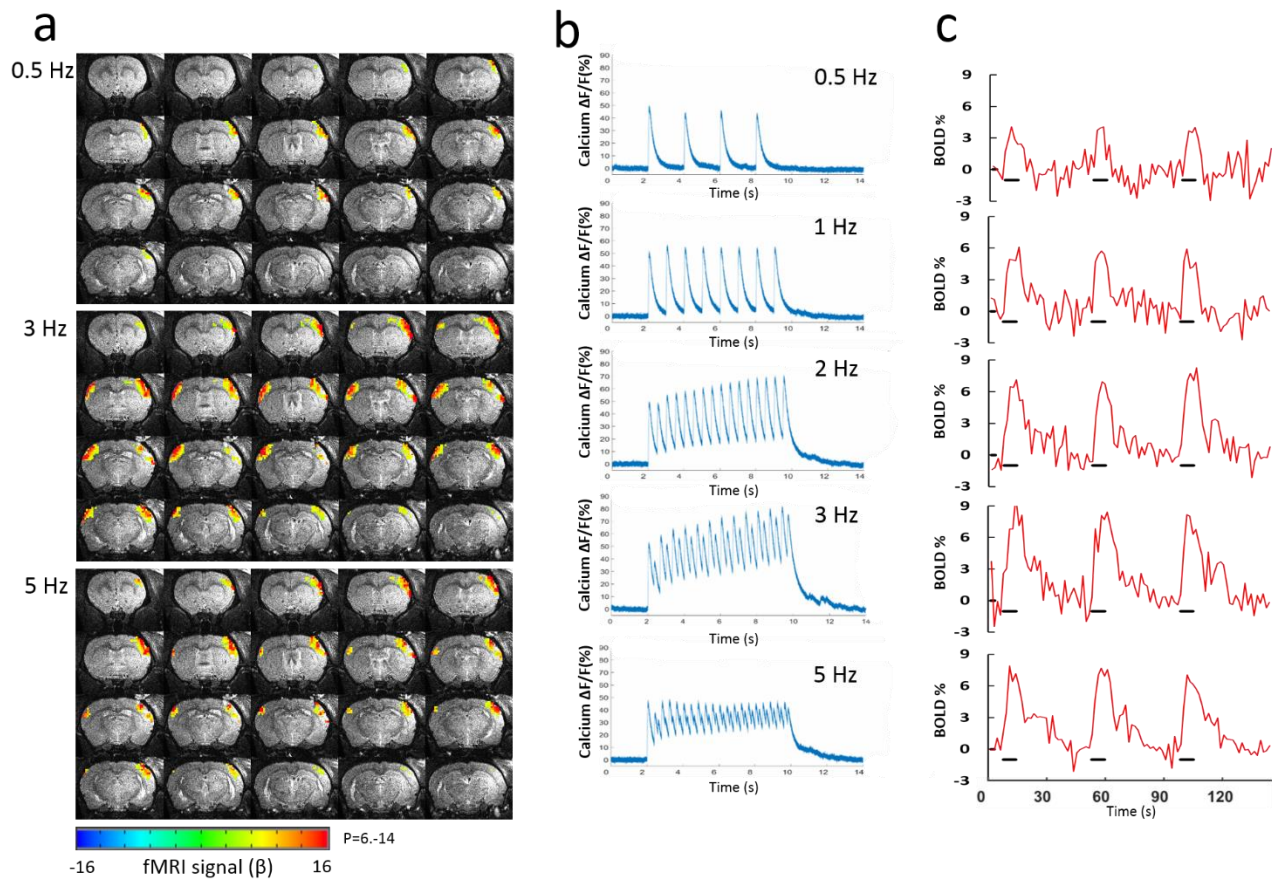
Supplementary Figure 5. Whole brain activity maps in response to 15s LH optogenetic stimulation at different pulse widths. **a** Anatomical image showing the position of the optical fiber for delivering light. **b** BOLD activation maps of a representative animal exhibited a pulse width-dependent pattern in response to 20ms, 15ms, 10ms and 5ms pulse widths (5 Hz, laser power of 12.6 mW, 15 s on 45 s off, 12 epochs). GLM-based t-statistics in AFNI is used.



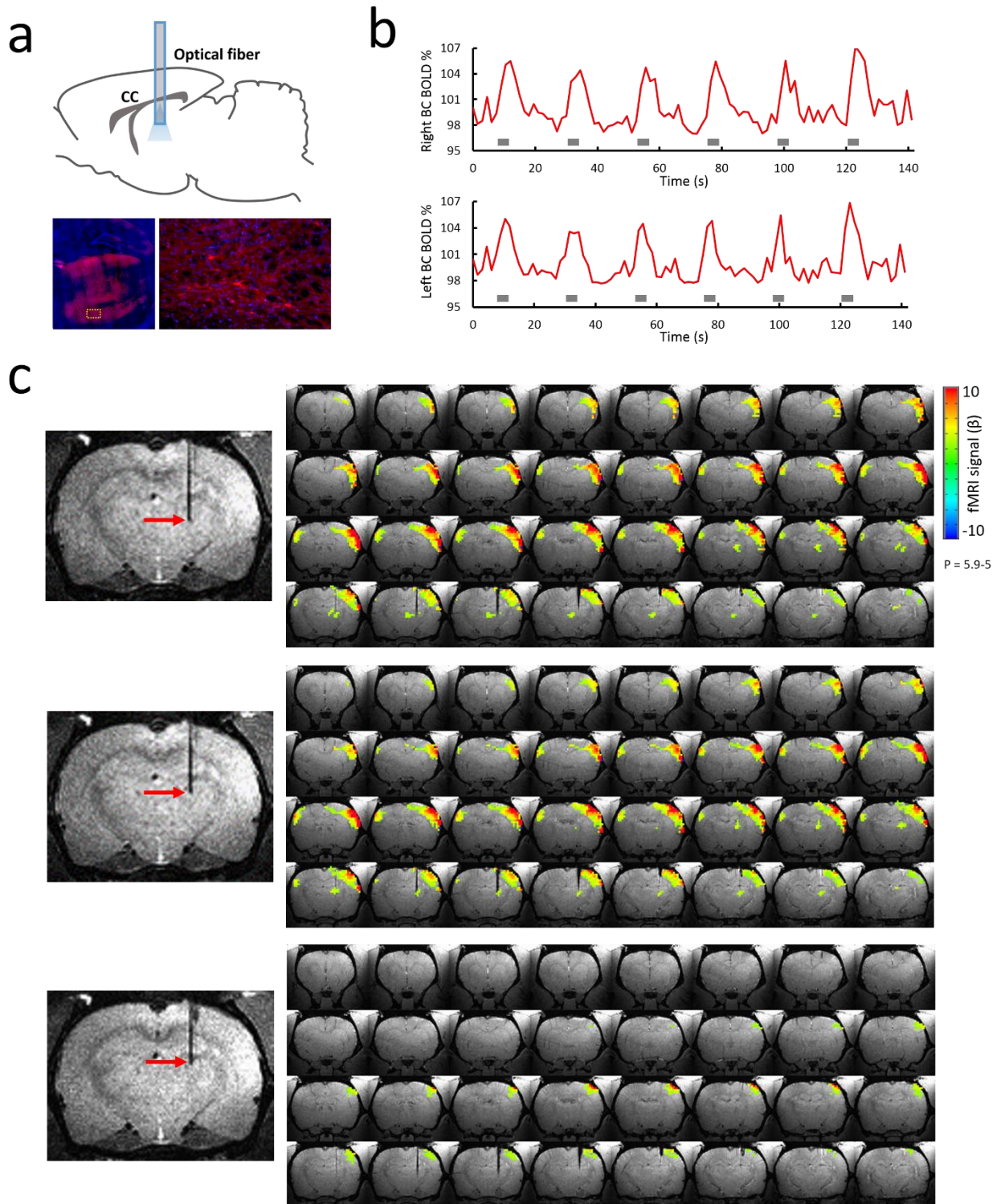
Supplementary Figure 6. Sensory-evoked neuronal Ca^{2+} recordings with simultaneous BOLD fMRI. **a** Representative color-coded BOLD-fMRI in response to a block design whisker-electrical stimulation. GLM-based t-statistics in AFNI is used. **b** The time course of evoked fMRI signal from BC-S1 ROI (see **a**) in the left hemisphere. **c** Average of simultaneously optical fiber (red arrow in **a**) recorded Ca^{2+} signals for one epoch (3 Hz, 4 s, 2 mA).



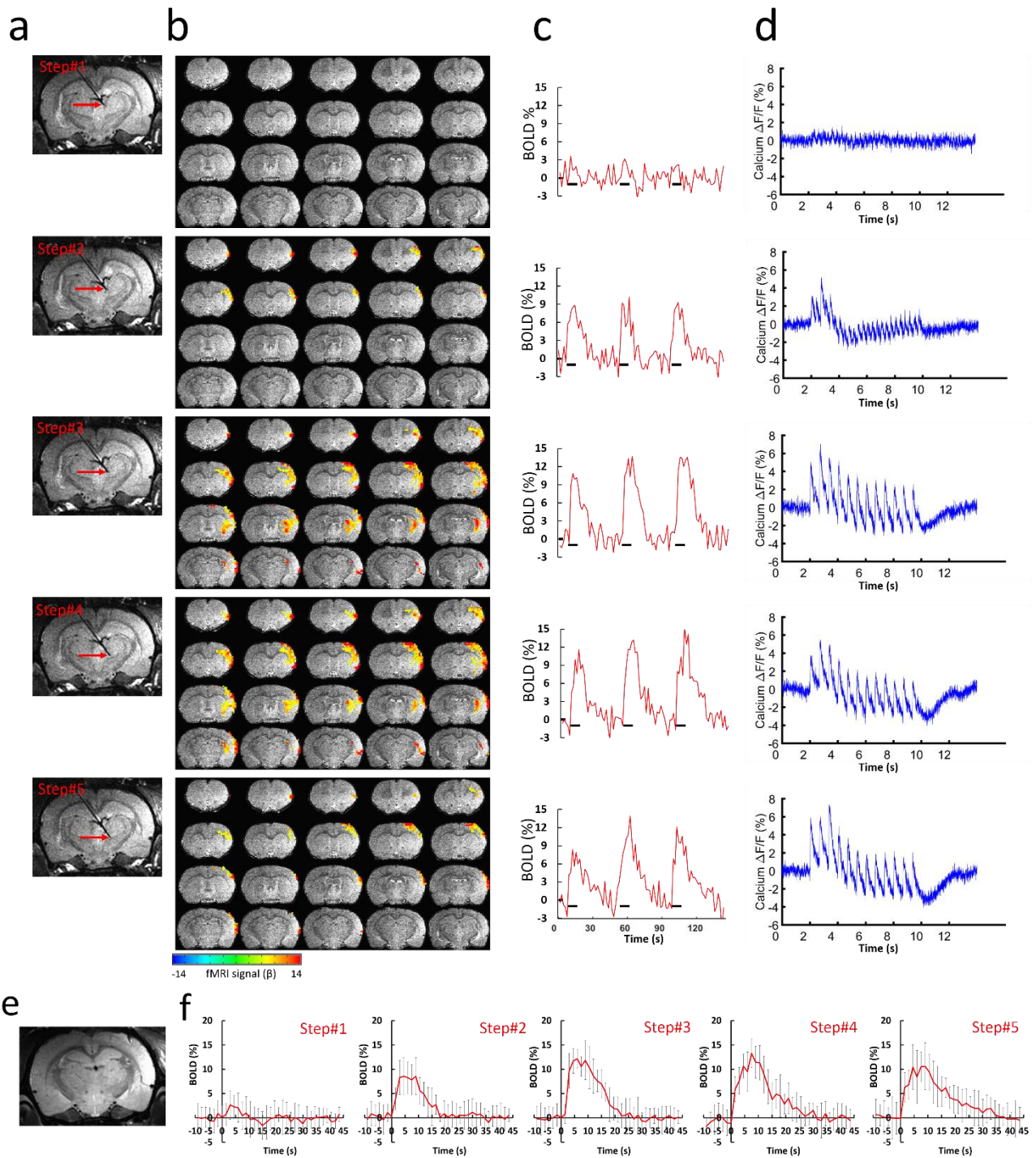
Supplementary Figure 7. Laser power dependent BOLD signals in S1 with simultaneous Ca^{2+} recordings (S1BF) upon light exposure in VPM. **a** Representative percentage changes of calcium signal (top) and BOLD responses (lower) for 3 epochs detected at 5 different laser powers. At 0.6 mW, hardly any fMRI and calcium signal was detected. BOLD and calcium signal increased proportionally with increased laser power. **b** Examples of whole brain activity maps at 0.6 mW, 3.7 mW and 6.8 mW.



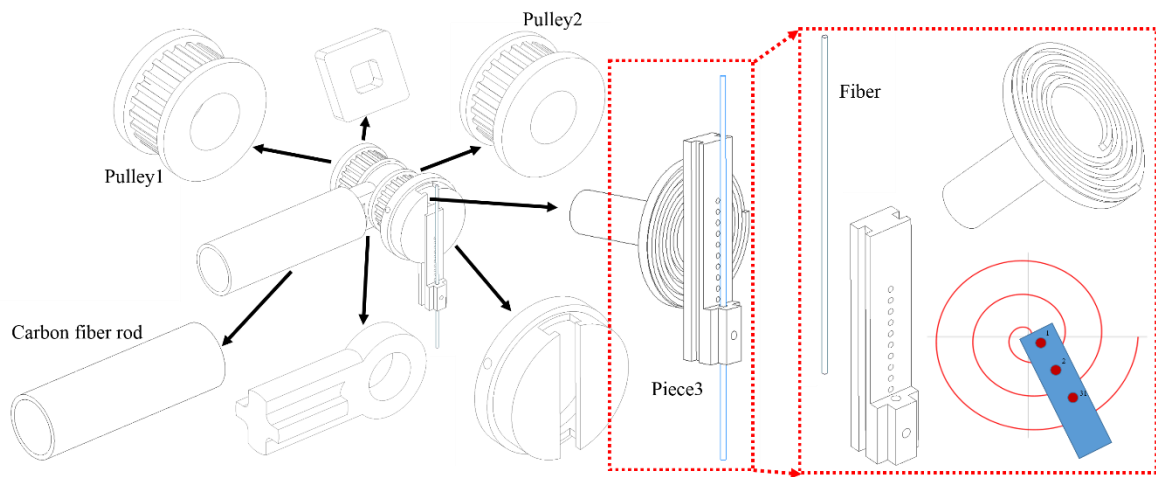
Supplementary Figure 8. Frequency dependent BOLD signals in S1 with simultaneous Ca^{2+} recordings (S1BF) upon light exposure in the Thalamus. **a** Examples of BOLD maps in response to 0.5 Hz, 3 Hz, 5 Hz. The strongest response was induced by 3 Hz stimulation, instead of 5 Hz. GLM-based t-statistics in AFNI is used. **b** Averaged calcium signal percentage change in one epoch. Evoked calcium spikes with almost full recovery to the baseline in 2 s per spike at 0.5 Hz. From 1 Hz to 3 Hz, the calcium signal was elevated through the 8 s stimulation period, while at 5 Hz, some of the spikes per pulse were even missed and the overall plateau amplitude was not further increased. **c** BOLD signal for 3 epochs upon stimulation (black line) was increased according to the increased frequency, but not at 5 Hz, which is consistent with the calcium signal observation.



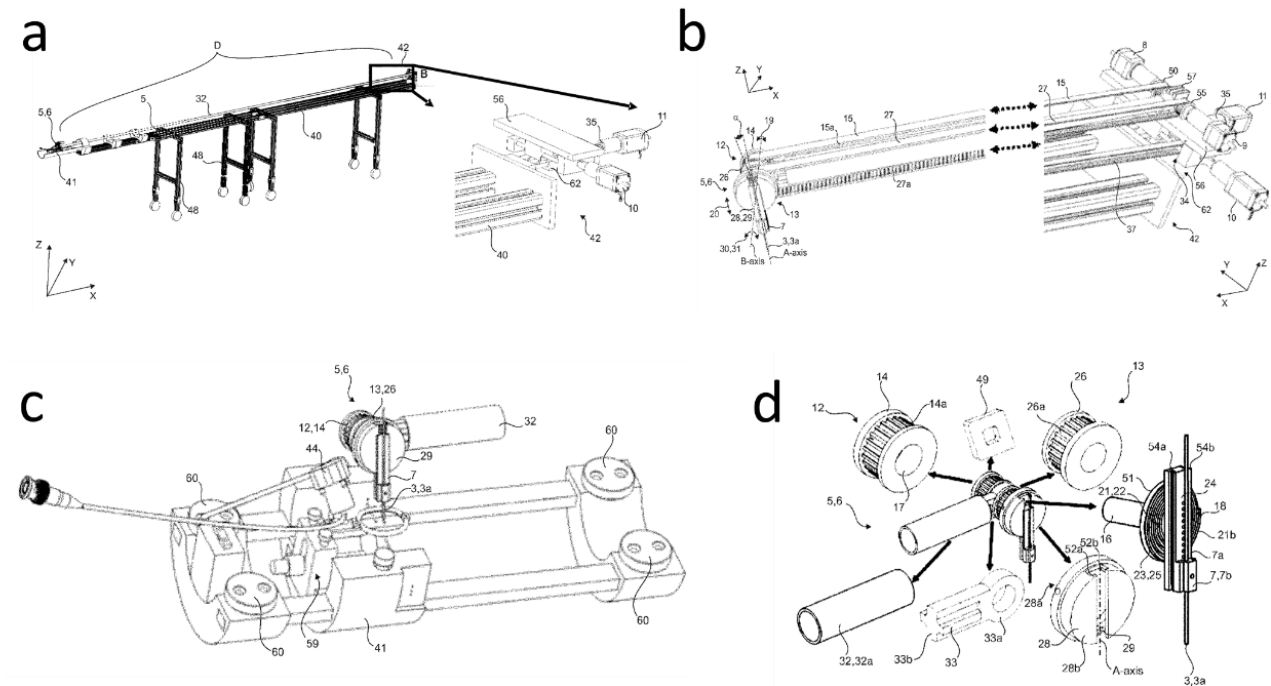
Supplementary Figure 9. Optogenetic excitation of thalamic cells drives local and Somatosensory cortical positive BOLD. **a** Top: Sketch showing the point of thalamic injection of AAV5.CAG.ChR2-mCherry and optical stimulation. Lower: histological image of ChR2-mCherry expression in the thalamus (left); higher magnification (right). Red, ChR2-mCherry; blue, 4',6-Diamidin-2-phenylindol (DAPI). **b** Opto-fMRI haemodynamic response (averaged across activated voxels in Somatosensory cortical ROI, see **c**, whole brain top right) in both hemispheres during optical stimuli (5Hz, 4s on 18.5s off, 10 ms pulse width, laser power 5.5 mW). **c** BOLD activation at 3 different locations along the vertical insertion trajectory. GLM-based t-statistics in AFNI is used.



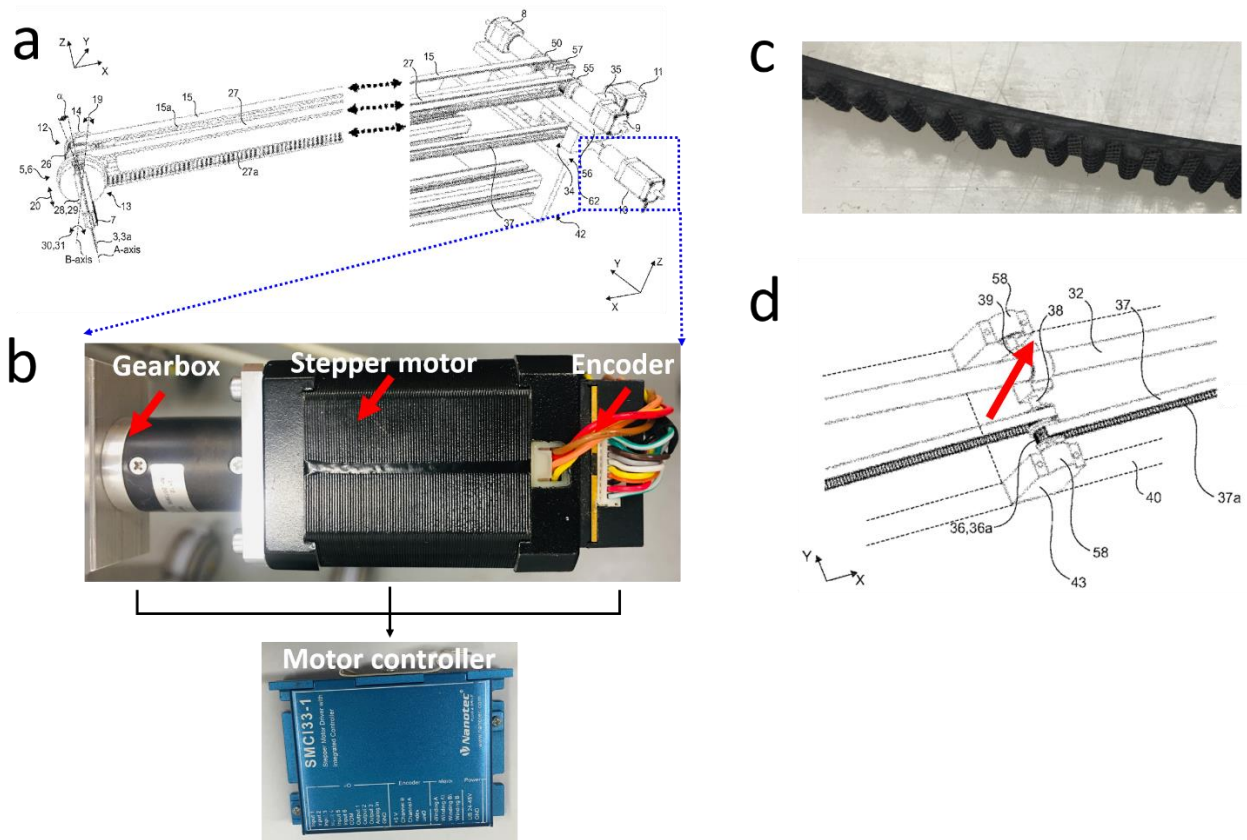
Supplementary Figure 10. Region-specific optogenetic activated neuronal Ca^{2+} recordings with simultaneous BOLD fMRI. **a** T2-weighted anatomical images illustrate five fiber locations. **b** Different BOLD fMRI in Somatosensory cortex evoked by optogenetic stimuli in different thalamic regions. **c** BOLD signals for 3 epochs (3 Hz, Laser power 4.2 mW, 8 s on 37 s off, 10 epochs) within ipsilateral Somatosensory cortex ROI (see **b** middle panel) corresponding to the different locations. **d** Simultaneously recorded evoked calcium signal through the 8 s stimulation period. **e** Anatomical RARE MR image illustrates the fiber tip location for calcium recording in Barrel cortex. **f** The average BOLD signals of ipsilateral hemisphere at different fiber tip locations. Error bars represent mean \pm SD.



Supplementary Figure 11. Detailed design for the head part of the MgRA.



Supplementary Figure 12. Detailed design of the MgRA (figures from the approved European patent). **a** The schematic view of the whole MgRA mechanical design including the cross table to mount the stepper motors. **b** The coupling of the stepper motors (back part) to the matching toothed pulley in the head was achieved by a synchronous belt drive in a form-fit manner. **c** Custom-designed rat holder with a built-in MRI compatible camera, surface coil and head part of the MgRA. **d** The components of the head part of the MgRA. For more details see the approved European patent as following link: (<https://patentscope.wipo.int/search/en/detail.jsf?docId=EP215319263&tab=PCTDESCRIPTION&maxRec=1000>).



Supplementary Figure 13. Detailed design of the back part of the MgRA. **a** The coupling of the stepper motors (back part) to the matching toothed pulley in the head was achieved by a synchronous belt drive in a form-fit manner. **b** The encoder (NOE2-05-B14, Nanotec, Germany) is used with motor controller (SMCI33-1, Nanotec, Germany) so that the stepper motor (ST4118D1804-B, Nanotec, Germany) can be run in a close-loop mode. **c** Multi-groove belt (optibelt OMEGA 3M, Optibelt, Germany) used to fit into a matching toothed pulley. **d** Closed belts can be cascaded to transfer the motion (red arrow). All schematic figures shown here are from the approved MgRA European patent.